RĪGAS
TEHNISKĀ
UNIVERSITĀTE

Shapla Bhattacharya

ENZĪMU INŽENIERIJA BIOMEDICĪNAS UN VIDES PROBLĒMU RISINĀJUMIEM

Promocijas darbs

ENZYME ENGINEERING FOR BIOMEDICAL AND ENVIRONMENTAL APPLICATION

Doctoral Thesis

RTU Izdevniecība
RTU Press
Rīga 2026

RĪGAS TEHNISKĀ UNIVERSITĀTE
Dabaszinātņu un tehnoloģiju fakultāte
Ķīmijas un ķīmijas tehnoloģijas institūts

RIGA TECHNICAL UNIVERSITY
Faculty of Natural Sciences and Technology
Institute of Chemistry and Chemical Technology

Shapla Bhattacharya
Doktora studiju programmas “Ķīmija, materiālzinātne un tehnoloģijas” doktorante
Doctoral Student of the Study Programme “Chemistry, Materials Science and Engineering”

ENZĪMU INŽENIERIJA BIOMEDICĪNAS UN VIDES PROBLĒMU RISINĀJUMIEM

Promocijas darbs

ENZYME ENGINEERING FOR BIOMEDICAL AND ENVIRONMENTAL APPLICATIONS

Doctoral Thesis

Zinātniskais vadītājs / Scientific Supervisor
docents, vadošais pētnieks / Prof. Dr. EMILIO PARISINI

Konsultanti / Consultants
profesors / Prof. Dr. chem.
AIGARS JIRGENSONS
Dr. ROSSELLA CASTAGNA

RTU Izdevniecība / RTU Press
Rīga 2026 / Riga 2026

Bhattacharya, S. Enzīmu inženierija biomedicīnas un vides problēmu risinājumiem. Promocijas darbs. – Rīga: RTU Izdevniecība, 2026. 168 lpp.

Bhattacharya, S. Enzyme Engineering for Biomedical and Environmental Application. Doctoral Thesis. – Riga: RTU Press, 2026. 168 p.

Publicēts saskaņā ar promocijas padomes “RTU P-01” 2026. gada 22. aprīļa lēmumu Nr. 04030-9.1/82.

Published in accordance with the decision of the Promotion Council “RTU P-01” of 22 April 2026, Minutes No. 04030-9.1/82.

Promocijas darbs izstrādāts ar Eiropas Sociālā fonda atbalstu darbības programmas “Izaugsme un nodarbinātība” 8.2.2. specifiskā atbalsta mērķa “Stiprināt augstākās izglītības institūciju akadēmisko personālu stratēģiskās specializācijas jomās” projektā Nr. 8.2.2.0/20/I/008 “Rīgas Tehniskās universitātes un Banku augstskolas doktorantu un akadēmiskā personāla stiprināšana stratēģiskās specializācijas jomās” un Rīgas Tehniskās universitātes Doktorantūras grantu programmas atbalstu.

NACIONĀLAIS ATTĪSTĪBAS PLĀNS 2020

EIROPAS SAVIENĪBA
Eiropas Sociālais fonds

IEGULDĪJUMS TAVĀ NĀKOTNĒ

This work has been supported by the European Social Fund within Project No. 8.2.2.0/20/I/008, “Strengthening of PhD students and academic personnel of Riga Technical University and BA School of Business and Finance in the strategic fields of specialization” of the Specific Objective 8.2.2 “To Strengthen Academic Staff of Higher Education Institutions in Strategic Specialization Areas” of the Operational Programme “Growth and Employment” and by Riga Technical University's Doctoral Grant programme.

NATIONAL DEVELOPMENT PLAN 2020

EUROPEAN UNION
European Social Fund

INVESTING IN YOUR FUTURE

Vāka attēla autore Shapla Bhattacharya.
Cover image by Shapla Bhattacharya.

PROMOCIJAS DARBS IZVIRZĪTS ZINĀTNES DOKTORA GRĀDA IEGŪŠANAI RĪGAS TEHNISKAJĀ UNIVERSITĀTĒ

Promocijas darbs zinātnes doktora (*Ph. D.*) grāda iegūšanai tiek publiski aizstāvēts 2026. gada 23. jūlijā plkst. 15.00 Rīgas Tehniskās universitātes Dabaszinātņu un tehnoloģiju fakultātē, Rīgā, Paula Valdena ielā 3/7, 272. auditorijā. Atklātajā sēdē būs iespējams piedalīties arī tiešsaistē *Zoom* platformā (*https://rtucloud1.zoom.us/j/9352086644*).

OFICIĀLIE RECENZENTI

Profesors *Dr. chem.* Kristaps Jaudzems
Latvijas Universitāte, Latvija

Profesors *Dr. chem.* Ioannis Pavlidis
Krētas Universitāte, Grieķija

Profesors *Dr. biol.* Gianluca Molla
Insubrijas Universitāte, Itālija

APSTIPRINĀJUMS

Apstiprinu, ka esmu izstrādājusi šo promocijas darbu, kas iesniegts izskatīšanai Rīgas Tehniskajā universitātē zinātnes doktora (*Ph. D.*) grāda iegūšana. Promocijas darbs zinātniskā grāda iegūšanai nav iesniegts nevienā citā universitātē.

Shapla Bhattacharya.......................(paraksts)
Datums: ………………………

Promocijas darbs sagatavots kā tematiski saistītu zinātnisko publikāciju kopa. Tas ietver kopsavilkumu un četras zinātniskās publikācijas. Zinātniskās publikācijas ir uzrakstītas angļu valodā, to kopējais apjoms, ieskaitot elektroniski pieejo informāciju, ir 168 lappuses.

SATURS

PROMOCIJAS DARBA VISPĀRĒJS RAKSTUROJUMS

Ievads

Enzīmi ir ļoti efektīvi dabas biokatalizatori, kas ļauj veikt sarežģītas bioķīmiskas reakcijas maigos apstākļos ar augstu specifiskumu un selektivitāti. To lietojums aptver plašu nozaru spektru, tostarp farmāciju, lauksaimniecību, diagnostiku un vides sanāciju. Tomēr dabiskajiem enzīmiem nereti ir novērojami tādi ierobežojumi kā zema stabilitāte rūpnieciskos apstākļos, nepietiekama aktivitāte vai slikta substrāta saderība, kas ierobežo to plašāku lietojumu.

Enzīmu inženierija ir sarežģīts process, kas ļauj modificēt dabā sastopamos enzīmus, lai uzlabotu to katalītisko efektivitāti, stabilitāti vai specifiskumu. Mērķtiecīgi mainot to aminoskābju secību un strukturālās īpašības, dabiskos enzīmus var pārvērst par efektīvākiem un izturīgākiem biokatalizatoriem, kas piemēroti plašam rūpniecisko lietojumu klāstam. Šajā sarežģītajā procesā bieži tiek izmantotas tādas metodes kā virzītā evolūcija, vietas virzītā mutagēze un datormodelēšana. Promocijas darba autores un viņas kolēģu laboratorijā plaši tiek izmantota strukturālā informācija, koncentrējoties uz racionālā dizaina pieejām.

Racionālajā dizainā tika izmantoti skaitļošanas rīki un molekulārā modelēšana, lai simulētu enzīma aminoskābju secības modifikāciju ietekmi. Analizējot enzīma trīsdimensiju struktūru, var identificēt kritiskos fragmentus, kas ietekmē katalītisko aktivitāti, stabilitāti un specifiskumu. Šī informācija ļauj ieviest mērķtiecīgas mutācijas, lai optimizētu īpašības, radot modificētus enzīmus, kas atbilst konkrētām rūpnieciskām vajadzībām.

Savā promocijas darbā autore strādāja ar divu enzīmu grupu dizainu – fruktozilpeptīdu oksidāzes (*FPOX*) un PETāzes. Abi šie enzīmi ir ļoti nozīmīgi biomedicīniskiem lietojumiem vai vides problēmu risinājumiem.

Fruktozilpeptīdu oksidāzes (*FPOX*) un fruktozilaminooksidāzes (*FAOX*) ir deglikozējoši fermenti, kas tiek izmantoti kā galvenās fermentatīvās sastāvdaļas diabēta uzraudzības ierīcēs. To izmantošana asins paraugos ļauj noteikt glikētā hemoglobīna un glikētā albumīna koncentrāciju, kas ir divi labi zināmi diabēta marķieri. Tomēr *FPOX*, ko pašlaik izmanto fermentu testos, nevar tieši noteikt visus glikētos proteīnus, tāpēc ir nepieciešams veikt mērķa proteīna proteolītisku pirmapstrādi, lai radītu mazus glikētus peptīdus, kas var darboties kā dzīvotspējīgi enzīma substrāti. Tas ir dārgs un laikietilpīgs process. Šis solis ir nepieciešams, lai piekļūtu grūti pieejamajai aktīvajai vietai, un šaurā tuneļa, kas nodrošina piekļuvi to katalītiskajai kabatai dēļ. Šie ierobežojumi ir pierādīti ar *FPOX* un *FAOX* enzīmu kristāliskajām struktūrām. Proocijas darbā tika veikta šīs enzīmu grupas dizaina izstrāde, lai paplašinātu to substrātu klāstu un uzlabotu to termisko stabilitāti biomedicīniskiem lietojumiem. Mērķis ir izmantot šos enzīmus, lai deglikētu neskartus proteīnus vai samazinātu to glikācijas līmeni laikā. Ar uzlaboto enzīmu promocijas darba autore vēlas izstrādāt fermentatīvu rīku glikēta hemoglobīna vai glikēta albumīna, divu pazīstamu diabēta marķieru, mērīšanai asinīs.

Izmantojot to pašu enzīmu inženierijas pieeju, tika strādāts arī ar plastmasas depolimerizācijas fermentiem (PETāzēm), kas ir fermenti, kas var sadalīt polietilēntereftalātu (PET) tā monomēros – tereftālskābē un etilēnglikolā. Šie enzīmi pieder pie lielākas hidrolāžu saimes, kas darbojas, degradējot PET estera saites un izraisot tā sadalīšanos mazākās monomērās.

Lai gan ir aprakstītas vairākas PETāzes, to katalītiskā efektivitāte un termiskā stabilitāte joprojām ir nepietiekama ekonomiski dzīvotspējīgai PET depolimerizācijai rūpniecībā, jo īpaši salīdzinājumā ar tradicionālajiem ķīmiskajiem un mehāniskajiem pārstrādes procesiem. Ierobežotā enzīmu darbība, jo īpaši zemā aktivitāte un sliktā stabilitāte tuvu PET stiklošanās temperatūrai, ir galvenais šķērslis ekonomiski pamatotai PET enzimātiskai pārstrādei. Tāpēc tika izmantota datorizētu fermentu inženierijas pieeja, lai uzlabotu katalītisko efektivitāti un darbības stabilitāti rūpnieciskai lietošanai.

Kopumā šis darbs veicina racionālas enzīmu inženierijas attīstību, parādot efektīvu, reproducējamu dizaina validācijas darba plūsmu un piemērojot to diviem atšķirīgiem, bet rūpniecībā nozīmīgiem fermentiem. Šī pētījuma rezultāti ir nozīmīgi turpmākai biokatalizatoru attīstībai un kritisku problēmu risināšanai medicīniskajā un vides biotehnoloģijā.

Pētījuma mērķis un uzdevumi

Promocijas darba galvenais mērķis ir veicināt enzīmu inženierijas attīstību, racionāli dizainējot, izstrādājot un raksturojot uzlabotus enzīmu variantus ar tiešu biomedicīnisko un vides lietojumu. Pētījums koncentrējas uz divām enzīmu saimēm – fruktozilpeptīdu oksidāzēm (*FPOX*) diabēta diagnostikai un polietilēntereftalāta hidrolāzēm (PETāzēm) plastmasas sadalīšanai.

Mērķi

Lietojums biomedicīnā – *FPOX* enzīmi diabēta diagnostikai

1. Pētīt savvaļas tipa *FPOX* enzīmu strukturālos ierobežojumus, kas kavē to spēju apstrādāt veselas glikētas olbaltumvielas.

2. Piemērot aprēķinu tunelēšanas paplašināšanas un struktūras vadītas inženierijas stratēģijas, lai radītu *FPOX* variantus ar uzlabotu substrāta pieejamību, uzlabotu termisko stabilitāti un paplašinātu substrāta specifiskumu.

3. Novērtēt inženierijas *FPOX* variantu aktivitāti uz glikētiem substrātiem, lai noteiktu to diagnostisko potenciālu.

Piemērošana vides jomā – PETāzes plastmasas sadalīšanai

1. Identificēt kustīgus un nestabilus pazīstamu PETāžu reģionus, izmantojot strukturālos datus un molekulārās dinamikas simulācijas.
2. Izstrādāt un ieviest mērķtiecīgas mutācijas, kuru mērķis ir uzlabot PETāzes termisko stabilitāti un katalītisko efektivitāti.
3. Novērtēt inženierijas PETāzes variantu ietekmi uz polietilēna tereftalāta sadalīšanās efektivitāti apstākļos, kas atbilst rūpnieciskajai pārstrādei.
4. Veikt mehānisma pētījumus, lai noteiktu, kā konkrētas mutācijas ietekmē PET sadalīšanās procesu.

Zinātniskā novitāte un galvenie rezultāti

Promocijas darba zinātniskā novitāte saistīta ar aprēķinu un eksperimentālo pieeju integrāciju uzlabotu enzīmu variantu racionālai dizainēšanai un raksturošanai, koncentrējoties uz divām atšķirīgiem enzīmiem – *FPOX* un PETāzi. Apvienojot *in silico* proteīnu inženieriju, molekulārās dinamikas simulācijas un strukturālo bioloģiju ar ekspresiju, attīrīšanu un detalizētu bioķīmisko un biofizikālo analīzi, šis darbs izveido starpdisciplināru validācijas darba plūsmu. Iegūtie rezultāti sniedz vērtīgas zināšanas un instrumentus enzīmu inženierijas jomā, vienlaikus piedāvājot potenciālu rūpnieciskai un vides lietošanai.

Promocijas draba pirmajā daļā autore koncentrējas uz termiski stabilizētu *FPOX* enzīmu. Tika piemērota *in silico* proteīnu inženierijas pieeja, lai uzlabotu enzīma kopējo termisko stabilitāti un tā katalītisko aktivitāti attiecībā uz lieliem substrātiem. Galīgais dizains uzrādīja ievērojamu termiskās stabilitātes uzlabojumu, salīdzinot ar savvaļas tipa fermentu, kā arī izteiktu tā piekļuves tuneļa paplašināšanos. Šīs izmaiņas izpaudās kā nozīmīga fermentatīvā aktivitāte virknē glikēto substrātu, parādot datorizētā dizaina potenciālu enzīmu funkciju pielāgošanai.

Promocijas darba otrajā daļā PET hidrolizējošais enzīma ICCG variants no lapu-zaru komposta kutināzes (*LCC-ICCG*; zelta standarts) tika tālāk modificēts, izmantojot datorizētu dizainu. Šie pētījumo rezultējās ar mutāciju *LCC-ICCG-C09,* kam piemita par 3,5 °C augstāka kušanas temperatūra (T_m), salīdzinot ar *LCC-ICCG*. Optimālos reakcijas apstākļos (68 °C) *LCC-ICCG-C09* hidrolizēja amorfo PET par tereftālskābi (TPA) ar divkārt augstāku efektivitāti, salīdzinot ar sākotnējo variantu. *LCC-ICCG-C09* ar uzlabotu termisko stabilitāti un katalītisko veiktspēju ir daudzsološs kandidāts turpmākai izmantošanai rūpnieciskajā PET pārstrādē.

Paralēli tika izstrādāts jauns PETāzei līdzīgs enzīms (PETāze SM14) no *Streptomyces sp. SM14*, kas tika ekspresēts *Escherichia coli* un novērtēts uz pēcpārstrādes plastmasas substrātiem. Aktivitātes analīzes kopā ar augstas veiktspējas šķidruma hromatogrāfiju (*HPLC*) produkta kvantificēšanai, kā arī skenējošo elektronu mikroskopiju un atomu spēku mikroskopiju substrāta virsmas analīzei atklāja, ka PETāze SM14 piemīt augsta sāls tolerance (līdz 1,5 M), laba siltuma izturība (T_m 56,26 °C) un optimāla aktivitāte, ja pH = 9,0. Tās rentgena kristāla struktūra, ko autore izrēķināja 1,43 Å gadījumā, apstiprināja PETāzes saimes konservatīvās īpašības un nodrošināja pamatu turpmākajām inženierijas stratēģijām.

Lai turpinātu pētīt strukturālos un funkcionālos mehānismus, visu atomu molekulārās dinamikas (MD) simulācijas tika apvienotas ar *in vitro* testiem, lai salīdzinātu *PETase* SM14 un *Ideonella sakaiensis* PETāze (IsPETāze) dažādās NaCl koncentrācijās (150 mM un 900 mM). Rezultāti parādīja, ka, pateicoties cilpas pagarinājumam, IsPETāze izrāda elastīgu un plašu saistīšanās vietu, kas uzlabo substrāta uzņemšanu, bet arī izspiež katalītiskos fragmentus, izraisot ātru deaktivāciju, īpaši augstās sāls koncentrācijās. Savukārt PETāze SM14 uzrāda stingru un šaurāku saistīšanās kabatu, kas paaugstinātā sāls koncentrācijā pakļaujas mērenai paplašināšanai, tādējādi veicinot ūdens un substrāta piesaistīšanu. Turklāt adsorbcijas uz PET plāksnītēm pētījumi parādīja, ka *PETase* SM14 augstas sāls koncentrācijas apstākļos un *IsPETase* zemas sāls koncentrācijas apstākļos saistās ar PET substrāta ķēdēm tādā pašā *trans:gauche* konformācijas sadalījumā, kāds novērots amorfa PET gadījumā. Šīs atziņas ne tikai izskaidro novērotos aktivitātes profilus, bet arī sniedz jaunas strukturālas detaļas, piemēram, substrāta saistīšanās plaisu arhitektūru un elektrostatisko vidi, galvenos aromātiskos atlikumus, kas iesaistīti polimēru ķēžu stabilizācijā, un virsmas lādiņa sadalījumu, lai veiktu PET noārdošo enzīmu izstrādi dažādiem vides apstākļiem.

Praktiskais lietojums

Šim darbam ir nozīmīgs praktisks potenciāls gan rūpnieciskajā, gan vides biotehnoloģijā. Inženierijas ceļā radītie *FPOX* varianti ar uzlabotu termisko stabilitāti un substrāta specifiskumu nodrošina stabilu pamatu jutīgu un praktisku biosensorisko platformu izstrādei tiešai glikēta hemoglobīna (HbA1c) noteikšanai. Uzlabotu PET hidrolizējošo enzīmu, tostarp *LCC-ICCG-C09* un *PETase* SM14, izstrāde piedāvā daudzsološus risinājumus polietilēna tereftalāta (PET) enzimātiskai pārstrādei, ļaujot slēgtā ciklā atgūt tereftālskābi un veicinot ilgtspējīgu plastmasas atkritumu apsaimniekošanu.

Darba struktūra un apjoms

Promocijas darbs ir tematiski saistītu zinātnisko publikāciju kopa par enzīnu inženieriju biomedicīniskiem un vides lietojumiem. Tajā apkopoti četru oriģinālo zinātnisko publikāciju rezultāti.

Darba aprobācija un publikācijas

Promocijas darba galvenie rezultāti ir publicēti četros zinātniskajos rakstos, kā arī divos patenta pieteikumos. Pētījuma rezultāti ir prezentēti 13 zinātniskajās konferencēs.

Zinātniskās publikācijas

1. Estiri, H.,* **Bhattacharya, S**.,* Rodriguez Buitrago, J. A., Castagna, R., Legzdiņa, L., Casucci, G., Ricci, A., Parisini, E., Gautieri, A. Tailoring FPOX Enzymes for Enhanced Stability and Expanded Substrate Recognition. *Scientific Reports*. 2023, 13, 18610. Pieejams: https://doi.org/10.1038/s41598-023-45428-1. * Autori šajā darbā ir ieguldījuši vienlīdzīgu darbu.

2. Carletti, A., **Bhattacharya, S**., Pedroni, S., Berto, M., Bonettini, R., Castagna, R., Parisini, E., Di Rocco, G. Functional and Structural Characterization of PETase SM14 from Marine-Sponge *Streptomyces* sp. Active on Polyethylene Terephthalate. *ACS Sustainable Chemistry & Engineering.*. 2025, 13, 7460. Pieejams: https://doi.org/10.1021/acssuschemeng.5c00737.

3. **Bhattacharya, S**., * Castagna, R.,* Estiri,* H., Upmanis, T., Gautieri, A., Parisini, E. Development of a Highly Active Engineered PETase Enzyme for Polyester Degradation. *FEBS Journal*. 2025, 23. augusts, raksta ID febs.70228. Pieejams: https://doi.org/10.1111/febs.70228. * Autori šajā darbā ir ieguldījuši vienlīdzīgu darbu.

4. Berselli, A., Carletti, A., Menziani, M. C., **Bhattacharya, S**., Castagna, R., Parisini, E., Di Rocco, G., & Muniz-Miranda, F. The effect of ionic strength on PETase enzymes: An experimental and computational study. *Protein Science*, 2026, 35, e70386. https://doi.org/10.1002/pro.70386.

Patentu pieteikumi

1. Gautieri A, Parisini E, Estiri H, Castagna R, **Bhattacharya S**. “Thermostable engineered enzyme”. IT102023000014223, prioritātes datums 07.07.2023, piešķirts 25.07.2025. PCT/IB2024/056641, iesniegts 08.07.2024. https://patents.google.com/patent/WO2025012799A1/en.

2. Gautieri A, Perazzoli A, Castagna R, Parisini E, **Bhattacharya S**, Enzima fruttosil peptide ossidasi (FPOX) ingegnerizzato e suoi usi. Itālijas patenta pieteikums Nr. 102025000025639, iesniegts 2025. gada 8. oktobrī.

Citas publikācijas par šo tēmu, kas nav iekļautas promocijas darbā

1. Brangulis, K., Akopjana, I., Drunka, L., Matisone, S., Zelencova-Gopejenko, D., **Bhattacharya, S**., Bogans, J., Tars, K. Members of the Paralogous Gene Family 12 from the Lyme Disease Agent *Borrelia burgdorferi* Are Non-Specific DNA-Binding Proteins.. *PLOS ONE*. 2024, 19, e0296127. Pieejams: https://doi.org/10.1371/journal.pone.0296127.

2. **Bhattacharya, S**., Tempra, G., Colleoni, A., Matera, C., Castagna, R., Parisini, E. Synthesis, photochemical and biological evaluation of novel photoswitchable glycomimetic ligands of *Pseudomonas aeruginosa* LecB. *RSC Advances*. 2025, 15, 49796. Pieejams: https://doi.org/10.1039/D5RA06897E.

Starptautiskās konferences, kurās prezentēti promocijas darba rezultāti

1. **Bhattacharya S**, Estiri H, Castagna R, Gautieri A, Parisini E, Enzyme engineering of fructosyl peptide oxidase to widen its active site access tunnel and improve its thermal stability, 15.–17. jūnijs, 2022, FEBS3+ konference Tallinā https://biokeemiaselts.ee/wp-content/uploads/2022/06/ABSTRACT-BOOK_FEBS32022_Tallinn.pdf.

2. **Bhattacharya S**, Estiri H, Castagna R, Gautieri A, Parisini E, Enzyme engineering of fructosyl peptide oxidase to widen its active site access tunnel and improve its thermal stability, EMBO praktiskais kurss Augstas caurlaidspējas proteīnu ražošana un kristalizācija, 2022. gada 4.–12. jūlijs, Marseļa, Francija https://books.google.lv/books/about/High_Throughput_Protein_Production_and_C.html?id=J_GYzwEACAAJ&redir_esc=y.

3. **Bhattacharya S**, Estiri H, Castagna R, Gautieri A, Parisini E, Enzyme engineering of fructosyl peptide oxidase to widen its active site access tunnel and improve its thermal stability, 2. ZĀĻU ATKLĀŠANAS KONFERENCE 2022. gada 22.–24. septembris, Rīga https://drugdiscovery.osi.lv/content/files/DDC_Abstract_Book.pdf.

4. **Bhattacharya S**, Estiri H, Castagna R, Gautieri A, Parisini E, Enzyme engineering of fructosyl peptide oxidase to widen its active site access tunnel and improve its thermal stability, iNEXT DISCOVERY darbseminārs par kristalogrāfisko fragmentu skrīningu, 2023. gada 1.–3. marts, Berlīne https://www.helmholtz-berlin.de/events/inext-discovery-workshop/index_en.html.

5. **Bhattacharya S**, Estiri H, Castagna R, Gautieri A, Parisini E, Enzyme Engineering, mutiska prezentācija ALLIANCE4LIFE_ACTIONS ESR atpūtas pasākums 2023. gada 23.–24. janvārī (pasākums Viļņā) https://alliance4life.com/media/3803646/d35-report-on-early-stage-researchers-retreats_964997.pdf.

6. **Bhattacharya S**, Castagna R, Estiri H, Gautieri A, Parisini E, Thermostable PETase enzyme for plastic degradation, BioDrug conference, BioDrug konference 22.–24. septembris, 2023, Rīga https://biodrugconference.osi.lv/content/Abstract_Book_BioDrug_Conference_2023.pdf.

7. **Bhattacharya S**, Castagna R, Estiri H, Gautieri A, Parisini E, Enzyme engineering of fructosyl peptide oxidase to widen its active site access tunnel and improve its thermal stability, FEBS papildu kurss: Skaitļošanas pieejas enzīmu katalīzes izpratnei un inženierijai, kas notika Zagrebā no 2023. gada 25. līdz 29. septembrim. https://digitalna.nsk.hr/?pr=i&id=658275.

8. **Bhattacharya S**, Castagna R., Estiri H., Gautieri A., Parisini E., SPRINGBOARD projekta sasniegumi, pasākums 2024. gada 2. un 3. maijā Rīgā, nolasot referātu "Development of a highly optimized engineered PETase enzyme for plastic degradation" https://springboard.osi.lv/content/abstracts/Springboard_CONFERENCE_Abstract_.pdf.

9. **Bhattacharya S**, Castagna R, Estiri H, Gautieri A, Parisini E, Tailoring Enzymes for tomorrow "Strukturālā bioloģija Latvijā un ārpus tās", atzīmējot Latvijas dalību Instruct-ERIC, https://instruct-eric.org/news/structural-biology-in-latvia-and-beyond/.

10. **Bhattacharya S**, Development of a Highly Optimized Engineered PETase Enzyme for Polyester Degradation, WIDEnzymes darbnīca 1: Milāna, Itālija, aprēķinu metodes fermentu inženierijā, 2025. gada 27.–31. janvāris. https://widenzymes.eu/workshops-series/workshop-1/.

11. **Bhattacharya S**, Enzyme Engineering, uzstājās ar referātu WIDEnzymes darbnīcā 2, Enzīmu virzīta evolūcija, Ķīmijas fakultāte, Krētas Universitāte, 2025. gada 2.–6. jūnijs. https://widenzymes.eu/workshops-series/workshop-2/.

12. **Bhattacharya S**, Large Scale Production of PETase Enzyme, uzstājās ar referātu WIDEnzymes darbnīcā 3, Rekombinantā fermenta ražošana bioreaktorā, Slovākijas

Tehnoloģiju universitāte Bratislavā (STUBA), 2026. gada 26.–30. janvāris. https://widenzymes.eu/workshops-series/widenzymes-workshop-3-stuba/.

13. **Bhattacharya S**, pasniedzis OneHealthdrugs apmācību skolā (Cost Action CA21111), mērķa proteīnu paraugu ekspresija, attīrīšana un pamata raksturojums zāļu saistīšanās pētījumiem, Latvijas Organiskās sintēzes institūts, 2025. gada septembris. https://onehealthdrugs.com/events/training-schools/expression-purification-and-basic-characterization-of-target-protein-samples-for-drug-binding-studies.

GALVENIE PROMOCIJAS DARBA REZULTĀTI

1. *FPOX* enzīmi

1.1. Enzīmu racionāla projektēšana

Racionāla projektēšana ir datorizēta stratēģija enzīmu inženierijā, kas vērsta uz konkrētām proteīna daļām, lai uzlabotu stabilitāti, aktivitāti vai substrāta specifiskumu, risinot dabisko enzīmu ierobežojumus, kas bieži darbojas fizioloģiskajos apstākļos. Enzīmi slikti tolerē ar industriālo procesu apstākļiem, piemēram, augstu temperatūru, ekstremālu pH, augstu jonu spēku vai organiskajiem šķīdinātājiem.[1] Atšķirībā no *de novo* dizaina vai virzītas evolūcijas racionālais dizains ievieš rūpīgi atlasītas mutācijas, lai radītu ierobežotu mutantu kopumu, kas saglabā kopējo struktūru, vienlaikus uzlabojot vēlamās funkcionālās īpašības, izmantojot tādus paņēmienus kā polāro atlikumu ieviešana, lai veicinātu ūdeņraža saišu veidošanos, cisteīna fragmenta ievietošana, lai veidotu disulfīda tiltiņus, virsmas lādiņa mijiedarbības optimizēšana, mērķtiecīga ietekme uz kustīgajām zonām un termofīlo homologu izmantošana[2, 3] (1. att.).

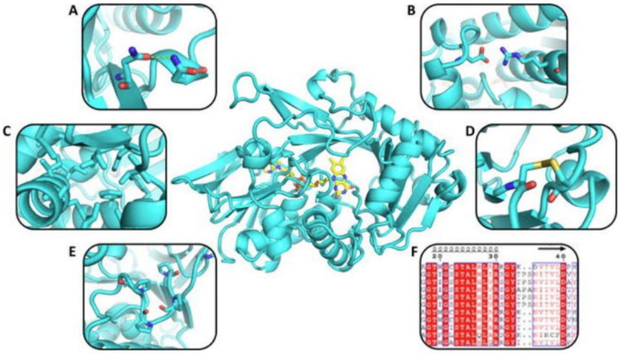

1. attēls. Racionālā enzīmu dizainā izmantotas stabilizējošās stratēģijas: virsmas ūdeņraža saišu (a) un sāls tiltiņu (b) ieviešana, hidrofobā kodola (c) stabilizēšana, disulfīda tiltiņu ieviešana (d) un kustīgo cilpu stabilizēšana, izmantojot prolīnu (e). Filoģenētisko analīzi (f) var izmantot atsevišķi vai kombinācijā ar iepriekšējām stratēģijām, lai vadītu fermentu racionālās projektēšanas procesu.

Mūsdienīgās pieejās tiek izmantotas daudzpunktu mutācijas un aprēķinu platformas, piemēram, *FireProt*[4], lai ņemtu vērā sinerģiskas vai antagonistiskas mijiedarbības,[5] savukārt tādi rīki kā *CAVER*[6], *Rosetta Remodel*[7] un molekulārās dinamikas (MD) simulācijas sniedz ieskatu proteīnu elastībā atomu līmenī, tuneļu arhitektūrā un konformāciju stabilitātē[8]. MD simulācijas modelē atomu kustības laika gaitā, identificējot reģionus, kas ir pakļauti nestabilitātei, un prognozējot ierosināto mutāciju ietekmi, tostarp izmaiņas ūdeņraža saites veidošanā, disulfīda tiltiņa veidošanā vai citās stabilizējošās mijiedarbībās pirms eksperimentālās testēšanas, tādējādi samazinot darba slodzi un minimizējot veidojamo mutāciju skaitu. Integrējot racionālo dizainu ar MD simulācijām, strukturālo modelēšanu un evolūcijas analīzi, enzīmu inženierija var paplašināt substrāta specifiskumu, optimizēt selektivitāti un uzlabot stabilitāti sarežģītos rūpnieciskos apstākļos. Inženierijas enzīmi ar paaugstinātu kušanas temperatūru vai samazinātu denaturācijas uzņēmību var efektīvi darboties augstā temperatūrā, ekstremālā pH līmenī vai paaugstinātā sāļumā, savukārt MD simulāciju vidējās kvadrātiskās svārstību (*RMSF*) analīzes var reproducēt eksperimentālos β-faktorus, lai precīzi noteiktu elastīgas zonas stabilizācijai[5, 9, 10] (2. att.).

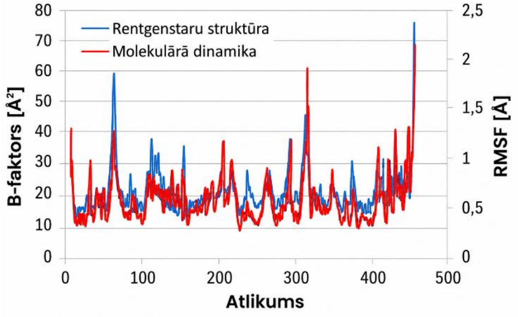

2. att. Savvaļas tipa *FPOX* fermenta *RMSF* un eksperimentālā β-faktora superpozīcija, kas parāda, kā MD simulāciju *RMSF* reproducē to pašu eksperimentālo β-faktoru tendenci un ļauj precīzi noteikt tos pašus maksimumus, kas pārstāv ļoti elastīgas proteīnu zonas.

Fruktozilaminoskābes (vai peptīdu) oksidāzes (*FPOX*), pazīstamas arī kā amadoriāzes, ir specializēta flavīna atkarīgu oksidāžu saime, kas katalizē glikēto aminoskābju vai īsu glikēto peptīdu deglikāciju. Šie enzīmi pieder oksidoreduktāžu klasei un ir plaši izplatīti raugos, sēnēs un baktērijās. Tie katalizē zemas molekulmasas Amadori produktu oksidatīvo sadalīšanos, dodot brīvus amīnus, glikozonus un ūdeņraža peroksīdu.[11] Reakcijā notiek C-N saites oksidēšanās, kas savieno fruktozilgrupas C1 ar aminoskābes slāpekli, un šo procesu mediē *FAD* kofaktors, kura flavīna grupa veido fermenta katalītisko centru.

Strukturāli *FPOX* parāda labi definētus *FAD* saistīšanās motīvus un konservatīvas arhitektūras iezīmes, kas ir tipiskas glikozes–metanola–holīna oksidoreduktāzes klasei. Līdz šim ir aprakstītas vairākas *FPOX* kristāla struktūras, kas sniedz detalizētu ieskatu aktīvās vietas organizācijā un vārstu elementos, kas regulē substrāta piekļuvi.[12] Šie strukturālie pētījumi ir parādījuši, ka katalītiskā kabata atrodas dziļi proteīnā un ir savienota ar šķīdinātāju ar šauru piekļuves tuneli. Šai pazīmei ir galvenā nozīme substrāta specifiskuma noteikšanā (3. A att.).

FPOX ir nozīmīgi biomedicīnā, jo tos izmanto fermentu komplektos glikēta hemoglobīna (HbA1c) mērīšanai, kas ir galvenais biomarķieris ilgtermiņa glikēmijas kontrolei diabēta pacientiem, tiem ir arī potenciāls glikēta albumīna noteikšanai.[13] Standarta diagnostikas testos hemoglobīns vispirms tiek denaturēts un proteolītiski sadalīts, lai atbrīvotu mazus glikētos peptīdus, piemēram, fruktozilvalilhistidīnu (F-VH), kas pēc tam tiek oksidēti ar *FPOX*. Tad izveidotais ūdeņraža peroksīds tiek kvantificēts vai nu kolorimetriski, izmantojot mārrutku peroksidāzi, vai elektromehāniski, kas ļauj netieši noteikt HbA1c līmeni[13] (3. B att.).

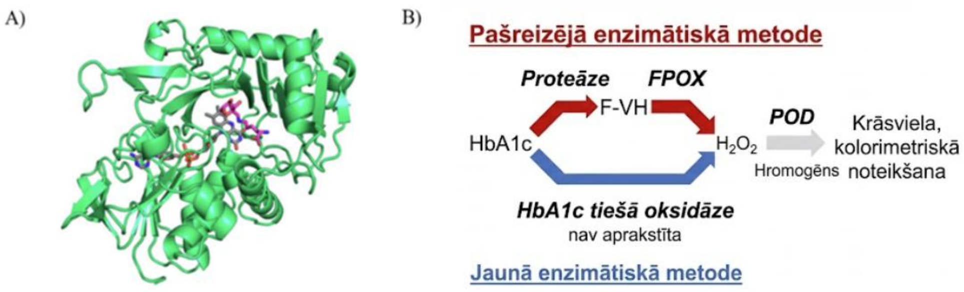

3. att. (A) Amadoriāzes I kristālstruktūra kompleksā ar fruktozillizīnu (PDB kods 4XWZ). (B) HbA1c fermentatīvās metodes reakcijas shēma (adaptēta no[13]).

Neskatoties uz to daudzpusību un diagnostisko vērtību, *FPOX* enzīmiem ir būtisks ierobežojums – tie nespēj efektīvi katalizēt neskartu proteīnu deglikāciju.[14] Struktūras pētījumi ir parādījuši, ka šī ierobežojuma pamatā ir šaurais substrāta piekļuves tunelis, kas savieno ar enzīma aktīvo vietu un atļaut piekļūt tikai mazām glikētām aminoskābēm vai īsiem peptīdiem.[15] Tā rezultātā dabiskie *FPOX* izrāda ierobežotu aktivitāti pret apjomīgiem substrātiem, piemēram, neskartām glikētajām olbaltumvielām.

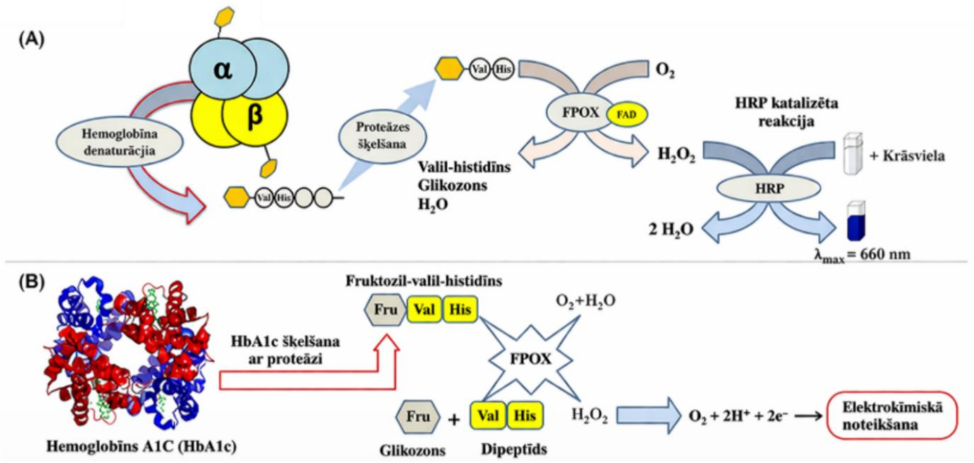

4. att. Hemoglobīna A1c (HbA1c) denaturācija un sadalīšana ar proteāzi, lai atbrīvotu fruktozilvalilhistidīnu (F-VH). (A) F-VH oksidējas ar fruktozilpeptīda oksidāzes (*FPOX*) palīdzību, un rezultātā iegūtais H_2O_2 kalpo par *HR*P substrātu, veidojot krāsvielu, kuras absorbcija ir 660 nm un kas tiek izmantota, lai aprēķinātu HbA1c procentuālo daudzumu. (B). HbA1c noteikšanas mentode, elektromehāniski mērot H_2O_2 (adaptēta no[18]).

Tomēr šīs pašas strukturālās atziņas ir nodrošinājušas stingru pamatu enzīmu inženierijai. Mērķējot uz atlikumiem, kas veido substrāta piekļuves tuneli, un stabilizējot *FAD* saistīšanās domēnu, pētnieki ir veiksmīgi radījuši *FPOX* mutācijas ar uzlabotu termisko stabilitāti, pastiprinātu katalītisko aktivitāti un palielinātu selektivitāti pret specifiskiem glikētiem substrātiem.[16, 17] Šādas inženierijas variācijas ne tikai nodrošina uzlabotu veiktspēju diagnostiskajos testos, tostarp kolorimetriskajos un elektroķīmiskajos HbA1c mērījumos[18], bet arī kalpo kā vērtīgas modeļsistēmas, lai plašāk pētītu proteīnu inženierijas stratēģijas flavīna atkarīgajās oksidāzēs (4. att.).

Profesora Emilio Parisini grupa jau vairākus gadus strādā ar fruktozilpeptīdu oksidāzēm (*FPOX*), koncentrējoties uz to racionālu inženieriju, lai uzlabotu veiktspēju praktiskos lietojumos. Pētījumā tika veikts racionāls *Phaeosphaeria nodorum FPOX* (*Pn-FPOX*) pirmā mutanta, kas iegūts no savvaļas tipa enzīma, dizains, kam sekoja sistemātiskas modifikācijas, tostarp tuneļa paplašināšana, termiskā stabilizācija un aktivitātes optimizācija. Pēc vairākiem inženierijas posmiem tika iegūts mutants L3-35A, kam ir platāks un īsāks piekļuves tunelis. Tas tika panākts, izdzēšot piecas aminoskābes, kas izklāj vārtu struktūru (5. att.). Promocijas darba izstrādes gaitā turpmākos pētījumus autore sāka ar šo iepriekš izstrādāto mutāciju L3-35A, kas saglabāja paplašināto piekļuves tuneli un kalpoja par sākuma punktu turpmākai optimizācijai. Balstoties L3-35A, tika piemērotas racionālas projektēšanas stratēģijas, lai atjaunotu stabilitāti un uzlabotu enzimātisko aktivitāti, vienlaikus saglabājot paplašināto piekļuves tuneli, kas nepieciešams lielākiem substrātiem. Tika ieviestas trīs mutāciju klases: D sērija, kas vērsta uz strukturālo svārstību samazināšanu; C sērija, kas vērsta uz stabilizējošo sāls tiltiņu veidošanās palielināšanu; X sērija, kas paredzēta disulfīda saišu ieviešanai papildu termiskai stabilitātei. Šīs mutācijas tika veidotas, izmantojot MD simulācijas, kas sniedza ieskatu enzīma dinamiskajā uzvedībā, elastībā un nestabilitātei pakļautajās zonās, ļaujot noteikt prioritātes daudzsološākajām modifikācijām.

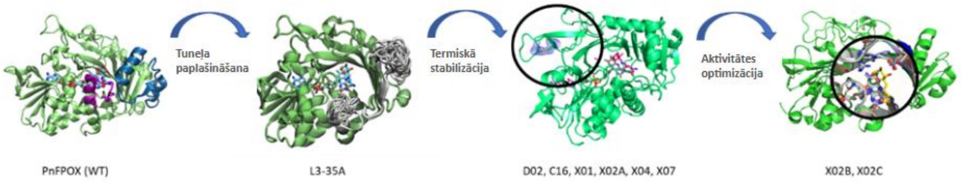

5. att. Racionālās projektēšanas stratēģijas shēma, kurā parādīti katrā posmā iegūto attiecīgo fermentu variantu nosaukumi.

Kombinētā daudzpusējā pieeja radīja *FPOX* variantus, kas bija gan termiski stabili, gan ļoti aktīvi. Labākos rezultātus uzrādīja mutācija X02C. Eksperimentālie testi apstiprināja, ka inženierijas mutācijas saglabāja strukturālo integritāti un nozīmīgu katalītisko aktivitāti, salīdzinot ar savvaļas tipa enzīmu.

Enzīms X02C ar labāko katalītisko spēju attiecībā uz dažāda garuma glikētiem substrātiem (glikēta valīna (f-V) un glikēta heksapeptīda, fruktozil-Val-His-Leu-Thr-Pro-Glu (F6P)) tika izvēlēts nākamajai inženierijas kārtai.

Nākamajā kārtā no enzīma X02C struktūras tika izņemts viens ceturtās spirāles pagrieziens (6. A att.) (zilā krāsā), lai paplašinātu piekļuves tuneli. Kopumā tika izņemtas deviņas aminoskābes. Šī spirāle pieder pie vienas no četrām vārstu struktūrām, kas apņem aktīvo vietu.

Pēc tam tā tika atjaunota, izmantojot mazāku atlieku skaitu (no divām līdz piecām). Turklāt, lai kompensētu šīs saīsināšanas izraisīto dabisko mijiedarbību zudumu, tika mutēti visi nekonservētie atlikumi 5 Å attālumā no pārveidotās posma. Šis 5 Å slieksnis tika izvēlēts, ņemot vērā ūdeņraža saites attālumus (~3 Å) un tipiskās mugurkaula svārstības (*RMSD* ~1,5 Å). Tika nolemts atturēties no atlieku mutācijas, kas bija noteiktas, X02C salīdzinot ar diviem citiem ļoti aktīviem *FPOX* – *Coniochaeta* sp. *FPOX* (*FPOX-C*)[19] un *Aspergillus nidulans FPOX-47* (*AnFPOX-47*).[20]

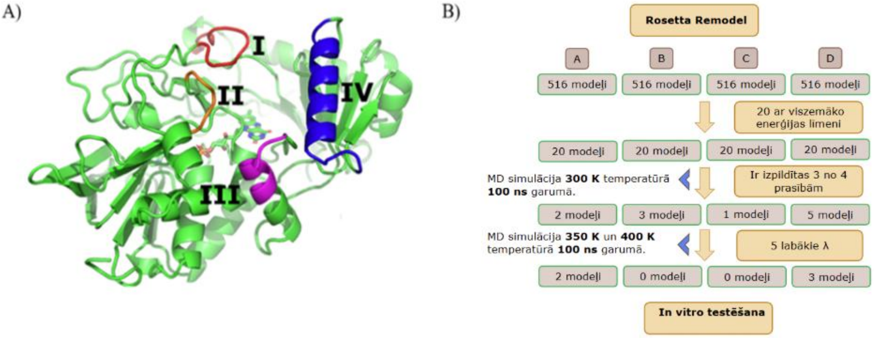

6. att. A) X02C modelis, kas izmantots pārveidošanai. B) X02C enzīmu inženierijas aprēķinu daļas kopsavilkums.

Lai ieviestu izvēlētās mutācijas, tika izmantots *Rosetta Remodel*, radot 516 variantus katram rekonstruētajam cilpas garumam, kas ir divreiz vairāk nekā iepriekšējā pētījumā pārbaudīto mutāciju skaits. Katram cilpas garumam tika izvēlēti 20 radītie modeļi ar zemāko enerģētisko rādītāju, kas ir bezvienības *Rosetta Remodel* parametrs, kas kvalitatīvi apraksta modeļa kopējo stabilitāti (6. B att.). Pēc tam tika pētītas šīs struktūras, izmantojot molekulārās dinamikas 300 K, 350 K un 400 K simulācijas temperatūrā 100 ns simulētā laika periodā, un novērtēta šo mutāciju vidējā kvadrātiskā novirze (*RMSD*) un vidējā kvadrātiskā svārstība (*RMSF*). Mutanti, kas bija labāki par X02C vismaz trīs no četriem parametriem (vidējā *RMSD*, vidējā *RMSF*, mediāns *RMSF* un *RMSF* standarta novirze), tika izvēlēti nākamajai molekulārās dinamikas simulāciju kārtai (7. att.).

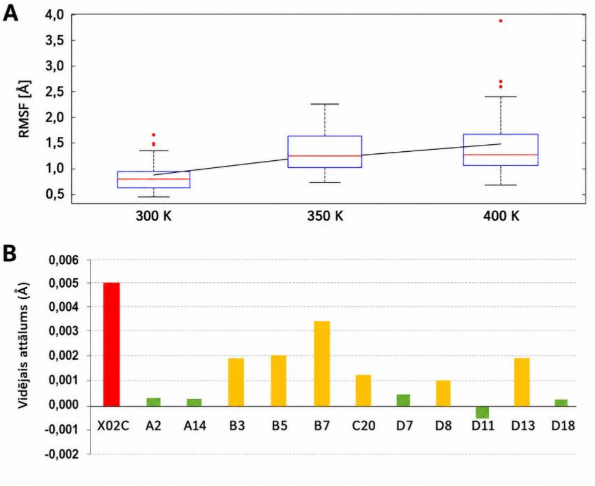

7. att. *RMSF* analīze pieaugošās temperatūrās. (A) *RMSF* pārveidotajai X02C cilpai kā funkcija no temperatūras (T). Lineārās regresijas analīze nodrošināja leņķa koeficientu (slīpumu) *RMSF* pret T attiecībai. (B) Dažādu enzīmu variantu leņķa koeficients, mutanti ar zemākajām vērtībām (zaļā krāsā) tika izvēlēti eksperimentālai validācijai.

Optimizētie varianti tika eksperimentāli ekspresēti, attīrīti un bioloģiski raksturoti. Tika pārbaudīta arī to katalītiskā aktivitāte pret glikētiem peptīdiem un *ex vivo* glikētiem cilvēka audiem. Starp tiem *PnFPOX-A14* parādīja ievērojami uzlabotu aktivitāti, salīdzinot ar sākotnējo inženierijas variantu X02C, īpaši attiecībā uz apjomīgākiem substrātiem. Jāatzīmē, ka X02C saglabāja ierobežotu aktivitāti pret pilna garuma glikētiem proteīniem, savukārt PnFPOX-A14 spēja tieši atpazīt un iedarboties uz neskartu HbA1c, parādot uzlabotu substrāta pieejamību un katalītisko veiktspēju. Šie rezultāti apstiprināja aprēķinu dizaina stratēģiju un parādīja *PnFPOX-A14* kā uzlabotu platformu turpmākai inženierijai diagnostikas un potenciālu terapeitisko lietojumu jomā. Šie rezultāti ir apkopoti zinātniskajā rakstā, kas pievienots 5. pielikumā.

1.2 **Enzīmu ekspresija un attīrīšana**

Promocijas darba ietvaros tika izmantota rekombinantā DNS tehnoloģija, lai ekspresētu visus enzīmus *Escherichia coli*, galvenokārt izmantojot BL21(DE3) prokariotiskās olbaltumvielas un BL21(DE3) atvasinājumus, kas papildināti ar retām tRNA eikariotiskajām olbaltumvielām, lai mazinātu kodonu novirzi, izmantojot ekspresijas vektoram atbilstošu antibiotiku selekciju (ampicilīnu, kanamicīnu vai hloramfenikolu).[21, 22] Pirms liela mēroga ekspresijas tika veikti maza mēroga ekspresijas testi, kuros katrs mutants tika audzēts dažādās temperatūrās un inducēts ar dažādām *IPTG* koncentrācijām, lai identificētu optimālos apstākļus maksimālai šķīstošo proteīnu ekspresijai. Pēc optimālo parametru noteikšanas proteīnu ražošana tika palielināta, parasti līdz 4 litriem, un attīrīšana tika veikta, izmantojot divpakāpju darba plūsmas *ÄKTA* šķidruma hromatogrāfijas sistēmu (*Cytiva*). *FPOX* klasei ekspresija *E. coli* BL21 Star (DE3) 25 °C temperatūrā deva iznākumu no 10 mg/l līdz 30 mg/l, ar vislielāko iznākumu (30 mg/l) tika iegūts L3-35A. Vairāki *FPOX* mutanti, kam raksturīgas disulfīda saites, tika ekspresēti no SHuffle T7 celma[23] 18 °C temperatūrā, uzrādot dažādus ražošanas apjomus, sākot no zemas ekspresijas X01 (5 mg/l) līdz salīdzinoši augstiem līmeņiem X02C (29 mg/l) (1. tab.).

1. tabula

Enzīmu ekspresijas iznākumi

Enzīms	**Ekspresijas iznākums (mg/L)**	**Ekspresijas temperatūra (°C)**	**Ekspresijas šūnas**
PnFPOX	10	25	BL21 Star (DE3)
L3-35A	30	25	BL21 Star (DE3)
D02	15	25	BL21 Star (DE3)
C16	12	25	BL21 Star (DE3)
X01	5	18	SHuffle T7 E
X02A	20	18	SHuffle T7 E
			1. tabulas turpinājums
X04	10	18	SHuffle T7 E
X07	6	18	SHuffle T7 E
X02B	16	18	SHuffle T7 E
X02C	29	18	SHuffle T7 E

Pirmajā posmā tika veikta imobilizēta metāla afinitātes hromatogrāfija (*IMAC*), izmantojot *HisTrap* 5 ml niķeļa kolonnu ar *N* terminālo His_6 afinitātes marķieri uz rekombinantajiem proteīniem un imidazolu saturošu buferi kā eluentu (8. A att.). Otrajā posmā proteīni turpināti attīrīt ar izmēra izslēgšanas hromatogrāfiju (*SEC*), izmantojot *HiPrep* 26/60 *Sephacryl* S-200 kolonnu, kas noņēma agregātus, ļāva veikt bufera apmaiņu un nodrošināja enzīmu monodispersitāti.[24] Proteīnu koncentrācija tika mērīta, izmantojot *NanoDrop One* spektrofotometru (*Thermo Fisher Scientific*), molekulārais svars un tīrība tika novērtēta ar *SDS-PAGE* ar *Coomassie* zilo krāsojumu, kas nodrošināja uzticamu proteīnu izmēra un viendabīguma apstiprinājumu[25] (8. B att.). Šī baktēriju ekspresijas, indukcijas apstākļu optimizācijas un secīgas *IMAC* un *SEC* attīrīšanas kombinācija ļāva iegūt augstas tīrības funkcionālus enzīmus, kas piemēroti detalizētai bioloģiskai un strukturālai raksturošanai, veidojot stabilu pamatu turpmākiem enzīmu inženierijas pētījumiem.

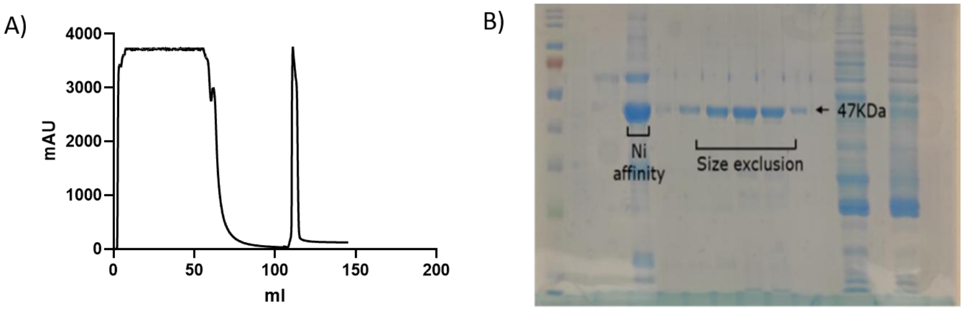

8. att. A) Tipiska niķeļa afinitātes hromatogrāfijas (*IMAC*) hromatogramma (no *FPOX* fermenta X02C attīrīšanas). Zilā līkne attēlo UV absorbanci (A280), kas izmantota proteīna eluācijas uzraudzībai. B) *FPOX* fermenta-X02C elektroforēzes aina.

1.3 Biofizikālā raksturošana

Biofizikālā raksturošana ir būtiska proteīnu strukturālās integritātes, stabilitātes un funkcionalitātes novērtēšanai, jo pareiza salocīšanās un molekulārā integritāte ir enzimātiskās aktivitātes priekšnoteikums. Tādas metodes kā cirkulārā dihroisma (CD) spektroskopija, diferenciālā skenējošā fluorimetrija (DSF) un *MALDI* masspektrometrija sniedz papildu informāciju par sekundāro struktūru, termisko stabilitāti un molekulmasu.[26] CD spektroskopija novērtē sekundāro struktūru, mērot cirkulāri polarizētas gaismas diferenciālo absorbciju – tālais ultravioletais spektrs dod informāciju par α-spirālēm, β-lapām un nesakārtotajiem reģioniem, savukārt no temperatūras atkarīgie CD mērījumi ļauj izpētīt termiskos izkliedēšanās procesus.[27] DSF, izmantojot uz vidi reaģējošas krāsvielas, piemēram, *SYPRO Orange*, mēra fluorescences izmaiņas proteīnu struktūras maiņas laikā un ļauj noteikt kušanas temperatūras (T_m), un tā rezultātā ir iespējams kvantitatīvi salīdzināt stabilitāti dažādos variantos, buferu apstākļos vai liganda saistītos stāvokļos.[28] Šajā pētījumā gan DSF, gan CD tika izmantoti, lai novērtētu inženierijas *FPOX* variantu termisko stabilitāti, iegūstot konsekventas tendences un salīdzināmas absolūtās T_m vērtības, tādējādi apstiprinot mērījumu stabilitāti. Rezultāti liecina, ka piemērota racionālā dizaina stratēģija efektīvi uzlaboja references enzīma L3-35A termisko stabilitāti (9. att.). D02 variants, kas satur divas papildu mutācijas (V110R un D115G), uzrādīja kušanas temperatūras paaugstināšanos aptuveni par 1,5 °C, salīdzinot ar sākotnējo enzīmu. Turpmāka stabilizācija tika panākta, ieviešot plašus virsmas lādiņus un sāls tiltiņus mutācijā

C16, kas radīja papildu T_m paaugstināšanos par aptuveni 1,5 °C, sasniedzot 55,2 °C (2. tab.). Vienas disulfīda saites iekļaušana dažādās pozīcijās L3-35A skeleta struktūrā radīja ievērojamus uzlabojumus termiskajā stabilitātē. Visas šīs sērijas variācijas – X01 (54,1 °C), X02A (60,0 °C), X04 (55,2 °C) un X07 (55,3 °C) – uzrādīja ievērojami paaugstinātu kušanas temperatūru, salīdzinot ar sākotnējo enzīmu (2. tab., 9. att.). Kopumā šie rezultāti liecina, ka gan elektrostatiskā optimizācija, gan disulfīda saites inženierija ir efektīvas stratēģijas *FPOX* termiskās stabilitātes uzlabošanai, un apstiprina papildu biofizikālo metožu izmantošanu proteīnu stabilizācijas rezultātu kvantitatīvai novērtēšanai.

2. tabula

References enzīma (L3-35A) un tā mutāciju kušanas temperatūra*

Ferments	**T_m [°C]** ^{a}	**T_m [°C]** ^{b}
PnFPOX (*WT*)	53,2± 0,2	53,5 ± 0,1
L3-35A	52,3 ± 0,2	52,9 ± 0,1
D02	53,1 ± 0,5	54,8 ± 0,1
C16	55,2 ± 0,1	55,0 ± 0,1
X01	54,1 ± 0,1	54,2 ± 0,1
X02A	60,0 ± 0,4	60,1 ± 0,1
X04	55,2 ± 0,3	55,0 ± 0,1
X07	55,3 ± 0,4	55,4 ± 0,1
X02B	60,2 ± 0,7	60,6 ± 0,1
X02C	64,0 ± 0,2	63,3 ± 0,1

* Temperatūra noteikta ar termiskās nobīdes analīzi (a) un cirkulāro dihroismu (b). Kā atsauce ir norādīta arī savvaļas tipa fermenta (*PnFPOX*) kušanas temperatūra.

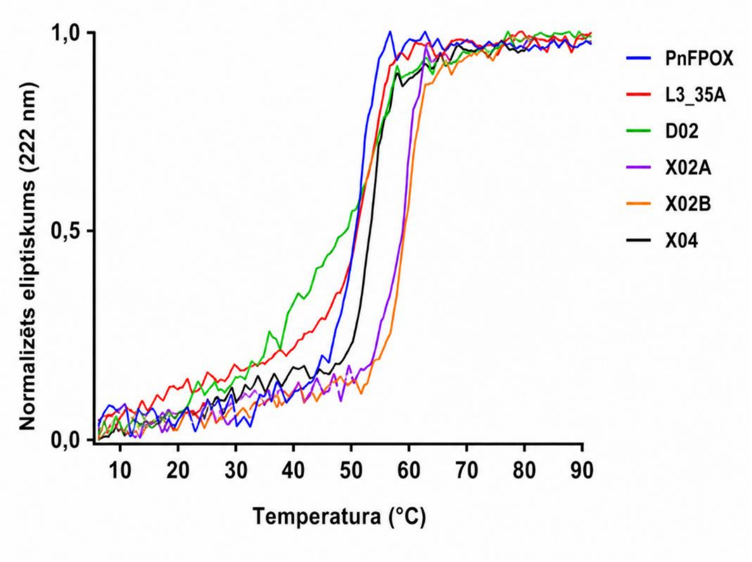

9. att. Dažādu *FPOX* variantu T_m vērtību salīdzinājums, kas izmērīts ar cirkulāro dihroismu 222 nm diapazonā no 5 °C līdz 95 °C.

1.4 Funkcionālais tests

Visu *FPOX* variantu enzimātiskā aktivitāte tika novērtēta istabas temperatūrā, kvantitatīvi nosakot glikozona daudzumu, kas laika gaitā atbrīvojās no substrāta, ievērojot iepriekš izstrādātās metodes[29] (10. att.).

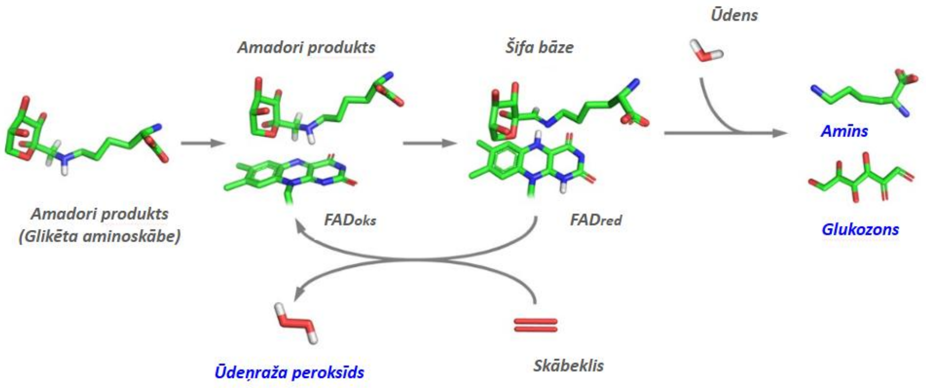

10. att. Amadoriāzes I katalizētās aminoskābju deglikācijas reakcijas shēma (adaptēta no Rigoldi u. c.[30]).

Absorbcijas pieaugums pie 322 nm ($\varepsilon_{322} = 149{,}25\ M^{-1}\ cm^{-1}$ glikozonam) nepārtraukti tika noteikts, izmantojot *Infinite M1000* mikroplašu lasītāju (*Tecan*) 25 °C temperatūrā. Katra reakcijas maisījuma (200 µL) sastāvā bija 20 mM Tris-HCl buferis, pH 7,4, kas saturēja 20 mM *o*-fenilēndiamīnu un 2 mM attiecīgā substrāta (fruktozillizīna (fK), fruktozilvalīna (fV), fruktozil-valīna-histidīnu (fVH) vai heksapeptīdu 1-dezoksifruktozil-Val-His-Leu-Thr-Pro-Glu (F6P)). *FPOX* katalizē fruktozilsubstrātu oksidēšanu, radot glikozonu kā reakcijas produktu. *OPD* reaģē ar glikozonu, veidojot hinoksalīna atvasinājumu, kas absorbē pie 322 nm. Pēc 1 minūtes iepriekšējas inkubācijas reakcijas maisījumam tika pievienots enzīms koncentrācijā 0,04–1 mg/ml, atkarībā no varianta aktivitātes (3. tab.).

3. tabula

Enzīmu specifiskās aktivitātes (U/mg) uz dažādiem glikētiem peptīdu substrātiem salīdzinājums

Enzīms	**Specifiskā aktivitāte (U/mg)**			
	fK	**fV**	**fVH**	**F6P**
PnFPOX	30,18 ± 0,67	29,67 ± 2,56	32,60 ± 1,18	0,78 ± 0,09
AnFPOX-47	–	–	–	0,082 ± 0,002
L3-35A	0,21 ± 0,02	0,16 ± 0,04	–	–
D02	0,30 ± 0,03	0,32 ± 0,01	–	–
C16	ND	ND	–	–
X01	ND	ND	–	–
X02A	0,15 ± 0,01	0,11 ± 0,01	–	–
X04	ND	0,13 ± 0,01	–	–
X07	–	0,08 ± 0,01	–	–
X02B	2,24 ± 0,07	32,50 ± 0,44	0,87 ± 0,03	0,18 ± 0,06
X02C	1,06 ± 0,01	17,95 ± 2,46	1,62 ± 0,02	0,43 ± 0,06

Testi tika veikti trīs reizes. ND – nav konstatēts.

Viena enzīma aktivitātes vienība (U) tika definēta kā enzīma daudzums, kas noteiktos analīzes apstākļos 1 minūtē katalizē 1 µmol glikozona veidošanos, specifiskā aktivitāte tika izteikta kā U mg^{-1} enzīma. Kinētiskās konstantes (V_{max}, K_m, k_{cat} un k_{cat}/K_m) tika noteiktas ar testiem, kas veikti ar dažādām substrāta koncentrācijām (0,05–10 mM fruktozilvalīnam; 0,05–1 mM heksapeptīda substrātam), izmantojot *Michaelis-Menten* vienādojuma nelineāro regresijas analīzi, ko papildināja *Lineweaver-Burk* diagrammas pielāgojums. Visi dati atspoguļo vismaz divu neatkarīgu eksperimentu vidējos rādītājus (4. tab.).

4. tabula

Kinētiskie parametri savvaļas tipa *PnFPOX* un inženierijas X02C enzīmiem

Enzīms	**Substrāts**	K_m (mM)	V_{max} (mM/min)	k_{cat} (s^{-1})	k_{cat}/K_m ($mM^{-1}\ s^{-1}$)
PnFPOX	fV	5,93 ± 1,61	41,67 ± 8,34	99,33 ± 19,86	16,75
X02C	fV	0,94 ± 0,06	10,56 ± 0,56	20,83 ± 1,10	22,16
PnFPOX	F6P	0,81 ± 0,30	15,48 ± 1,20	36,83 ± 2,83	45,47
X02C	F6P	0,03 ± 0,01	0,26 ± 0,01	0,52 ± 0,02	17,22

Kinetiskā analīze parādīja, ka inženierijas variants X02C uzrādīja ievērojami zemāku K_m (0,94 mM) nekā savvaļas tips *PnFPOX* (5,93 mM), liecinot par uzlabotu substrāta afinitāti. Lai gan K_{cat} nedaudz samazinājās, katalītiskā efektivitāte (K_{cat}/K_m) palika salīdzināma vai uzlabojās, uzsverot kompromisu starp substrāta saistīšanos un reakcijas ātrumu, ko bieži tiek novērota enzīmu inženierijā (3. tab.).

1.5 Rentgena kristalogrāfija

Rentgena kristalogrāfija tika izmantota, lai noteiktu inženierijas fruktozilpeptīda oksidāzes (*FPOX*) variantu trīsdimensiju struktūras, sniedzot atomāra līmeņa ieskatu to strukturālajā organizācijā, katalītiskajā arhitektūrā un stabilizējošajās īpašībās. Difrakcijai piemēroti kristāli tika iegūti, izmantojot tvaika difūzijas metodes optimizētos supersaturācijas apstākļos. Augstas izšķirtspējas difrakcijas dati tika ievākti sinhronizācijas avotā, kas ļāva precīzi noteikt un precizēt struktūru.[31–33]

Struktūras analīze atklāja galvenās iezīmes, kas ir enzīmu stabilitātes, substrāta pieejamības un katalītiskās efektivitātes pamatā. Vairāki inženierijas *FPOX* varianti tika veiksmīgi atrisināti un iesniegti proteīnu datu bankā, tostarp X02B (PDB ID: 8BJY), D02 (8BLZ), X02A (8BLX) un X04 (8BMU). Šīs struktūras sniedz detalizētu strukturālo pamatu, lai izprastu racionāli ieviesto mutāciju ietekmi, un apstiprina to nozīmi *FPOX* enzīmu stabilitātes un veiktspējas uzlabošanā (11. att.).

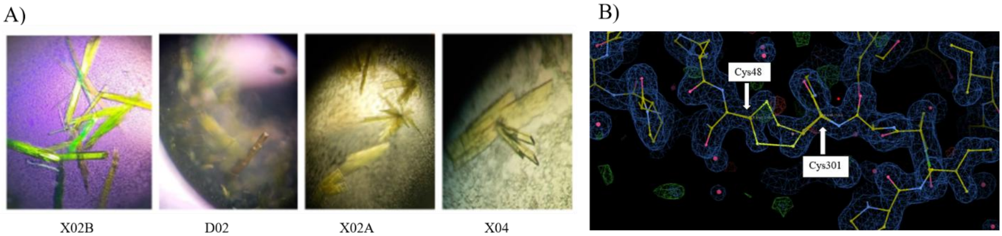

11. att. A) *FPOX* variantu kristāli. B) X02A (PDB: 8BLX) elektronu blīvuma karte, kas parāda disulfīda saites veidošanos starp cisteīniem 48 un 301.

1.6 Struktūras un funkcijas korelācijas analīze

Rentgena kristalogrāfiskā struktūra skaidri parāda saikni starp molekulāro arhitektūru un proteīna funkcionālajām īpašībām. Augstas izšķirtspējas modelis atklāj labi definētus sekundāros un terciāros elementus, kas veido stabilu struktūru, kas atbalsta aktīvās vietas organizāciju un substrāta saistīšanos. Galvenie atlikumi ir precīzi novietoti, lai nodrošinātu katalīzi vai liganda mijiedarbību, kas atbilst bioķīmiskajiem novērojumiem. Struktūras īpatnības, piemēram, ūdeņraža saites, hidrofobie kontakti un elektrostatiskās mijiedarbības, vēl vairāk veicina substrāta specifiskumu un stabilitāti. Visos promocijas darba izstrādes gaitā veiktajos enzīmu pētījumos detalizēta kristalogrāfiskā analīze ir bijusi centrālā, lai izprastu, kā trīsdimensiju struktūra regulē bioloģisko funkciju un katalītisko mehānismu. *FPOX* enzīmu gadījumā tika novērots, ka visas kopējās *RMSD* vērtības starp mutantiem un savvaļas tipa *PnFPOX* (PDB 5T1E) bija 1,8 Å robežās, norādot, ka kopējā struktūra lielā mērā paliek nemainīga (5. tab.).

5. tabula

Aprēķinātās *RMSD* vērtības starp *WT* fermentu *PnFPOX* un dažādiem mutantiem, kā arī tuneļa ģeometrija

Ferments	***RMSD* [Å]**	**Tuneļa šaurākās vietas rādiuss [Å]**	**Tuneļa garums [Å]**
PnFPOX	–	2,2	13,3
L3-35A	1,8	3,7	6,4
D02	1,4	2,9	11,7
X02A	1,7	3,1	9,4
X04	1,8	3,0	10,9
X02B	1,5	3,0	10,2

Salīdzinot katalītisko vietu veidojošos atlikumus (W235, E278, G372, R415), tika konstatēts, ka to orientācija ir saglabājusies visos variantos (12. att.). Šie atlikumi, kas ir ļoti konservatīvi *FPOX* enzīmos, ir atbildīgi par substrāta cukura daļas saistīšanu. Tāpēc variantu katalītiskās aktivitātes atšķirības, visticamāk, nav saistītas ar izmaiņām katalītiskās struktūras ģeometrijā, bet gan ar smalkākām izmaiņām ap substrāta tuneli.

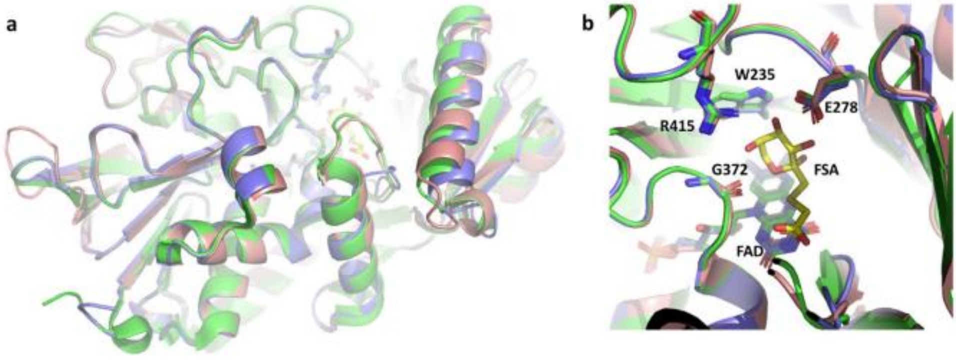

12. att. Attiecīgo *FPOX* enzīmu strukturālais salīdzinājums: *PnFPOX* (zaļš), *AnFPOX-47* (rozā) un X02B (violets). *FSA* inhibitors attēlots dzeltenā krāsā. (a) Kopējā strukturālā saskaņotība neuzrāda nozīmīgas atšķirības starp enzīmiem, izņemot ieejas tuneli. (b) Katalītiskās vietas pozīcija ir ļoti konservatīva.

Tika novērots, ka mutācijas galvenokārt ietekmē tuneļa izklājuma atlieku ģeometriju un dinamisko uzvedību. Savvaļas tipa enzīmam ir šaurs un pagarināts tunelis (šaurākā vieta – 2,2 Å, garums – 13,3 Å), kas, visticamāk, ierobežo piekļuvi lielākiem substrātiem, vienlaikus stabilizējot mazākus. Turpretim L3-35A variants ir daudz platāks un īsāks tunelis (attiecīgi 3,7 Å un 6,4 Å), savukārt X02B mutants ir ar vidēju ģeometriju (3,0 Å, 10,2 Å). Šīs strukturālās atšķirības liecina, ka mutaģēze ir mainījusi ne tikai tuneļa statiskos izmērus, bet arī apkārtējo atlikumu korelēto elastību, tādējādi ietekmējot substrāta pieejamību un stabilizāciju.

1.7 Pašreizējie virzieni un nākotnes iespējas

Balstoties inženierijas *FPOX* variantos, pašreiz tiek strādāts, lai integrētu šos optimizētos enzīmus jutīgās biosensoros platformās HbA1c noteikšanai (5. pielikums). Pašreizējie centieni ir vērsti uz kolorimetrisko un elektroķīmisko sensoru formātu izstrādi, enzīmu imobilizācijas un signāla pārraides uzlabošanu, kā arī veiktspējas novērtēšanu ar klīniski nozīmīgiem paraugiem. *FPOX* bāzes sensori tiek izstrādāti, lai nodrošinātu tiešu, ātru un rentablu glikēto proteīnu mērīšanu.

2. PETāzes enzīmi

Plastmasas piesārņojums ir būtiska vides problēma, un polietilēntereftalāts (PET) ir viens no visplašāk izmantotajiem un noturīgākajiem plastmasas veidiem. Tā izturība pret ķīmisko un bioloģisko sadalīšanos ir izraisījusi tā plašu uzkrāšanos atkritumu poligonos un dabiskajās ekosistēmās, savukārt tradicionālās apglabāšanas metodes, piemēram, sadedzināšana un mehāniskā pārstrāde, joprojām ir neefektīvas vai kaitīgas videi. PETāzes atklāšana, kas ir enzīms, kas spēj depolimerizēt PET mazākos bioloģiski noārdāmos produktos, ir nozīmīgs biotehnoloģisks sasniegums un daudzsološa bioloģiska pieeja plastmasas piesārņojuma mazināšanai[34, 35] (13. att.).

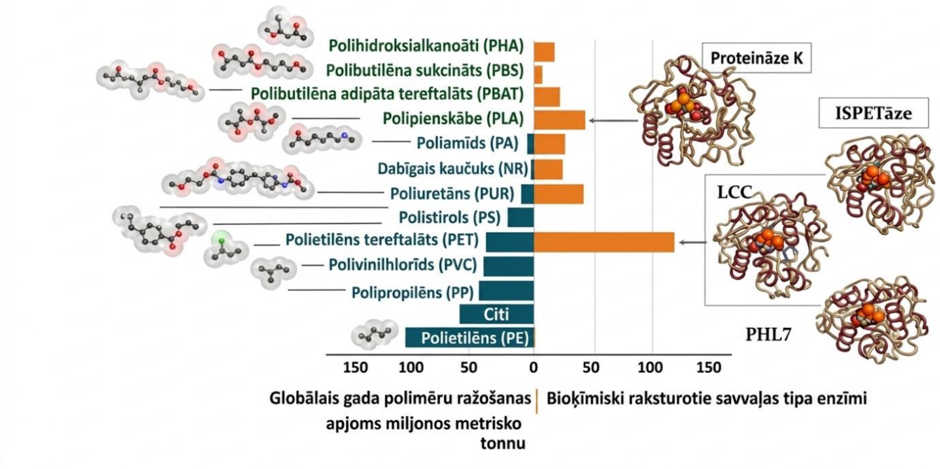

13. att. Galveno plastmasas polimēru ražošana pasaulē un bioloģiski raksturotu savvaļas tipa depolimerāžu pieejamība.[35]

Nesenie pētījumi liecina, ka noteikti mikroorganismi var ražot hidrolītiskos enzīmus, kas spēj sadalīt un metabolizēt PET. Līdz šim pētnieki ir izolējuši un identificējuši dažādus PET sadalošos enzīmus, galvenokārt esterāzes, lipāzes, hidrolāzes un kutināzes. PET sadalošie proteīni tika nosaukti par PETāzēm, un tām ir piešķirts Enzīmu komisijas numurs EC 3.1.1.101. 2016. gadā no PET piesārņotas pārstrādes vietas Japānā, kas izmanto PET kā galveno oglekļa un enerģijas avotu, tika izolēta baktērija *Ideonella sakaiensis,* kurai ir unikāla spēja starp zināmajiem mikroorganismiem. Enzīms PETāze ļauj baktērijai hidrolizēt PET polimērā esošās estera saites, ražojot mazākas molekulas, piemēram, mono(2-hidroksietil)tereftalātu (MHET), tereftālskābi (TPA) un etilēnglikolu (EG)[37, 38] (14. att.).

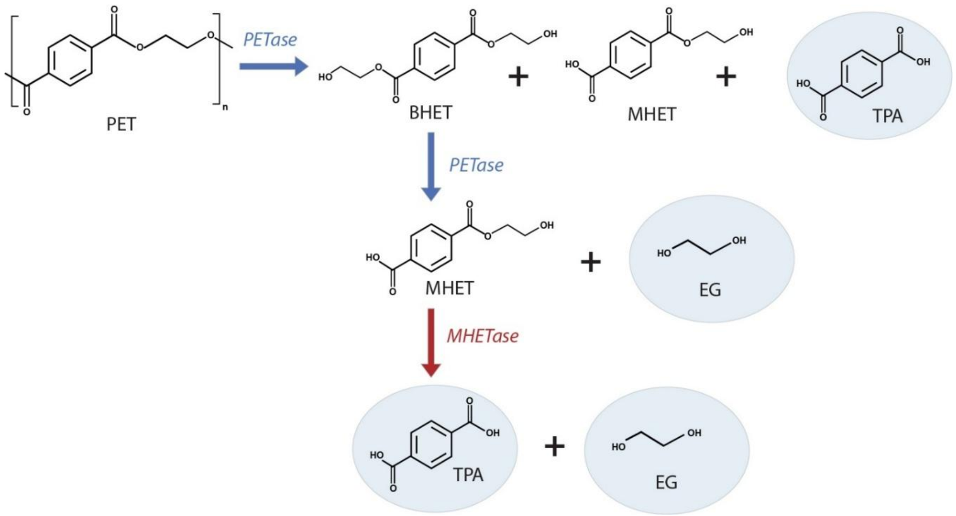

14. att. PET depolimerizācijas shēma: PETāze katalizē PET depolimerizāciju līdz *bis*(2-hidroksietil)tereftalātam (BHET), mono(2-hidroksietil)tereftalātam (MHET) un tereftālskābei (TPA). MHETāze pārvērš MHET monomēros – tereftalskābē TPA un etilēnglikolā EG.

Šie sadalīšanās produkti ir mazāk kaitīgi videi un turpmāk var tikt metabolizēti ar baktēriju palīdzību vai izmantoti rūpnieciskos pārstrādes procesos. Struktūras ziņā PETāze pieder pie hidrolāžu cutināžu saimes, kas ir enzīmi, kas parasti sadala dabiskos poliesterus, piemēram, kutīnu un vaskus, kas atrodama augu kutikulās. PETāzei piemīt šīs evolūcijas mantojums, bet tā ir pielāgojusies atpazīt un iedarboties uz sintētisko PET. Tās aktīvā vieta satur galvenos aminoskābju atlikumus, kas veicina esteru saišu hidrolīzi, ļaujot sadalīt garās polimēru ķēdes mazākos fragmentos. Šīs strukturālās īpašības ir bijušas izšķirošas centienos izstrādāt PETāzes variantus ar uzlabotu aktivitāti, stabilitāti un termisko izturību.[39, 40]

Kopš PET depolimerizējošo enzīmu atklāšanas enzimātiska PET pārstrāde tiek uzskatīta par daudzsološu plastmasas atkritumu apstrādes metodi, jo īpaši saistībā ar aprites ekonomikas stratēģiju.[41] Fermentatīvā pārstrāde piedāvā videi draudzīgu alternatīvu ķīmiskajām metodēm, pārvēršot PET tā monomēros, ko var atkārtoti izmantot jaunu plastmasas izstrādājumu sintēzei. Tomēr līdz šim izstrādātajiem PET sadalošajiem enzīmiem ir vairākas problēmas, kas ierobežo to izmantošanu rūpniecībā. Līdz šim PET rūpnieciskās enzīmu pārstrādes izmaksas ir ievērojami augstākas nekā jauna PET ražošanas izmaksas, jo pastāv vairāki ierobežojumi, kas saistīti ar pašlaik pieejamajām PETāzēm.[42] Lai gan rūpnieciskā ieviešana ir pierādīta, piemēram, Francijas uzņēmumā “*Carbios*”, daudzām PETāzes joprojām piemīt zema termostabilitāte, ierobežota katalītiskā efektivitāte un degradācijas starpproduktu izsaukta PETāzes inhibīcija, kas padara liela mēroga PET pārstrādi nepraktisku.[43, 44] Lai pārvarētu šos ierobežojumus, promocijas darbs ir vērsts uz PETāzes enzīmu inženierijas izstrādi, izmantojot progresīvas racionālas projektēšanas stratēģijas, lai izstrādātu efektīvu variantu rūpnieciskai PET enzīmu degradācijai. Darba izstrādes gaitā tika modificēts pašreizējais PET hidrolizējošo enzīmu zelta standarts [*ICCG* variantu lapu un zaru komposta kutināzes (*LCC-ICCG*)], izmantojot *in silico* proteīnu projektēšanas metodes, lai izstrādātu PET hidrolizējošu enzīmu, kam ir uzlabota termiskā stabilitāte un PET depolimerizācijas aktivitāte.

2.1. Inženierijas *LCC-ICCG* PETāzes fermenta izstrāde

Lapu un zaru komposta kutināze (*LCC*) ir ļoti efektīva, dabīgi sastopama PETāze, tās kušanas temperatūra (T_m) ir 84,7 °C.[45] 2020. gadā *Tournier* u. c. to tālāk modificēja, lai radītu *ICCG* (*LCC-ICCG*) variantu, kas sasniedz T_m vērtības 91,7–94,0 °C un pašlaik tiek uzskatīts par zelta standartu PETāžu jomā.[45, 46] Neskatoties uz šo izcilo stabilitāti, *LCC* plašais sekvenču telpas diapazons piedāvā ievērojamu potenciālu turpmākai optimizācijai. Balstoties uz *LCC-ICCG* skeletu, tika sākta stabilāka un aktīvāka PETāzes izstrāde, vadoties no hipotēzes, ka uzlabota termiskā stabilitāte korelē ar uzlabotu ekspresiju un katalītisko veiktspēju.

2.1.1. Racionālā inženierija

In silico enzīmu inženierija tika iesākta no *LCC-ICCG* varianta, stabilizēta lapu un zaru komposta kutināzes atvasinājuma, kas satur četras mutācijas (F243I, Y127G, S283C un D238C), tostarp papildu disulfīda saiti un 165. pozīcijā atjaunotu katalītisku serīna atlikumu.[46, 45, 47] Atlikumi 5 Å attālumā no aktīvās vietas tika izslēgti no mutaģēzes, lai saglabātu katalītisko funkciju. Lai radītu stabilizējošas variācijas, tika piemērotas trīs papildinošas aprēķinu stratēģijas: *Rosetta Supercharge*[48], *PROSS*[49] un *Disulfide-by-Design*[3]. *Rosetta Supercharge* pieeja uzlabo proteīna stabilitāti, palielinot virsmas hidrofilitāti, kas parasti ir saistīta ar uzlabotu strukturālo izturību. Plaši izmantota un vienkārša stabilizācijas stratēģija ir viena vai vairāku disulfīda saišu ieviešana, kas var nostiprināt proteīna mugurkaulu un uzlabot stabilitāti[50]. Papildu stabilizācijas pieejas mērķis ir paplašināt iekšmolekulāro ūdeņraža saišu tīklus, ieviest stabilizējošas sāls tiltiņus vai uzlabot hidrofobisko kodolu iepakojumu, kā tas ir īstenots *PROSS*[49]. Šīs pieejas deva attiecīgi 1000, 9 un 125 kandidātu variantus, no kuriem tika atlasītas apakškopas ar vislabvēlīgākajiem rezultātiem (C01-C10, P01-P09 un X01-X10). Visas 29 atlasītās variācijas tika pakļautas 1 µs molekulārās dinamikas simulācijām eksplicītā šķīdinātājā un klasificētas, pamatojoties uz *RMSF* atvasinātiem stabilitātes rādītājiem. Šī atlase identificēja sešus vislabākos kandidātus – C08, C09, P06, P08, X05 un X09, kas tika atlasīti eksperimentālai ekspresijai un raksturošanai, pamatojoties uz to prognozēto uzlaboto strukturālo stabilitāti (15. att.).

15. att. Sekvenču salīdzinājums. Savvaļas tipa *LCC* fermenta (*Uniprot ID G9BY57*), *ICCG* varianta, ko izstrādāja *Tournier et al.*,[46] un šajā darbā izstrādāto inženierijas fermentu (C08, C09, P06, P08, X05, X09) sekvenču salīdzinājums. Saskaņošana veikta ar *Clustal Omega*, grafiskais attēlojums iegūts, izmantojot *ESPrit 3* tīmekļa serveri[51].

2.1.2. Fermentu ekspresija un attīrīšana

Izvēlētie enzīmu kandidāti tika ekspresēti *E. coli* un attīrīti, izmantojot niķeļa afinitātes hromatogrāfiju (*IMAC*) un izmēra izslēgšanas hromatogrāfiju (*SEC*) (16. att.). PETāze enzīmiem efektīvs izrādījās BL21 Star (DE3) 18 °C temperatūrā ar iznākumu no 12 mg/l līdz 22 mg/l. No tiem variants X09 ekspresēja vislielāko daudzumu (22 mg/l), P08 – vismazāko (12 mg/l).

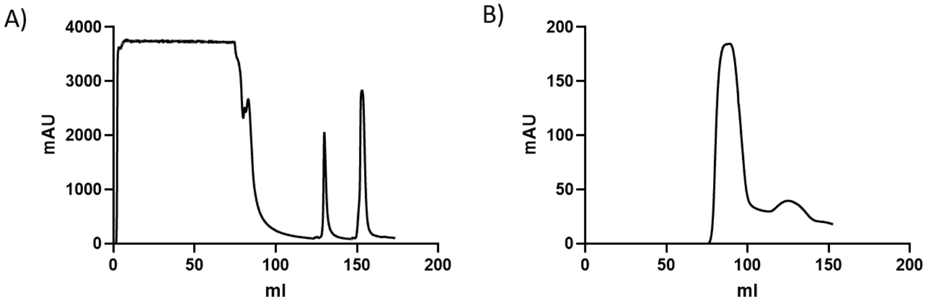

16. att. Tipiskas hromatogrammas no C09 enzīma attīrīšanas, kas parāda (A) niķeļa afinitātes hromatogrāfiju (*IMAC*) un (B) izmēra izslēgšanas hromatogrāfiju (*SEC*). Zilā līkne attēlo UV absorbanci (A280), kas izmantota proteīna eluācijas uzraudzībai.

2.1.3. Biofizikālā raksturošana

Pēc moficēto enzīmu izdalīšanas tika pārbaudīta sešu inženierijas variantu sekundārā struktūra (17. att.) un termiskā stabilitāte (18. att.). Tika atklāts, ka C09 (T_m = 97,1 °C) un X05 (T_m = 96,9 °C) variantiem ir augstāka T_m nekā references *LCC-ICCG* (T_m = 93,6 °C). X09 (T_m = 93,8 °C) variants uzrāda līdzīgu termisko stabilitāti kā *LCC-ICCG* (17. att.). P06 un P08 kušanas temperatūra netika noteikta, jo to enzimātiskā aktivitāte iepriekšējos eksperimentos bija niecīga, bet C08 gadījumā nebija iespējams iegūt uzticamu rezultātu.

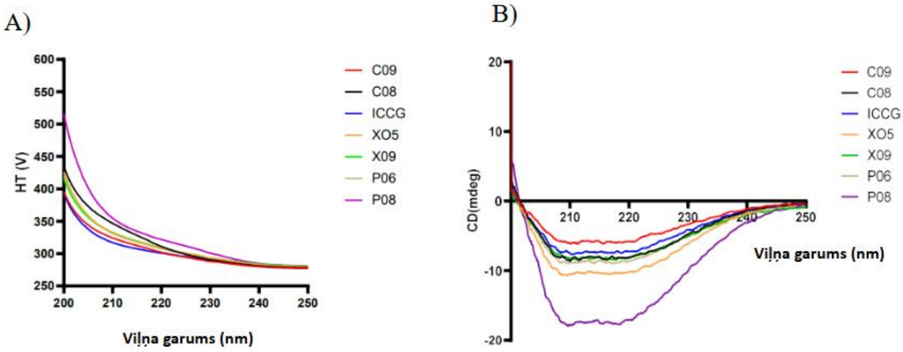

17. att. Sekundārās struktūras mērījumi ar cirkulāro dihroismu. A) Dažādu enzīmu spriegumu atkarība no viļņa garumu. B) Dažādu enzīmu eliptiskumu atkarība no viļņa garuma.

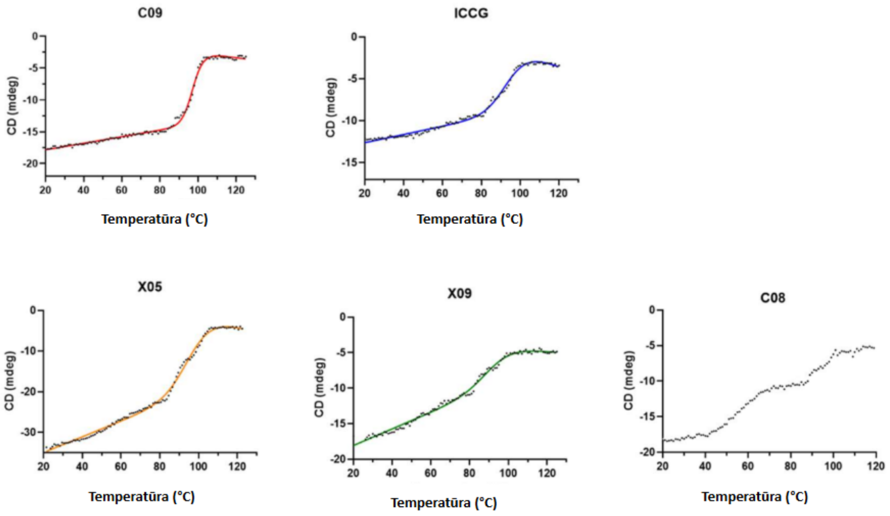

18. att. Tipiskas kušanas līknes. Katrs attēls parāda tipisku kušanas līkni, kas mērīta ar cirkulāro dihroismu 222 nm diapazonā no 20 °C līdz 120 °C atbilstošajam paraugam; melnie punkti attēlo eksperimentālos datus, nepārtraukta līnija norāda pielāgoto līkni.

2.1.4. Funkcionālais tests

Polietilēntereftalāta (PET) fermentatīvā hidrolīze tika novērtēta, kvantitatīvi nosakot galveno depolimerizācijas produktu veidošanos – *bis*(hidroksietil)tereftalātu (BHET), mono(hidroksietil)tereftalātu (MHET), tereftālskābi (TPA) un etilēnglikolu (EG), izmantojot apgrieztās fāzes *HPLC*. Reakcijas tika veiktas 68 °C temperatūrā ar 40 nM enzīma klātbūtnē 20 mM Tris-HCl buferšķīdumā (pH 8,0), kas satur 300 mM NaCl. Amorfās PET plēves (biezums – 250 µm, *Goodfellow, USA*) tika izgrieztas 6 mm diskos (~8,4 mg) un inkubētas atsevišķi 2 ml mikrocentrifūgas mēģenēs. Visi testi tika veikti piecas reizes, lai nodrošinātu reproducējamību. Produkta kvantitatīvā noteikšana tika veikta, izmantojot *Shimadzu LC-2030C 3D Plus* sistēmu, kas aprīkota ar *Kinetex C18* kolonnu (2,7 µm, 4,6 mm × 150 mm) 40 °C temperatūrā, plūsmas ātrum – 1 ml min^{-1}. Mobilā fāze sastāvēja no 0,1 % H_3PO_4 (A) un acetonitrila (B) ar lineāru gradientu. Alikvoti tika savākti dažādos laika punktos (0–144 h), atbilstoši atšķaidīti (21 reizi 0–72 h, 101 reizi 96–144 h) un analizēti pie 220 nm. Kalibrēšanas līknes *TPA* un MHET (0,1–50 µg ml^{-1}) un BHET (0,09–43,9 µg ml^{-1}) ļāva precīzi kvantificēt produkta veidošanos.

TPA un MHET uzkrāšanās laika gaitā atspoguļoja pakāpenisku PET hidrolīzi. No testētajiem variantiem daži uzrādīja paaugstinātu degradācijas ātrumu, salīdzinot ar savvaļas tipa PETāzi, kas labi korelēja ar uzlaboto termostabilitāti un salocīšanās īpašībām, kas noteiktas biofizikālajā raksturojumā.

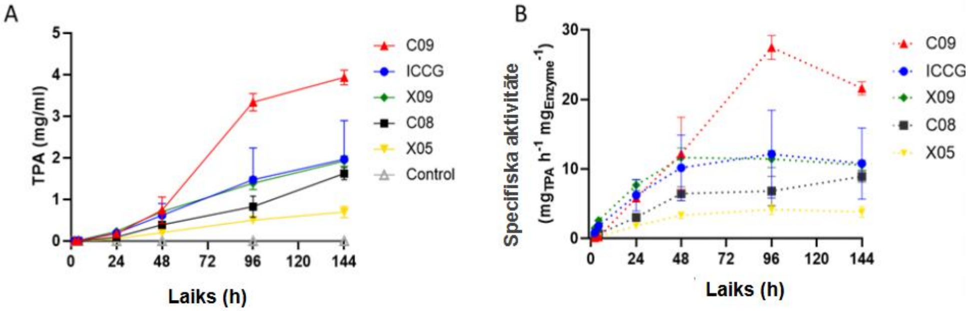

19. att. Dažādu enzīmu ietekme uz polietilēntereftalāta (PET) depolimerizāciju. (A) Tereftālskābes (TPA) veidošanās laika gaitā 68 °C temperatūrā (*LCC-ICCG* – C09 – X05 – X09 – C08 40 n M, pH 8,0). (B) TPA veidošanās 68 °C temperatūrā pēc četrām stundām un pēc 144 stundām.

Rezultāti liecina, ka 68 °C temperatūrā vidējā TPA koncentrācija dažādos laika punktos ir ievērojami augstāka C09 mutācijai nekā *ICCG* līdz sestajai dienai (144 h). Turklāt C09 specifiskā aktivitāte ir arī ievērojami augstāka (≈ 2 reizes) nekā zelta standartam *LCC-ICCG* tajā pašā laika periodā (19. att.).

2.1.5. Rentgena kristalogrāfija

C09 varianta kristāli tika iegūti ar tvaika difūziju 0,1 M nātrija citrāta pH 5,6, 20 % PEG 4000 un 20 % izopropanola vidē, un dati tika savākti pēc krioprotektīvas apstrādes ar 25 % glicerīnu. Rezultātā iegūtā struktūra, kas tika precizēta līdz 1,28 Å izšķirtspējai, sniedza atomāras detaļas par inženierijas ceļā radītajām stabilizējošajām mutācijām.

C09 enzīms satur 13 aizvietojumus, salīdzinot ar savvaļas tipa *LCC*, tostarp papildu lādētus atlikumus (piemēram, S36D, Q40R, S57K), kas stratēģiski izvietoti uz virsmas. Neskatoties uz šīm plašajām modifikācijām, kristalogrāfiskā analīze neuzrādīja nozīmīgas novirzes salocīšanā (*RMSD* 0,26 Å, salīdzinot ar *WT*; 0,15 Å, salīdzinot ar *LCC-ICCG*). Katalītiskā triāde (D210, H242, S265) saglabāja savu kanonisko ģeometriju, apstiprinot, ka struktūras integritāte ir saglabāta (24. att.).

Struktūras salīdzinājums un RMSF simulācijas parādīja, ka C09 uzrāda samazinātu lokālo elastību, īpaši ap katalītisko His242, kas izskaidro varianta izcilo termisko izturību ($T_m > 95$ °C) un divkārt augstāku PET degradācijas efektivitāti, salīdzinot ar *LCC-ICCG*. Autore uzskata, ka papildu virsmas lādiņi stabilizē virsmai pakļautās cilpas un novērš katalītiskās vietas atkārtošanos ilgstošas augstas temperatūras katalīzes laikā. Tādējādi, lai gan katalītiskā arhitektūra paliek nemainīga, dinamiskā stabilizācija, izmantojot racionālu dizainu, šķiet, ir galvenais faktors, kas nosaka C09 uzlaboto veiktspēju (20. att.).

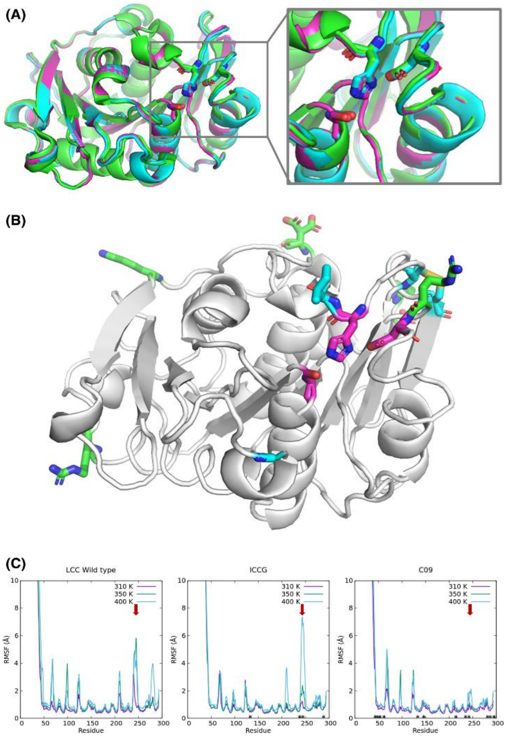

20. attēls. (A) PETāzes enzīmu struktūras salīdzinājums: savvaļas tips LCC (zaļā krāsā), *ICCG* variants (ciānkrāsas) un C09 variants (rozā krāsā). Kopējā struktūras salīdzinājumā nav redzamas nozīmīgas atšķirības starp enzīmiem, tostarp katalītiskās triādes pozīcija un orientācija. (B) mutāciju (stieņi) pozīcija *ICCG* (ciānkrāsā) un C09 (rozā krāsā) attiecībā pret

katalītisko vietu (rozā stieņi). (C) *LCC, LCC-ICCG* un C09 vidējā kvadrātiskā svārstību amplitūdas (RMSF) salīdzinājums dažādās temperatūrās (310 K, 350 K un 400 K).

2.2 Jaunās PETāzes SM14 raksturojums

Lai gan fermentatīvā PET sadalīšanās ir kļuvusi par daudzsološu ilgtspējīgu alternatīvu tradicionālajām pārstrādes metodēm, lielākā daļa pazīstamo PET sadalīšanās fermentu uzrāda ierobežotu katalītisko efektivitāti un šauru darbības diapazonu, jo īpaši vides apstākļos. Šis ierobežojums ir īpaši kritisks jūras piesārņojuma kontekstā, kur lielos daudzumos uzkrājas un saglabājas PET, jo tur ir augsts sāļums, zema temperatūra un trūkst efektīvu dabisko sadalīšanās procesu. Šajā kontekstā tika raksturots jauns PET sadalošs ferments, kas izdalīts no pie jūras sūkļiem saistītas baktērijas *Streptomyces* sp. SM14 (*PETase* SM14). Šis projekts tiek īstenots sadarbībā ar prof. *Giulia Di Rocco* no Modenas un *Reggio Emilia* Universitātes (Itālija), kur tika veikta daļa no projekta.

2.2.1. Enzīma ekspresija un attīrīšana

Gēns, kas kodē nobriedušu PETāzi SM14 no *Streptomyces sp.* SM14, tika klonēts pLATE52 vektorā, izmantojot ligācijas neatkarīgu klonēšanu, un ekspresēts *E. coli* BL21 (DE3). Proteīna ekspresija tika inducēta ar *IPTG*, pēc tam sekoja šūnu līze un attīrīšana ar niķeļa afinitātes hromatogrāfiju, izmantojot *HisTrap HP* kolonnu. PETāze SM14 tika eluēta ar imidazola gradientu, un tika savāktas frakcijas ar augstāko proteīna koncentrāciju, nosakot to ar UV absorbciju pie 280 nm un pamatojoties uz tā aprēķinātajām molekulārām īpašībām.

2.2.2. Biofizikālā raksturošana

Tālās UV CD spektroskopija tika izmantota, lai novērtētu PETāzes SM14 sekundārās struktūras saturu un salīdzinātu tās salocīšanos ar references PETāzi no *Ideonella sakaiensis.*[36, 52] CD spektri parādīja labi definētas minimālās vērtības aptuveni pie 208 nm un 222 nm, kas ir raksturīgas α/β-hidrolāzes salocījumam, kurā dominē α-spirāles un β-lapu elementi. (18. att.) PETāzes SM14 spektrālais profils ļoti līdzinājās *I. sakaiensis* PETāzes spektrālam profilam, norādot, ka enzīms saglabā līdzīgu kopējo sekundāro struktūru, neskatoties uz sekvences atšķirībām. Dati apstiprina pareizu proteīna salocīšanos un atbilstību PETāzes SM14 struktūrai, kas noteikta ar rentgenkristalogrāfijas metodi.

Termiskās denaturācijas eksperimenti, kas tika kontrolēti, mērot eliptiskumu 222 nm kā funkciju no temperatūras, noteica PETāzes SM14 kušanas temperatūru (T_m) 56,3 °C, kas liecina par ievērojamu termisko stabilitāti. Salīdzinājumā ar *Ideonella sakaiensis* PETase T_m tika noteikta 45,0 °C, kas liecina, ka SM14 ir vairāk nekā par 10 °C termiski stabilāka (21. att.). Šis T_m pieaugums liecina par uzlabotu struktūras stingrību vai uzlabotām iekšmolekulārām mijiedarbībām PETāzē SM14, kas, visticamāk, veicina tās izturību vides apstākļos. Atvērtā pāreja liecināja par labi salocītu monomēru proteīnu.

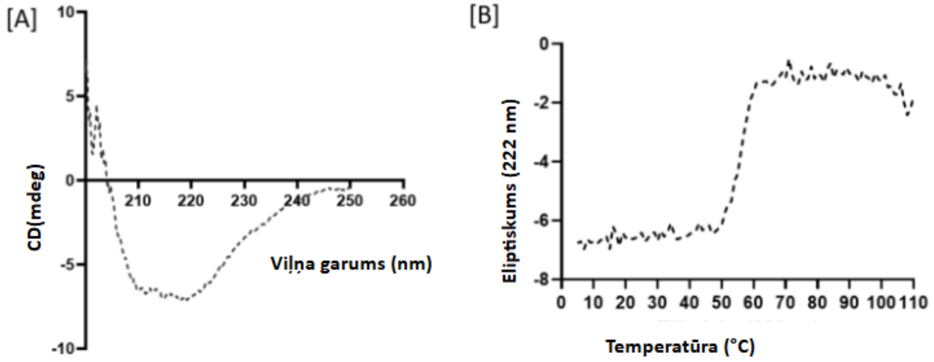

21. att. Cirkulārā dichroisma (CD) analīze, lai noteiktu fermenta sekundāro struktūru (A) un enzīma termostabilitāti (B).

Proteīna termiskā stabilitāte tika novērtēta, izmantojot arī diferenciālo skenēšanas fluorimetriju (DSF) ar *SYPRO Orange* krāsvielu (*Thermo Fisher Scientific*) uz 7500 *Real-Time PCR* sistēmas (*Applied Biosystems*). Katra reakcija saturēja 5 µM fermentu un 5× krāsvielu analizējamājā tilpumā 25 µL, kas tika sagatavots, sajaucot vienādus fermenta šķīduma (10 µM) un 10× krāsvielas (atšķaidīta no 5000× stamndartšķīduma) tilpumus atbilstošajā proteīna buferšķīdumā. Fluorescence tika novērota temperatūras paaugstināšanās laikā no 15 °C līdz 95,3 °C, kušanas temperatūras (Tm) tika noteiktas no denaturācijas līkņu infleksijas punktiem. Lai novērtētu stabilitāti dažādos fizikāli ķīmiskajos apstākļos, tika veikti testi pH diapazonā no 6,0 līdz 9,0 un NaCl koncentrācijās no 100 Mm līdz 700 Mm (22. att.). pH izmaiņas minimāli ietekmēja T_m, kas palika salīdzinoši nemainīga, savukārt NaCl koncentrācijas palielināšana līdz 700 mM Tris buferšķīdumā (pH 8,0) neizraisīja proteīna struktūras izmaiņas. Šie rezultāti liecina, ka enzīms saglabā augstu strukturālo stabilitāti plašā sāls koncentrācijas un pH vērtību diapazonā.

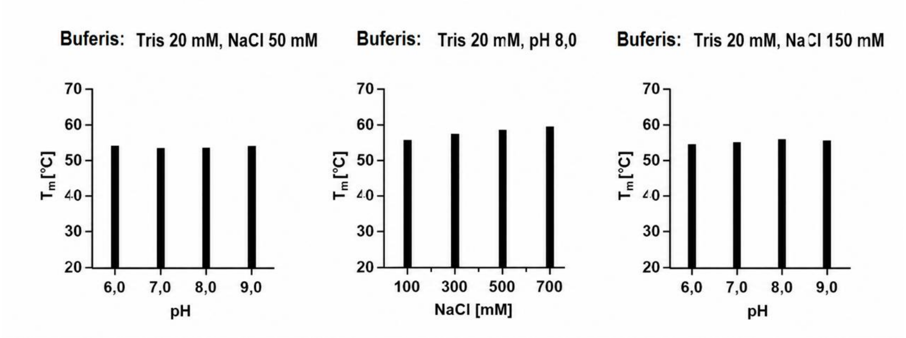

22. att. *PETase* SM14 kušanas temperatūras izmaiņas dažādos buferšķīdumos, kas noteiktas ar *SYPRO Orange* temperatūras atkarīgo fluorescences izmaiņu palīdzību.

MALDI masspektrometrija nodrošina precīzu molekulmasas noteikšanu un sekvences verifikāciju, ļaujot noteikt degradāciju, pēctranslācijas modifikācijas un apstiprināt ekspresijas produktus[53]. *MALDI-TOF* masspektrometrija tika izmantota, lai apstiprinātu attīrīta PETāzes SM14 fermenta molekulmasu un sekvences integritāti.

Mērījumi tika reģistrēti ar *FLEX-PC autoflex TOF/TOF* (*Bruker*). Datu ieguves režīms bija lineārs, polaritātes spriegums *POS*. Uzņēmumu skaits bija 500. Tika sajaukti proteīns un skābeņskābe (viens paraugs ar 1 µL un viens ar 0,5 µL). Viens piliens šī šķīduma tika sajaukts ar matricu SA (sinapīnskābe), ļaujot tai sacietēt. Proteīna koncentrācija bija 10 mg/ml.

Eksperimentālā molekulmasa (aptuveni 28 kDa) precīzi atbilda teorētiskajai masai, kas aprēķināta no aminoskābju secības (23. att.), apstiprinot veiksmīgu neizmainīta proteīna ekspresiju un attīrīšanu. Netika novērotas proteolītiskas sadalīšanās, saīsināšanas vai pēctranslācijas modifikācijas pazīmes. Masas precizitāte (± 0,1 kDa) un nozīmīgu piemaisījumu pīķu neesamība apstiprināja parauga, kas iegūts pēc divpakāpju hromatogrāfiskās attīrīšanas, augsto tīrību.

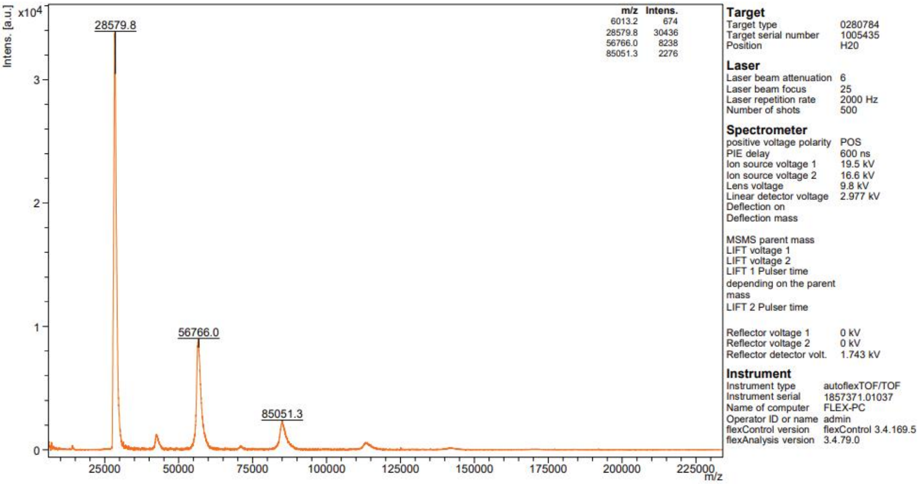

m/z	Intens.
6013.2	674
28579.8	30436
56766.0	8238
85051.3	2276

Target
Target type 0280784
Target serial number 1005435
Position H20

Laser
Laser beam attenuation 6
Laser beam focus 25
Laser repetition rate 2000 Hz
Number of shots 500

Spectrometer
positive voltage polarity POS
PIE delay 600 ns
Ion source voltage 1 19.5 kV
Ion source voltage 2 16.6 kV
Lens voltage 9.8 kV
Linear detector voltage 2.977 kV
Deflection on
Deflection mass

MSMS parent mass
LIFT voltage 1
LIFT voltage 2
LIFT 1 Pulser time
depending on the parent mass
LIFT 2 Pulser time

Reflector voltage 1 0 kV
Reflector voltage 2 0 kV
Reflector detector volt. 1.743 kV

Instrument
Instrument type autoflexTOF/TOF
Instrument serial 1857371.01037
Name of computer FLEX-PC
Operator ID or name admin
flexControl version flexControl 3.4.169.5
flexAnalysis version 3.4.79.0

23. att. PETāzes SM14 *MALDI-TOF* analīze. Šī vērtība tika iegūta ar 5 mg/ml proteīna koncentrāciju, atšķaidītu ar 50 % TFA un sinapīnskābi (SA) kā matricu.

Turklāt peptīda masas nospiedums pēc triptona hidrolīzes apstiprināja sekvences pārklājumu virs 90 %, apstiprinot, ka ekspresētais produkts precīzi atbilst paredzētajam PETāzes SM14 konstruktam (24. att.). Saskaņa starp sagaidāmo un novēroto masu vēl vairāk apstiprināja strukturālos datus, kas iegūti CD un DSF analīzēs, kopumā apstiprinot, ka PETāze SM14 ir stabils, pareizi salocīts un strukturāli neskarts enzīms.

1 AQNPHERGPD PSNSYIEQAR GSYSVSQRSI SRLGSDGFRD GTMYYPTSTA
51 DGRFGVVAIS PGYTASESTI AWLGPRLASF GFVVVTINTD SRYDQPRQRA
101 TQLHAALDHA IGDSVVGPRI DTSRQAVMGH SMGGGGALQA AEERDEIRAA
151 VPLTPWNLKK GWSGVDAATL VIGAENDAIA PVRSHSIPFY ESLTNAERRA
201 YLELRREGHF APNSSNTLIA KYSVSWLKRY VDNDLRYDQF IDPGPRTGIT
251 TGVSDYRLG

24. att. MS/MS spektri (100–1200 m/z), kas iegūti no *PETase* SM14 joslas pēc attīrīšanas, ekstrahēti un hidrolizēti ar tripsīnu un analizēti ar ESI-MS/MS spektrometriju. Sekvences pārklājums 95 %.

2.2.3. Funkcionālais tests

PETāzes SM14 enzimātiskā aktivitāte tika novērtēta, izmantojot PET pēcpārstrādes plastmasu (PCP) kontrolētos reakcijas apstākļos, mainot galvenos parametrus, tostarp pH, temperatūru un NaCl koncentrāciju. PETase SM14 efektīvi sadalīja PCP, atbrīvojot tereftālskābi (TPA), kas kvantitatīvi noteikta ar *HPLC*, un optimāla aktivitāte tika novērota pie pH 9,0. TPA iznākums palielinājās aptuveni 10 reizes bāziskos apstākļos un bija lielā mērā neatkarīga no temperatūras starp 40 °C un 50 °C. Enzimātiskā aktivitāte tika ievērojami pastiprināta ar sāļumu, parādot vairāk nekā 100 reizes palielinātu TPA atbrīvošanu NaCl klātbūtnē, ar optimālo koncentrāciju pie apmēram 900 mM.

2.2.4. Rentgena kristalogrāfija

Promocijas darba izstrādes gaitā tika noteikta PETāzes SM14 augstas izšķirtspējas kristāla struktūra no *Streptomyces* sugas, kas izolēta no jūras sūkļa. Enzīma kristāli bez marķiera tika audzēti, izmantojot tvaika difūzijas metodi, un difraktēti līdz 1,43 Å izšķirtspējai *Diamond Light Source* I03 staru līnijā Oksfordā, Apvienotajā Karalistē. Struktūra tika atrisināta, izmantojot molekulāro aizstāšanu, kā meklēšanas šablonu izmantojot *AlphaFold* prognozēto modeli, kam sekoja iteratīva manuāla precizēšana *Coot*[54] un automatizēti cikli *REFMAC5*[55].

PETāzes SM14 struktūra uzrādīja klasisko α/β-hidrolāzes locījumu ar konservētu Ser–His–Asp katalītisko triādi, kas atradās sekla substrāta saistīšanās plaisā. Struktūras superpozīcija ar *Ideonella sakaiensis* PETāze (IsPETāze) un poliestera hidrolāzi (PE-H) (25. att.) atklāja augstu struktūras konservatīvumu ar *RMSD* 0,69 Å (IsPETāze) un 0,81 Å (PE-H). Katalītiskie atlikumi precīzi saskaņojās, apstiprinot kopīgu serīna hidrolāzes mehānismu.

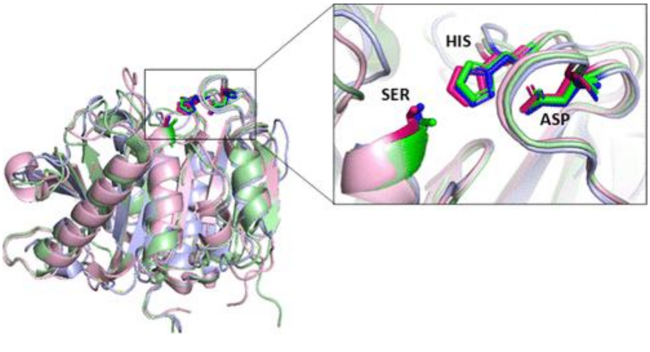

25. att. PETāzes SM14 (gaiši zilā krāsā), IsPETāzes (PDB kods 6ILW, gaiši zaļā krāsā) un PE-H no *P. aestusnigri* (PDB kods: 6SBN, gaiši rozā krāsā) struktūras salīdzinājums, kas veikts, izmantojot *PyMOL*.

Jāatzīmē, ka SM14 izrādīja izteiktas cilpas konformācijas blakus aktīvajai vietai, kas sašaurināja katalītisko kabatu, salīdzinot ar IsPETāzi. Šī nelielā aizvēršanās var nodrošināt uzlabotu substrāta saistīšanos un palielinātu stingrību, kas atbilst enzīma augstajai kušanas temperatūrai (T_m 56,3 °C) un izteiktajai sāls toleranci līdz 1,5 M NaCl. Elektrostatiskās virsmas analīzes liecināja par mazāk polarizētu un vienmērīgāk sadalītu lādiņa potenciālu, salīdzinot ar IsPETāzi (pI 6,67 pret 9,41), kas potenciāli stabilizē proteīnu jūras vai sārmainā vidē. Kopumā šīs īpašības liecina, ka PETāze SM14 ir attīstījusies, lai nodrošinātu katalītisko noturību augsta sāļuma un viegli termofīlos apstākļos, kas ir daudzsološa pielāgošanās PET sadalīšanai vidē.

2.2.5. Struktūras un funkcijas korelācijas analīze

Promocijas darba izstrādes gaitā detalizēti tika pētīta PETāzes SM14 struktūra, lai izprastu jonu stipruma ietekmi uz PETāzes fermentiem. Lai padziļināti izpētītu korelētas elastības ietekmi uz enzīmu adaptāciju, tika apvienotas molekulārās dinamikas (MD) simulācijas ar *in vitro* enzīmu testiem uz IsPETāzi (no *Ideonella sakaiensis*) un PETāzi SM14. Mērķis bija noteikt, kā lokālas kustības un dinamiskā saistība ietekmē katalītisko efektivitāti dažādās jonu vidēs. IsPETāze, ko izdalīja *Ideonella Sakaiensis* 201-f6, un PETāze SM14, ko izdalīja jūras sūklis *Streptomyces sp.* SM14, raksturo vienāds katalītiskais skelets, tomēr ir attīstījušās būtiskas atšķirības, lai katrs enzīms pielāgotos savai dabiskajai videi. Šajā pētījumā veiktie PET pulvera sadalīšanās aktivitātes testi un literatūrā atrodamie pierādījumi liecina, ka NaCl koncentrācija pozitīvi ietekmē PETāzes SM14 aktivitāti, kas atbilst tās hipersāļajai jūras izcelsmei, bet negatīvi ietekmē IsPETāzi. Līdz šim šis fenomens ir novērots, izmantojot analītiskas metodes, piemēram, *HPLC*, SEM un AFM, kas neizskaidro šo efektu strukturālo pamatu.

Lai novērstu šo nepilnību, tika izmantota molekulārā modelēšana un MD simulācijas, lai veiktu detalizētu strukturālo salīdzinājumu un molekulāra līmeņa izskaidrojumu eksperimentā novērotajām atšķirībām starp diviem homoloģiskiem plastmasas sadalīšanas enzīmiem. No 500 ns garām MD simulācijām iegūtie rezultāti liecina, ka IsPETāzes saistīšanās vieta ir ievērojami platāka un elastīgāka nekā PETāzē SM14 atrastā saistīšanās vieta, ko apstiprina lielāki vidējie atlieku attālumi un atvērtāka elektrostatiskā virsma (26. att.). Šo inaktivāciju galvenokārt izraisa konformācijas pārkārtošanās, kas saistīta ar atlieku W159 apgriešanu, kas izspiež katalītisko histidīnu (H237) no serīna (S160), traucējot aktīvās vietas ģeometriju. Pretstatā PETāze SM14 saglabāja stingrāku struktūru, kas augsta sāls satura apstākļos piedzīvoja nelielas, bet labvēlīgas konformācijas izmaiņas. Šīs smalkās pārkārtošanās veicināja aktīvās vietas hidratāciju, un papildu ūdens molekulas atviegloja substrāta mijiedarbību un uzturēja katalītisko efektivitāti.

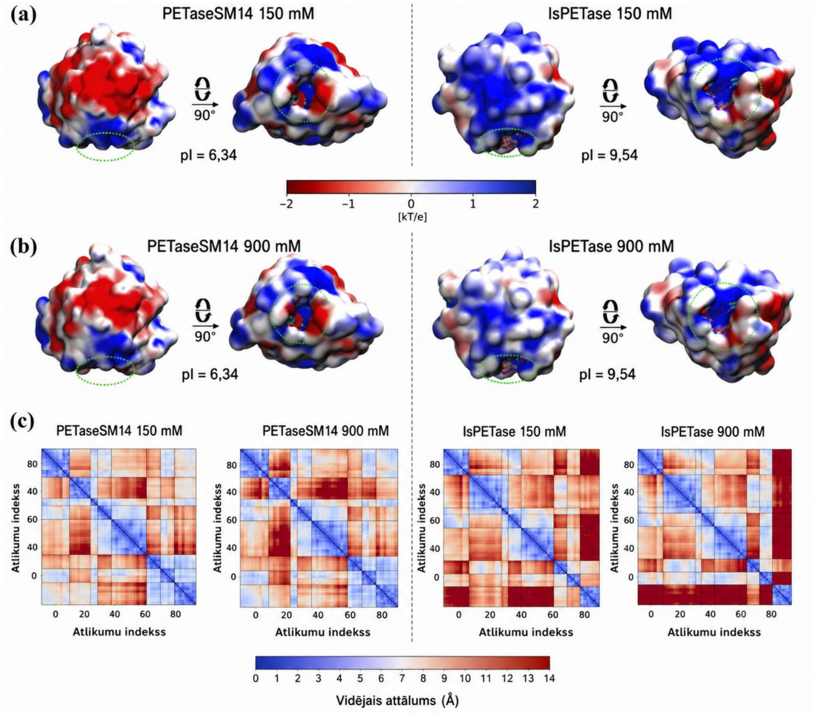

26. att. Jonu koncentrācijas ietekme uz PETāzi SM14 un IsPETāzi. PETāzes SM14 un IsPETāzes elektrostatiskā potenciāla virsma pie (A) 150 mM un (B) 900 mM NaCl koncentrācijas. Saistīšanās vietu atrašanās vietas un galvenie atlikumi ir norādīti ar zaļas krāsas punktētiem apļiem. (C) Atlikumu, kas veido PETāzes SM14 un IsPETāzes saistīšanās vietas, attāluma kartes abās jonu koncentrācijās. Kartēs norādītas vidējās vērtības katram krustattālumam, kas aprēķināts, izmantojot trīs 500 ns MD simulācijas replikas. Krāsu skala ir no 0 Å (punkti zilā krāsā) līdz ≥ 14 Å (punkti sarkanā krāsā).

PET saistīšanās modelēšana, izmantojot deviņu monomēru PET ķēdes, apstiprināja, ka PETāze SM14 augstā sāļumā un IsPETāze zemā sāļumā sasniedz optimālu substrāta pielāgošanos un katalītisko izlīdzināšanu. Pie 900 mM NaCl PETāze SM14 uzrādīja aptuveni divas reizes vairāk reaktīvo enzīmu-substrātu konfigurāciju, salīdzinot ar tā darbību pie 150 mM, savukārt IsPETāze parādīja 50 % samazinājumu šādos stāvokļos tādos pašos apstākļos. Šie atklājumi labi korelē ar novērotajām eksperimentālajām aktivitātes tendencēm un sniedz molekulāra līmeņa izskaidrojumu abu enzīmu atšķirīgajām jonu adaptācijām.

2.3. Pašreizējās tendences un nākotnes iespējas

Balstoties izveidotajā aprēķinu un eksperimentuā, promocijas darba autore un viņas kolēģi ir iesākuši turpmākos pētījumus, lai izstrādātu racionālu un simulāciju vadītu inženierijas risinājumu, kura mērķis ir uzlabot PETāzes SM14 stabilitāti un katalītisko efektivitāti. Paralēli tiek strādāts pie fermentatīvās PET depolimerizācijas mēroga palielināšanas, izmantojot inženierijas *LCC-ICCG*-C09 variantu bioreaktoru sistēmās, ar mērķi uzlabot procesa stabilitāti, substrāta pieejamību un kopējo katalītisko produktivitāti, lai to varētu ieviest rūpniecībā.

SECINĀJUMI

Šajā darbā tika izstrādāta integrēta skaitļošanas un eksperimentālā sistēma racionālai enzīmu inženierijai ar uzlabotu stabilitāti, aktivitāti un izturību pret vides ietekmi. Šajā pieejā tika apvienota molekulārā modelēšana, molekulārās dinamikas simulācijas, proteīnu inženierija, bioķīmiskā raksturošana un strukturālā analīze, lai nodrošinātu efektīvu enzīmu optimizāciju.

- Fruktozilpeptīda oksidāzes (FPOX) variantiem tika uzlabota termostabilitāte, izmantojot tādas enzīmu inženierijas metodes kā RMSF vadītas mutācijas, sāls tiltiņi un disulfīda saites (1. pielikums).
- Lai gan optimizētie FPOX varianti uzrāda uzlabotu stabilitāti un aktivitāti, turpmākā attīstība ir vērsta uz to veiktspējas uzlabošanu attiecībā uz glikēto hemoglobīnu. Pašreizējie dati par šo mērķi ir atrodami manuskripta 5. pielikumā.
- PET noārdošo enzīmu inženierija parādīja šīs sistēmas plašāku pielietojamību rūpnieciskajā biokatalīzē. LCC-ICCG-C09 variants uzrādīja uzlabotu termisko stabilitāti un aptuveni divas reizes augstāku PET depolimerizācijas efektivitāti salīdzinājumā ar sākotnējo enzīmu, nodrošinot daudzsološu pamatu enzīmu izmantošanai plastmasas pārstrādē, neskatoties uz atlikušajām nepilnībām, kas ir saistītas ar substrāta kristāliskumu, jūtību pret pH un mērogojamību (3. pielikums).
- Tika atklāts un raksturots jauns no jūras sūkļiem iegūts enzīms PETāze SM14. Tika konstatēts, ka tas saglabā augstu aktivitāti sārmainā vidē, pie augsta sāls satura un paaugstinātas temperatūras (2. pielikums).
- PETāzes SM14 strukturālās un molekulārās dinamikas analīzes atklāja adaptīvās īpašības, kas atbalsta katalīzi hipersāļā vidē, uzsverot tās potenciālu jūras plastmasas bioloģiskajā attīrīšanā (4. pielikums).

DOCTORAL THESIS PROPOSED TO RIGA TECHNICAL UNIVERSITY FOR PROMOTION TO THE SCIENTIFIC DEGREE OF DOCTOR OF SCIENCE

To be granted the scientific degree of Doctor of Science (PhD), the present Doctoral Thesis has been submitted for defence at the open meeting of RTU Promotion Council on 23 July 2026 at 15.00 at the Faculty of Natural Sciences and Technology of Riga Technical University, 3/7 Paula Valdena Street, Room 272, with online participation option at the Zoom link https://rtucloud1.zoom.us/j/9352086644.

OFFICIAL REVIEWERS

Professor Dr. Kristaps Jaudzems
University of Latvia, Latvia

Professor Dr. Ioannis Pavlidis
University of Crete, Greece

Professor Dr. Gianluca Molla
University of Insubria, Italy

DECLARATION OF ACADEMIC INTEGRITY

I hereby declare that the Doctoral Thesis submitted for review to Riga Technical University for promotion to the scientific degree of Doctor of Science (PhD) is my own. I confirm that this Doctoral Thesis has not been submitted to any other university for promotion to a scientific degree.

Shapla Bhattacharya.................................(signature)
Date: ………………………

The Doctoral Thesis has been prepared as a collection of thematically related scientific publications complemented by summaries in both Latvian and English. The Doctoral Thesis unites four scientific publications. The scientific publications have been written in English, with a total volume of 168 pages, including supplementary data.

CONTENTS

GENERAL OVERVIEW OF THE THESIS

Introduction

Enzymes are nature's highly efficient biocatalysts, enabling complex biochemical reactions under mild conditions with remarkable specificity and selectivity. Their applications span a wide range of industries, including pharmaceuticals, agriculture, diagnostics, and environmental remediation. However, native enzymes often exhibit limitations such as low stability under industrial conditions, suboptimal activity, or poor substrate compatibility, which restrict their broader application.

Enzyme engineering is a sophisticated process that enables naturally occurring enzymes to be modified in order to enhance their catalytic efficiency, stability, or specificity. Through targeted alterations of their amino acid sequence and structural features, biological catalysts can be transformed into more effective and resilient biocatalysts, tailored for a wide array of industrial applications. This intricate process often employs techniques such as directed evolution, site-directed mutagenesis, and computational modeling. In the lab, the author makes extensive use of structural information, and focuses on rational design approaches.

In rational design, the author leverages computational tools and molecular modeling to simulate the effects of modifications to the amino acid sequence of the enzyme. By analyzing the enzyme's three-dimensional structure, the author can identify critical residues that influence catalytic activity, stability, and specificity. This insight allows us to introduce targeted mutations to optimize these properties, ultimately creating engineered enzymes that meet specific industrial needs.

For my PhD project, the author has been working on the engineering of two groups of enzymes: Fructosyl Peptide Oxidases (FPOX) and PETases. Both of these enzymes are highly relevant for either biomedical or environmental applications.

Fructosyl peptide oxidases (FPOX), and fructosyl amino oxidases (FAOX) alike, are deglycating enzymes that find application as key enzymatic components in diabetes monitoring devices. Indeed, their use with blood samples can provide a measurement of the concentration of glycated hemoglobin and glycated albumin, two well-known diabetes markers. However, the FPOX currently employed in enzymatic assays cannot directly detect whole glycated proteins, making it necessary to perform a preliminary proteolytic treatment of the target protein to generate small glycated peptides that can act as viable substrates for the enzyme. This is a costly and time-consuming step. This preliminary step is due to their buried active site and to the narrow tunnel that provides access to their catalytic pocket, as shown by multiple crystal structures of FPOX and FAOX enzymes. In this project, the author is engineering this group of enzymes to expand their substrate range and to improve their thermal stability for biomedical applications. In particular, the aim is to use these enzymes for deglycating intact proteins, or for mitigating their level of glycation over time. Ultimately, with the improved enzyme, the author aims to develop an enzymatic tool for the measurement of glycated hemoglobin or glycated albumin, two known diabetes markers, in the blood.

Using the same enzyme engineering approach, the author is also working on plastic depolymerizing enzymes (PETases), which are enzymes that can break down polyethylene terephthalate (PET) into its monomeric subunits, terephthalic acid and ethylene glycol. These enzymes belong to the larger family of hydrolases, which work by cleaving the ester bonds in PET and lead to its degradation into smaller monomers.

Although several PETases from different origins have been reported, their catalytic efficiency and thermal stability remain insufficient for economically viable industrial PET depolymerization, particularly compared to conventional chemical and mechanical recycling processes. Limited enzyme performance, especially low activity and poor stability near PET's glass transition temperature, is a major bottleneck for cost-effective enzymatic recycling. Therefore, the author applies a computer-aided enzyme engineering approach to enhance catalytic efficiency and operational stability for industrial application.

Overall, this work contributes to the advancement of rational enzyme engineering by demonstrating an efficient, reproducible design–validation workflow and applying it to two distinct yet industrially relevant enzymes. The outcomes of this research have implications for future biocatalyst development and for addressing critical challenges in medical and environmental biotechnology.

The Aims of the Doctoral Thesis

The primary aim of this Doctoral Thesis is to advance enzyme engineering through the rational design, development, and characterization of improved enzyme variants with direct biomedical and environmental applications. The research focuses on two enzyme families: fructosyl peptide oxidases (FPOXs) for diabetes diagnostics and polyethylene terephthalate hydrolases (PETases) for plastic degradation.

Objectives

Biomedical application: FPOX enzymes for diabetes diagnostics

4. To investigate the structural limitations of wild-type FPOX enzymes that hinder their ability to process whole glycated proteins.

5. To apply computational tunnel-widening and structure-guided engineering strategies to generate FPOX variants with improved substrate accessibility, enhanced thermostability, and broadened substrate specificity.

6. To evaluate the activity of engineered FPOX variants directly on glycated substrates for their diagnostic potential.

Environmental application: PETases for plastic degradation

5. To identify flexible and unstable regions of known PETases using structural data and molecular dynamics simulations.
6. To design and introduce targeted mutations aimed at improving PETase thermal stability and catalytic efficiency.
7. To assess the degradation efficiency of engineered PETase variants on polyethylene terephthalate under conditions relevant to industrial recycling.
8. To conduct mechanistic studies to determine how specific mutations influence the PET degradation pathway.

Scientific novelty and main results

The scientific novelty of this Doctoral Thesis lies in the integration of computational and experimental approaches for the rational design and characterization of improved enzyme variants, focusing on two distinct enzyme families: FPOX and PETase. By combining *in silico* protein engineering, molecular dynamics simulations, and structural biology with expression, purification, and detailed biochemical and biophysical analysis, this study establishes a multi-disciplinary validation workflow. The resulting findings contribute valuable knowledge and tools to the field of enzyme engineering while offering potential for industrial and environmental applications.

In the first part of my doctoral study, where I focused on a thermally stabilized FPOX enzyme, an *in silico* protein engineering approach was applied to further enhance the overall thermal stability of the enzyme and to improve its catalytic activity toward large substrates.

The final design exhibited a marked improvement in thermal stability relative to the wild-type enzyme, along with a distinct widening of its access tunnel. These changes translated into significant enzymatic activity across a range of glycated substrates, underscoring the potential of computational design for tailoring enzyme function.

Building upon this framework, in the second part of my doctoral study, the PET-hydrolyzing enzyme gold standard, the ICCG variant of the leaf-branch compost cutinase (LCC-ICCG), was further engineered using computational design. This effort yielded the mutant LCC-ICCG-C09, which displayed a 3.5 °C increase in melting temperature (Tm) compared to LCC-ICCG. Under optimal reaction conditions (68 °C), LCC-ICCG-C09 hydrolyzed amorphous PET into terephthalic acid (TPA) with a two-fold higher efficiency relative to the parental variant. With its improved thermal stability and catalytic performance, LCC-ICCG-C09 represents a promising candidate for future applications in industrial PET recycling.

In parallel, a novel PETase-like enzyme (PETase SM14) from Streptomyces sp. SM14 was expressed in *Escherichia coli* and evaluated on post-consumer plastic substrates. Activity assays coupled with high-performance liquid chromatography (HPLC) for product quantification, as well as scanning electron microscopy and atomic force microscopy for substrate surface analysis, revealed that PETase SM14 possesses high salt tolerance (up to 1.5 M), good heat resistance (T_m 56.26 °C), and optimal activity at pH 9.0. Its X-ray crystal structure, which I solved at 1.43 Å, confirmed conserved PETase family features and provided a foundation for future engineering strategies.

To further probe structural and functional mechanisms, all-atom molecular dynamics (MD) simulations were combined with *in vitro* assays to compare PETase SM14 and *Ideonella sakaiensis* PETase (IsPETase) under different NaCl concentrations (150 mM and 900 mM). The results demonstrated that, due to loop elongation, IsPETase exhibits a flexible and wide binding site that enhances substrate accommodation but also displaces catalytic residues, leading to rapid deactivation, especially at high-salt concentrations. Conversely, PETase SM14 displays a rigid and narrower binding pocket, which undergoes moderate widening at elevated salt concentrations, thereby facilitating water and substrate recruitment. Moreover, adsorption studies on PET slabs revealed that PETase SM14 under high-salt conditions and IsPETase under low-salt conditions bind PET substrate chains in the same trans:gauche conformational distribution observed in amorphous PET. These insights not only explain the observed activity profiles but also provide novel structural details such as the architecture and electrostatic environment of the substrate-binding cleft, key aromatic residues involved in polymer chain stabilization, and surface charge distribution to guide the engineering of PET-degrading enzymes for diverse environmental conditions.

Practical application

This study holds significant practical potential in both industrial and environmental biotechnology. The engineered FPOX variants with enhanced thermal stability and substrate specificity provide a robust foundation for the development of sensitive and practical biosensing platforms for direct glycated hemoglobin |(HbA1c) detection. The development of improved PET-hydrolyzing enzymes, including LCC-ICCG-C09 and PETase SM14, offers promising solutions for the enzymatic recycling of polyethylene terephthalate (PET), enabling closed-loop recovery of terephthalic acid and contributing to sustainable plastic waste management.

Structure and volume of the Thesis

This Thesis is a collection of thematically related scientific publications on enzyme engineering for biomedical and environmental applications. It compiles results from four original scientific papers indexed in Scopus and Web of Science.

Publications and approbation of the Thesis

The results of the Thesis have been published in four scientific papers. Additionally, the results have also been disseminated at 13 scientific conferences and two pitch sessions.

Scientific publications

5. Estiri, H.,* **Bhattacharya, S**.,* Rodriguez Buitrago, J. A., Castagna, R., Legzdiņa, L., Casucci, G., Ricci, A., Parisini, E., Gautieri, A. Tailoring FPOX Enzymes for Enhanced Stability and Expanded Substrate Recognition. *Scientific Reports*. 2023, 13, 18610. Available from: https://doi.org/10.1038/s41598-023-45428-1.*These authors contributed equally to this work.

6. Carletti, A., **Bhattacharya, S**., Pedroni, S., Berto, M., Bonettini, R., Castagna, R., Parisini, E., Di Rocco, G. Functional and Structural Characterization of PETase SM14 from Marine-Sponge *Streptomyces* sp. Active on Polyethylene Terephthalate. *ACS*

Sustainable Chemistry & Engineering. 2025, 13, 7460. Available from: https://doi.org/10.1021/acssuschemeng.5c00737

7. **Bhattacharya, S.**, * Castagna, R.,* Estiri,* H., Upmanis, T., Gautieri, A., Parisini, E. Development of a Highly Active Engineered PETase Enzyme for Polyester Degradation. *The FEBS Journal.* 2025, 23 August, article ID febs.70228. Available from: https://doi.org/10.1111/febs.70228. *These authors contributed equally to this work.

8. Berselli, A., Carletti, A., Menziani, M. C., **Bhattacharya, S.**, Castagna, R., Parisini, E., Di Rocco, G., & Muniz-Miranda, F. The effect of ionic strength on PETase enzymes: An experimental and computational study. *Protein Science*, 2026, 35, e70386. https://doi.org/10.1002/pro.70386

Patent applications

3. Gautieri, A., Parisini, E., Estiri, H., Castagna, R., **Bhattacharya, S**. "Thermostable engineered enzyme". IT102023000014223, priority date 07.07.2023, granted 25.07.2025. PCT/IB2024/056641, filed on 08.07.2024 https://patents.google.com/patent/WO2025012799A1/en

4. Gautieri, A., Perazzoli, A., Castagna, R., Parisini, E., **Bhattacharya, S.** Enzima fruttosil peptide ossidasi (FPOX) ingegnerizzato e suoi usi. Italian Patent Application No. 102025000025639, filed on 8 October 2025.

Other publications on the topic not included in the Doctoral Thesis

3. Brangulis, K., Akopjana, I., Drunka, L., Matisone, S., Zelencova-Gopejenko, D., **Bhattacharya, S.**, Bogans, J., Tars, K. Members of the Paralogous Gene Family 12 from the Lyme Disease Agent *Borrelia burgdorferi* Are Non-Specific DNA-Binding Proteins. *PLOS ONE.* 2024, 19, e0296127. Available from: https://doi.org/10.1371/journal.pone.0296127.

4. **Bhattacharya, S.**, Tempra, G., Colleoni, A., Matera, C., Castagna, R., Parisini, E. Synthesis, photochemical and biological evaluation of novel photoswitchable glycomimetic ligands of *Pseudomonas aeruginosa* LecB. *RSC Advances*. 2025, 15, 49796. Available from: https://doi.org/10.1039/D5RA06897E.

The results of this Thesis were presented at the following international conferences

14. **Bhattacharya, S.**, Estiri, H., Castagna, R., Gautieri, A., Parisini, E. Enzyme engineering of fructosyl peptide oxidase to widen its active site access tunnel and improve its thermal stability, June 15–17, 2022, FEBS3+ Conference in Tallinn, Estonia. https://biokeemiaselts.ee/wp-content/uploads/2022/06/ABSTRACT-BOOK_FEBS32022_Tallinn.pdf

15. **Bhattacharya, S.**, Estiri, H., Castagna, R., Gautieri, A., Parisini, E. Enzyme engineering of fructosyl peptide oxidase to widen its active site access tunnel and improve its thermal stability, EMBO practical course High throughput protein

production and crystallization, 04–12 July 2022, Marseille, France https://books.google.lv/books/about/High_Throughput_Protein_Production_and_C.html?id=J_GYzwEACAAJ&redir_esc=y

16. **Bhattacharya, S.**, Estiri, H., Castagna, R., Gautieri, A., Parisini, E. Enzyme engineering of fructosyl peptide oxidase to widen its active site access tunnel and improve its thermal stability, 2nd DRUG DISCOVERY CONFERENCE, September 22–24, 2022, Riga, Latvia. https://drugdiscovery.osi.lv/content/files/DDC_Abstract_Book.pdf

17. **Bhattacharya, S.**, Estiri, H., Castagna, R., Gautieri, A., Parisini, E. Enzyme engineering of fructosyl peptide oxidase to widen its active site access tunnel and improve its thermal stability, iNEXT DISCOVERY workshop on crystallographic fragment screening, 1–3 March 2023, Berlin, Germany. https://www.helmholtz-berlin.de/events/inext-discovery-workshop/index_en.html

18. **Bhattacharya, S.**, Estiri, H., Castagna, R., Gautieri, A., Parisini, E. Enzyme Engineering, Oral presentation ALLIANCE4LIFE_ACTIONS ESR retreat, 23–24 January 2023 (Vilnius, Lithuania) https://alliance4life.com/media/3803646/d35-report-on-early-stage-researchers-retreats_964997.pdf

19. **Bhattacharya, S.**, Castagna, R., Estiri, H., Gautieri, A., Parisini, E. Thermostable PETase enzyme for plastic degradation, BioDrug conference, September 22–24, 2023, Riga, Latvia. https://biodrugconference.osi.lv/content/Abstract_Book_BioDrug_Conference_2023.pdf

20. **Bhattacharya, S.**, Castagna, R., Estiri, H., Gautieri, A., Parisini, E. Enzyme engineering of fructosyl peptide oxidase to widen its active site access tunnel and improve its thermal stability, FEBS advanced course: Computational Approaches to understanding and Engineering Enzyme Catalysis held in Zagreb, Croatia, 25–29 September 2023. https://digitalna.nsk.hr/?pr=i&id=658275

21. **Bhattacharya, S.**, Castagna, R., Estiri, H., Gautieri, A., Parisini, E. Achievements of the SPRINGBOARD project, event on 2–3 May 2024, Riga, Latvia. A delivered presentation titled "Development of a highly optimized engineered PETase enzyme for plastic degradation". https://springboard.osi.lv/content/abstracts/Springboard_CONFERENCE_Abstract_.pdf

22. **Bhattacharya, S.**, Castagna, R., Estiri, H., Gautieri, A., Parisini, E. Tailoring Enzymes for tomorrow, Structural Biology in Latvia and Beyond, conference Instruct-ERIC, https://instruct-eric.org/news/structural-biology-in-latvia-and-beyond/ held in Riga, Latvia on 3 December 2024.

23. **Bhattacharya, S.** Development of a Highly Optimized Engineered PETase Enzyme for Polyester Degradation, WIDEnzymes Workshop 1: Milan, Italy, Computational Methods for Enzyme Engineering, 27–31 January 2025. https://widenzymes.eu/workshops-series/workshop-1/

24. **Bhattacharya, S.** Enzyme Engineering, presentation at WIDEnzymes Workshop 2, Directed Evolution of Enzymes, Department of Chemistry, University of Crete, Greece, 2–6 June 2025. https://widenzymes.eu/workshops-series/workshop-2/

25. **Bhattacharya, S.** Large Scale Production of PETase Enzyme, presentation at WIDEnzymes Workshop 3, Bioreactor Production of Recombinant Enzymes, Slovak University of Technology in Bratislava (STUBA), Slovakia, 26–30 January 2026. https://widenzymes.eu/workshops-series/widenzymes-workshop-3-stuba/

26. **Bhattacharya, S.** served as a trainer at OneHealthdrugs Training School (Cost Action CA21111), Expression, Purification and Basic Characterization of Target Protein Samples for Drug Binding Studies, Latvian Institute of Organic Synthesis, Riga, Latvia, September 2025. https://onehealthdrugs.com/events/training-schools/expression-purification-and-basic-characterization-of-target-protein-samples-for-drug-binding-studies

MAIN RESULTS OF THE THESIS

1. FPOX enzymes

1.1. Rational design of enzymes

Rational design is a computationally guided strategy for enzyme engineering that targets specific regions of a protein to enhance stability, activity, or substrate specificity, addressing the limitations of natural enzymes, which often operate at mild physiological conditions. Generally speaking, enzymes are poorly tolerant to industrial stresses such as high temperature, extreme pH, high ionic strength, or organic solvents[1]. Unlike *de novo* design or directed evolution, rational design introduces carefully selected mutations to generate a limited set of mutants that retain the overall fold while improving desired functional traits, using strategies such as introducing polar residues to strengthen hydrogen bonding, inserting cysteines to form disulfide bridges, optimizing surface charge interactions, targeting flexible regions, and leveraging thermophilic homologs[2, 3] (Fig. 1).

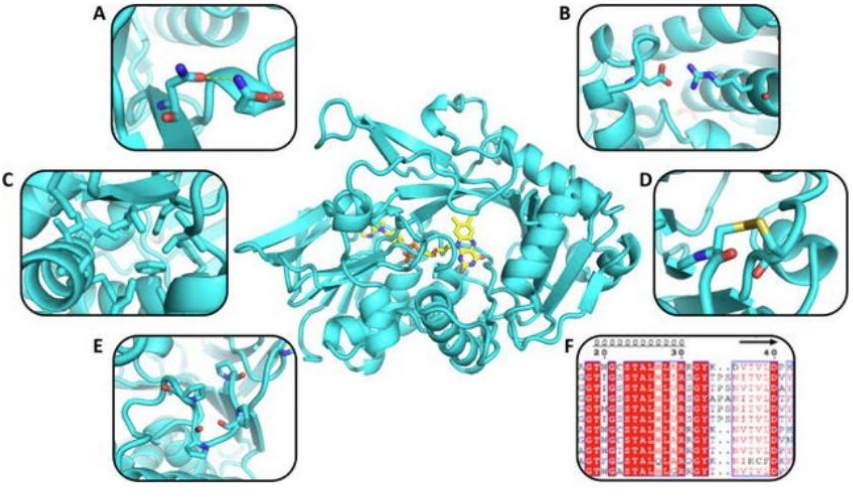

Fig. 1. Stabilizing strategies used in rational enzyme design. The most common strategies involve the introduction of surface hydrogen bonds (A) and salt bridges (B), the stabilization of the hydrophobic core (C), the introduction of disulfide bridges (D), and the stabilization of mobile loops using prolines (E). Phylogenetic analysis (F) can be used alone or in combination with previous strategies to guide the enzyme rational design process.

Modern approaches employ multiple-point mutations and computational platforms like FireProt[4] to account for synergistic or antagonistic interactions[5], while tools such as CAVER[6], Rosetta Remodel[7], and molecular dynamics (MD) simulations provide atomistic insights into protein flexibility, tunnel architecture, and conformational stability[8]. MD simulations model atomic movements over time, identifying regions prone to instability and predicting the effects of proposed mutations, including changes in hydrogen bonding, disulfide formation, or other stabilizing interactions prior to experimental testing, thereby reducing workload and minimizing the number of mutants to construct. By integrating rational design with MD simulations, structural modeling, and evolutionary analysis, enzyme engineering projects can expand substrate specificity, optimize selectivity, and improve stability under challenging industrial conditions. Engineered enzymes with increased melting temperatures or reduced denaturation susceptibility can function efficiently at high temperatures, extreme pH, or elevated salinity, while Root Mean Square Fluctuation (RMSF) analyses from MD simulations can reproduce experimental β-factors to pinpoint highly flexible regions for stabilization[5, 9, 10] (Fig. 2).

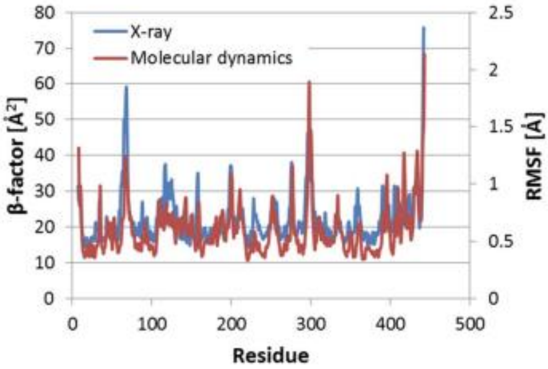

Fig. 2. Superposition of the RMSF of wild-type FPOX enzyme and experimental β-factor, showing how the RMSF from MD simulations reproduces the same trend of the experimental β-factors and allows pinpointing the same peaks, which represent highly flexible protein regions.

Fructosyl amino acid (or peptide) oxidases (FPOXs), also known as Amadoriases, are a specialized family of flavin-dependent oxidases that catalyze the deglycation of glycated amino acids or short glycated peptides. These enzymes belong to the oxidoreductase family and are widely distributed in yeasts, fungi, and bacteria. They catalyze the oxidative cleavage of low-molecular-weight Amadori products, yielding a free amine, glucosone, and hydrogen peroxide[11]. The reaction involves oxidation of the C-N bond linking the C1 of the fructosyl moiety to the amino nitrogen, a process mediated by the FAD cofactor, whose flavinic moiety forms the catalytic center of the enzyme.

Structurally, FPOXs display well-defined FAD-binding motifs and conserved architectural features typical of the glucose–methanol–choline oxidoreductase family. To date, numerous FPOX crystal structures have been solved, providing detailed insight into the organization of the active site and the gating elements that regulate substrate access[12]. These structural studies have revealed that the catalytic pocket is buried within the protein and connected to the solvent by a narrow access tunnel, a feature that plays a key role in determining substrate specificity (Fig. 3 A)).

FPOXs are of considerable biomedical relevance, as they are used in enzymatic kits for the measurement of glycated hemoglobin (HbA1c), a key biomarker for long-term glycemic control in diabetic patients, and they also show potential for detecting glycated albumin[13]. In standard diagnostic assays, hemoglobin is first denatured and proteolytically digested to release small glycated peptides, such as fructosyl-valylhistidine (F-VH), which are subsequently oxidized by FPOX. The generated hydrogen peroxide is then quantified either colorimetrically via horseradish peroxidase or electrochemically, enabling indirect determination of HbA1c levels[13] (Fig. 3 B)).

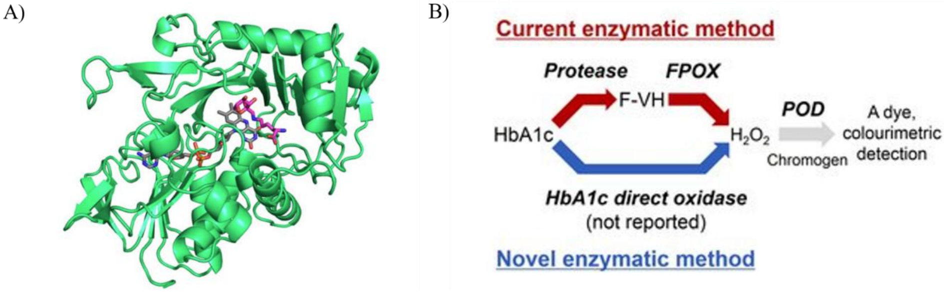

Fig. 3. A) – Crystal structure of Amadoriase I in complex with fructosyl-lysine (PDB code 4XWZ). B) – Reaction scheme of the HbA1c enzymatic method (adapted from[13]).

Despite their versatility and diagnostic value, FPOXs exhibit an important limitation: they are unable to efficiently catalyze the deglycation of intact proteins[14]. Structural studies have shown that this limitation arises from the narrow substrate-access tunnel leading to the buried active site, which restricts entry to small glycated amino acids or short peptides[15].

Consequently, native FPOXs display limited activity toward bulky substrates such as intact glycated proteins.

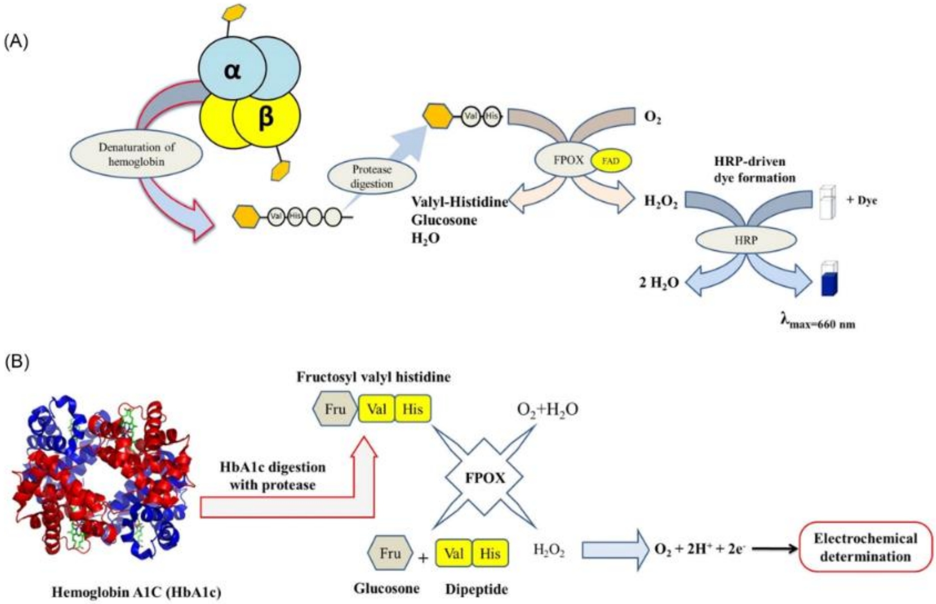

Fig 4. The denaturation and digestion of hemoglobin A1c (HbA1c) by protease to release fructosyl-valylhistidine (F-VH). (A) – F-VH undergoes oxidation by fructosyl peptide oxidase (FPOX), and the resulting H_2O_2 serves as a substrate for HRP, forming a dye whose absorbance at 660 nm is used to calculate the HbA1c percentage. (B) – HbA1c assay by electrochemical measurement of H_2O_2 (adapted from[18]).

Nevertheless, these same structural insights have provided a strong foundation for enzyme engineering. By targeting residues lining the substrate-access tunnel and stabilizing the FAD-binding domain, researchers have successfully generated FPOX mutants with improved thermal stability, enhanced catalytic activity, and increased selectivity toward specific glycated substrates[16, 17]. Such engineered variants not only offer improved performance in diagnostic assays, including colorimetric and electrochemical HbA1c measurements[18], but also serve as valuable model systems for studying protein engineering strategies in flavin-dependent oxidases more broadly (Fig. 4).

Professor Emilio Parisini's group has been working on fructosyl peptide oxidases (FPOX) for several years, focusing on their rational engineering to enhance performance for practical applications. The research involved the rational design of the first mutant of *Phaeosphaeria nodorum FPOX* (Pn-FPOX), derived from the wild-type enzyme, followed by systematic modifications including tunnel widening, thermal stabilization, and activity optimization. After several rounds of engineering, the mutant L3-35A was obtained, featuring a wider and shorter access tunnel achieved by deleting five amino acids lining the gate structure (Fig. 5). In the first year of my PhD, I began working on this previously engineered mutant, L3-35A, which retained the enlarged access tunnel and served as the starting point for further optimization. Building on L3-35A, I applied rational design strategies to restore stability and enhance enzymatic activity while preserving the widened access tunnel necessary for larger substrates. Three classes of mutations were introduced: the D-series, targeting reduction of structural fluctuations; the C-series, aimed at increasing the formation of stabilizing salt bridges; and the X-series, designed to introduce disulfide bonds for additional thermal stability. These mutations were guided by MD simulations, which provided insights into the enzyme's dynamic behavior, flexibility, and regions prone to instability, allowing to prioritize the most promising modifications.

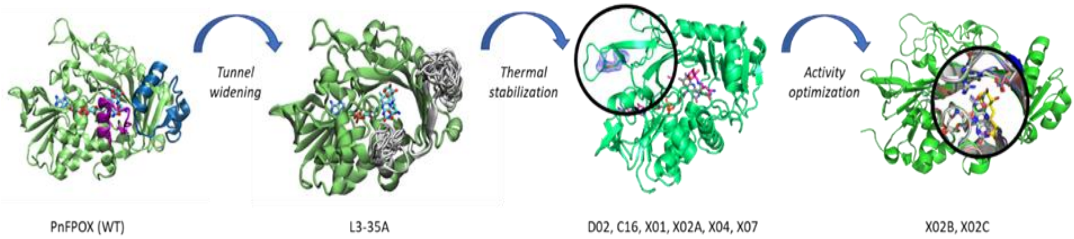

Fig. 5. Schematic of the rational design strategy, showing the names of the relevant enzyme variants obtained at each stage.

The combined multi-pronged approach successfully produced FPOX variants that were both thermostable and highly active, with the best mutant X02C. Experimental testing confirmed that the engineered mutants maintained structural integrity and significant catalytic activity relative to the wild-type enzyme.

The enzyme (X02C) with the best catalytic ability towards glycated substrates of different lengths (glycated valine (f-V), and the glycated hexa-peptide, fructosyl-Val-His-Leu-Thr-Pro-Glu (F6P)) was chosen for another round of engineering.

Starting from the X02C structure, the author removed one turn of helix 4 (Fig. 6 A)) (highlighted in blue) to widen the access tunnel. In total, nine amino acids were removed. This helix belongs to one of the four gating structures surrounding the active site. It was then rebuilt using a smaller number of residues (two to five). Additionally, to compensate for the loss of native interactions caused by this truncation, the author mutated all non-conserved residues within 5 Å of the remodeled section. This 5 Å threshold was chosen to account for hydrogen bond distances (~3 Å) and typical backbone fluctuations (RMSD ~1.5 Å). The author refrained from mutating residues that were conserved in the alignment of X02C with the other two highly active FPOXs, such as *Coniochaeta* sp. FPOX (FPOX-C)[19] and *Aspergillus nidulans* FPOX-47 (AnFPOX-47)[20].

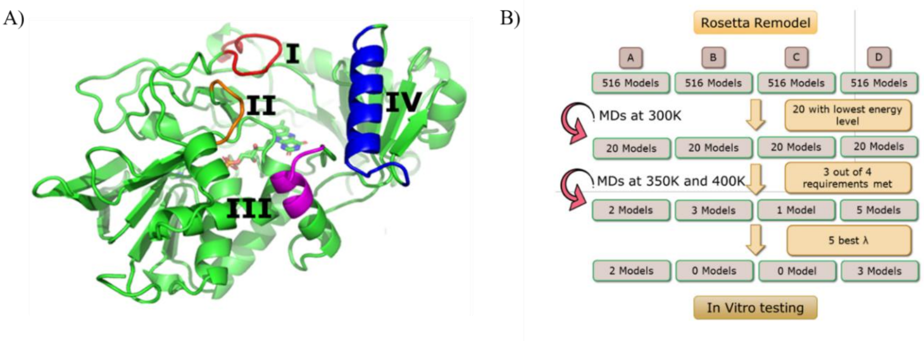

Fig. 6. A) – Model of X02C used for redesign. B) – Summary scheme of the computational part of enzyme engineering on X02C.

The author used Rosetta Remodel to introduce the selected mutations, generating 516 variants for each reconstructed loop length, twice the number of mutants screened in the previous study. For each loop length, the author selected the 20 generated models with the lowest energetic score, a unitless Rosetta Remodel parameter that qualitatively describes the overall stability of the model (Fig. 6 B)). The author then studied these structures using molecular dynamics simulations at a temperature of 300 K, 350 K, and 400 K for a simulated time period of 100 ns. The author evaluated the root mean square deviation (RMSD) and root mean square fluctuation (RMSF) from these simulations. The mutants that bested X02C on at least three of the four parameters (mean RMSD, mean RMSF, median RMSF and standard deviation of RMSF) were chosen for another round of molecular dynamic simulations (Fig. 7).

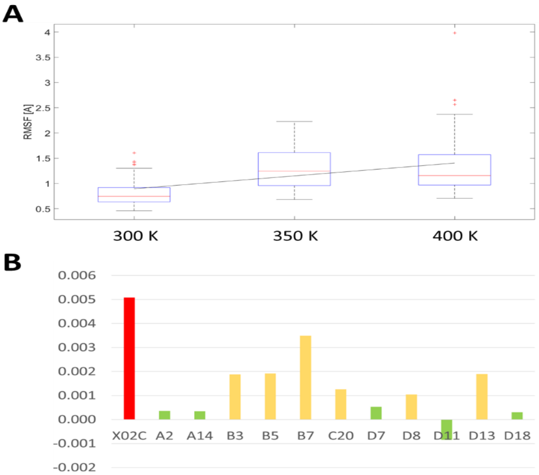

Fig. 7. RMSF analysis at increasing temperatures. A – RMSF of the redesigned loop of X02C as a function of the temperature (T). The linear regression analysis provided the angular coefficient (slope) of the RMSF vs. T relationship. B – The angular coefficient of the different enzyme variants is compared, and those with the lower values (green) are selected for experimental validation.

These optimized variants were experimentally expressed, purified, and biochemically characterized. They were also screened for catalytic activity against glycated peptides and *ex vivo* glycated human tissues. Among them, PnFPOX-A14 showed significantly enhanced activity compared to the parental engineered variant X02C, particularly toward bulkier substrates. Notably, while X02C retained limited activity on full-length glycated proteins, PnFPOX-A14 was able to directly recognize and act on intact HbA1c, demonstrating improved substrate accessibility and catalytic performance. These results validate the computational design strategy and establish PnFPOX-A14 as an improved platform for further engineering toward diagnostic and potential therapeutic applications. These results are summarized in Appendix 5 of the manuscript attached.

1.2. Enzyme expression and purification

For my Doctoral Thesis, recombinant DNA technology was employed to express all enzymes in *Escherichia coli*, primarily using BL21(DE3) for prokaryotic proteins and BL21(DE3) derivatives supplemented with rare tRNAs for eukaryotic proteins to mitigate codon bias, with antibiotic selection (ampicillin, kanamycin, or chloramphenicol) chosen according to the expression vector[21, 22]. Prior to large-scale production, small-scale expression tests were conducted in which each mutant was grown under varying temperatures and induced with different IPTG concentrations to identify the optimal conditions for maximal soluble protein expression. Once optimal parameters were established, protein production was scaled up, typically to 4 liters, and purification was performed using a two-step workflow on an ÄKTA liquid chromatography system (Cytiva). For the FPOX family, expression in *E. coli* BL21 Star (DE3) at 25 °C resulted in yields ranging from 10 mg/L to 30 mg/L, with L3-35A producing the highest yield (30 mg/L). Alternatively, several FPOX mutants that feature disulfide bonds were expressed in the SHuffle T7 strain[23] at 18 °C, showing diverse yields, from low expression in X01 (5 mg/L) to relatively high levels in X02C (29 mg/L) (Table 1).

Table 1

Expression Yield of Enzymes

Enzyme	**Expression yield (mg/L)**	**Expression temperature (°C)**	**Expression cells**
PnFPOX	10	25	BL21 Star (DE3)
L3-35A	30	25	BL21 Star (DE3)
D02	15	25	BL21 Star (DE3)
C16	12	25	BL21 Star (DE3)
X01	5	18	SHuffle T7 E
X02A	20	18	SHuffle T7 E
X04	10	18	SHuffle T7 E
X07	6	18	SHuffle T7 E
X02B	16	18	SHuffle T7 E
X02C	29	18	SHuffle T7 E

In the first step, immobilized metal affinity chromatography (IMAC) was carried out using a HisTrap 5 mL nickel column, exploiting the N-terminal His_6 affinity tag on the recombinant proteins, with elution achieved using imidazole-containing buffer (Fig. 8 A)). In the second step, proteins were further polished by size-exclusion chromatography (SEC) using a HiPrep 26/60 Sephacryl S-200 column, which removed aggregates, enabled buffer exchange, and ensured monodispersity of the enzyme preparations[24]. Protein concentration was measured using a NanoDrop One spectrophotometer (Thermo Fisher Scientific), while molecular weight and purity were assessed by SDS-PAGE with Coomassie blue staining, providing reliable confirmation of protein size and homogeneity [25] (Fig. 8 B)). This combination of bacterial expression, optimization of induction conditions, and sequential IMAC and SEC purification enabled the production of high-purity, functional enzymes suitable for detailed biochemical and structural characterization, forming a robust foundation for downstream enzyme engineering studies.

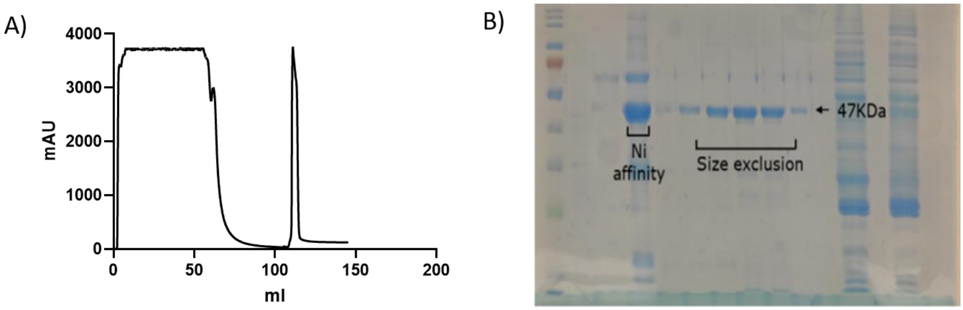

Fig. 8. A) – Representative nickel affinity chromatography (IMAC) chromatogram from the purification of the FPOX enzyme-X02C. The blue trace represents UV absorbance (A280) used to monitor protein elution. B) – Electrophoresis results for FPOX enzyme-X02C.

1.3. Biophysical characterization

Biophysical characterization is essential for assessing the structural integrity, stability, and functionality of proteins, as correct folding and molecular integrity are prerequisites for enzymatic activity. Techniques such as Circular Dichroism (CD) spectroscopy, Differential Scanning Fluorimetry (DSF), and MALDI mass spectrometry provide complementary information on secondary structure, thermal stability, and molecular mass, respectively[26]. CD spectroscopy evaluates secondary structure by measuring the differential absorption of circularly polarized light, with far-UV spectra revealing α-helices, β-sheets, and disordered regions, while temperature-dependent CD measurements enable monitoring of thermal unfolding processes[27]. DSF, using environment-sensitive dyes such as SYPRO Orange, detects fluorescence changes during protein unfolding and provides melting temperatures (Tm) that allow quantitative comparison of stability across different variants, buffer conditions, or ligand-bound states[28]. In this study, both DSF and CD were employed to assess the thermal stability of engineered FPOX variants, yielding consistent trends and comparable absolute Tm values, thereby validating the robustness of the measurements. The results demonstrate that the applied rational design strategy effectively enhanced the thermal stability of the reference enzyme L3-35A (Fig. 9). Specifically, the D02 variant, containing two additional mutations (V110R and D115G), exhibited an increase in melting temperature of approximately 1.5 °C relative to the parent enzyme. Further stabilization was achieved through the introduction of extensive surface charges and salt bridges in mutant C16, which produced an additional ≈ 1.5 °C increase in Tm, reaching 55.2 °C (Table 2). Moreover, incorporation of a single disulfide bond at different positions within the L3-35A scaffold resulted in pronounced improvements in thermal stability. All variants in this series X01 (54.1 °C), X02A (60.0 °C), X04 (55.2 °C), and X07 (55.3 °C) displayed significantly elevated melting temperatures compared with the parent enzyme, as determined by both DSF and CD measurements (Table 2) (Fig. 9). Collectively, these results demonstrate that both electrostatic optimization and disulfide bond engineering are effective strategies for enhancing FPOX thermal stability and validate the use of complementary biophysical techniques for quantitatively evaluating protein stabilization outcomes.

Table 2

Melting Temperature of the Parent Enzyme (L3-35A) and Its Mutants

Enzyme	**T_m [°C] [a]**	**T_m [°C] [b]**
PnFPOX (WT)	53.2 ± 0.2	53.5 ± 0.1
L3-35A	52.3 ± 0.2	52.9 ± 0.1
D02	53.1 ± 0.5	54.8 ± 0.1
C16	55.2 ± 0.1	55.0 ± 0.1
X01	54.1 ± 0.1	54.2 ± 0.1
X02A	60.0 ± 0.4	60.1 ± 0.1
X04	55.2 ± 0.3	55.0 ± 0.1
X07	55.3 ± 0.4	55.4 ± 0.1
X02B	60.2 ± 0.7	60.6 ± 0.1
X02C	64.0 ± 0.2	63.3 ± 0.1

[a] Determined by thermal shift assay.
[b] Determined by circular dichroism.

The melting temperature of the wild-type enzyme (PnFPOX) is provided as a reference.

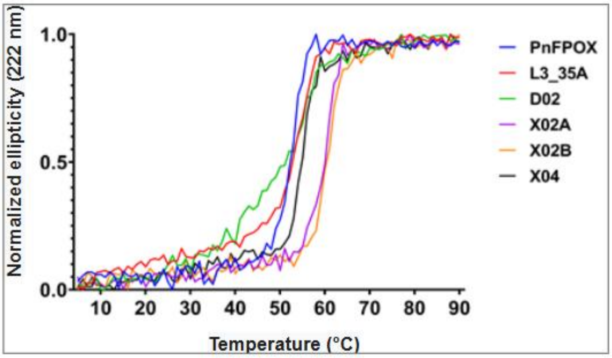

Fig. 9. Comparison of the Tm values of the different FPOX variants as measured by circular dichroism at 222 nm from 5 °C to 95 °C.

1.4. Functional assay

The enzymatic activity of all FPOX variants was assessed at room temperature by quantifying the amount of glucosone released from the substrate over time, following previously established methods[29] (Fig. 10).

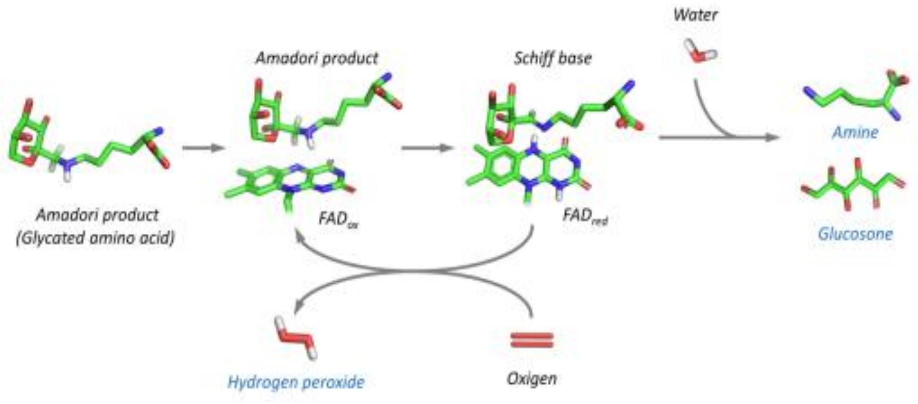

Fig. 10. Schematic of the amino acid deglycation reaction catalyzed by Amadoriase I (adapted from[30]).

The increase in absorbance at 322 nm (ε_{322} = 149.25 M^{-1} cm^{-1} for glucosone) was continuously monitored using an Infinite M1000 microplate reader (Tecan) at 25 °C. Each reaction mixture (200 µL) contained 20 mM Tris-HCl buffer, pH 7.4, supplemented with 20 mM o-phenylenediamine and 2 mM of the respective substrate: *fructosyl-lysine (fK), fructosyl-valine (fV), fructosyl-valine-histidine (fVH),* or the hexapeptide *1-Deoxyfructosyl-Val-His-Leu-Thr-Pro-Glu (F6P).* FPOX catalyzes the oxidation of fructosyl substrates, generating glucosone as a reaction product. OPD reacts with glucosone to form a quinoxaline derivative, which absorbs at 322 nm. Following a 1 min pre-incubation, reactions were initiated by adding enzyme to final concentrations between 0.04 mg/mL and 1 mg/mL, depending on variant activity (Table 3).

Table 3

Comparison of the Enzymatic Specific Activity (U/mg) on Different Glycated Peptide Substrates

Enzyme	**Specific activity (U/mg)**			
	fK	**fV**	**fVH**	**F6P**
PnFPOX	30.18 ± 0.67	29.67 ± 2.56	32.60 ± 1.18	0.78 ± 0.09
AnFPOX-47	-	-	-	0.082 ± 0.002
L3-35A	0.21 ± 0.02	0.16 ± 0.04	-	-
D02	0.30 ± 0.03	0.32 ± 0.01	-	-
C16	ND	ND	-	-
X01	ND	ND	-	-
X02A	0.15 ± 0.01	0.11 ± 0.01	-	-
X04	ND	0.13 ± 0.01	-	-
X07	-	0.08 ± 0.01	-	-
X02B	2.24 ± 0.07	32.50 ± 0.44	0.87 ± 0.03	0.18 ± 0.06
X02C	1.06 ± 0.01	17.95 ± 2.46	1.62 ± 0.02	0.43 ± 0.06

Note: Tests are performed in triplicates. ND – not detected.

One unit (U) of enzyme activity was defined as the amount of enzyme catalyzing the formation of 1 μmol of glucosone per minute under the specified assay conditions, and the specific activity was expressed as U mg^{-1} of enzyme. Kinetic constants ($V_{\max}$, K_m, k_{cat}, and k_{cat}/K_m) were derived from assays performed with varying substrate concentrations (0.05–10 mM for fructosyl-valine; 0.05–1 mM for the hexapeptide substrate) using nonlinear regression analysis of the Michaelis -Menten equation, confirmed by Lineweaver–Burk plot fitting. All data represent the mean of at least two independent experiments (Table 4).

Table 4

Kinetic Parameters of Wild-Type PnFPOX and the Engineered X02C Enzymes

Enzyme	**Substrate**	K_m (mM)	$V_{\max}$ (mM/min)	k_{cat} (s^{-1})	k_{cat}/K_m ($mM^{-1}\,s^{-1}$)
PnFPOX	fV	5.93 ± 1.61	41.67 ± 8.34	99.33 ± 19.86	16.75
X02C	fV	0.94 ± 0.06	10.56 ± 0.56	20.83 ± 1.10	22.16
PnFPOX	F6P	0.81 ± 0.30	15.48 ± 1.20	36.83 ± 2.83	45.47
X02C	F6P	0.03 ± 0.01	0.26 ± 0.01	0.52 ± 0.02	17.22

The kinetic analysis revealed that the engineered variant X02C demonstrated a significantly lower K_m (0.94 mM) than the wild-type PnFPOX (5.93 mM), indicating enhanced substrate affinity. Although Kcat decreased slightly, the catalytic efficiency (K_{cat}/K_m) remained comparable or improved, highlighting a trade-off between substrate binding and turnover rate often observed in enzyme engineering (Table 3).

1.5. X-ray crystallography

X-ray crystallography was used to determine the three-dimensional structures of engineered fructosyl peptide oxidase (FPOX) variants, providing atomic-level insight into their structural organization, catalytic architecture, and stabilizing features. Crystals suitable for diffraction were obtained using vapor-diffusion methods under optimized supersaturation conditions, and high-resolution diffraction data were collected at a synchrotron source, enabling accurate structure determination and refinement[31–33].

Structural analysis revealed key features underlying enzyme stability, substrate accessibility, and catalytic efficiency. Several engineered FPOX variants were successfully solved and deposited in the Protein Data Bank, including X02B (PDB ID: 8BJY), D02 (8BLZ), X02A (8BLX), and X04 (8BMU). These structures provide a detailed structural basis for understanding the effects of rationally introduced mutations and support their role in enhancing the stability and performance of FPOX enzymes (Fig. 11).

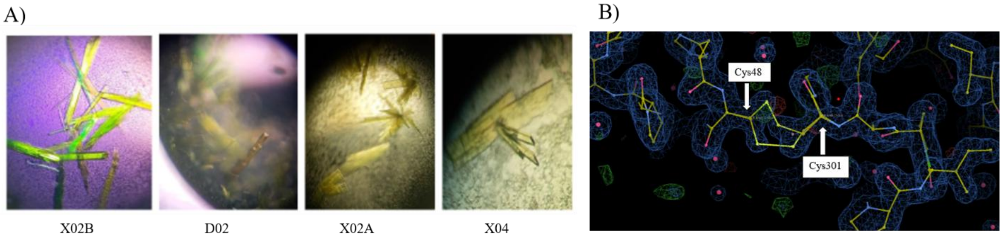

Fig. 11. A) – Crystals of FPOX variants. B) – Electron density map of X02A (PDB: 8BLX) showing the formation of a disulphide bond between Cysteines 48 and 301.

1.6. Structure-function correlation analysis

The X-ray crystallographic structure clearly illustrates the link between the molecular architecture and functional properties of the protein. The high-resolution model reveals well-defined secondary and tertiary elements forming a stable framework that supports active site organization and substrate binding. Key residues are precisely positioned to enable catalysis or ligand interaction, consistent with biochemical observations. Structural features such as hydrogen bonds, hydrophobic contacts, and electrostatic interactions further contribute to substrate specificity and stability. Across all these enzyme studies, detailed crystallographic analysis has been central to understanding how three-dimensional structure governs biological function and catalytic mechanism. In the case of FPOX enzymes, the author observed that the overall RMSD values between the mutants and wild-type PnFPOX (PDB 5T1E) were all within 1.8 Å, indicating that the global fold remained largely conserved (Table 5).

Table 5

Calculated RMSDs Between the WT Enzyme PnFPOX and the Different Mutants, and Tunnel Geometry

Enzyme	RMSD [Å]	Tunnel bottleneck radius [Å]	Tunnel length [Å]
PnFPOX	-	2.2	13.3
L3-35A	1.8	3.7	6.4
D02	1.4	2.9	11.7
X02A	1.7	3.1	9.4
X04	1.8	3.0	10.9
X02B	1.5	3.0	10.2

When the author compared the residues forming the catalytic site (W235, E278, G372, R415), it was found that their orientation was preserved across all variants (Fig. 12). These residues, which are highly conserved among FPOX enzymes, are responsible for binding the sugar moiety of the substrate. Therefore, the differences in catalytic activity among the variants are unlikely to result from changes in the core catalytic geometry, but rather from subtler alterations in the regions surrounding the substrate tunnel.

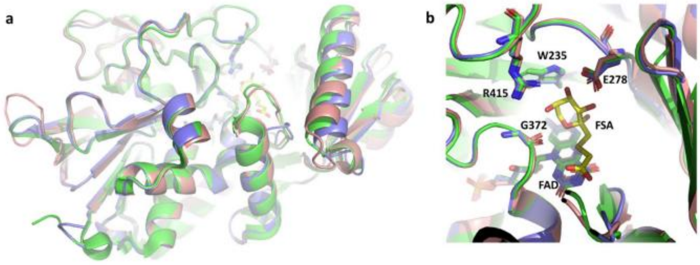

Fig.12. Structural comparison of relevant FPOX enzyme: PnFPOX (green), AnFPOX-47 (pink) and X02B (violet). The FSA inhibitor is depicted in yellow. a – The overall structural alignment shows no significant differences between the enzymes, except for the entrance tunnel. b – The position of the catalytic site is also highly conserved.

The author observed that the mutations primarily affected the geometry and dynamic behavior of the tunnel-lining residues. The wild-type enzyme features a narrow and elongated tunnel (bottleneck radius 2.2 Å, length 13.3 Å), which likely restricts access to larger substrates while stabilizing smaller ones. In contrast, the L3-35A variant exhibits a much wider and shorter tunnel (3.7 Å and 6.4 Å, respectively), while the X02B mutant presents an intermediate geometry (3.0 Å, 10.2 Å). These structural differences suggest that mutagenesis reshaped not only the static dimensions of the tunnel but also the correlated flexibility of the surrounding residues, thereby influencing substrate accessibility and stabilization.

1.7. Current directions and future opportunities

Building on the engineered FPOX variants, the author is now working to integrate these optimized enzymes into sensitive biosensing platforms for HbA1c detection (Appendix 5). Current efforts focus on the development of colorimetric and electrochemical sensor formats, improving enzyme immobilization and signal transduction, and evaluating performance with clinically relevant samples. FPOX-based sensors are being developed to enable direct, rapid, and cost-effective measurement of glycated proteins.

2. PETase enzymes

Plastic pollution is a major environmental challenge, with polyethylene terephthalate (PET) being one of the most widely used and persistent plastics. Its resistance to chemical and biological degradation has led to extensive accumulation in landfills and natural ecosystems, while conventional disposal methods such as incineration and mechanical recycling remain inefficient or environmentally harmful. The discovery of PETase, an enzyme capable of depolymerizing PET into smaller, biodegradable products, represents a significant biotechnological advance and a promising biological approach to mitigating plastic pollution[34, 35] (Fig. 13).

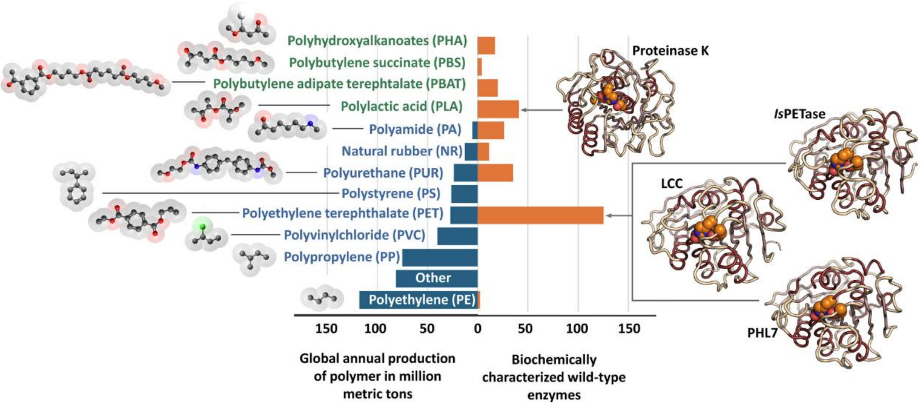

Fig. 13. Global production of major plastic polymers and availability of biochemically characterized wild-type depolymerases[35].

Recent studies have shown that certain microorganisms can produce hydrolytic enzymes that are capable of degrading and metabolizing PET. To date, researchers have isolated and identified various PET-degrading enzymes, primarily esterases, lipases, hydrolases and cutinases. The PET-degrading proteins were named PETase and given the Enzyme Commission number EC 3.1.1.101. In 2016, the bacterium *Ideonella sakaiensis* was isolated from a PET-contaminated recycling site in Japan, which uses PET as its primary carbon and energy source, a unique capability among known microorganisms[36]. The enzyme PETase enables the bacterium to hydrolyze the ester bonds present in the PET polymer, producing smaller molecules such as mono(2-hydroxyethyl) terephthalate (MHET), terephthalic acid (TPA), and ethylene glycol (EG)[37, 38] (Fig. 14).

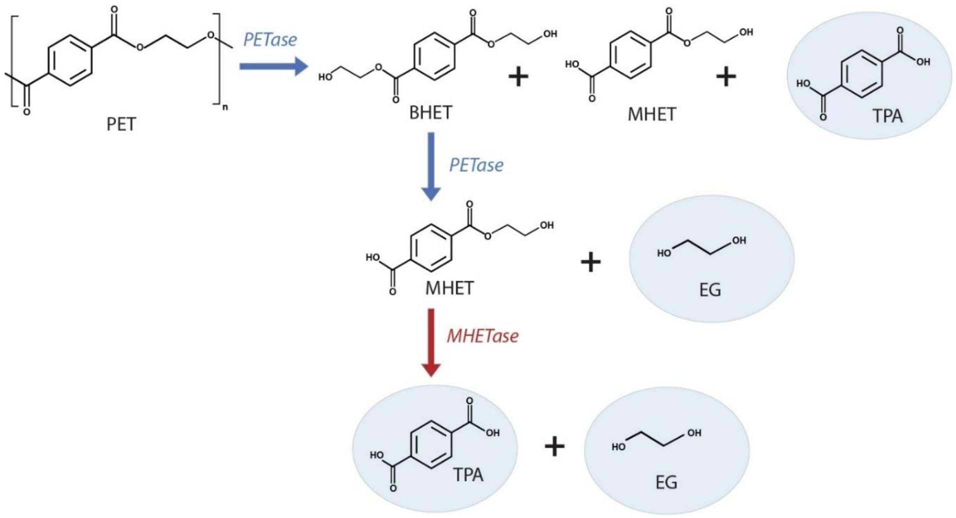

Fig. 14. PET depolymerization scheme: PETase catalyzes the depolymerization of PET to bis(2-hydroxyethyl)-TPA (BHET), mono(2-hydroxyethyl) terephthalate (MHET), and terephthalic acid (TPA). MHETase converts MHET to monomers TPA and ethylene glycol (EG).

These breakdown products are less harmful to the environment and can be further metabolized by the bacterium or used in industrial recycling processes. Structurally, PETase belongs to the cutinase family of hydrolases, enzymes that typically degrade natural polyesters such as cutin, a waxy substance found in plant cuticles. PETase shares this evolutionary heritage but has adapted to recognize and act on synthetic PET. Its active site contains key amino acid residues that facilitate the hydrolysis of ester bonds, allowing it to break down long polymer chains into smaller fragments. These structural insights have been crucial for efforts to engineer PETase variants with improved activity, stability, and thermal tolerance[39, 40].

Since the discovery of PET-depolymerizing enzymes, enzymatic PET recycling has been regarded as a promising method for plastic disposal, particularly in the context of a circular economy strategy[41]. Enzyme-based recycling offers an environmentally friendly alternative to chemical methods by converting PET into its monomers, which can be reused to synthesize new plastic products. However, the PET-degrading enzymes developed so far face several challenges that limit their industrial application. To date, the cost of industrial enzymatic recycling of PET is significantly higher than the production of virgin PET due to several limitations associated with currently available PETases[42]. Although industrial implementation has been demonstrated, for example by the French company Carbios, many PETases still suffer from low thermostability, limited catalytic efficiency, and inhibition by degradation intermediates, making large-scale PET recycling impractical[43, 44]. To overcome these limitations, the author's Doctoral Thesis focused on the engineering of PETase enzymes through advanced rational design strategies to develop an efficient variant for industrial enzymatic PET degradation. The author engineered the current PET-hydrolyzing enzyme gold standard [the ICCG variant of leaf-branch compost cutinase (LCC-ICCG)] using *in silico* protein design methods to develop a PET-hydrolyzing enzyme that features enhanced thermal stability and PET depolymerization activity.

2.1. Development of engineered LCC-ICCG PETase enzyme

Leaf-branch compost cutinase (LCC) is a highly efficient, naturally occurring PETase with a melting temperature (T_m) of 84.7 °C[45]. It was further engineered by Tournier et al. in 2020 to generate the ICCG (LCC-ICCG) variant, reported to reach T_m values of 91.7–94.0 °C and currently regarded as the gold-standard PETase[45, 46]. Despite this exceptional stability, the vast sequence space of LCC offers substantial potential for further optimization. Building on the LCC-ICCG scaffold, the author set out to design more stable and active PETases, guided by the hypothesis that enhanced thermal stability correlates with improved expression and catalytic performance.

2.1.1. Rational engineering

In silico enzyme engineering was initiated from the LCC-ICCG variant, a stabilized derivative of leaf-branch compost cutinase containing four substitutions (F243I, Y127G, S283C, and D238C), including an additional disulfide bond, with the catalytic serine restored at position 165[46, 45, 47]. Residues within 5 Å of the active site were excluded from mutagenesis to preserve catalytic function. Three complementary computational strategies were applied to generate stabilizing variants: Rosetta Supercharge[48], PROSS[49] and Disulfide-by-Design[3]. The Rosetta Supercharge approach enhances protein stability by increasing surface hydrophilicity, a property commonly associated with improved structural robustness[48]. A widely used and straightforward stabilization strategy is the introduction of one or more disulfide bonds, which can rigidify the protein backbone and enhance stability[50]. Additional stabilization approaches aim to extend intramolecular hydrogen-bonding networks, introduce stabilizing salt bridges, or improve hydrophobic core packing, as implemented in PROSS[49]. These approaches yielded 1000, 9, and 125 candidate variants, respectively, from which subsets with the most favorable scores were selected (C01-C10, P01-P09, and X01-X10). All 29 selected variants were subjected to 1 µs molecular dynamics simulations in explicit solvent and ranked based on RMSF-derived stability metrics. This screening identified six top-performing candidates, C08, C09, P06, P08, X05, and X09, which were selected for experimental expression and characterization based on their predicted enhanced structural stability (Fig. 15).

```
WT   MDGVLWRVRTAALMAALLALAAWALVWASPSVEAQSNPYQRGPNPTRSALTADGPFSVATYTVSRLSVSGFGGGVIYYPT
ICCG MDGVLWRVRTAALMAALLALAAWALVWASPSVEAQSNPYQRGPNPTRSALTADGPFSVATYTVSRLSVSGFGGGVIYYPT
C08  MDGVLWRVRTAALMAALLALAAWALVWASPSVEAQSNPYQRGPNPTRDALTADGPFKVATYTVSRLSVSGFGGGVIYYPT
C09  MDGVLWRVRTAALMAALLALAAWALVWASPSVEAQDNPYRRGPNPTRDALTADGPFKVATYTVSRLSVSGFGGGVIYYPT
P06  MDGVLWRVRTAALMAALLALAAWALVWASPSVEAQSNPYQRGPNPTRSALTADGPFSVATYTVSRLSVSGFGGGTIYYPT
P08  MDGVLWRVRTAALMAALLALAAWALVWASPSVEAQSNPYQRGPNPTRSALTADGPFSVATYTVPRLSVSGFGGGTIYYPT
X05  MDGVLWRVRTAALMAALLALAAWALVWASPSVEAQSNPYQRGPNPTRSALTADGPFSVATYTVSRLSVSGFGGGVIYYPT
X09  MDGVLWRVRTAALMAALLALAAWALVWASPSVEAQSNPYQRGPNPTRSALTADGPFSVATYTVSRLSVSGFGGGVIYYPT

WT   GTSLTFGGIAMSPGYTADASSLAWLGRRLASHGFVVLVINTNSRFDYPDSRASQLSAALNYLRTSSPSAVRARLDANRLA
ICCG GTSLTFGGIAMSPGYTADASSLAWLGRRLASHGFVVLVINTNSRFDGPDSRASQLSAALNYLRTSSPSAVRARLDANRLA
C08  GTSLTFGGIAMSPGYTADASSLAWLGRRLASHGFVVLVINTNSRFDGPDSRASQLSAALNYLRTRSPSAVRARLDANRLA
C09  GTSLTFGGIAMSPGYTADASSLAWLGRRLASHGFVVLVINTNSRFDGPDSRASQLSAALNYLRTRSPSAVRARLDANRLA
P06  GTSETFGGIAISPGYTADASSLAWLGRRLASHGFVVLVIDTNSRFDGPDSRARQLLAALDYLRTSSPSAVRARLDPNRLA
P08  GTSETFGGIAISPGYTADQSSLAWLGRRLASHGFVVLVIDTNSRFDGPDSRARQLLAALDYLVTSSPSAVRSRLDPNRLA
X05  GTSLTFGGIAMSPGYTADASSLAWLGRRLASHGFVVLVINTNSRFDGPDSRASQLSAALNYLRTSSPSAVRARLDANRLA
X09  GTSLTFGGIAMSPGYTADASSLAWLGRRLASHGFVVLVINTNSRFCGPDCRASQLSAALNYLRTSSPSAVRARLDANRLA

WT   VAGHSMGGGGTLRIAEQNPSLKAAVPLTPWHTDKTFNTSVPVLIVGAEADTVAPVSQHAIPFYQNLPSTTPKVYVELDNA
ICCG VAGHSMGGGGTLRIAEQNPSLKAAVPLTPWHTDKTFNTSVPVLIVGAEADTVAPVSQHAIPFYQNLPSTTPKVYVELCNA
C08  VAGHSMGGGGTLRIAEQNPSLKAAVPLTPWHTDKTFNTSVPVLIVGAERDTVAPVSQHAIPFYQNLPSTTPKVYVELCNA
C09  VAGHSMGGGGTLRIAEQNPSLKAAVPLTPWHTDKTFNTSVPVLIVGAERDTVAPVSQHAIPFYQNLPSTTPKVYVELCNA
P06  VAGHSMGGGGTLRAAEQNPSLKAAVPLTPWHTDKTFNTSVPVLIVGAENDTVAPVSQHAIPFYQNLPSTTPKVYVELCNA
P08  VAGHSMGGGGTLRAAEQDPSLKAAVPLCPWHTDKTFNTSVPVLIVGAENDTVAPVSQHAIPFYNNLPSTTPKMYIELCNA
X05  VAGHSMGGGGTLRIAEQNPSLKAAVPLTPWHTDKTFNTSVPVLIVCAEADTVAPCSQHAIPFYQNLPSTTPKVYVELCNA
X09  VAGHSMGGGGTLRIAEQNPSLKAAVPLTPWHTDKTFNTSVPVLIVGAEADTVAPVSQHAIPFYQNLPSTTPKVYVELCNA

WT   SHFAPNSNNAAISVYTISWMKLWVDNDTRYRQFLCNVNDPALSDFRTNNRHCQ
ICCG SHIAPNSNNAAISVYTISWMKLWVDNDTRYRQFLCNVNDPALCDFRTNNRHCQ
C08  DHIAPNSNNAAISVYTISWMKLWVDNDTRYRQFLCDVKDPALCDFRTNNRHCK
C09  SHIAPNSNNAAISVYTISWMKLWVDNDTRYRQFLCDVKDPALCDFRTNNRHCK
P06  SHIAPNSNNTAIAVYTISWMKLWVDNDTRYRQFLCNVNDPALCDFRTNNRHCQ
P08  SHIAPNSSNTAIAVYTIAWMKLWVDNDTRYRQFLCNVNDPALCDFRTNNRHCQ
X05  SHIAPNSNNAAISVYTISWMKLWVDNDTRYRQFLCNVNDPALCDFRTNNRHCQ
X09  SHIAPNSNNAAISVYTISWMKLWVDNDTRYRQFLCNVNDPALCDFRTNNRHCQ
```

Fig. 15. Sequence alignment. Sequence alignment of the wild-type LCC enzyme (Uniprot ID G9BY57), the ICCG variant developed by Tournier et al.[46], and the engineered enzymes developed in this study (C08, C09, P06, P08, X05, X09). Alignment is performed with Clustal Omega, while the graphical representation is obtained using ESPrit 3 web server[51].

2.1.2. Enzyme expression and purification

The selected candidate enzymes were expressed in *E. coli* and purified using nickel affinity chromatography (IMAC) and size-exclusion chromatography (SEC) (Fig. 16). For PETase enzymes, BL21 Star (DE3) at 18 °C proved effective, with yields ranging from 12 mg/L to

22 mg/L. Among these, variant X09 expressed the highest amount (22 mg/L), while P08 produced the lowest (12 mg/L).

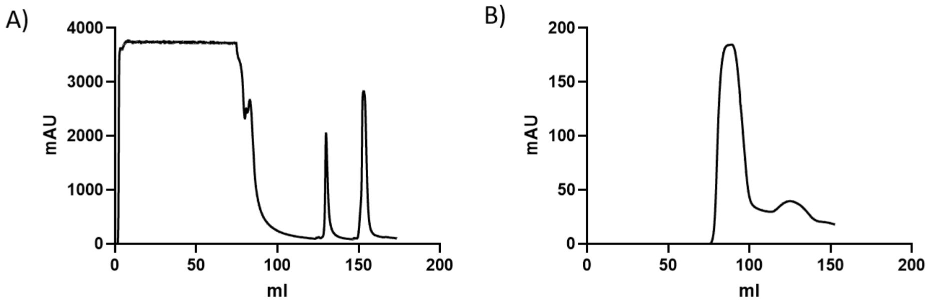

Fig. 16. Representative chromatograms from the purification of the C09 enzyme showing A) nickel affinity chromatography (IMAC) and B) Size-exclusion chromatography (SEC). The blue trace represents UV absorbance (A280) used to monitor protein elution.

2.1.3. Biophysical characterization

After enzyme design campaign, the author tested the secondary structure (Fig. 17) and the thermal stability of the six engineered variants (Fig. 18). It was found that the C09 (T_m = 97.1 °C) and X05 (T_m = 96.9 °C) variants have a higher T_m than the reference LCC-ICCG (T_m = 93.6 °C). The X09 (T_m = 93.8 °C) variant exhibits similar thermal stability to LCC-ICCG (Fig. 17). The author did not determine the melting temperature of P06 and P08 due to their negligible enzymatic activity in preliminary experiments, while for C08, it was not possible to obtain a reliable fit.

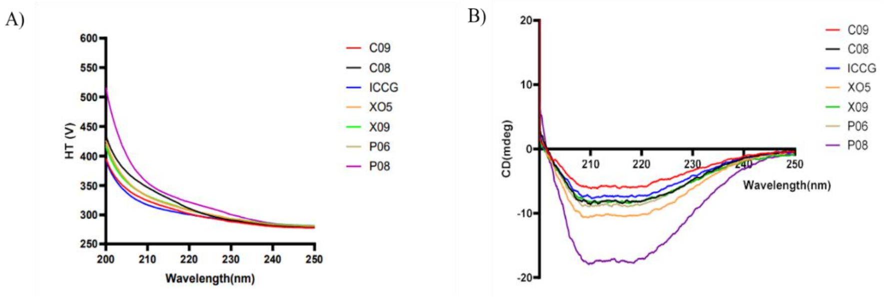

Fig. 17. Secondary structure measurements by circular dichroism. A) – The plot shows voltage vs. wavelength for the different enzymes. B) – The plot shows ellipticity vs. wavelength for the different enzymes.

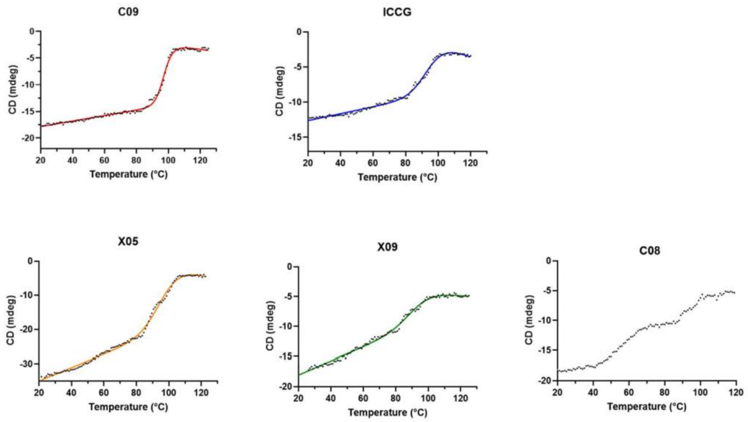

Fig. 18. Representative melting curves. Each panel shows a representative melting curve measured by circular dichroism at 222 nm from 20 °C to 120 °C for the corresponding sample; black dots represent experimental data points, and the solid line indicates the fitted curve.

2.1.4. Functional assay

The enzymatic hydrolysis of polyethylene terephthalate (PET) was evaluated by quantifying the formation of major depolymerization products – bis(hydroxyethyl) terephthalate (BHET), mono(hydroxyethyl) terephthalate (MHET), terephthalic acid (TPA), and ethylene glycol (EG) using reversed-phase HPLC. Reactions were carried out at 68 °C with 40 nM enzyme in 20 mM Tris-HCl (pH 8.0) containing 300 mM NaCl. Amorphous PET films (250 μm thickness, Goodfellow USA) were punched into 6 mm discs (~8.4 mg) and incubated individually in 2 mL microcentrifuge tubes. All assays were performed in quintuplicate to ensure reproducibility. Product quantification was conducted using a Shimadzu LC-2030C 3D Plus system equipped with a Kinetex C18 column (2.7 µm, 4.6 × 150 mm) at 40 °C and 1 mL min^{-1} flow rate. The mobile phase consisted of 0.1 % H_3PO_4 (A) and acetonitrile (B) with a linear gradient. Aliquots were collected at various time points (0–144 h), diluted accordingly (21× for 0–72 h, 101× for 96–144 h), and analyzed at 220 nm. Calibration curves for TPA and MHET (0.1–50 μg mL^{-1}) and BHET (0.09–43.9 μg mL^{-1}) enabled precise quantification of product formation.

The accumulation of TPA and MHET over time reflected progressive PET hydrolysis. Among the tested variants, some demonstrated enhanced degradation rates compared to wild-type PETase, correlating well with the improved thermostability and folding properties revealed by biophysical characterisation.

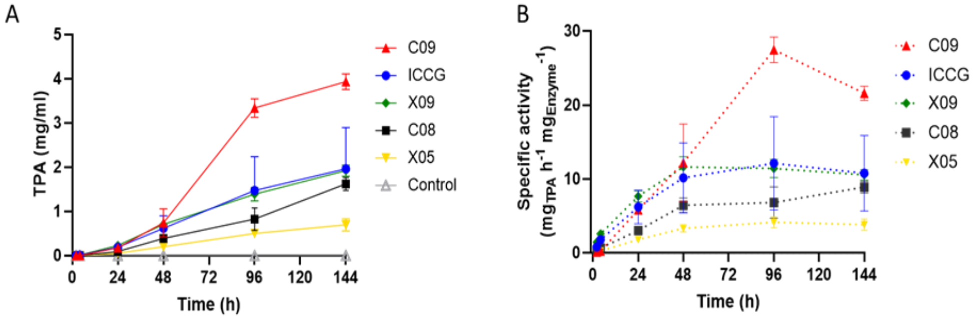

Fig. 19. Comparison of polyethylene terephthalate (PET) depolymerization over time for all enzymes. A – Terephthalic acid (TPA) production over time at 68 °C (LCC-ICCG – C09 – X05 – X09 – C08 40 n M, pH 8.0). B – Comparison of TPA production at 68 °C at 4 h and at 144 h.

The results show that at 68 °C, the mean TPA concentration at the different time points is significantly higher for the C09 mutant than for ICCG up until day 6 (144 h). Moreover, the specific activity of C09 is also significantly higher (≈2-fold) than that of the gold standard LCC-ICCG over the same length of time (Fig. 19).

2.1.5. X-ray crystallography

Crystals of the C09 variant were obtained by vapor diffusion in 0.1 M sodium citrate pH 5.6, 20 % PEG 4000, and 20 % isopropanol, and data were collected after cryoprotection with 25 % glycerol. The resulting structure, refined to 1.28 Å resolution, provided atomic detail of the engineered stabilizing mutations.

The C09 enzyme contains thirteen substitutions relative to wild-type LCC, including additional charged residues (e.g., S36D, Q40R, S57K) strategically positioned on the surface. Despite these extensive modifications, the crystallographic analysis showed no significant deviation in folding (RMSD 0.26 Å vs. WT; 0.15 Å vs. LCC-ICCG). The catalytic triad (D210, H242, S265) retained its canonical geometry, confirming that structural integrity was preserved (Fig. 24).

Structural comparison and RMSF simulations demonstrated that C09 exhibited reduced local flexibility, particularly around the catalytic His242, explaining the variant's exceptional thermal resilience (T_m > 95 °C) and 2-fold higher PET degradation efficiency relative to LCC-ICCG. The added surface charges are hypothesized to stabilize surface-exposed loops and prevent unfolding of the catalytic site during prolonged high-temperature catalysis. Thus, while catalytic architecture remains unchanged, dynamic stabilization through rational design appears to be the key determinant of enhanced performance in C09 (Fig. 20).

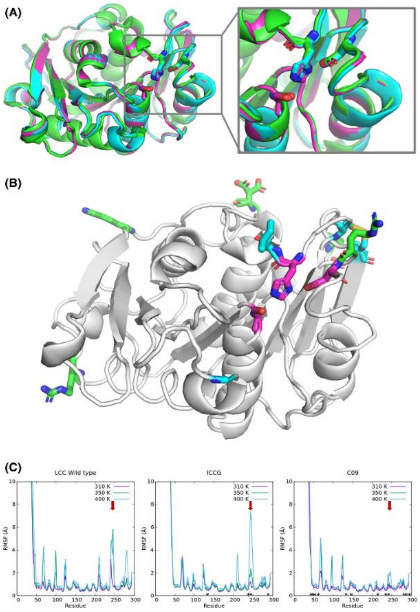

Fig. 20. Structural comparison of relevant PETase enzymes: wild-type LCC (green), ICCG variant (cyan), and C09 variant (pink). (A) – The overall structural alignment shows no significant differences between the enzymes, including the position and the orientation of the catalytic triad. Panel (B) shows the position of mutations (sticks) in ICCG (cyan) and C09 (pink) with respect to the catalytic site (pink sticks). Panel (C) shows a comparison between the root mean square fluctuation (RMSF) of LCC, LCC-ICCG, and C09 at different temperatures (310 K, 350 K, and 400 K).

2.2. Characterization of novel PETase SM14

While enzymatic PET degradation has emerged as a promising sustainable alternative to conventional recycling methods, most known PET-degrading enzymes display limited catalytic efficiency and narrow operational windows, particularly under environmentally relevant conditions. This limitation is especially critical in the context of marine pollution, where large quantities of PET accumulate and persist due to high salinity, low temperatures, and the scarcity of effective natural degradation processes. In this context, the author characterised a novel PET-degrading enzyme isolated from the marine-sponge-associated bacterium *Streptomyces* sp. SM14 (PETase SM14). This project is conducted in collaboration with Prof. Giulia Di Rocco at the University of Modena and Reggio Emilia (Italy), where a part of the project was carried out.

2.2.1. Enzyme expression and purification

The gene encoding mature PETase SM14 from *Streptomyces* sp. SM14 was cloned into the pLATE52 vector using ligation-independent cloning and expressed in *E. coli* BL21 (DE3). Protein expression was induced with IPTG, followed by cell lysis and purification via Ni^{2+}-affinity chromatography using a HisTrap HP column. PETase SM14 was eluted with an imidazole gradient, and peak fractions were collected, with protein concentration determined by UV absorbance at 280 nm based on its calculated molecular properties.

2.2.2. Biophysical characterization

Far-UV CD spectroscopy was employed to assess the secondary structure content of PETase SM14 and to compare its folding with that of the reference PETase from *Ideonella sakaiensis*[36, 52]. The CD spectra displayed well-defined minima at approximately 208 nm and 222 nm, characteristic of an α/β-hydrolase fold dominated by α-helical and β-sheet elements (Fig. 18). The spectral profile of PETase SM14 closely resembled that of *I. sakaiensis* PETase, indicating that the enzyme retains a similar overall secondary structure architecture despite sequence divergence. The data confirm proper protein folding and align with the structure determined by X-ray crystallography of PETase SM14.

Thermal denaturation experiments, monitored by measuring ellipticity at 222 nm as a function of temperature, revealed a melting temperature (T_m) of 56.3 °C for PETase SM14, indicating remarkable thermal stability. In comparison, the T_m of *Ideonella sakaiensis* PETase was determined to be 45.0 °C, indicating that SM14 is more than 10 °C more thermostable (Fig. 21). This increase in Tm suggests enhanced structural rigidity or improved intramolecular interactions within PETase SM14, likely contributing to its robustness under environmental conditions. The unfolding transition represented a well-folded, monomeric protein.

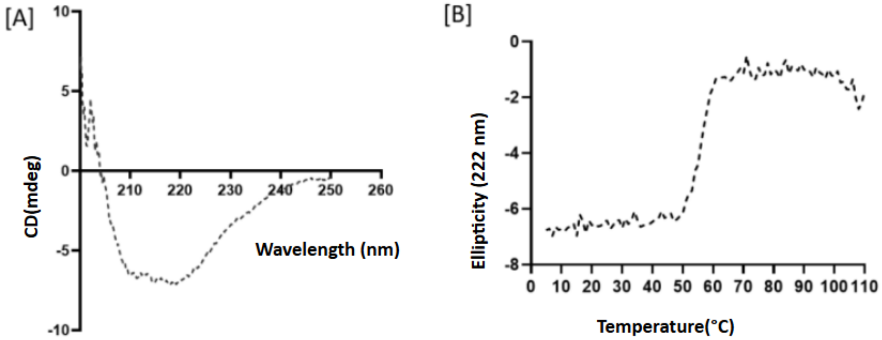

Fig. 21. Circular dichroism (CD) analysis to detect the secondary structure of the enzyme [A] and to measure the thermostability of the enzyme [B].

Protein thermal stability was also assessed using differential scanning fluorimetry (DSF) with SYPRO Orange dye (Thermo Fisher Scientific) on a 7500 Real-Time PCR system (Applied Biosystems). Each reaction contained 5 µM enzyme and 5× dye in a final volume of 25 µL, prepared by mixing equal volumes of enzyme solution (10 µM) and 10× dye (diluted from a 5000× stock) in the corresponding protein buffer. Fluorescence was monitored during temperature ramping from 15 °C to 95.3 °C, and melting temperatures (T_m) were determined from the inflection points of the denaturation curves. To evaluate stability under different physicochemical conditions, assays were performed across a pH range of 6.0–9.0, and NaCl concentrations from 100 mM to 700 mM (Fig. 22). Variations in pH had minimal effect on Tm, which remained relatively constant, while increasing NaCl concentration up to 700 mM in Tris buffer (pH 8.0) did not induce protein unfolding. These results demonstrate that the enzyme maintains high structural stability across a broad range of salt concentrations and pH values.

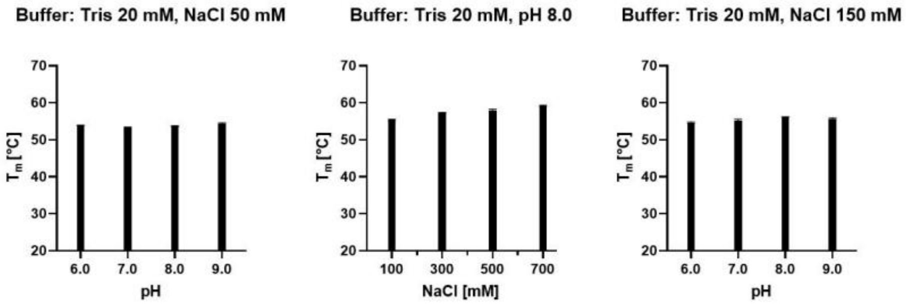

Fig. 22. Shift in melting temperature of PETase SM14 in different buffer conditions detected via temperature-dependent fluorescence shifts of SYPRO Orange.

MALDI mass spectrometry provides accurate molecular mass determination and sequence verification, enabling detection of degradation, post-translational modifications, and confirmation of expression products[53]. MALDI-TOF mass spectrometry was used to confirm the molecular mass and sequence integrity of the purified PETase SM14 enzyme.

Measurements were recorded with a FLEX-PC autoflex TOF/TOF (Bruker). The acquisition operation mode was Linear, polarity voltage POS. The number of shots was 500. Protein and formic acid (one sample with 1 μL and one with 0.5 μL) were mixed. One drop of this solution was mixed with matrix SA (sinapinic acid) and allowed to solidify. The concentration of the protein was 10 mg/mL.

The experimental molecular mass (approximately 28 kDa) closely matched the theoretical mass calculated from the amino acid sequence (Fig. 23), verifying successful expression and purification of the intact protein. No evidence of proteolytic cleavage, truncation, or post-translational modification was observed. The mass accuracy (± 0.1 kDa) and absence of significant impurity peaks confirmed the high purity of the sample obtained after the two-step chromatographic purification.

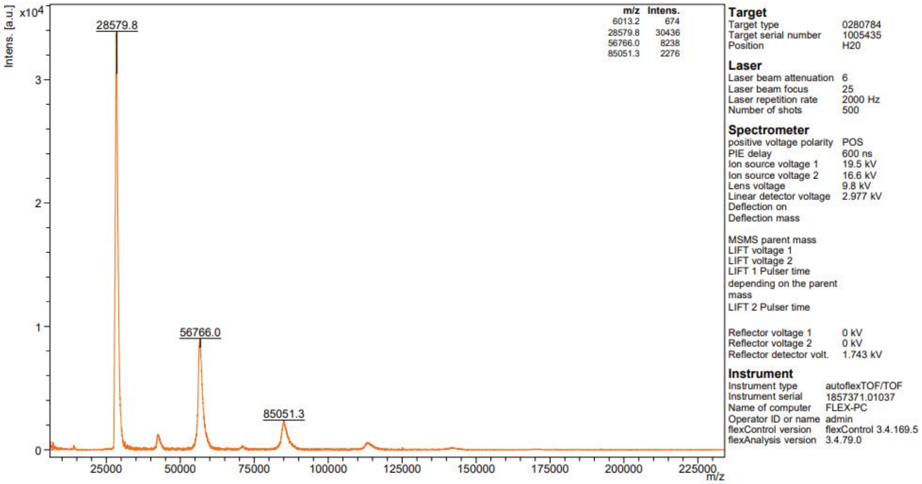

m/z	Intens.
6013.2	674
28579.8	30436
56766.0	8238
85051.3	2276

Target	
Target type	0280784
Target serial number	1005435
Position	H20
Laser	
Laser beam attenuation	6
Laser beam focus	25
Laser repetition rate	2000 Hz
Number of shots	500
Spectrometer	
positive voltage polarity	POS
PIE delay	600 ns
Ion source voltage 1	19.5 kV
Ion source voltage 2	16.6 kV
Lens voltage	9.8 kV
Linear detector voltage	2.977 kV
Deflection on	
Deflection mass	
MSMS parent mass	
LIFT voltage 1	
LIFT voltage 2	
LIFT 1 Pulser time depending on the parent mass	
LIFT 2 Pulser time	
Reflector voltage 1	0 kV
Reflector voltage 2	0 kV
Reflector detector volt.	1.743 kV
Instrument	
Instrument type	autoflexTOF/TOF
Instrument serial	1857371.01037
Name of computer	FLEX-PC
Operator ID or name	admin
flexControl version	flexControl 3.4.169.5
flexAnalysis version	3.4.79.0

Fig. 23. MALDI-TOF analysis of PETase SM14. This value was obtained with a 5 mg/mL protein concentration, diluted with TFA 50 %, and sinapinic acid (SA) as the matrix.

Furthermore, peptide mass fingerprinting following tryptic digestion confirmed sequence coverage above 90 %, validating that the expressed product corresponded precisely to the intended PETase SM14 construct (Fig. 24). The consistency between the expected and observed mass further corroborated the structural data obtained from CD and DSF analyses, collectively confirming that PETase SM14 is a stable, properly folded, and structurally intact enzyme.

1 **AQNPHERGPD PSNSYIEQAR GSYSVSQRSI SRLGSDGFRD GTMYYPTSTA**

51 **DGRFGVVAIS PGYTASESTI AWLGPRLASF GFVVVTINTD SRYDQPRQRA**

101 **TQLHAALDHA IGDSVVGPRI DTSRQAVMGH SMGGGGALQA AEERDEIRAA**

151 **VPLTPWNLKK GWSGVDAATL VIGAENDAIA PVRSHSIPFY ESLTNAERRA**

201 **YLELRREGHF APNSSNTLIA KYSVSWLKRY VDNDLRYDQF IDPGPRTGIT**

251 **TGVSDYRLG**

Fig. 24. MS/MS spectra (100–1200 m/z) obtained from the band of PETase SM14 after purification, extracted and digested with trypsin and analyzed via ESI-MS/MS spectrometry. Sequence coverage of 95 %.

2.2.3. Functional assay

The enzymatic activity of PETase SM14 was evaluated using PET post-consumer plastic (PCP) under controlled reaction conditions, varying key parameters including pH, temperature, and NaCl concentration. PETase SM14 effectively degraded PCP, releasing terephthalic acid (TPA) as quantified by HPLC, with optimal activity observed at pH 9.0. TPA production increased approximately 10-fold under basic conditions and was largely independent of temperature between 40 °C and 50 °C. Enzymatic activity was strongly enhanced by salinity, showing over a 100-fold increase in TPA release in the presence of NaCl, with an optimal concentration around 900 mM,

2.2.4 X-ray crystallography

The author determined the high-resolution crystal structure of PETase SM14 from a *Streptomyces* species isolated from a marine sponge. Crystals of the tag-free enzyme were grown using the vapor diffusion method and diffracted to 1.43 Å resolution on the Diamond Light Source I03 beamline in Oxford, UK. The structure was solved by molecular replacement using an AlphaFold-predicted model as the search template, followed by iterative manual refinement in *Coot*[54] and automated cycles in *REFMAC5*[55].

The PETase SM14 structure exhibited the classical α/β-hydrolase fold, with a conserved Ser–His–Asp catalytic triad positioned in a shallow substrate-binding cleft. Structural superposition with *Ideonella sakaiensis* PETase (IsPETase) and a polyester hydrolase (PE-H) (Fig. 25) revealed high structural conservation, with RMSDs of 0.69 Å (IsPETase) and 0.81 Å (PE-H). The catalytic residues aligned precisely, supporting a shared serine-hydrolase mechanism.

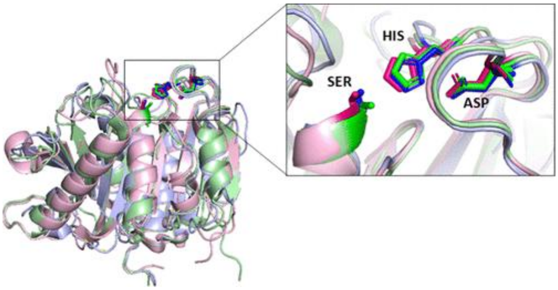

Fig. 25. Overall structure comparison of PETase SM14 (light blue), *Is*PETase (PDB code 6ILW, light green), and PE-H from *P. aestusnigri* (PDB code: 6SBN, light pink) performed using PyMOL.

Notably, SM14 displayed distinctive loop conformations adjacent to the active site that narrowed the catalytic pocket relative to IsPETase. This subtle closure may confer enhanced substrate binding and increased rigidity, consistent with the enzyme's high melting temperature (T_m 56.3 °C) and pronounced salt tolerance up to 1.5 M NaCl. Electrostatic surface analyses indicated a less polarized and more evenly distributed charge potential compared with IsPETase (pI 6.67 vs. 9.41), potentially stabilizing the protein in marine or alkaline environments. Together, these features suggest that PETase SM14 evolved for catalytic persistence under high-salinity and mildly thermophilic conditions, an adaptation promising for environmental PET degradation.

2.2.5 Structure-function correlation analysis

The author studied the structure of PETase SM14 in detail in order to understand the effect of ionic strength on PETase enzymes. To further dissect the contribution of correlated flexibility to enzymatic adaptation, the author combined molecular dynamics (MD) simulations with *in vitro* enzymatic assays on IsPETase (from *Ideonella sakaiensis*) and PETase SM14. The objective was to determine how local motions and dynamic coupling contribute to catalytic efficiency across ionic environments. IsPETase, secreted by *Ideonella Sakaiensis* 201-f6, and PETase SM14, expressed by the marine-sponge Streptomyces sp. SM14, are characterized by the same catalytic scaffold; however, significant differences have evolved to adapt each enzyme to its native environment. Activity assays on PET powder degradation performed in this study and supporting evidence from the literature indicate that NaCl concentration exerts a positive effect on the activity of PETase SM14, consistent with its hypersaline marine origin, while having a negative effect on IsPETase. To date, this phenomenon has been observed using analytical techniques such as HPLC, SEM, and AFM, which do not elucidate the structural basis of these effects.

To address this gap, the author employed molecular modeling and MD simulations to deliver a detailed structural comparison and molecular-level explanation of the experimentally observed differences between the two homologous plastic-degrading enzymes. The results obtained from 500-ns-long MD simulations reveal that the IsPETase binding site is significantly wider and more flexible than that found for PETase SM14, as supported by the larger average residue-residue distances and the more open electrostatic surface observed in Fig. 26. This inactivation is primarily caused by a conformational rearrangement involving the flipping of residue W159, which displaces the catalytic histidine (H237) from serine (S160), disrupting the active site geometry. In contrast, PETase SM14 maintained a more rigid structure that underwent minor yet beneficial conformational changes under high-salt conditions. These subtle rearrangements promoted enhanced hydration of the active site, with additional water molecules facilitating substrate interaction and sustaining catalytic efficiency.

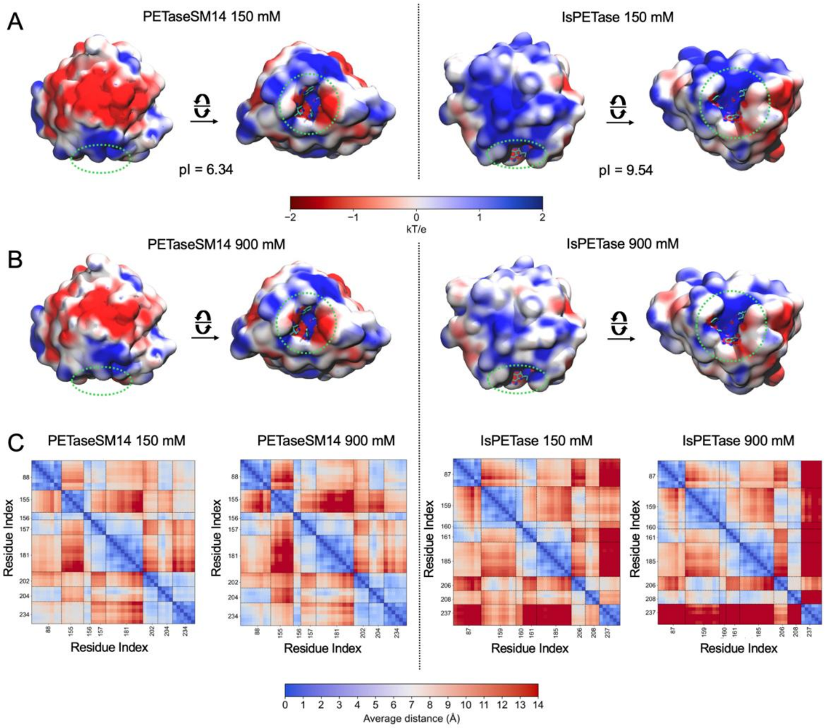

Fig. 26. Effect of ion concentrations on the PETase SM14 and IsPETase. Electrostatic potential surface of PETase SM14 and IsPETase at (A) 150 mM and (B) 900 mM of NaCl concentration. The binding site locations and key residues are indicated with the green dotted circles. C – Distance maps of residues forming the PETase SM14 and IsPETase binding sites at the two ion concentrations. The maps report the average values of each cross-distance calculated over the three 500-ns MD simulation replicas. The color scale ranges from 0 Å (blue spots) to ≥14 Å (red spots).

Modeling of PET binding using 9-monomer PET chains confirmed that PETase SM14 at high salinity and IsPETase at low salinity both achieve optimal substrate accommodation and catalytic alignment. At 900 mM NaCl, PETase SM14 displayed approximately twice as many reactive enzyme–substrate configurations compared to its performance at 150 mM, whereas

IsPETase exhibited a 50 % reduction in such states under the same conditions. These findings correlate well with the observed experimental activity trends and provide a molecular-level explanation for the distinct ionic adaptations of the two enzymes.

2.3 Current directions and future opportunities

Building on the established computational-experimental framework, the author has initiated further exploration towards rational and simulation-guided engineering aimed at enhancing the stability and catalytic efficiency of PETase SM14. In parallel, the author is working towards the scale-up of enzymatic PET depolymerisation using the engineered LCC-ICCG-C09 variant in bioreactor systems, with the goal of improving process robustness, substrate accessibility, and overall catalytic productivity toward industrial implementation.

CONCLUSIONS

This thesis developed an integrated computational-experimental framework for the rational engineering of enzymes with improved stability, activity, and environmental robustness. The approach combined molecular modeling, molecular dynamics simulations, protein engineering, biochemical characterization, and structural analysis to guide efficient enzyme optimization.

- Fructosyl peptide oxidase (FPOX) variants were successfully engineered with enhanced thermostability using RMSF-guided mutations, salt bridges, and disulfide bonds (Appendix 1).
- Although the optimized FPOX variants exhibit enhanced stability and activity, further development is focused on improving their performance toward glycated haemoglobin. Current data addressing this objective can be found in the manuscript provided in the Appendix 5.
- Engineering of PET-degrading enzymes demonstrated the broader applicability of the framework to industrial biocatalysis. The LCC-ICCG-C09 variant showed improved thermal stability and approximately two-fold higher PET depolymerization efficiency compared to the parent enzyme, providing a promising foundation for enzymatic plastic recycling despite remaining challenges related to substrate crystallinity, pH sensitivity, and scalability (Appendix 2).
- A novel marine sponge derived enzyme, PETase SM14, was discovered and characterized. It was found to maintain high activity in alkaline, high-salt, and high-temperature environments (Appendix 3).
- Structural and molecular dynamics analyses of PETase SM14 revealed adaptive features supporting catalysis in hypersaline environments, highlighting its potential for marine plastic bioremediation (Appendix 4).

REFERENCES

(1) Gautieri, A.; Rigoldi, F.; Torretta, A.; Redaelli, A.; Parisini, E. In Silico Engineering of Enzyme Access Tunnels. In *Enzyme Engineering: Methods and Protocols*; Magnani, F., Marabelli, C., Paradisi, F., Eds.; Springer US: New York, NY, 2022; pp 203–225. https://doi.org/10.1007/978-1-0716-1826-4_11.

(2) Gribenko, A. V.; Patel, M. M.; Liu, J.; McCallum, S. A.; Wang, C.; Makhatadze, G. I. Rational Stabilization of Enzymes by Computational Redesign of Surface Charge-Charge Interactions. *Proc. Natl. Acad. Sci.* **2009**, *106* (8), 2601–2606. https://doi.org/10.1073/pnas.0808220106.

(3) Dombkowski, A. A. Disulfide by Design: A Computational Method for the Rational Design of Disulfide Bonds in Proteins. *Bioinforma. Oxf. Engl.* **2003**, *19* (14), 1852–1853. https://doi.org/10.1093/bioinformatics/btg231.

(4) Musil, M.; Jezik, A.; Horackova, J.; Borko, S.; Kabourek, P.; Damborsky, J.; Bednar, D. FireProt 2.0: Web-Based Platform for the Fully Automated Design of Thermostable Proteins. *Brief. Bioinform.* **2024**, *25* (1), bbad425. https://doi.org/10.1093/bib/bbad425.

(5) Rigoldi, F.; Donini, S.; Redaelli, A.; Parisini, E.; Gautieri, A. Review: Engineering of Thermostable Enzymes for Industrial Applications. *APL Bioeng.* **2018**, *2* (1), 011501. https://doi.org/10.1063/1.4997367.

(6) Chovancova, E.; Pavelka, A.; Benes, P.; Strnad, O.; Brezovsky, J.; Kozlikova, B.; Gora, A.; Sustr, V.; Klvana, M.; Medek, P.; Biedermannova, L.; Sochor, J.; Damborsky, J. CAVER 3.0: A Tool for the Analysis of Transport Pathways in Dynamic Protein Structures. *PLOS Comput. Biol.* **2012**, *8* (10), e1002708. https://doi.org/10.1371/journal.pcbi.1002708.

(7) Huang, P.-S.; Ban, Y.-E. A.; Richter, F.; Andre, I.; Vernon, R.; Schief, W. R.; Baker, D. RosettaRemodel: A Generalized Framework for Flexible Backbone Protein Design. *PLoS ONE* **2011**, *6* (8), e24109. https://doi.org/10.1371/journal.pone.0024109.

(8) Kokkonen, P.; Bednar, D.; Pinto, G.; Prokop, Z.; Damborsky, J. Engineering Enzyme Access Tunnels. *Biotechnol. Adv.* **2019**, *37* (6), 107386. https://doi.org/10.1016/j.biotechadv.2019.04.008.

(9) Zhou, J.; Huang, M. Navigating the Landscape of Enzyme Design: From Molecular Simulations to Machine Learning. *Chem. Soc. Rev.* **2024**, *53* (16), 8202–8239. https://doi.org/10.1039/D4CS00196F.

(10) Lin, H.-Y.; Chen, X.; Dong, J.; Yang, J.-F.; Xiao, H.; Ye, Y.; Li, L.-H.; Zhan, C.-G.; Yang, W.-C.; Yang, G.-F. Rational Redesign of Enzyme via the Combination of Quantum Mechanics/Molecular Mechanics, Molecular Dynamics, and Structural Biology Study. *J. Am. Chem. Soc.* **2021**, *143* (38), 15674–15687. https://doi.org/10.1021/jacs.1c06227.

(11) Rigoldi, F.; Gautieri, A.; Dalle Vedove, A.; Lucarelli, A. P.; Vesentini, S.; Parisini, E. Crystal Structure of the Deglycating Enzyme Amadoriase I in Its Free Form and Substrate-Bound Complex. *Proteins Struct. Funct. Bioinforma.* **2016**, *84* (6), 744–758. https://doi.org/10.1002/prot.25015.

(12) Ogawa, N.; Kimura, T.; Umehara, F.; Katayama, Y.; Nagai, G.; Suzuki, K.; Aisaka, K.; Maruyama, Y.; Itoh, T.; Hashimoto, W.; Murata, K.; Ichimura, M. Creation of Haemoglobin A1c Direct Oxidase from Fructosyl Peptide Oxidase by Combined Structure-Based Site Specific Mutagenesis and Random Mutagenesis. *Sci. Rep.* **2019**, *9* (1), 942. https://doi.org/10.1038/s41598-018-37806-x.

(13) Rahmatabadi, S. S.; Bashiri, H.; Soleymani, B. A Comprehensive Review on Fructosyl Peptide Oxidase as an Important Enzyme for Present Hemoglobin A1c Assays. *Biotechnol. Appl. Biochem.* **2025**, *72* (1), 268–281. https://doi.org/10.1002/bab.2647.

(14) Rescalli, A.; Varoni, E. M.; Cellesi, F.; Cerveri, P.; Rescalli, A.; Varoni, E. M.; Cellesi, F.; Cerveri, P. Analytical Challenges in Diabetes Management: Towards Glycated Albumin Point-of-Care Detection. *Biosensors* **2022**, *12* (9). https://doi.org/10.3390/bios12090687.

(15) Yonehara, S.; Inamura, N.; Fukuda, M.; Sugiyama, K. Use of Fructosyl Peptide Oxidase for HbA1c Assay. *J. Diabetes Sci. Technol.* **2015**, *9* (2), 200–205. https://doi.org/10.1177/1932296815569573.

(16) *Rational backbone redesign of a fructosyl peptide oxidase to widen its active site access tunnel – Rigoldi – 2020 – Biotechnology and Bioengineering – Wiley Online Library*.

https://analyticalsciencejournals.onlinelibrary.wiley.com/doi/10.1002/bit.27535 (accessed 2025-12-28).

(17) Ferri, S.; Kim, S.; Tsugawa, W.; Sode, K. Review of Fructosyl Amino Acid Oxidase Engineering Research: A Glimpse into the Future of Hemoglobin A1c Biosensing. *J. Diabetes Sci. Technol.* **2009**, *3* (3), 585–592. https://doi.org/10.1177/193229680900300324.

(18) Rahmatabadi, S. S.; Bashiri, H.; Soleymani, B. A Comprehensive Review on Fructosyl Peptide Oxidase as an Important Enzyme for Present Hemoglobin A1c Assays. *Biotechnol. Appl. Biochem.* **2025**, *72* (1), 268–281. https://doi.org/10.1002/bab.2647.

(19) Ferri, S.; Miyamoto, Y.; Sakaguchi-Mikami, A.; Tsugawa, W.; Sode, K. Engineering Fructosyl Peptide Oxidase to Improve Activity toward the Fructosyl Hexapeptide Standard for HbA1c Measurement. *Mol. Biotechnol.* **2013**, *54* (3), 939–943. https://doi.org/10.1007/s12033-012-9644-2.

(20) Ogawa, N.; Kimura, T.; Umehara, F.; Katayama, Y.; Nagai, G.; Suzuki, K.; Aisaka, K.; Maruyama, Y.; Itoh, T.; Hashimoto, W.; Murata, K.; Ichimura, M. Creation of Haemoglobin A1c Direct Oxidase from Fructosyl Peptide Oxidase by Combined Structure-Based Site Specific Mutagenesis and Random Mutagenesis. *Sci. Rep.* **2019**, *9* (1), 942. https://doi.org/10.1038/s41598-018-37806-x.

(21) Cid, R.; Bolívar, J.; Cid, R.; Bolívar, J. Platforms for Production of Protein-Based Vaccines: From Classical to Next-Generation Strategies. *Biomolecules* **2021**, *11* (8). https://doi.org/10.3390/biom11081072.

(22) Pratama, F.; Linton, D.; Dixon, N. Genetic and Process Engineering Strategies for Enhanced Recombinant N-Glycoprotein Production in Bacteria. *Microb. Cell Factories* **2021**, *20* (1), 198. https://doi.org/10.1186/s12934-021-01689-x.

(23) Nasiri, M.; Babaie, J.; Amiri, S.; Azimi, E.; Shamshiri, S.; Khalaj, V.; Golkar, M.; Fard-Esfahani, P. *SHuffle*^{TM} *T7* Strain Is Capable of Producing High Amount of Recombinant Human Fibroblast Growth Factor-1 (rhFGF-1) with Proper Physicochemical and Biological Properties. *J. Biotechnol.* **2017**, *259*, 30–38. https://doi.org/10.1016/j.jbiotec.2017.08.015.

(24) Young, C. L.; Britton, Z. T.; Robinson, A. S. Recombinant Protein Expression and Purification: A Comprehensive Review of Affinity Tags and Microbial Applications. *Biotechnol. J.* **2012**, *7* (5), 620–634. https://doi.org/10.1002/biot.201100155.

(25) [16] Purification of Proteins Using Polyhistidine Affinity Tags. In *Methods in Enzymology*; Academic Press, 2000; Vol. 326, pp 245–254. https://doi.org/10.1016/S0076-6879(00)26058-8.

(26) Vedadi, M.; Arrowsmith, C. H.; Allali-Hassani, A.; Senisterra, G.; Wasney, G. A. Biophysical Characterization of Recombinant Proteins: A Key to Higher Structural Genomics Success. *J. Struct. Biol.* **2010**, *172* (1), 107–119. https://doi.org/10.1016/j.jsb.2010.05.005.

(27) Circular Dichroism Spectroscopy for Protein Characterization: Biopharmaceutical Applications. In *Biophysical Characterization of Proteins in Developing Biopharmaceuticals*; Elsevier, 2015; pp 109–137. https://doi.org/10.1016/B978-0-444-59573-7.00006-3.

(28) Niesen, F. H.; Berglund, H.; Vedadi, M. The Use of Differential Scanning Fluorimetry to Detect Ligand Interactions That Promote Protein Stability. *Nat. Protoc.* **2007**, *2* (9), 2212–2221. https://doi.org/10.1038/nprot.2007.321.

(29) Rigoldi, F.; Donini, S.; Giacomina, F.; Sorana, F.; Redaelli, A.; Bandiera, T.; Parisini, E.; Gautieri, A. Thermal Stabilization of the Deglycating Enzyme Amadoriase I by Rational Design. *Sci. Rep.* **2018**, *8* (1), 3042. https://doi.org/10.1038/s41598-018-19991-x.

(30) Rigoldi, F.; Donini, S.; Giacomina, F.; Sorana, F.; Redaelli, A.; Bandiera, T.; Parisini, E.; Gautieri, A. Thermal Stabilization of the Deglycating Enzyme Amadoriase I by Rational Design. *Sci. Rep.* **2018**, *8* (1), 3042. https://doi.org/10.1038/s41598-018-19991-x.

(31) Rathore, I.; Mishra, V.; Bhaumik, P. Advancements in Macromolecular Crystallography: From Past to Present. *Emerg. Top. Life Sci.* **2021**, *5* (1), 127–149. https://doi.org/10.1042/ETLS20200316.

(32) Helliwell, J. R. New Developments in Crystallography: Exploring Its Technology, Methods and Scope in the Molecular Biosciences. *Biosci. Rep.* **2017**, *37* (4), BSR20170204. https://doi.org/10.1042/BSR20170204.

(33) *A Beginner's Guide to Protein Crystallography – Creative Biostructure*. https://www.creative-biostructure.com/protein-crystallography-452.htm (accessed 2025-12-28).

(34) Qiu, J.; Chen, Y.; Zhang, L.; Wu, J.; Zeng, X.; Shi, X.; Liu, L.; Chen, J. A Comprehensive Review on Enzymatic Biodegradation of Polyethylene Terephthalate. *Environ. Res.* **2024**, *240*, 117427. https://doi.org/10.1016/j.envres.2023.117427.

(35) Rosini, E.; Antonelli, N.; Molla, G. Rethinking Plastic Waste: Innovations in Enzymatic Breakdown of Oil-Based Polyesters and Bioplastics. *FEBS Open Bio n/a* (n/a). https://doi.org/10.1002/2211-5463.70120.

(36) Yoshida, S.; Hiraga, K.; Takehana, T.; Taniguchi, I.; Yamaji, H.; Maeda, Y.; Toyohara, K.; Miyamoto, K.; Kimura, Y.; Oda, K. A Bacterium That Degrades and Assimilates Poly(Ethylene Terephthalate). *Science* **2016**, *351* (6278), 1196–1199. https://doi.org/10.1126/science.aad6359.

(37) Di Rocco, G.; Taunt, H. N.; Berto, M.; Jackson, H. O.; Piccinini, D.; Carletti, A.; Scurani, G.; Braidi, N.; Purton, S. A PETase Enzyme Synthesised in the Chloroplast of the Microalga Chlamydomonas Reinhardtii Is Active against Post-Consumer Plastics. *Sci. Rep.* **2023**, *13* (1), 10028. https://doi.org/10.1038/s41598-023-37227-5.

(38) Tournier, V.; Duquesne, S.; Guillamot, F.; Cramail, H.; Taton, D.; Marty, A.; André, I. Enzymes' Power for Plastics Degradation. *Chem. Rev.* **2023**, *123* (9), 5612–5701. https://doi.org/10.1021/acs.chemrev.2c00644.

(39) Han, X.; Liu, W.; Huang, J.-W.; Ma, J.; Zheng, Y.; Ko, T.-P.; Xu, L.; Cheng, Y.-S.; Chen, C.-C.; Guo, R.-T. Structural Insight into Catalytic Mechanism of PET Hydrolase. *Nat. Commun.* **2017**, *8* (1), 2106. https://doi.org/10.1038/s41467-017-02255-z.

(40) Ahituv, N.; Freund, D.; Mireles, R.; Noda-García, L. The Diversity of PET Degrading Enzymes: A Systematic Review of Sequence, Structure, and Function. *Protein Sci.* **2025**, *34* (10), e70282. https://doi.org/10.1002/pro.70282.

(41) Kawai, F.; Kawabata, T.; Oda, M. Current Knowledge on Enzymatic PET Degradation and Its Possible Application to Waste Stream Management and Other Fields. *Appl. Microbiol. Biotechnol.* **2019**, *103* (11), 4253–4268. https://doi.org/10.1007/s00253-019-09717-y.

(42) Ermis, H. A Mini-Review on the Role of PETase in Polyethylene Terephthalate Degradation. *Rev. Environ. Sci. Biotechnol.* **2025**, *24* (3), 545–555. https://doi.org/10.1007/s11157-025-09737-3.

(43) Barclay, A.; Acharya, K. R.; Barclay, A.; Acharya, K. R. Engineering Plastic Eating Enzymes Using Structural Biology. *Biomolecules* **2023**, *13* (9). https://doi.org/10.3390/biom13091407.

(44) Jerves, C.; Neves, R. P. P.; Ramos, M. J.; da Silva, S.; Fernandes, P. A. Reaction Mechanism of the PET Degrading Enzyme PETase Studied with DFT/MM Molecular Dynamics Simulations. *ACS Catal.* **2021**, *11* (18), 11626–11638. https://doi.org/10.1021/acscatal.1c03700.

(45) Arnal, G.; Anglade, J.; Gavalda, S.; Tournier, V.; Chabot, N.; Bornscheuer, U. T.; Weber, G.; Marty, A. Assessment of Four Engineered PET Degrading Enzymes Considering Large-Scale Industrial Applications. *ACS Catal.* **2023**, *13* (20), 13156–13166. https://doi.org/10.1021/acscatal.3c02922.

(46) Tournier, V.; Topham, C. M.; Gilles, A.; David, B.; Folgoas, C.; Moya-Leclair, E.; Kamionka, E.; Desrousseaux, M.-L.; Texier, H.; Gavalda, S.; Cot, M.; Guémard, E.; Dalibey, M.; Nomme, J.; Cioci, G.; Barbe, S.; Chateau, M.; André, I.; Duquesne, S.; Marty, A. An Engineered PET Depolymerase to Break down and Recycle Plastic Bottles. *Nature* **2020**, *580* (7802), 216–219. https://doi.org/10.1038/s41586-020-2149-4.

(47) Wang, H.; Cun, Y.; Wang, M.; Du, X.; Yang, Z.; Wang, H.; Zhang, J.; Wang, P.; Feng, Y.; Zhu, Y. Computational Loop Reconstruction Based Design of Efficient PET Hydrolases. *Commun. Biol.* **2025**, *8* (1), 934. https://doi.org/10.1038/s42003-025-08364-6.

(48) Der, B. S.; Kluwe, C.; Miklos, A. E.; Jacak, R.; Lyskov, S.; Gray, J. J.; Georgiou, G.; Ellington, A. D.; Kuhlman, B. Alternative Computational Protocols for Supercharging Protein Surfaces for Reversible Unfolding and Retention of Stability. *PloS One* **2013**, *8* (5), e64363. https://doi.org/10.1371/journal.pone.0064363.

(49) Goldenzweig, A.; Goldsmith, M.; Hill, S. E.; Gertman, O.; Laurino, P.; Ashani, Y.; Dym, O.; Unger, T.; Albeck, S.; Prilusky, J.; Lieberman, R. L.; Aharoni, A.; Silman, I.; Sussman, J. L.; Tawfik, D. S.; Fleishman, S. J. Automated Structure- and Sequence-Based Design of Proteins for High Bacterial Expression and Stability. *Mol. Cell* **2016**, *63* (2), 337–346. https://doi.org/10.1016/j.molcel.2016.06.012.

(50) Huang, D.; Zhang, L.; Sun, Y. Rational Design of Disulfide Bridges in BbPETaseCD for Enhancing the Enzymatic Performance in PET Degradation. *Molecules* **2023**, *28* (8), 3528. https://doi.org/10.3390/molecules28083528.

(51) *ESPript 3*. ESPript 3. https://espript.ibcp.fr/ESPript/ESPript/ (accessed 2026-01-05).

(52) Burgin, T.; Pollard, B. C.; Knott, B. C.; Mayes, H. B.; Crowley, M. F.; McGeehan, J. E.; Beckham, G. T.; Woodcock, H. L. The Reaction Mechanism of the Ideonella Sakaiensis PETase Enzyme. *Commun. Chem.* **2024**, *7* (1), 65. https://doi.org/10.1038/s42004-024-01154-x.

(53) Liu, Z.; Schey, K. L. Optimization of a MALDI TOF-TOF Mass Spectrometer for Intact Protein Analysis. *J. Am. Soc. Mass Spectrom.* **2005**, *16* (4), 482–490. https://doi.org/10.1016/j.jasms.2004.12.018.

(54) Winn, M. D.; Ballard, C. C.; Cowtan, K. D.; Dodson, E. J.; Emsley, P.; Evans, P. R.; Keegan, R. M.; Krissinel, E. B.; Leslie, A. G. W.; McCoy, A.; McNicholas, S. J.; Murshudov, G. N.; Pannu, N. S.; Potterton, E. A.; Powell, H. R.; Read, R. J.; Vagin, A.; Wilson, K. S. Overview of the CCP4 Suite and Current Developments. *Acta Crystallogr. D Biol. Crystallogr.* **2011**, *67* (Pt 4), 235–242. https://doi.org/10.1107/S0907444910045749.

(55) Murshudov, G. N.; Skubák, P.; Lebedev, A. A.; Pannu, N. S.; Steiner, R. A.; Nicholls, R. A.; Winn, M. D.; Long, F.; Vagin, A. A. REFMAC5 for the Refinement of Macromolecular Crystal Structures. *Acta Crystallogr. D Biol. Crystallogr.* **2011**, *67* (Pt 4), 355–367. https://doi.org/10.1107/S0907444911001314.

1. Pielikums
Appendix 1

Estiri, H.; * **Bhattacharya, S**.; * Rodriguez Buitrago, J. A.; Castagna, R.; Legzdiņa, L.; Casucci, G.; Ricci, A.; Parisini, E.; Gautieri, A.
Tailoring FPOX Enzymes for Enhanced Stability and Expanded Substrate Recognition

Scientific Reports, 2023, 13, 18610
doi:10.1038/s41598-023-45428-1

Publikācija un tās pielikums pieejams bez maksas izdevēja mājaslapā
The Publication and Supporting Information is available free of charge on the publisher's website

**These authors contributed equally to this work.*

www.nature.com/scientificreports

scientific reports

OPEN

Tailoring FPOX enzymes for enhanced stability and expanded substrate recognition

Hajar Estiri[1,6], Shapla Bhattacharya[1,2,6], Jhon Alexander Rodriguez Buitrago[1], Rossella Castagna[1,3], Linda Legzdiņa[1], Giorgia Casucci[1], Andrea Ricci[4], Emilio Parisini[1,5]✉ & Alfonso Gautieri[4]✉

Fructosyl peptide oxidases (FPOX) are deglycating enzymes that find application as key enzymatic components in diabetes monitoring devices. Indeed, their use with blood samples can provide a measurement of the concentration of glycated hemoglobin and glycated albumin, two well-known diabetes markers. However, the FPOX currently employed in enzymatic assays cannot directly detect whole glycated proteins, making it necessary to perform a preliminary proteolytic treatment of the target protein to generate small glycated peptides that can act as viable substrates for the enzyme. This is a costly and time consuming step. In this work, we used an in silico protein engineering approach to enhance the overall thermal stability of the enzyme and to improve its catalytic activity toward large substrates. The final design shows a marked improvement in thermal stability relative to the wild type enzyme, a distinct widening of its access tunnel and significant enzymatic activity towards a range of glycated substrates.

The current clinical standard for monitoring blood glucose levels is glycated hemoglobin (HbA1c). Indeed, thanks to its longevity (its half-life is up to 3 months), HbA1c is the marker of election for diabetes diagnosis. To this end, an effective protocol that includes the exploitation of fructosyl peptide oxidases (FPOX) for measuring HbA1c concentration in blood samples has been developed[1–3]. The first step of the protocol involves a proteolytic digestion of HbA1c to release the glycated N-terminal dipeptide, fructosyl-valine-histidine (fVH); the dipeptide is then hydrolyzed by a FPOX, a process that results in the production of hydrogen peroxide, which can be measured via a colorimetric assay by coupling horseradish peroxidase and an appropriate chromophore[4]. Likewise, FPOX-based methods can also be used to measure glycated albumin (GA), which is a short- and medium-term glycemic diabetes marker (half-life up to 3 weeks)[5].

FPOXs are suitable enzymes for diabetes assays thanks to their reactivity on up to six amino acid-long fructosyl peptides[6]. FPOxs belong to the larger family of Fructosyl Amino Acid Oxidases (FAOX)[7–9], which are enzymes of fungal or bacterial origin that cleave low molecular weight Amadori products, freeing the amine group and generating glucosone and hydrogen peroxide[10–12].

Other than diabetes detection and surveillance, FPOXs are also considered to be promising therapeutic tools for protein deglycation in biological tissues[13]. Protein glycation is a spontaneous and irreversible non-enzymatic reaction whereby a sugar binds to a protein and generates a covalent adduct named Amadori product[14]. Protein glycation triggers many diabetes-related clinical outcomes, such as for instance arterial stiffening[15], nephropathy[16], retinopathy[17] and neuropathy[18]. These complications have indeed been shown to be largely driven by the chemical modification of functional proteins[19,20].

The inability of wild type FPOXs to act on intact proteins is the most critical issue limiting both their diabetes detection efficiency and their protein deglycation potential[21,22]. This is due to their buried active site and

[1]Department of Biotechnology, Latvian Institute of Organic Synthesis, Aizkraukles 21, Riga 1006, Latvia. [2]Faculty of Materials Science and Applied Chemistry, Riga Technical University, Paula Valdena 3, Riga 1048, Latvia. [3]Dipartimento di Chimica, Materiali e Ingegneria Chimica "Giulio Natta", Politecnico di Milano, Piazza L. da Vinci 32, 20133 Milano, Italy. [4]Biomolecular Engineering Lab, Dipartimento di Elettronica, Informazione e Bioingegneria, Politecnico di Milano, Piazza Leonardo da Vinci 32, 20133 Milano, Italy. [5]Department of Chemistry "G. Ciamician", University of Bologna, Via Selmi 2, 40126 Bologna, Italy. [6]These authors contributed equally: Hajar Estiri and Shapla Bhattacharya. ✉email: emilio.parisini@osi.lv; alfonso.gautieri@polimi.it

narrow access tunnel, as determined in multiple crystal structures[6,12,23]. To the best of our knowledge, there is currently only one report describing an enzyme that shows direct activity on HbA1c without requiring any preliminary proteolytic step. This enzyme has been obtained by introducing a single point mutation (R61G) in a thermostable version of *Aspergillus nidulans*' FPOX (AnFPOX)[24]. Nonetheless, the activity and the stability profile of FPOX enzymes need to be further improved when considering their application in biosensors. Indeed, improving the ability of FPOXs to act on full-length glycated proteins may provide significant advantages in both the development of novel diabetes monitoring tools and in the design of innovative therapies aimed at reducing and/or preventing protein aging (i.e., the accumulation over time of advanced glycation end-products). These improvements may come from engineering an enzyme with a wider access tunnel to the catalytic site; in fact, access tunnel engineering can improve several characteristics of the enzyme, such as activity, specificity, promiscuity, enantioselectivity and stability[25,26].

Our group has previously reported on a successful engineering campaign aimed at widening the access tunnel to the catalytic site of *Phaeosphaeria nodorum* FPOX (PnFPOX)[27]. In that account, using a rational design approach involving a five-amino acid deletion at the entrance of the active site and a number of further mutations, we described a stable PnFPOX mutant (named L3-35A) that, relative to the wild type enzyme, features a significantly wider and shorter access tunnel. However, the backbone redesign also introduced structural instability and lowered the activity of the engineered enzyme. For this reason, in this work we aimed at improving the L3-35A design and restore the stability and activity of the enzyme, thus providing a FPOX that presents high activity and stability together with a wider access tunnel with respect to the parental enzyme PnFPOX.

In the present study, we set out to enhance the thermal stability of the L3-35A mutant by implementing a methodological approach whereby different thermal stabilization strategies are tested in parallel and their efficiency compared. These various strategies involved mutations to either improve the RMSF of the protein (generating mutants hereafter referred to as D-series mutants), increase the number of salt bridges (C-series mutants) or form disulfide bonds (X-series mutants). Whereas, of all methods, engineered disulfide bond formation usually provides the enzyme with the highest T_m, the other two methods may in fact be useful when engineering a protein that already contains one or more cysteines. In such cases, the introduction of further cysteine residues may interfere with natural disulfide bond patterns and result in high levels of insoluble protein formation. In essence, we used our PnFPOX mutant L3-35 as a platform to test our design approach on different thermal stabilization strategies, and to provide a systematic comparison of their efficiency relative to the same parent enzyme. Our design process involved the use of extensive molecular dynamics (MD) simulations and targeted optimization using Rosetta-based design[28], followed by experimental validation of a small number of selected high-scoring mutants. In our validation procedure, we assessed the activity of the selected mutants against several substrates, including small glycated amino acids such as fructosyl-Val (fV) and fructosyl-Lys (fK), the dipeptide fructosyl-Val-His (fVH) and the hexapeptide fructosyl-Val-His-Leu-Thr-Pro-Glu (F6P). Overall, the data shown herein provide evidence that our rational design approach allows the rapid identification of mutants featuring the desired phenotype.

Results and discussion

Stability optimization of the L3-35A PnFPOX mutant

Starting from the crystal structure of the L3-35A PnFPOX mutant (PDB code 6Y4J), we performed MD simulations at variable temperatures, followed by root mean square fluctuation (RMSF) analysis. Our data suggests that, with the exception of the N- and the C-termini, the most unstable regions of the enzyme are helix 96-111 and the surrounding structures (Fig. 1). The relative instability of this helix is likely due to the redesign of residues 58–65 of wild type PnFPOX (red circle in Fig. 1c)[27]. Indeed, while these changes resulted in the widening of the access tunnel to the active site, they also caused the removal of the amino acids facing helix 96-111, thus abrogating previously existing stabilizing interactions. Further regions that present a lower average stability are loops 240–247, 301–307, 401–410.

The use of the Rosetta "Supercharge" method, which aimed at increasing the charge on the surface of the enzyme, led to the design of 1000 enzyme variants, from which those 20 (named C01–C20) that featured the best Rosetta score were selected for further analysis. Similarly, single point mutations screening led to 8095 designs, from which the best 20 were retained (S01–S20). Double point mutations screening generated 271,000 designs (leading to the selection D01–D20), PROSS design produced 9 variants (P01–P09), and disulfide bond design identified 62 enzyme variants (from which we selected the best 8, named X01-X08).

The 77 candidate enzyme variants originating from our different screening methods were then subject to MD simulations and ranked based on their stability at increasing temperatures, as assessed by RMSF analysis. Our MD-based ranking led to the selection of six candidate mutants (C16, D02, X01, X02A, X04, and X07) for experimental production and characterization.

For measuring the thermal stability of the different mutants, we used both thermal shift assay (differential scanning fluorimetry or DSF) and circular dichroism (CD). Both of these methods are sensitive to the thermal stability of the enzymes and can provide information on the structural changes that occur as a function of temperature. As expected, the two methodologies provide very similar results in terms of trends and absolute values and demonstrate that the rational design procedure that we adopted was effective in enhancing the thermal stability (T_m) of our reference FPOX enzyme, L3-35A (see Table 1). The D02 variant, which relative to L3-35A features two additional mutations (V110R and D115G), shows an increase in T_m of ≈ 1.5 °C with respect to the parent enzyme. On the other hand, the introduction of extensive surface charges and salt bridges (mutant C16) resulted in a further increase in T_m of ≈ 1.5 °C (T_m = 55.2 °C). Finally, the incorporation of a single disulfide bond in different positions on the L3-35A scaffold led to a significant improvement in thermal stability of all the tested mutants of this series: X01 (54.1 °C), X02 (60.0 °C), X04 (55.2 °C) and X07 (55.3 °C).

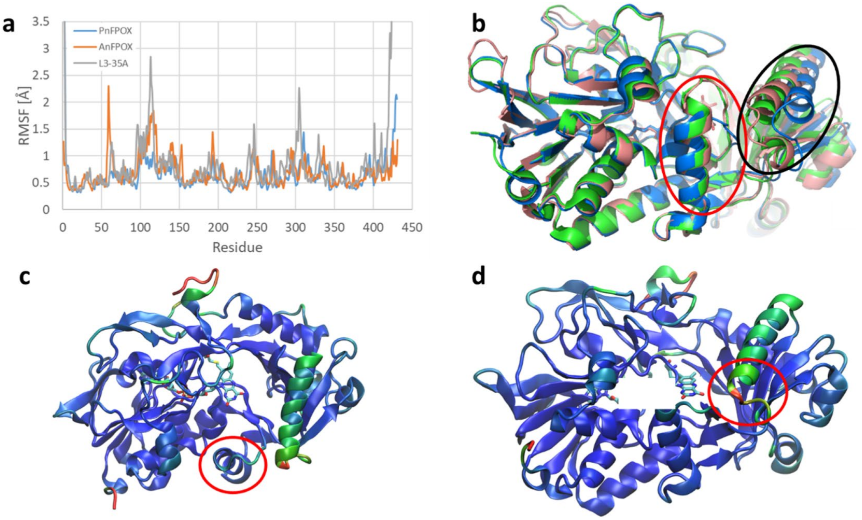

Figure 1. Stability analysis from MD simulations. The RMSF profile (**a**) shows that in the L3-35A, the helix 96–111 and the surrounding structures present a high degree of instability compared to the other enzymes. In the structural comparison (**b**, PnFPOX:green, AnFPOX:pink and L3-35A:blue), this helix (circled black) shows also a different fold compared to the other two enzymes. The instability and different structural arrangement could be due to design operated on L3-35A, which removed part of the helix blocking the tunnel (**c**, circled red). These removed residues were facing the helix 96–111 in the parental enzymes and were making stabilizing interactions, which could explain why helix 96–111 is unstable in L3-35A, possibly leading to its lower activity (**d**, color coded by RMSF, where blue represents lower RMSF and green–red the regions with higher RMSF). Comparison of RMSF and structure of PnFPOX (green), AnFPOX (pink) and L3-35A (blue).

Enzyme	T_m (°C)^a	T_m (°C)^b
PnFPOX (WT)	53.2 ± 0.2	53.5 ± 0.1
L3-35A	52.3 ± 0.2	52.9 ± 0.1
D02	53.1 ± 0.5	54.8 ± 0.1
C16	55.2 ± 0.1	55.0 ± 0.1
X01	54.1 ± 0.1	54.2 ± 0.1
X02A	60.0 ± 0.4	60.1 ± 0.1
X04	55.2 ± 0.3	55.0 ± 0.1
X07	55.3 ± 0.4	55.4 ± 0.1
X02B	60.2 ± 0.7	60.6 ± 0.1
X02C	64.0 ± 0.2	63.3 ± 0.1

Table 1. Melting temperature of the parent enzyme (L3-35A) and its mutants as determined by thermal shift assay (^{a}) and circular dichroism (^{b}). The melting temperature of the wild type enzyme (PnFPOX) is also provided as reference.

To assess the activity of these various enzyme variants, we employed a colorimetric enzymatic assay that allowed us to quantify the release of glucosone probed at 322 nm. We tested the activity of the enzymes on fructosyl-lysine (fK), fructosyl-valine (fV), fructosyl-valine-histidine (fVH) and fructosyl-Val-His-Leu-Thr-Pro-Glu (F6P) (see Table 2). We observed that the activity of the enzyme variants towards fK and fV remained similar to that of the parent enzyme, with a slight increase of activity in the case of D02 and a slight decrease in all the other cases. Overall, we observed that the activity of these mutant enzymes is several folds lower than that of PnFPOX, the naturally occurring enzyme. Also, similarly to the parent enzyme, none of these mutants shows any activity towards the dipeptide or the hexapeptide.

Based on our thermostability results, we selected the X02A variant for its high T_m, high expression yield, and detectable activity toward glycated amino acids and we set out to increase its activity toward larger substrates (i.e., fVH and F6P). The activity toward these substrates was present in the wild type enzyme PnFPOX but was lost

Enzyme	Specific activity (U/mg)			
	fK	fV	fVH	F6P
PnFPOX	30.18 ± 0.67	29.67 ± 2.56	32.60 ± 1.18	0.78 ± 0.09
AnFPOX-47	–	–	–	0.082 ± 0.002[a]
L3-35A	0.21 ± 0.02	0.16 ± 0.04	–	–
D02	0.30 ± 0.03	0.32 ± 0.01	–	–
C16	ND	ND	–	–
X01	ND	ND	–	–
X02A	0.15 ± 0.01	0.11 ± 0.01	–	–
X04	ND	0.13 ± 0.01	–	–
X07	–	0.08 ± 0.01	–	–
X02B	2.24 ± 0.07	32.50 ± 0.44	0.87 ± 0.03	0.18 ± 0.06
X02C	1.06 ± 0.01	17.95 ± 2.46	1.62 ± 0.02	0.43 ± 0.06

Table 2. Comparison of the enzymatic specific activity (U/mg) on different substrates. Tests are performed in triplicates. *ND* not detected. [a]Data from reference[24].

in the L3-35A design. The L3-35A design involved the engineering of the entry tunnel of the wild type PnFPOX enzyme via the shortening of a loop and a helix[27]. In this process, while the amino acids that are directly involved in the catalytic function were not modified, some tunnel-lining residues were replaced. This could explain the reduced activity of both the L3-35A enzyme previously reported and its thermally-stabilized mutants described so far (D02, C16, X01, X02A, X04, X07). Hence, we set out to design mutations to enhance the catalytic activity of X02A, the most thermally-stable mutant of our library (Table 1).

To improve the catalytic activity of the engineered enzymes, the most promising variants resulting from the stabilization steps were sequence- and structurally-aligned with the most active enzymes against the fructosyl-hexapeptide F6P that are available in the literature, namely PnFPOX, FPOX-C and related variants[6] and AnFPOX and related variants[24]. Specifically, tunnel-lining residues associated with improvements in the catalytic activity were selected to be introduced in the engineered enzyme (Fig. 2). Based on this comparison, we identified two designs in which enzyme activity could be partially restored. In the first design (X02B), four mutations were introduced in positions that are directly facing the tunnel in order to match the residues found in PnFPOX (D60G, A61V, D62S, D368H). In the second design (X02C), we also introduced the N56A mutation, which was shown to improve activity in the PnFPOX enzyme[6], as well as a series of mutations in the loop 61–71. These mutations (A61I, D62S, A63G, D64A, A66L, A67S, D68L, A69E, R71F) were derived from the consensus sequence of PnFPOX and AnFPOX-47, the most active FPOX enzymes currently available.

In essence, by reintroducing conserved tunnel-lining residues in the X02A sequence, we generated the X02B and X02C mutants (Fig. 3) and we tested their activity toward the same panel of substrates that were tested with the parent enzyme (Table 2). It is worth noting that the X02B and X02C enzymes present limited activity toward the dipeptide (≈ 0.87 and 1.62 U/mg, respectively) compared to the WT (32.60 U/mg). However, while the WT significantly shows little, if any, ability to catalyze the oxidative reaction on the F6P hexapeptide (0.78 U/mg, which is equivalent to 2.4% of the activity on fVH), the X02B and X02C mutants feature significant activity also on the hexapeptide (0.18 and 0.43 U/mg, which are equivalent to 20.7% and 26.5% of the activity observed on the fVH). We measured the kinetic parameters (Table 3) for the WT and the latest engineered enzyme (X02C) against the fructosyl-valine substrate, which are found consistent with those reported in the literature for the enzyme family[7,10,27,29]. For the substrate fructosyl-hexapeptide, a comparison of the K_m of our mutant X02C (0.03 mM) with the wild type PnFPOX (0.81 mM) shows higher affinity for the substrate.

To further compare our final design with similar FPOX, we compared it with a recently published engineered FPOX, named AnFPOX-47, which is reported to be the most active on intact glycated hemoglobin among the reported designs that present a wider tunnel[24]. The comparison shows that X02B and X02C have significantly higher activity than AnFPOX-47 toward F6P. Moreover, X02B and X02C feature a much higher T_m relative to all the other L3-35A mutants, i.e. 60.17 °C and 64.02 °C respectively (Table 1). Overall, within our panel of mutated enzymes the thermal stability of X02C increased significantly (more than 10 °C) with respect to the wild type PnFPOX. Interestingly, thermal stabilization also resulted in a significant increase in the production yield, the X02C variant featuring a nearly three-fold increase in expression yield with respect to the WT.

Structural correlation analysis

To identify the possible molecular mechanism underlying the differences in enzymatic activity observed in our study, we determined the crystal structures of some of our best performing variants and we compared their overall fold as well as their tunnel and catalytic site. At the structural level, the tridimensional architecture of all mutants reported herein is maintained, confirming that our mutagenesis campaign did not impair the conformational stability of the enzyme. Indeed, when comparing the overall RMSD values of all the crystallized mutants to the wild type PnFPOX (PDB code 5T1E), the differences are all within a maximum of 1.8 Å (see Table 4).

We then compared the residues in the catalytic site (W235, E278, G372, R415) of our mutants with those of the WT enzyme. These residues are highly conserved in all FPOX enzymes and bind to the sugar moiety of

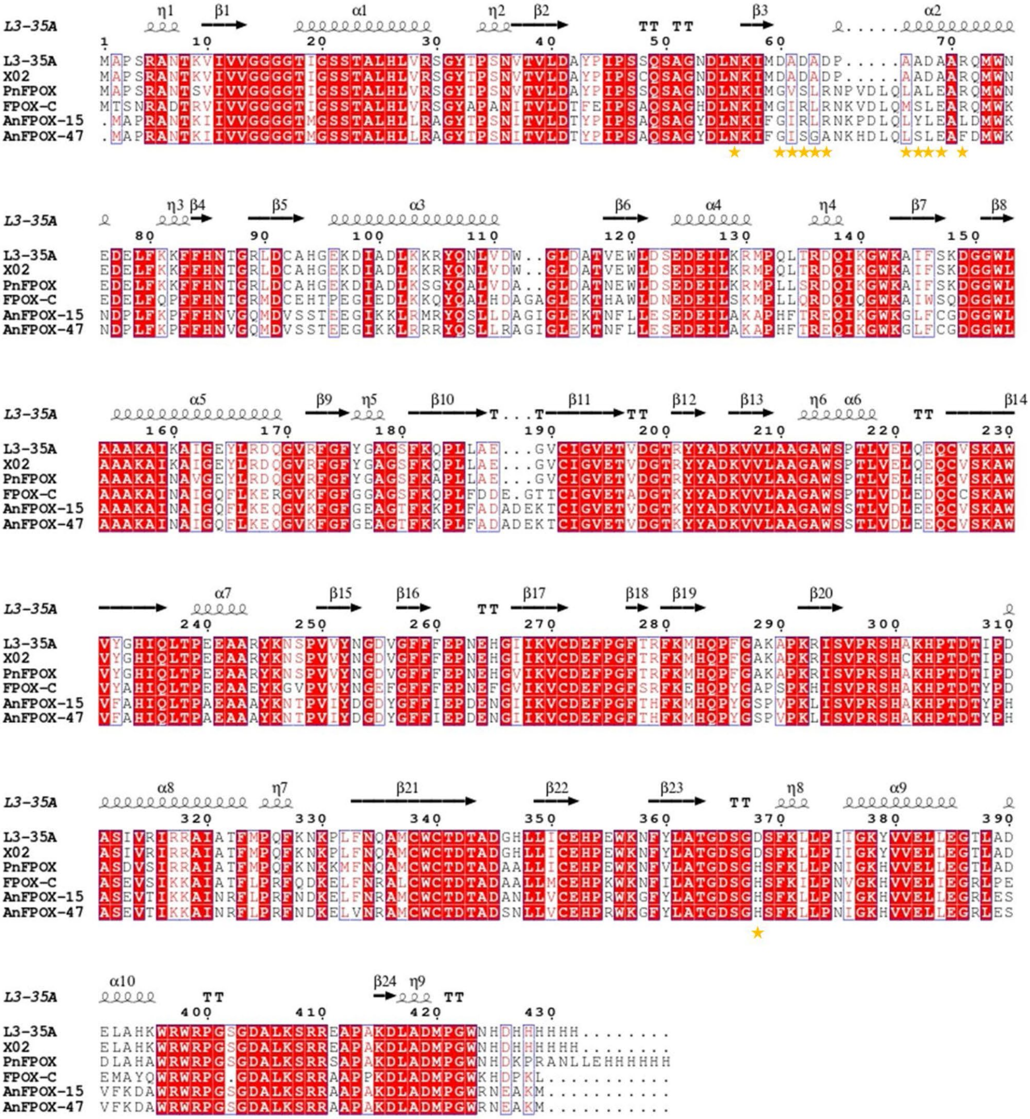

Figure 2. Sequence alignment of homologous enzymes used to design mutations for enzyme activity enhancement. The L3-35A and X02A enzymes were sequence- and structurally-aligned against the most active enzymes on the fructosyl-hexapeptide F6P that are available in the literature, namely PnFPOX and FPOX-C[6], AnFPOX-15 and AnFPOX-47[24]. Yellow stars represent positions considered for mutagenesis.

the substrates. We observed that the orientation of these residues is maintained (see Fig. 4), suggesting that the differences in the catalytic activity are not due to differences in the core catalytic site.

These results could be explained by the modification of the tunnel size and of its lining residues (see Fig. 5 and Table 4). In the WT, the small and long tunnel (bottleneck radius 2.2 Å, length 13.3 Å) allows greater stabilization of small substrates while limiting the entrance of larger substrates, hence explaining the marked decrease of activity when moving from glycated amino acids to the glycated hexapeptide. On the other hand, the AnFPOX-47 developed by Ogawa and coworkers[24] presents a slightly larger tunnel (bottleneck radius of 2.7 Å) with comparable length (13.2 Å), which may explain its activity towards larger substrates. Our previously developed L3-35A enzyme variant[27] exhibits a much wider and shorter tunnel (bottleneck radius of 3.7 Å and length of 6.4 Å) but shows limited activity on both small and large substrates, which could be due to the limited

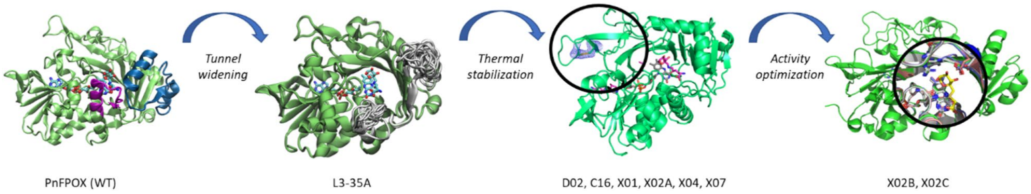

Figure 3. Schematic of the rational design strategy, showing the names of the relevant enzyme variants obtained at each stage.

Enzyme	Substrate	K_m (mM)	V_{max} (mM/min)	k_{cat} (s^{-1})	k_{cat}/K_m (mM^{-1} s^{-1})
PnFPOX	fV	5.93 ± 1.61	41.67 ± 8.34	99.33 ± 19.86	16.75
X02C	fV	0.94 ± 0.06	10.56 ± 0.56	20.83 ± 1.10	22.16
PnFPOX	F6P	0.81 ± 0.30	15.48 ± 1.20	36.83 ± 2.83	45.47
X02C	F6P	0.03 ± 0.01	0.26 ± 0.01	0.52 ± 0.02	17.22

Table 3. Kinetic parameters of wild-type PnFPOX and the engineered X02C enzymes.

Enzyme	RMSD (Å)	Tunnel bottleneck radius (Å)	Tunnel length (Å)
PnFPOX	–	2.2	13.3
L3-35A	1.8	3.7	6.4
D02	1.4	2.9	11.7
X02A	1.7	3.1	9.4
X04	1.8	3.0	10.9
X02B	1.5	3.0	10.2

Table 4. Calculated RMSDs between the WT enzyme PnFPOX and the different mutants, and tunnel geometry. For selected enzymes, it was not possible to obtain the crystal structure.

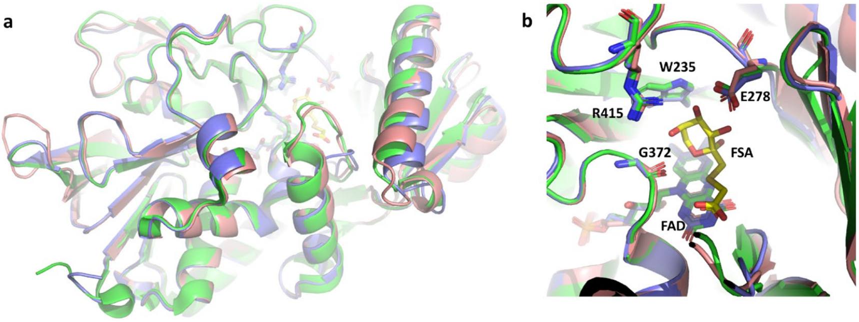

Figure 4. Structural comparison of relevant FPOX enzyme: PnFPOX (green), AnFPOX-47 (pink) and X02B (violet). The FSA inhibitor is depicted in yellow. The overall structural alignment shows no significant differences between the enzymes, except for the entrance tunnel (**a**). The position of the catalytic site is also highly conserved (**b**).

constraints of bound substrates due to the wider catalytic pocket, as well as to the removal of tunnel lining residues that contribute to the specific binding and stabilization of substrates. In an effort to revert the latter effect, we re-engineered the tunnel-lining residues in the X02B and X02C enzymes. The X02B enzyme features a wide and short tunnel (bottleneck radius of 3.0 Å and length of 10.2 Å), in between the WT and its parent L3-35A, while at the same time showing a similar activity on both small and larger substrates. Hence, the wider tunnel of

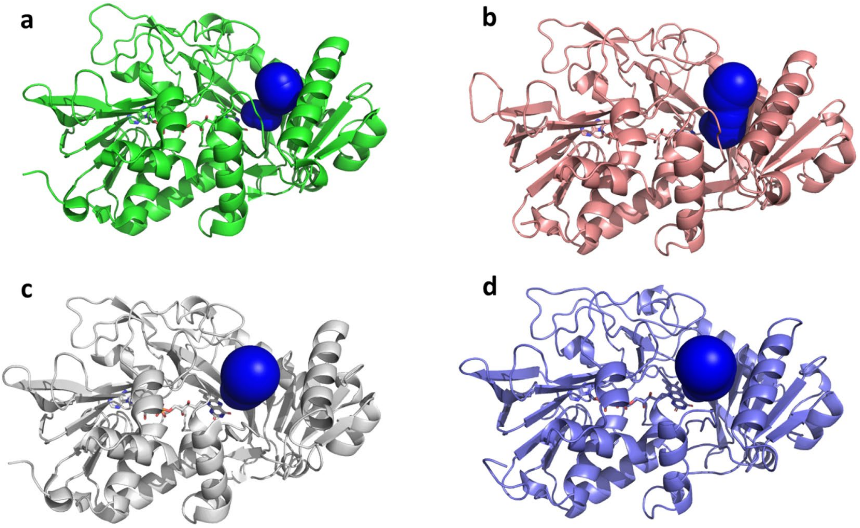

Figure 5. Comparison of the binding tunnel of PnFPOX (**a**), AnFPOX-47 (**b**), L3-35A (**c**) and X02B (**d**).

X02B, while reducing the stabilization of small substrates (and, as a consequence, the catalytic activity towards them) allows larger substrates to access the catalytic site more easily, leading to comparable enzymatic activity.

Conclusions

As part of an ongoing investigation aimed at engineering an FPOX enzyme to provide it with both enhanced thermostability and a wider access tunnel to the catalytic site, we set out to design a number of novel FPOX mutants starting from our previously characterized mutant L3-35A of PnFPOX, which featured a much larger active site relative to the wild type enzyme. To increase enzyme thermostability, we tested several strategies, namely introducing mutations to either improve the RMSF of the protein, increase the number of salt bridges or form single disulfide bonds. Our thermostability findings align with the expectation that the improved RMSF, salt bridges formation, and disulfide bonds formation approaches can all effectively improve the thermal stability of enzymes, albeit to a different extent. In particular, we have shown that the introduction of a disulfide bond allowed us to produce a PnFPOX variant that shows remarkably higher thermal stability compared to the other mutants. Furthermore, the catalytic activity, which was significantly lost during the design process, was reintroduced by engineering ligand-binding and tunnel-lining position, which led to a new, thermally stabilized and active FPOX enzyme that features a wider access tunnel to the catalytic pocket. Ongoing efforts are aimed at testing the enzymes on whole glycated proteins (i.e., albumin and hemoglobin) to test whether the wider access tunnel of X02C, together with the restored catalytic activity, can actually provide catalytic activity directly on whole proteins. This may represent a significant step toward the use of these enzymes on larger substrates and on full proteins, thus possibly allowing the development of in vitro HbA1c diagnostic devices based on a direct enzymatic oxidation system. Indeed, there is a rapidly growing demand for cheap, efficient and rapid diabetes monitoring tests. This could be met by developing enzymatic assays for glycated hemoglobin and albumin that do not require a preliminary digestion of the proteins. The elimination of this step would provide several advantages to the test, such as the shortening of its measuring times, a simplification of its overall procedure and a substantial reduction of its costs.

From the perspective of protein engineering, the use of rational design methods like the one described in this work offers a promising strategy for the design of thermostable enzymes with improved performance in various industrial and biomedical applications. This study also highlights the potential of computational methods and targeted mutations to improve the activity and substrate range of enzymes, and it paves the way for the design of thermostable enzymes with improved performance toward different targets and applications. We believe that this rational approach can accelerate the production and the use of biocatalysts in different industrial sectors, thus in turn allowing the improvement of chemical processes through the application of green chemistry concepts.

Experimental procedures

Molecular dynamics simulations

To identify the most suitable regions for structural modifications in the L3-35A enzyme, we ran 100 ns MD simulations following previously adopted protocols[23,27,30]. Specifically, we used the AMBER19SB force field[31] for protein, water (TIP3P) and ions, while we used the general amber force field (GAFF)[32] for modeling the FAD cofactor. We solvated the molecular model with a 15 Å pad of TIP3P water and we introduced counter ions to neutralize the system charge, resulting in a final simulation box of ≈ 50.000 atoms. Hydrogen mass repartitioning was applied to allow a time step of 4 fs[33]. The system was subjected to 1000 energy minimization steps and it was equilibrated for 100 ps at a pressure of 1 atm and at a temperature of 300 K with NAMD software[34], using a non-bonded cut-off of 12 Å, rigid bonds and particle-mesh Ewald long-range electrostatics. During the equilibration simulation, the Cα atoms of the protein were restrained by a 10 kcal mol^{-1} $Å^{-2}$ spring constant. The 100 ns production runs were performed using a NVT ensemble whereby all the parameters (non-bonded cut-off, and PME) were the same as in the equilibration phase. Root mean square deviations (RMSD) were monitored after each MD run to assess structural convergence, while root mean square fluctuations (RMSF) were calculated to identify unstable regions for subsequent design. The tunnel dimension was analyzed with CAVER 3.0.3 software[35] using a probe radius of 1.4 Å, a shell depth of 5 Å, and a shell radius of 2 Å.

Design and selection of stabilizing mutations

The identification of stabilizing mutations was performed using five different tools. The design focused on the most unstable region of the enzyme as identified in the previous step, with the exclusion of the catalytic amino acids, the amino acids interacting with the FAD cofactor, and the residues lining the tunnel. The first design was performed using the Rosetta Supercharge tool[36]. This tool was employed to reengineer the protein surface with amino acids that present a high net charge, which is reported to prevent aggregation of partially unfolded states. The second design was performed using the Rosetta Point Mutant "pmut" scan application[37], which helped to identify stabilizing single point mutations. In the third approach, the *pmut* tool was used to identify stabilizing double point mutations, where only pair of residues that are close enough to interact with each other are tested (i.e., the distance of at least one of their atoms being closer than 4.5 Å). In the fourth approach, the PROSS web server[38] was used to generate 9 different enzyme designs with an incremental number of mutations. Disulfide bond engineering was performed by employing the disulfide-by-design web server[39]. For each of the 5 design strategies, the best 20 enzyme variants based on the internal scoring were retained (except for PROSS design, where all 9 variants were retained, and for disulfide design, where 8 variants were retained) for further analysis with MD simulations. Overall, library generation and ranking using the five different methods resulted in the selection of 77 different enzyme variants. Each model was simulated for 100 ns, as described for the reference L3-35A enzyme, and the best 6 variants in terms of RMSF stabilization[27,30] were selected for experimental validation.

Protein expression and purification

The DNA sequences of the different FPOX variants were cloned in either pET15(b) or pET17(b) expression vectors (Novagen), to generate C-terminal 6His-tagged proteins. Reference 5T1E and L3_35 DNA constructs, as well as the D02 and the C16 variants, were transformed and expressed in E. coli BL21 Star (DE3) cells (Invitrogen). Variants featuring cysteine mutations to allow disulfide bond formation (X02A, X04, X07, X02B, X02C) were transformed in SHuffle T7 E. coli cells (New England Biolabs). For each variant, 20 mL of an overnight culture was inoculated into 2L of Luria–Bertani (LB) broth supplemented with 100 mg/L ampicillin and grown at 37 °C until $OD_{600} = 0.6$. Protein expression was inducted using isopropyl 1-thio-β-ᴅ-galactopyranoside (IPTG) at a final concentration of either 0.4 mM or 0.1 mM, followed by overnight culture at either 25 °C or 18 °C respectively, with shacking speed of 220 rpm. Cells were collected by centrifugation and resuspended in lysis buffer (50 mM Tris-HCl pH 7.4, 150 mM NaCl, 0.5 mM FAD, and 5% glycerol), supplemented with 0.2 mM protease phenylmethylsulfonyl fluoride (PMSF) and DNAse and then lysed by sonication on ice. After centrifugation, the soluble fraction of the cell lysate was passed through a 0.45-micron filter and then loaded onto a HisTrap HP 5 mL (GE Healthcare) column equilibrated with buffer A (50 mM Tris-HCl pH 7.4, 150 mM NaCl, 5% glycerol, 20 mM imidazole). The Ni affinity column was washed using ten column volumes of buffer A, then the bound C-terminal His-tagged enzyme was eluted with the same buffer supplemented with 400 mM imidazole. The eluted fraction was loaded onto a Hiprep 26/60 Sephacryl S-100 size exclusion column (GE Healthcare) pre-equilibrated with buffer C (50 mM Tris-HCl pH 7.4, 150 mM NaCl, 5% glycerol). The desired protein was concentrated using an Amicon 20 centrifugal filter with a molecular cutoff of 10 KDa to ≈ 2 mg/mL, and stored at − 80 °C. Protein concentration was assessed using a NanoDrop (Thermo Scientific). Sample purity was evaluated by 12% SDS-PAGE.

Protein crystallization

Crystals of different mutants (D02, X02A, X04, X07, X02B) were grown at room temperature using the vapor diffusion method by mixing a 2 µL drop of a 10–15 mg/mL protein sample with a 2 µL drop of a solution containing 0.1 M MES monohydrate pH 6.5, 16–26% of different Polyethylene glycol (PEG) including 20 K (for D02, X02A and X02B) and 8 K (for X04). Crystals, which appeared after 1–4 days, were frozen using 25% (v/v) glycerol as cryoprotectant prior to X-ray diffraction data collection.

Data collection and processing

For the FPOX D02 crystals, diffraction data were collected using a Dectris PILATUS3 6 M detector and a radiation of $\lambda = 0.918$ Å on Bessy beamline 14.1 of the Deutsches Elektronen- Synchrotron (BESY II Light Source), Berlin, Germany. Reflection-image processing was performed using DIALS[40] and AIMLESS[41] from the CCP4 suite[42]. For FPOX X02A and X04, X-ray diffraction data were collected using radiation of $\lambda = 1.0$ Å and a PSI PILATUS 6 M detector on the X06DA beamline at Swiss Light Source (SLS). Data was processed using autoproc. For X02B, diffraction data were collected using a DECTRIS EIGER2 XE 16 M detector and a radiation of $\lambda = 0.9537$ Å on the I04 beamline at Diamond Light Source (Oxfordshire, United Kingdom). Data was processed using the autoproc package. Data collection and refinement statistics are shown in Table 5.

	D02	X02A	X02B	X04
PDB code	8BLZ	8BLX	8BJY	8BMU
Wavelength (Å)	0.918	1.000	0.9537	1.000
Space group	C 2 2 2$_1$	C 2 2 2$_1$	P 2$_1$ 2$_1$ 2$_1$	P 4$_2$ 2$_1$ 2
Unit cell (Å)	a = 91.10, b = 129.49, c = 86.78	a = 90.52, b = 130.26, c = 87.62	a = 63.11, b = 88.49, c = 90.94	a = 90.24, b = 90.24, c = 131.44
Resolution range (Å)	64.75–1.70 (1.73–1.70)	56.68–1.71 (1.74–1.71)	63.42–1.48 (1.50–1.48)	74.39–1.645 (1.673–1.645)
Total reflections	707,191 (38,534)	641,243 (29,830)	1,053,583 (48,251)	1,012,704 (25,719)
Unique reflections	55,830 (2946)	55,592 (2685)	82,805 (4255)	62,950 (2416)
Multiplicity	12.70 (13.10)	11.5 (11.10)	12.7 (11.3)	16.1 (10.6)
Completeness (%)	98.70 (99.30)	98.9 (96.5)	96.0 (100.0)	94.7 (74.1)
mean(I)/sig(I)	12.60 (2.20)	12.7 (1.0)	16.7 (0.4)	20.5 (1.1)
Wilson B-factor	12.08	21.4	27.04	11.12
Rmerge	0.17 (1.40)	0.152 (2.416)	0.067 (4.526)	0.106 (2.013)
Rmeas	0.17 (1.45)	0.159 (2.532)	0.070 (4.743)	0.110 (2.104)
Rpim	0.05 (0.39)	0.046 (0.743)	0.020 (1.406)	0.026 (0.589)
CC1/2 (%)	1.00 (0.75)	0.998 (0.461)	1.000 (0.419)	0.999 (0.458)
Reflections in refinement	55,772 (3879)	55,537 (5360)	80,561 (7099)	60,833 (939)
Reflections in free set	2729 (209)	2755 (264)	3995 (332)	3043 (44)
Rwork	0.177	0.1812	0.19	0.1766
Rfree	0.199	0.2103	0.215	0.2009
RMSD bonds (Å)	0.0144	0.011	0.012	0.012
RMSD angles (Å)	2.214	1.74	1.75	1.84
Ramachandran favoured (%)	97.2	95.74	96.71	95.52
Ramachandran allowed (%)	2.8	3.78	3.06	4.01
Ramachandran outliers (%)	0	0.47	0.24	0.47
Rotamer outliers (%)	1.1	3.68	0.85	2.53
Clash score	1.2	5.38	4.28	6.23
Overall number of atoms (non-H)	3745	3788	3758	3917
In macromolecules	3350	3354	3364	3376
In ligands	99	119	65	113
In solvent	296	315	329	428
Average B-factor (Å^2)	21.7	30.07	30.39	22.03
For macromolecules	21	29.46	29.53	20.32
For ligands	23.9	37.65	32.17	34.43
For solvent	28.3	33.68	38.91	32.23

Table 5. Diffraction data collection and refinement statistics. Statistics for the highest-resolution shell are shown in parentheses.

Structure determination and refinement

For all four structures, the initial phases were obtained by molecular replacement using Phaser[43] and the atomic coordinates of the L3-35A FPOX mutant (PDB code 6Y4J[27]) as a search model. Refinement was performed by alternating rounds of REFMAC5[44] and manual adjustments in Coot[42]. Water molecules were added both manually and automatically using the Coot_refine tool from the CCP4 cloud package[45].

Thermal shift assay

The melting temperature of each variant was measured using differential scanning fluorimetry (DSF) with Sypro-Orange dye (TermoFisher Scientific) on an Applied Biosystems 7500 Real-Time PCR system (TermoFisher Scientific). For each mutant, 12.5 μL of enzyme at the starting concentration of 10 μM was added to 12.5 μL of a 10× Sypro-Orange dye solution diluted from a 5000× stock in the same buffer that was used for the protein: 50 mM Tris-HCl pH 7.4, 150 mM NaCl, 5% glycerol) to reach the final volume of 25 μL, a 5× final concentration of the dye and a 5 μM concentration of the enzyme. All the Tm measurements were performed in 4 replicates. Fluorescence was monitored during the thermal denaturation occurring to the protein upon increasing the temperature from 15 to 95.3 °C.

Circular dichroism

Circular dichroism (CD) measurements were performed on a Jasco J-1500 spectrophotometer at 20 °C. CD was performed to detect the secondary structure of different variants and to measure the thermostability of the enzyme. The spectra were the average of five scans, recorded using a 1.0 mm path length quartz cuvette on 5 μM samples of the different FPOX variants in a 50 mM Tris pH 8.0, 150 mM NaCl, 5% glycerol buffer solution. The thermal denaturation curves were measured in 1.0 mm path length cuvettes closed with a parafilm on 5 μM samples. The increasing temperature-induced denaturation at a rate of 1 °C/min from 5 to 95 °C and the ellipticity at 222 nm were recorded at 0.2 °C intervals using a 1-nm bandwidth and a response of 10 s. Using the Boltzmann function, the midpoints of the thermal-denaturation curves (T_m) were determined by fitting the data to a sigmoidal transition curve. The secondary structure of different variants was measured at 200–250 nm wavelengths at 20 °C. Mean residue ellipticity [θ]MR was calculated and plotted versus wavelength. Each spectrum was determined as the average of three scans. The CD spectra of all the enzymes described here are shown in Figs. S1–S7 in the Supplementary Information.

Enzymatic activity

The enzymatic activity of all variants was assessed at room temperature by measuring the amount of glucosone released from the substrate over time, as described previously[27]. The increase in absorbance at 322 nm (glucosone $\varepsilon_{322} = 149.25\ M^{-1}\ cm^{-1}$) was monitored in an Infinite M1000 (Tecan) at 25 °C. The 200 μL reaction mixture contained 20 mM Tris HCl pH 7.4, 20 mM o-phenylenediamine, 2 mM fructosyl-lysine, or fructosyl-valine or dipeptide (fructosyl-valine histidine) or hexapeptide (1-Deoxyfructosyl-Val-His-Leu-Thr-Pro-Glu) as a substrate. After 1 min of pre-incubation, the reaction was started by adding the enzyme at a final concentration of 0.04–1 mg/mL depending on the activity of the variant. One unit (U) is defined as the amount of enzyme required to produce 1 μmol of glucosone per minute, and specific activity is expressed as U/mg of the enzyme. Enzyme kinetic constants (Vmax, Km, kcat and kcat/Km) were determined using different substrate concentration in the assay (fructosyl-valine from 0.05 to 10 mM, fructosyl hexapeptide from 0.05 to 1 mM). Data points are the result of two independent experiments and the estimation of Micheaelis-Menten parameters was derived by Lineweaver-Burk plot fitting.

Data availability

The final crystallographic coordinates of the crystal structures shown here are available in the RCSB PDB (accession codes: 8BJY, 8BLZ, 8BLX, 8BMU).

Received: 13 July 2023; Accepted: 19 October 2023

References

1. Miura, S., Ferri, S., Tsugawa, W., Kim, S. & Sode, K. Development of fructosyl amine oxidase specific to fructosyl valine by site-directed mutagenesis. *Protein Eng. Des. Sel.* **21**, 233–239 (2008).
2. Kim, S., Miura, S., Ferri, S., Tsugawa, W. & Sode, K. Cumulative effect of amino acid substitution for the development of fructosyl valine-specific fructosyl amine oxidase. *Enzyme Microb. Technol.* **44**, 52–56 (2009).
3. Miura, S., Ferri, S., Tsugawa, W., Kim, S. & Sode, K. Active site analysis of fructosyl amine oxidase using homology modeling and site-directed mutagenesis. *Biotechnol. Lett.* **28**, 1895–1900 (2006).
4. Collard, F. *et al.* Crystal structure of the deglycating enzyme fructosamine oxidase (amadoriase II). *J. Biol. Chem.* **283**, 27007–27016 (2008).
5. Hatada, M. *et al.* Development of a screen-printed carbon electrode based disposable enzyme sensor strip for the measurement of glycated albumin. *Biosens. Bioelectron.* **88**, 167–173 (2017).
6. Ferri, S., Miyamoto, Y., Sakaguchi-Mikami, A., Tsugawa, W. & Sode, K. Engineering fructosyl peptide oxidase to improve activity toward the fructosyl hexapeptide standard for HbA1c measurement. *Mol. Biotechnol.* **54**, 939–943 (2013).
7. Takahashi, M., Pischetsrieder, M. & Monnier, V. M. Isolation, purification, and characterization of amadoriase isoenzymes (fructosyl amine-oxygen oxidoreductase EC 1.5.3) from *Aspergillus* sp. *J. Biol. Chem.* **272**, 3437–3443 (1997).
8. Ferri, S., Kim, S., Tsugawa, W. & Sode, K. Review of fructosyl amino acid oxidase engineering research: A glimpse into the future of hemoglobin A1c biosensing. *J. Diabetes Sci. Technol.* **3**, 585–592 (2009).
9. Lin, Z. & Zheng, J. Occurrence, characteristics, and applications of fructosyl amine oxidases (amadoriases). *Appl. Microbiol. Biotechnol.* **86**, 1613–1619 (2010).
10. Wu, X., Palfey, B. A., Mossine, V. V. & Monnier, V. M. Kinetic studies, mechanism, and substrate specificity of amadoriase I from *Aspergillus* sp. *Biochemistry* **40**, 12886–12895 (2001).
11. Gan, W. *et al.* Structural basis of the substrate specificity of the FPOD/FAOD family revealed by fructosyl peptide oxidase from *Eupenicillium terrenum*. *Acta Crystallogr. Sect. F Struct. Biol. Commun.* **71**, 381–387 (2015).
12. Rigoldi, F. *et al.* Molecular dynamics simulations provide insights into the substrate specificity of FAOX family members. *Mol. BioSyst.* **12**, 2622–2633 (2016).
13. Monnier, V. M. & Wu, X. Enzymatic deglycation with amadoriase enzymes from *Aspergillus* sp. as a potential strategy against the complications of diabetes and aging. *Biochem. Soc. Trans.* **31**, 1349–1353 (2003).
14. Paul, R. G. & Bailey, A. J. Glycation of collagen: The basis of its central role in the late complications of ageing and diabetes. *Int. J. Biochem. Cell Biol.* **28**, 1297–1310 (1996).
15. Sell, D. R. & Monnier, V. M. Molecular basis of arterial stiffening: Role of glycation—A mini-review. *Gerontology* **58**, 227–237 (2012).
16. Goh, S. Y. & Cooper, M. E. Clinical review: The role of advanced glycation end products in progression and complications of diabetes. *J. Clin. Endocrinol. Metab.* **93**, 1143–1152 (2008).
17. Nagaraj, R. H., Linetsky, M. & Stitt, A. W. The pathogenic role of Maillard reaction in the aging eye. *Amino Acids* **42**, 1205–1220 (2012).
18. Vincent, A. M., Russell, J. W., Low, P. & Feldman, E. L. Oxidative stress in the pathogenesis of diabetic neuropathy. *Endocr. Rev.* **25**, 612–628 (2004).
19. Gautieri, A., Redaelli, A., Buehler, M. J. & Vesentini, S. Age- and diabetes-related nonenzymatic crosslinks in collagen fibrils: Candidate amino acids involved in advanced glycation end-products. *Matrix Biol.* **34**, 89–95 (2014).
20. Snedeker, J. G. & Gautieri, A. The role of collagen crosslinks in ageing and diabetes—The good, the bad, and the ugly. *Muscles Ligaments Tendons J.* **4**, 303–308 (2014).
21. Capuano, E. *et al.* Studies on the effect of Amadoriase from *Aspergillus fumigatus* on peptide and protein glycation in vitro. *J. Agric. Food Chem.* **55**, 4189–4195 (2007).
22. Qian, Y., Zheng, J. & Lin, Z. Loop engineering of amadoriase II and mutational cooperativity. *Appl. Microbiol. Biotechnol.* **97**, 8599–8607 (2013).

23. Rigoldi, F. *et al.* Crystal structure of the deglycating enzyme Amadoriase I in its free form and substrate-bound complex. *Proteins Struct. Funct. Bioinform.* **84**, 744–758 (2016).
24. Ogawa, N. *et al.* Creation of haemoglobin A1c direct oxidase from fructosyl peptide oxidase by combined structure-based site specific mutagenesis and random mutagenesis. *Sci. Rep.* **9**, 942 (2019).
25. Kokkonen, P., Bednar, D., Pinto, G., Prokop, Z. & Damborsky, J. Engineering enzyme access tunnels. *Biotechnol. Adv.* **37**, 107386 (2019).
26. Gautieri, A., Rigoldi, F., Torretta, A., Redaelli, A. & Parisini, E. In silico engineering of enzyme access tunnels. *Methods Mol. Biol.* **2397**, 203–225 (2022).
27. Rigoldi, F. *et al.* Rational backbone redesign of a fructosyl peptide oxidase to widen its active site access tunnel. *Biotechnol. Bioeng.* https://doi.org/10.1002/bit.27535 (2020).
28. Kaufmann, K. W., Lemmon, G. H., Deluca, S. L., Sheehan, J. H. & Meiler, J. Practically useful: What the Rosetta protein modeling suite can do for you. *Biochemistry* **49**, 2987–2998 (2010).
29. Kim, S., Ferri, S., Tsugawa, W., Mori, K. & Sode, K. Motif-based search for a novel fructosyl peptide oxidase from genome databases. *Biotechnol. Bioeng.* **106**, 358–366 (2010).
30. Rigoldi, F. *et al.* Thermal stabilization of the deglycating enzyme Amadoriase I by rational design. *Sci. Rep.* **8**, 3042 (2018).
31. Tian, C. *et al.* Ff19SB: Amino-acid-specific protein backbone parameters trained against quantum mechanics energy surfaces in solution. *J. Chem. Theory Comput.* **16**, 528–552 (2020).
32. Wang, J. M., Wolf, R. M., Caldwell, J. W., Kollman, P. A. & Case, D. A. Development and testing of a general amber force field. *J. Comput. Chem.* **25**, 1157–1174 (2004).
33. Hopkins, C. W., Le Grand, S., Walker, R. C. & Roitberg, A. E. Long-time-step molecular dynamics through hydrogen mass repartitioning. *J. Chem. Theory Comput.* **11**, 1864–1874 (2015).
34. Humphrey, W. V. M. D. Visual molecular dynamics. *J. Mol. Graph.* **14**, 33–38 (1996).
35. Chovancova, E. *et al.* CAVER 3.0: A tool for the analysis of transport pathways in dynamic protein structures. *PLoS Comput. Biol.* **8**, e1002708 (2012).
36. Der, B. S. *et al.* Alternative computational protocols for supercharging protein surfaces for reversible unfolding and retention of stability. *PLoS ONE* https://doi.org/10.1371/journal.pone.0064363 (2013).
37. Kuhlman, B. *et al.* Design of a novel globular protein fold with atomic-level accuracy. *Science (80-)* **302**, 1364–1368 (2003).
38. Goldenzweig, A. *et al.* Automated structure- and sequence-based design of proteins for high bacterial expression and stability. *Mol. Cell* **63**, 337–346 (2016).
39. Craig, D. B. & Dombkowski, A. A. Disulfide by design 2.0: A web-based tool for disulfide engineering in proteins. *BMC Bioinform.* https://doi.org/10.1186/1471-2105-14-346 (2013).
40. Winter, G. *et al.* DIALS: Implementation and evaluation of a new integration package. *Acta Crystallogr. D Struct. Biol.* **74**, 85–97 (2018).
41. Evans, P. R. & Murshudov, G. N. How good are my data and what is the resolution?. *Acta Crystallogr. D Struct. Biol. Crystallogr.* **69**, 1204–1214 (2013).
42. Winn, M. D. *et al.* Overview of the CCP4 suite and current developments. *Acta Crystallogr. Sect. D Biol. Crystallogr.* **67**, 235–242 (2011).
43. McCoy, A. J. *et al.* Phaser crystallographic software. *J. Appl. Crystallogr.* https://doi.org/10.1107/S0021889807021206 (2007).
44. Murshudov, G. N. *et al.* REFMAC5 for the refinement of macromolecular crystal structures. *Acta Crystallogr. Sect. D Biol. Crystallogr.* **67**, 355–367 (2011).
45. Kovalevskiy, O., Lebedev, A. & Krissinel, E. Helping researchers to solve their structures: automation and user guidance in CCP4 Cloud. *Acta Crystallogr. Sect. A Found. Adv.* **77**, C766–C766 (2021).

Author contributions

Conceptualization: E.P., A.G.; methodology: H.E., J.A.R.B., R.C., E.P., A.G.; formal analysis: H.E., S.B., J.A.R.B., L.L., G.C., A.R.; investigation: H.E., S.B., J.A.R.B., L.L., G.C., A.R.; resources: R.C., E.P., A.G.; data curation: H.E., J.A.R.B., R.C., E.P., A.G.; writing, review and editing: H.E., S.B., J.A.R.B., R.C., L.L., G.C., A.R., E.P., A.G.; supervision: H.E., R.C., E.P., A.G.; funding acquisition: E.P., A.G. All authors have read and agreed to the published version of the manuscript.

Funding

The authors wish to thank the personnel of the Swiss Light Source (Proposal Number 20220753), the Diamond Light Source (proposal number mx32544) and the BESY II Light Source (proposal number MX-202-00211-ST) for help with the data collection. E.P. thanks the ERDF project BioDrug (No. 1.1.1.5/19/A/004) and the Latvian Council of Science (Grant No. lzp-2020/2-0013) for financial support. We acknowledge the CINECA award under the ISCRA initiative (Grant code IsB26_W2EB and IsCa2_REZYME) for the availability of high-performance computing resources and support.

Competing interests

The authors declare no competing interests.

Additional information

Supplementary Information The online version contains supplementary material available at https://doi.org/10.1038/s41598-023-45428-1.

Correspondence and requests for materials should be addressed to E.P. or A.G.

2. Pielikums
Appendix 2

Carletti, A.; **Bhattacharya, S**.; Pedroni, S.; Berto, M.; Bonettini, R.; Castagna, R.; Parisini, E.; Di Rocco, G.

Functional and Structural Characterization of PETase SM14 from Marine-Sponge *Streptomyces* sp. Active on Polyethylene Terephthalate

ACS Sustainable Chemistry & Engineering, 2025, 13, 7460
doi:10.1021/acssuschemeng.5c00737

Publikācija un tās pielikums pieejams bez maksas izdevēja mājaslapā
The Publication and Supporting Information is available free of charge on the publisher's website

ACS Sustainable Chemistry & Engineering

pubs.acs.org/journal/ascecg

Research Article

Functional and Structural Characterization of PETase SM14 from Marine-Sponge *Streptomyces* sp. Active on Polyethylene Terephthalate

Alan Carletti, Shapla Bhattacharya, Sara Pedroni, Marcello Berto, Riccardo Bonettini, Rossella Castagna, Emilio Parisini, and Giulia Di Rocco*

Cite This: *ACS Sustainable Chem. Eng.* 2025, 13, 7460−7468

Read Online

ACCESS | Metrics & More | Article Recommendations | Supporting Information

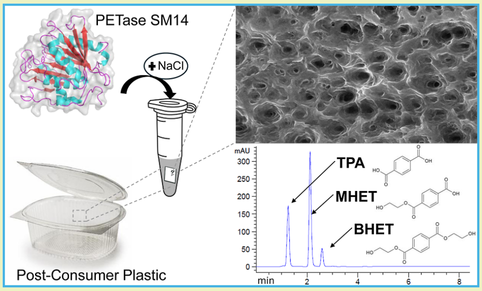

ABSTRACT: The recent discovery of the PETase enzyme family offers a sustainable solution for depolymerizing poly(ethylene terephthalate) (PET), one of the most widespread plastic compounds, under mild conditions. This enables the environmentally beneficial conversion of plastic waste into value-added products. Among this enzyme family, PETase from *Ideonella sakaiensis* has been the most extensively studied. Although other similar enzymes have been discovered, our knowledge about the catalytic and structural properties of this class remains limited. In this study, a PETase-like enzyme (PETase SM14) from *Streptomyces* sp. SM14 was heterologously produced in *Escherichia coli*, and its activity was tested on post-consumer plastic substrates using high-performance liquid chromatography for product quantification as well as scanning electron microscopy and atomic force microscopy for substrate surface imaging evaluation. PETase SM14 exhibited high salt tolerance (1.5 M), good heat resistance (Tm 56.26 °C), and optimal activity at pH 9.0, highlighting its potential for PET waste bioremediation. Furthermore, its X-ray crystal structure was solved at 1.43 Å resolution, revealing conserved features of the PETase family with potential relevance for future engineering applications.

KEYWORDS: *polyethylene terephthalate, PETase, X-ray structure, salt tolerance, plastic waste recovery*

INTRODUCTION

Plastic materials, known for being cost-effective, versatile, and durable, have seen rapid growth in global production, with 8.3 million tons produced between 1950 and 2015.[1,2] However, inadequate recycling and limited circular reuse have resulted in significant waste accumulation, raising serious environmental concerns due to plastics' resistance to natural degradation processes.[3] Polyethylene terephthalate (PET) is widely used, inherently stable, and environmentally persistent.[4] Although PET is technically recyclable, only a small fraction is currently processed through recycling efforts, while a majority of PET waste persists in natural habitats. The global PET market is projected to reach USD 109 billion by 2032, with a significant annual growth rate (9.5%),[5] highlighting an urgent need for sustainable management and recycling solutions, especially in developing countries, where advanced recycling infrastructures and regulatory frameworks are lacking.[6] While traditional PET recycling methods such as thermo-mechanical and chemical processes have been developed,[7] the efficiency remains limited, and there is a pressing demand for alternative approaches. One promising avenue lies in the discovery of microbial enzymes capable of degrading PET. Recent studies have identified enzymes—including members of the hydrolase family—cutinases (EC 3.1.1.74), lipases (EC 3.1.1.3), and carboxylesterases (EC 3.1.1.1/EC 3.1.1.101/EC 3.1.1.2)—that exhibit activity on low-crystallinity, low-density polymers of PET and related compounds. These microbial enzymes show varied structural adaptations that enhance their efficacy under distinct conditions. Bacterial PET-degrading enzymes, such as *Is*PETase,[8] have been categorized into types I and II based on structural characteristics; type II enzymes, in particular, feature modifications like additional disulfide bonds and extended loops near their active sites, enhancing substrate accessibility.[9] Despite over 20 years of research on the enzymatic degradation of PET, microbial enzymes still exhibit relatively low turnover rates, reflecting the unique challenges presented by PET as a non-natural substrate.[10] To date, 119 wild-type PET-active enzymes

Received: January 23, 2025
Revised: May 5, 2025
Accepted: May 6, 2025
Published: May 15, 2025

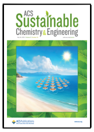

https://doi.org/10.1021/acssuschemeng.5c00737

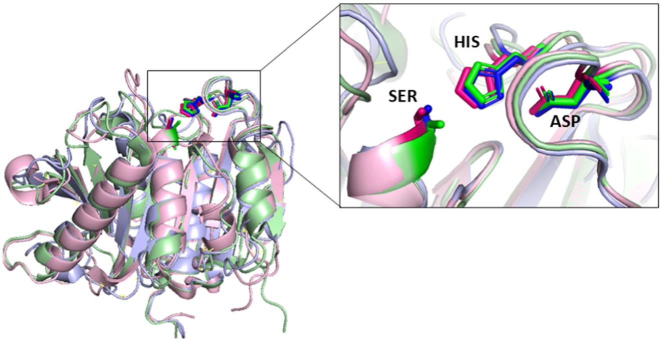

Figure 1. Overall structure comparison of PETase SM14 (light blue), *Is*PETase (PDB code 6ILW, light green), and PE-H from *P. aestusnigri* (PDB code: 6SBN, light pink) performed using PyMOL. The structures are displayed as cartoon models, with the catalytic triad regions highlighted as stick representations in the top right inset. The catalytic triad of PETase SM14 (blue sticks) comprises S156, D202, and H234, while that of *Is*PETase (green sticks) includes S160, D206, and H237 and S171, D217, and H249 for PE-H from *P. aestusnigri* (pink sticks).

have been characterized, with 35 enzymes having their 3D structures resolved.[11] This growing body of knowledge offers a foundation for advancing enzyme-based approaches to PET recycling, holding promise for more sustainable and efficient plastic waste management solutions in the future. In recent years, concerted efforts have been made to characterize each aspect of these enzymes[12−15] and enhance their performance through molecular engineering, which often resulted in the creation of mutants featuring greater thermal stability and increased catalytic properties.[16−19] Another emerging area of interest involves the influence of specific salts on the properties of these enzymes, particularly, their catalytic activity and thermostability. For instance, Ca^{2+} has been shown to alter the tertiary structure of PETases, leading to increased activity and thermal stability.[20,21] Similarly, K^+ and Na^+ ions may exert effects analogous to Ca^{2+}, as evidenced in a recent study.[22] Additionally, Schmidt et al.[23] demonstrated that the activity of the polyester hydrolases LCC and TfCut2 on PET films strongly depends on the type and concentration of the buffer. High initial hydrolysis rates were observed using sodium phosphate buffer concentrations exceeding 0.7 M, emphasizing the role of specific salts in modulating enzyme performance.

In this work, we describe a candidate PETase-like enzyme, SM14 (PETase SM14 hereafter), isolated from the marine-sponge *Streptomyces* sp. SM14.[24] The enzyme was heterologously expressed in *Escherichia coli* to characterize its polyesterase activity. This was confirmed using a PET-based post-consumer plastic (PCP) through liquid chromatography assays (HPLC) and scanning electron microscopy (SEM) analysis. Results revealed that the presence of NaCl was essential for enzymatic catalysis, corroborating the enzyme's halophilic nature and superior salt tolerance compared to *Is*PETase, which exhibits optimal activity at low salt concentrations. Further X-ray crystallographic analysis of PETase SM14 revealed its three-dimensional structure, which was compared to the well-characterized *Is*PETase and with a polyester hydrolase (PE-H) from *Pseudomonas aestusnigri*, another marine bacterium. All three enzymes share conserved motifs, including the serine hydrolase sequence Gly-x1-Ser-x2-Gly and the catalytic triad Ser-Asp-His. These findings enhance our understanding of PETase-like enzymes and their potential applications in PET degradation.

RESULTS AND DISCUSSION

Production of PETase SM14. The protein was expressed in *E. coli* BL21 (DE3) and purified as indicated in the Materials and Methods section. The procedure led to the production of 162 mg of pure protein from 4.5 g of cellular pellet, resulting in a yield of 3.6%. The identity of the protein was confirmed by peptide-mass fingerprinting. Using the MASCOT search database, the detected peptide sequences were compared against all sequences stored in an in-house database as well as the SwissProt database. This analysis revealed a match with the mature form of PETase SM14. Notably, the sample achieved a 95% sequence coverage (Figure S1). Circular dichroism (CD) data (Figure S2) confirm proper protein folding and align with the structure determined by X-ray crystallography. The melting temperature (Tm) of the enzyme was determined to be 56.26 °C (Figure S2) by CD spectroscopy. To evaluate the enzyme's stability at varying pH values and NaCl concentrations, its melting temperature (Tm) was determined using a thermal shift assay across a pH range of 6.0−9.0 with NaCl concentrations from 100 to 700 mM (Table S1). Changes in buffer pH had a minimal impact on Tm, which remained relatively constant. Increasing the salt concentration up to 700 mM in buffer Tris pH 8.0 did not result in unfolding of the protein, as shown by the non-decreasing Tm [°C]. This finding confirms the enzyme's stability at higher salt concentrations (Figure S3).

Structural Features. The X-ray structure of PETase SM14 (UniProt ID: A0A679PDB4) validated the accuracy of the predicted AlphaFold structure, exhibiting a high structural identity with a root-mean-square deviation (RMSD) of 0.278 Å. Notably, this extends to the loop regions, where the catalytic site is located. *Is*PETase, a well-known enzyme active on PET,[15,25] has been extensively characterized.[14,26] In this study, *Is*PETase and a polyester hydrolase (PE-H) identified in the genome of the marine hydrocarbonoclastic bacterium *P. aestusnigri*[27] were employed for comparative structural analysis of PETase SM14. Structural alignment of the three enzymes shows a high degree of similarity, with an RMSD of 0.691 Å across 190 $C\alpha$ atoms for *Is*PETase and an RMSD of 0.81 Å over 195 $C\alpha$ atoms for PE-H including the catalytic triad within the active site pocket (Figure 1). This indicates that these enzymes degrade PET through the same catalytic mechanism. The serine-hydrolase mechanism involves three conserved residues: serine, histidine, and

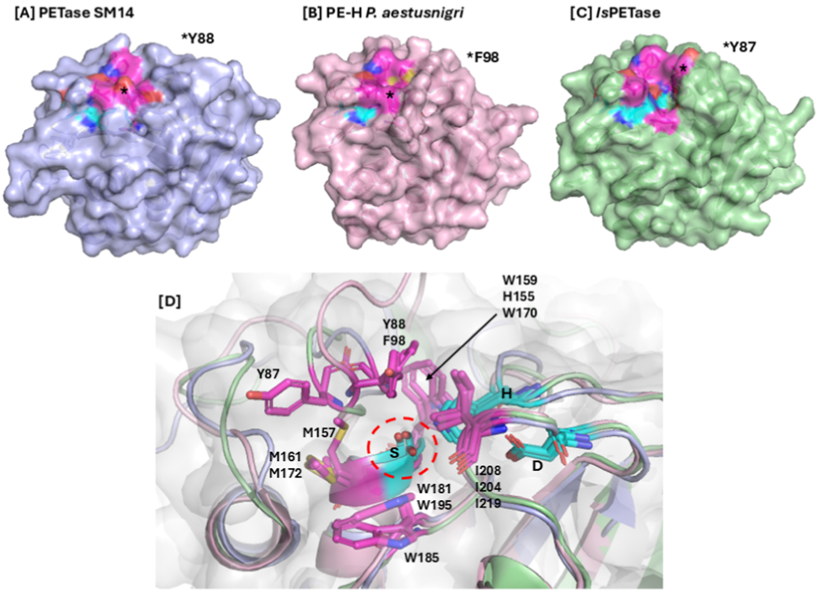

Figure 2. Surface representations of PETase SM14 (A), PE-H (B), and *Is*PETase (C) highlight the catalytic triad (light blue) and the putative binding site (violet). (D) Magnified view of the active site after structural alignment (cartoon model), showing the catalytic triad as light blue sticks (S156−D202−H234 of PETase SM14, S171−D217−H249 of PE-H, and S160−D206−H237 of *Is*PETase) and the putative binding site as violet sticks (Y88−H155−M157−W181−I204 of PETase SM14, F98−W170−M172−W195−I219 of PE-H, and Y87−W159−M161−W185−I208 of *Is*PETase).

aspartate, which retain their positions and orientation within the structures of the two enzymes.

The electrostatic surface potentials of PETase SM14, *Is*PETase, and PE-H are shown in Figure S4. *Is*PETase features a highly polarized surface charge, resulting in an isoelectric point (pI) of 9.41, whereas PETase SM14 and PE-H have a theoretical pI of 6.67 and 6.54, respectively (as determined by the ExPASy, ProtParam tool), and both exhibit a less polarized and more delocalized surface charge. This variation in surface charges seems to affect also the active site pocket; PETase SM14 and PE-H show a slightly negative potential around the active site (red regions in Figure S4A,B), in contrast with the more positively charged pocket in *Is*PETase (Figure S4C).

The three structures primarily differ in five loop regions. While the catalytic residues align across all three, the catalytic pocket appears more closed in PE-H and SM14 compared to that in *Is*PETase. In *Is*PETase, Y87 is positioned farther from the catalytic residues, creating a more open catalytic pocket. Additionally, in the PE-H enzyme, the P96-G97-F98-V99-S99-A100-E101 sequence forms an elongated and flexible loop, which may hinder substrate interaction with the catalytic residues, potentially contributing to lower activity. The catalytic site of *Is*PETase is surrounded by conserved hydrophobic residues involved in substrate binding, including Y87, W159, M161, W185, and I208[14] (Figure 2D). Structural alignment enabled the identification of the corresponding residues of PETase SM14 and PE-H, which have a nearly identical arrangement: Y88, H155, M157, W181, I204 and F98, W170, M172, W195, and I219 (Figure 2D). Hence, the catalytic site of the three enzymes exhibits a similar spatial arrangement of the aromatic and apolar residues involved in substrate binding, although some differences are present. For instance, Y88 and F98 in PETase SM14 and PE-H, respectively, are positioned in such a way that the catalytic pocket appears to be more closed (Figure 2A,B). In contrast, *Is*PETase Y87 is closer to M161, creating a more open catalytic pocket (Figure 2C). A second notable difference lies in the conserved serine-hydrolase motif Gly-x1-Ser-x2-Gly motif. In *Is*PETase, this motif consists of G158-W159-S160-M161-G162 located at the active site, typical of other enzymes in the α/β hydrolase family.[26] In PETase SM14, however, the motif includes a histidine (H155), instead of a tryptophan (W159), which is commonly found in *Is*PETase and related hydrolases,[14,25,26] also in PE-H (W170). Despite this substitution, the overall spatial arrangement remains analogous for both enzymes, preserving their functional capabilities.

Catalytic Activity. PETase SM14 successfully degraded PCP samples, confirming the enzyme's active form. Calibration curves of the HPLC assay method for terephthalic acid (TPA) and bis(2-hydroxyethyl) terephthalate (BHET) were created by using standard solutions. The relative standard deviation was calculated for three repeated runs, resulting in a good linear relationship with r^2 = 0.994 for TPA and r^2 = 0.982 for BHET (Figure S5). These linear regression parameters were then utilized to quantify all of the samples.

Temperature and pH Dependence. The pH dependence of enzymatic activity was analyzed across a range of pH values from 6.0 to 9.0, without added salt. After 72 h of incubation, the products were analyzed using reversed-phase high-performance liquid chromatography (HPLC). The results (Figure 3) show that the TPA production is strongly pH-dependent, with a 10-fold increase in TPA production at pH 9.0 compared to pH 7.0 (≅0.02 mM TPA at pH 7.0 versus ≅0.2 mM at pH 9.0). The

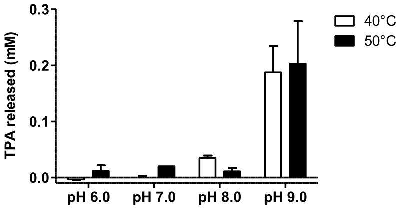

Figure 3. TPA production resulting from enzymatic degradation of PCP at different pH values (6.0, 7.0, 8.0, and 9.0) and temperatures (40 °C (white), 50 °C (black)) after 72 h. The black bars represent the data collected at 50 °C, while the white bars describe the data at 40 °C. The error bars show the standard deviation of the dataset relative to the mean.

highest concentration of released TPA was 0.187 mM at pH 9.0 and 40 °C (Figure 3), consistent with findings for *Is*PETase produced in the chloroplasts of *Chlamydomonas reinhardtii*,[28] which released TPA at a concentration of 0.191 mM under the same conditions (data not shown). The reactions conducted without the enzyme or substrate yielded negligible amounts of TPA in all measurements, confirming that PETase SM14 is responsible for product formation. The pH values of the reaction solutions remained unchanged throughout the entire reaction time.

Two temperatures, 50 °C and 40 °C, were tested, yielding very similar data. The optimal pH 9.0 is independent of the temperature, as the TPA released at pH 9.0 is consistent at the two temperatures (Figure 3). The glass transition temperature (Tg) of PET, defined as the temperature at which the polymer chain gain enhanced mobility, is approximately 80 °C. However, during the enzymatic hydrolysis, the Tg value of PET decreases to about 65 °C due to water molecules infiltrating the polymer chains.[29] While *Is*PETase activity naturally decreases above 40 °C,[30] PETase SM14 maintained structural stability up to 50 °C (Figure S2). The similar enzyme behavior at both temperatures suggests that under these reaction conditions, temperature has little effect on activity.

Within the residues of the canonical Ser-His-Asp triad, aspartate is negatively charged, while histidine and serine are partially ionized during catalysis. Notably, histidine must accept a proton from serine, creating a catalytic environment with a neutral or slightly basic optimal pH. However, the ideal pH depends on the electrostatic environment and on the structure of the active site in the presence of the substrate.[14,31,32] Variations of the pH of the medium result in changes in the ionic state of the active site, impacting the reaction mechanism and, consequently, TPA production.[33] For instance, histidine

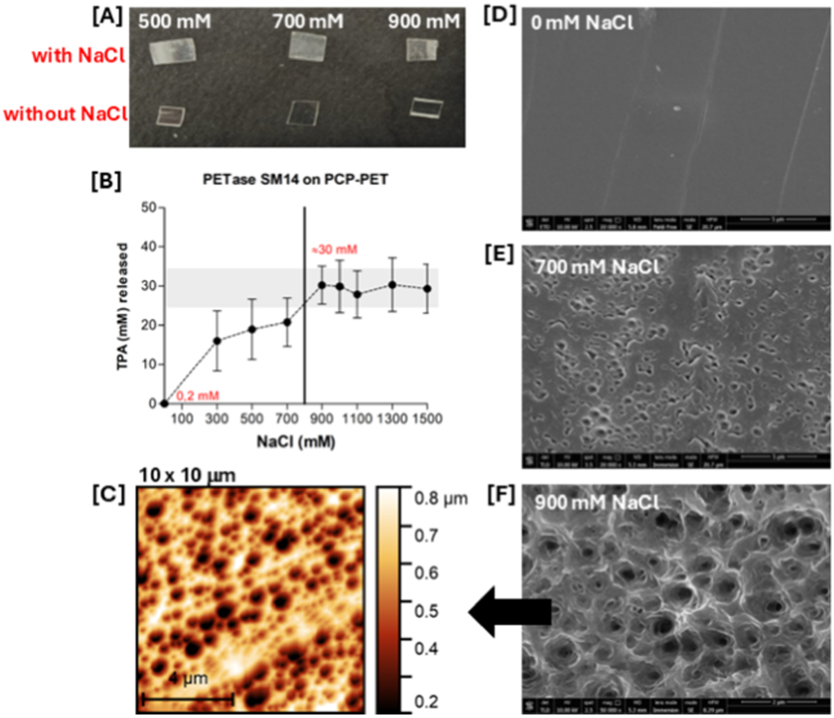

Figure 4. (A) Post-consumer plastic (PCP) pieces after one-week incubation with PETase under varying salinity conditions. (B) TPA release profile depending on salt concentration. Product release over 1 week (168 h) of incubation with PETase SM14 (1 μM) on PET PCP in 100 mM Tris−HCl buffer, pH 9.0, 40 °C, with sodium chloride concentrations ranging from 0 to 1500 mM. Quantification ($n = 4$) was done using the TPA standard curve. (C) AFM topographical images (10 μm × 10 μm) of PCP sample incubated with PETase SM14 and 0.9 M NaCl. (D−F) SEM micrographs of the PET PCP piece without salts (D), with 700 mM NaCl (E) and with 900 mM NaCl (F). All experiments were conducted in triplicate.

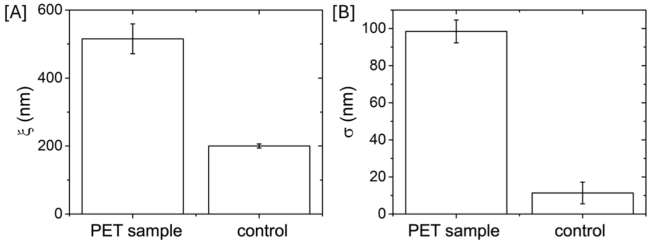

Figure 5. Morphological parameters extracted from AFM analysis. (A) Variation in correlation length (ξ) and (B) variation in roughness (σ_{rms}) between PET samples incubated with PETase SM14 and those incubated in the control solution, i.e., in the absence of the enzyme (Figure S6). Standard deviations, calculated from four images of each sample, are reported as errors bars.

residues contain one or two nitrogen-bonded proton(s) in their imidazole ring with a theoretical pKa of 6.5. However, studies have determined pKa ranging from 4.7 (or even 4) to 7.5, depending on the presence of positively charged residues within the LCC esterase cavity.[34,35] Another study calculated a pKa ≈ 10 due to the formation of a negatively charged complex.[34] Overall, achieving the best reaction conditions at basic pH appears to be a common feature of serine esterases.[33,36] Furthermore, the hydrophilicity of PET is accelerated by the partial alkaline hydrolysis reaction, which influences the mechanism and the dissolution rate of the reaction products, leading to the degradation of the PET outer surface.[37]

NaCl Dependence. The effect of environmental conditions on the PET-hydrolyzing activity of wild-type PETase SM14 was evaluated under halophilic conditions by supplementing sodium chloride in the reaction mixture (300−1500 mM). Figure 4 summarizes the results for all of the experiments conducted in the presence of NaCl at pH 9.0. Additional measurements at salt concentrations of 700 and 900 mM were performed at pH 5.0, 6.0, and 7.0; however, TPA release was negligible in all cases (data not shown). These findings indicate that a significant increase in enzyme activity due to salt concentration occurs only at pH 9.0. The concentration of TPA released as a function of salt addition is shown in Figure 4B. A notable increase in product formation is observed in the presence of salt, exceeding a 100-fold increase compared with the data obtained without salt (TPA released: 0.2 mM). From the graph in Figure 4B, two key transitions can be observed: the first one at the initial increase from no salt to a 300 mM solution and the second one between 700 and 900 mM. Thereafter, stabilization occurs, with product release remaining consistent at approximately 30 mM, even at higher salt concentrations. The PCP used in these experiments is PET-made of food packaging. The polymer matrix of this material is less homogeneous than that of a pure PET film and may exhibit regions of varied crystallinity. This contributes to the slight variability of the results, as indicated by the error bars representing the standard deviation in Figure 4B, even after four replicate analyses under the same conditions. Nevertheless, 900 mM NaCl clearly emerges as the optimal concentration for this enzyme. Morphological changes on the surfaces of PCP fragments, as examined by SEM (Figure 4D−F) after incubation with the enzyme, further confirm that 900 mM NaCl is the most effective concentration for PET degradation. The results of semi-contact atomic force microscopy (AFM) imaging in air are reported in Figure 4C, showing the effects of the protein on the morphology of the PCP sample. In particular, the samples incubated with the protein exhibit a dense network of holes on their surfaces, whereas no such features are present on the surface of the control sample (Figure S6). From AFM analysis, two parameters related to enzyme activity can be extracted: the average surface roughness of the samples σ_{rms} and the lateral correlation length ξ [Figure 5].[28,38,39] The average values of ξ were obtained from four images of each sample. The variation in ξ, which estimates the average dimensions of the holes on the surface, can be ascribed solely to the activity of the enzyme as no other sources of degradation were present during the experimental procedure. In the control sample, ξ is related to the microscopic structure of the polymeric film. PET film samples showed a two-fold increase in ξ, from 200 ± 9 nm (control sample) to 515 ± 44 nm (after enzyme incubation) (Figure 5A). Also, σ_{rms} significantly increased from 11 ± 6 nm in the control sample to 98 ± 6 nm following the protein activity (Figure 5B). Also in this case, the increase in σ_{rms} correlates with the presence of holes in the samples incubated with the enzyme. AFM analysis further allowed for the calculation of the average depth of the holes, which was determined to be approximately 340 ± 110 nm.

Several factors influence polymer biodegradation rates, including crystallinity, chemical properties, and molecular weight (MW). PET polymers have a crystallinity of 30−50%, an average MW of 25,000, and are hydrophobic due to chain packing,[40] even though PET's backbone contains ester bonds and polar functionalities such as carboxyl and hydroxyl groups that provide polarity to the polymer. The numerous benzene rings in the PET chain produce $\pi-\pi$ interactions that enhance dipole connections and encourage the polymer's crystalline organization by orienting the rings.[41] Positive and negative dipoles also play an essential role in electrostatic interactions between adjacent chains. The interaction between PETase and the dipoles on the PET's surfaces may be facilitated by a series of cationic or anionic residues on the enzyme's surface. These residues are known to establish extensive Coulombic interactions with the ligand's polar groups. However, ion-pair formation weakens at high salt concentrations due to increased overall entropy, which may contribute to the enhanced catalytic activity of PETase SM14 on PET despite these coulombic interactions.[42] Furthermore, because it belongs to the marine environment, this microbial hydrolase may exhibit enhanced enzymatic activity in ocean-like conditions. This observation aligns with studies suggesting that salt concentrations (0−1500 mM NaCl) increase PETase activity.[43] One possible explanation involves the loops in the active site where substrate-interacting residues are arranged. The high ionic force caused by dissolved salts may induce structural changes in this region, altering the spatial arrangement of the ester bond. This reorientation could bring the ester bond closer to the catalytic triad or change its orientation, thereby promoting hydrolysis.

CONCLUSIONS

The accumulation of poly(ethylene terephthalate) (PET), a highly resistant material with an annual production of 80 million tons, poses significant threats to the environment and health. Bioremediation with purified enzymes represents a promising and environmentally acceptable solution for plastic waste disposal. In this work, a new PETase was successfully produced in *E. coli* and purified by IMAC chromatography. ESI-ORBITRAP-MS for peptide-mass fingerprinting was performed to confirm the correct amino acid sequence of the enzyme. HPLC analysis of PET degradation products demonstrated the presence of TPA, MHET, and BHET, which are established markers of enzyme activity. PETase SM14 exhibited optimal performance at pH 9.0 and showed thermostability up to 50 °C. After 3 days of incubation, the highest concentration of released TPA was 0.187 mM. Notably, the addition of 900 mM NaCl enhanced enzyme activity by more than 100-fold, likely due to conformational changes in the protein at pH 9.0 and its interactions with the substrate. Additionally, the presence of salt may weaken the substrate's structure, further facilitating enzyme activity.[41,42] The crystal structure of PETase SM14 was solved at 1.43 Å resolution, and a comparative analysis with *Is*PETase and PE-H revealed high structural similarity, with RMSDs of 0.691 and 0.81 Å, respectively. Overall, our findings provide novel valuable insight into a polyester hydrolase from a marine source. Due to its thermostability and activity on PCP, PETase SM14 may represent an interesting tool for enzymatic PET waste management.

MATERIALS AND METHODS

PETase SM14 Sequence Analysis. The target protein (*PETase*) was identified in the PAZy database (https://www.pazy.eu/doku.php) among the 119 sequences recognized as acting on PET. The protein sequence spanning residues 25−284, classified by InterPro automatic annotation as a cutinase, is provided in the Supporting Information along with details of the expression vector (Figure S7).

Production of PETase SM14 in *E. coli*. The gene encoding the mature PETase sequence from *Streptomyces* sp. SM14 (UniProt ID: A0A679PDB4) was designed for Ligation Independent Cloning using the aLICatorR system (ThermoFisher) and purchased from IDT. LIC was used to generate the *PETase*-pLATE52 plasmid, which was then used to transform BL21 (DE3) *E. coli* competent cells. Transformed cells were selected on LB plates containing 100 μg/mL ampicillin. Positive colonies were screened by colony-PCR and grown overnight at 37 °C with shaking at 250 rpm. For protein expression, a 1 L LB/ampicillin culture was grown at 37 °C, 170 rpm, and induced with 0.5 mM isopropyl β-D-1-thiogalactopyranoside for 3 h (Figure S8). Cells were then harvested by centrifugation (10,000 rpm, 10 min), resuspended in 50 mM phosphate buffer pH 8.0 (5 mL/g of biomass), and sonicated on ice using a Microson Ultrasonic cell disruptor. The supernatant was loaded on a HisTrap HP column and purified using the following buffers: buffer A (50 mM phosphate buffer, pH 8.0) and buffer B (50 mM phosphate buffer pH 8.0, 500 mM imidazole). The column was washed with 2 column volumes of buffer A, and the protein was eluted using a linear gradient of buffer B. Peak fractions (Figure S9) were collected. Protein concentration was determined by measuring A_{280} and using an extinction coefficient (ε_{280}) of 45,380 M^{-1} cm^{-1} and a MW of 31,386 Da, as calculated using the ExPASy ProtParam Tool (https://web.expasy.org/protparam/).

PETase SM14 Mass Spectrometry. MS/MS analyses were performed using a UHPLC−MS Q Exactive instrument (ThermoFisher). Protein samples were extracted from a single band on the SDS−PAGE. The results were analyzed by MASCOT software (http://mascot.cigs.unimo.it/mascot/) to identify the protein and verify its sequence accuracy.

Circular Dichroism. CD spectra were recorded on a Jasco J-1500 spectrophotometer at 20 °C. CD spectroscopy was performed to analyze the enzyme's secondary structure and thermostability. Both experiments were conducted on the enzyme after the His tag removal. Spectra were averaged over three scans using a 2.0 mm quartz cuvette with 2.5 μM samples in a 50 mM Tris (pH 8.0) and 150 mM NaCl buffer. Thermal denaturation curves were recorded in 2.0 mm cuvettes sealed with Parafilm with 2.5 μM samples. Temperature-induced denaturation was monitored at 222 nm, increasing at a rate of 1 °C/min from 5 to 110 °C. Readings were taken at 1 °C intervals with a 1 nm bandwidth and a 10 s response time. Thermal-denaturation midpoints (Tm) were determined by fitting the data to a sigmoidal transition curve using the Boltzmann function. The secondary structure of different variants was measured at 200−250 nm wavelengths at 20 °C. Ellipticity versus wavelength was plotted using GraphPad Prism 10 software, with each spectrum averaged over three scans.

Thermal Shift Assay. The melting temperature of each variant was measured using differential scanning fluorimetry with Sypro-Orange dye (ThermoFisher Scientific) on an Applied Biosystems 7500 Real-Time PCR system (ThermoFisher Scientific). For each condition, 12.5 μL of enzyme at the starting concentration of 10 μM was added to 12.5 μL of a 10× Sypro-Orange dye solution diluted from a 5000× stock in the same buffer that was used for the protein to reach the final volume of 25 μL, a 5× final concentration of the dye and a 5 μM concentration of the enzyme. All the Tm measurements were performed in 3 replicates (Figures S10−S12). Fluorescence was monitored during the thermal denaturation occurring to the protein upon increasing the temperature from 15 °C to 95.3 °C.

Crystals of PETase SM14. Crystals of the enzyme without the His-tag were grown at room temperature by using the vapor diffusion method. A 1 μL aliquot of a 10 mg/mL protein sample was mixed with 1 μL of a solution containing 0.2 M ammonium sulfate, 0.1 M MES monohydrate pH 6.5, and 30% w/v polyethylene glycol monomethyl ether 5000. Crystals, which appeared within 1−2 weeks, were frozen in a chemically identical solution supplemented with 25% (v/v) glycerol prior to X-ray diffraction data collection.

Data Collection and Processing. Diffraction data were obtained using a Eiger2 XE 16M detector and a radiation of wavelength of 0.71326 Å on the I03 beamline at the Diamond Light Source (Oxfordshire, United Kingdom). Data processing was performed using the AutoPROC package. Data collection and refinement statistics are summarized in Table S2.

Structure Determination and Refinement. For PETase SM14 structure determination, initial data was obtained through molecular replacement using Phaser, with the atomic coordinates of the AlphaFold model (AF-A0A679PDB4-F1) serving as the starting model. Refinement was performed through iterative rounds of manual adjustments in Coot and automated refinement using REFMAC5. Water molecules were added manually and automatically using the refine tool in Coot from the CCP4 cloud package.

PETase SM14 Activity Assays. The enzymatic activity of PETase SM14 was evaluated using PET PCP, while varying parameters such as temperature and pH. Reaction tubes were set up by adding a squared piece of PCP ($A = 1$ cm^2) into 400 μL buffer containing 1 μM protein solution. The degrading activity of the enzyme toward post-consumer plastic was tested at different pH values; 100 mM phosphate buffer was used to run tests at pH 6.0 and 7.0, while 100 mM Tris−HCl was used for tests at pH 8.0 and 9.0. The range of NaCl concentration was 0 mM, 300 mM, 500 mM, 700 mM, 900 mM, 1000 mM, 1100 mM, 1300 mM, and 1500 mM. After an incubation time of 72 or 168 h, the reaction tubes containing the PCP were vigorously mixed using a Vortex mixer, and then the substrate was removed with tweezers, washed with SDS 1%, then rinsed with ddH_2O and finally with 98% ethanol, while the supernatant was filtered and further analyzed by RP-HPLC. For every set of reactions, two control samples were prepared following the same procedure: one was prepared without adding the protein to the reaction mixture, while the other was prepared without adding the substrate.

RP-HPLC Analyses. The reaction supernatants were dried using a Thermo ScientificTM SavantTM DNA SpeedVacTM Concentrator Kit and resuspended in H_2O/acetonitrile. Solution A consists of 10% formic acid Milli-Q water, while solution B is acetonitrile. An Agilent Poroshell 120 EC-C18 column was equilibrated with a mobile phase of 80:20 (solution A/solution B) until pressure and UV parameters reached stability. Then, 20 μL of each sample was loaded into the column and eluted over a 20 min run at a flow rate of 1 mL/min at room temperature with the following elution program: 80:20 (solution A/solution B), followed by a 15 min linear gradient 20:50 (solution A/solution B), and 2 min isocratic 50:50 (solution A/solution B). Then, to return to the starting point, 3 min linear gradient from 50:20 (solution A/solution B) and 2 min isocratic 80:20 (solution A/solution B) were applied. The absorbance was measured at 240 and 254 nm. To determine peak areas, the baseline was drawn manually and calculated using the instrument's software. TPA and BHET were the two main products obtained. Their calibration curves were generated by injecting standard solutions at concentrations of 0.5 2.5 mM, 10 mM, 20 mM, and 30 mM for TPA and 0.05, 0.1, 0.25, and 0.4 mM for BHET. According to Figure S13, the reaction product with the highest retention time was BHET (2.6 min), followed by MHET (2.2 min, assumed) and TPA (1.6 min).

Scanning Electron Microscopy Imaging. The morphology of PCP films before and after enzyme exposure was examined by SEM on a FEI Nova NanoSEM at an accelerating voltage of 10 kV. Samples were metallized in a Gold Sputter Coater Emitech K550 for 60 s at 18 mA. Digitized images were brought into Epax genesis software for assembly.

Atomic Force Microscopy. Protein activity was also assessed by analyzing the plastic pieces after incubation with the enzyme by AFM. Morphological characterization of PET samples was performed using an NT-MDT SMENA Solver platform (Moscow, Russia); the analysis was performed in semi-contact mode, and the images were analyzed using Gwyddion 2.67 freeware (http://gwyddion.net).

ASSOCIATED CONTENT

Supporting Information

The Supporting Information is available free of charge at https://pubs.acs.org/doi/10.1021/acssuschemeng.5c00737.

Gene sequence of PETase SM14 reported alongside the expression vector, SDS−PAGE analysis, purification chromatogram, peptide mass spectra of the amino acids sequence determined via MS/MS, protein's CD spectra, shift in melting temperature in different conditions, thermal shift assay results, HPLC analysis of reaction products with calibration curves, comparative surface electrostatic potential analysis, AFM image of the PCP sample control, and diffraction data collection and refinement statistics (PDF)

The final crystallographic coordinates of the crystal structure of PETase SM14 are available in the RCSB PDB (accession code: 9HYD)

AUTHOR INFORMATION

Corresponding Author

Giulia Di Rocco − *Department of Life Sciences, University of Modena and Reggio Emilia, 41125 Modena, Italy;* orcid.org/0000-0002-3187-2210; Email: giulia.dirocco@unimore.it

Authors

Alan Carletti − *Department of Life Sciences, University of Modena and Reggio Emilia, 41125 Modena, Italy*

Shapla Bhattacharya − *Department of Biotechnology, Latvian Institute of Organic Synthesis, LV-1006 Riga, Latvia; Faculty of Materials Science and Applied Chemistry, Riga Technical University, LV-1048 Riga, Latvia*

Sara Pedroni − *Department of Life Sciences, University of Modena and Reggio Emilia, 41125 Modena, Italy*

Marcello Berto − *Department of Life Sciences, University of Modena and Reggio Emilia, 41125 Modena, Italy;* orcid.org/0000-0002-3356-8829

Riccardo Bonettini − *Department of Life Sciences, University of Modena and Reggio Emilia, 41125 Modena, Italy*

Rossella Castagna − *Department of Biotechnology, Latvian Institute of Organic Synthesis, LV-1006 Riga, Latvia;* Present Address: Department of Chemistry, Materials and Chemical Engineering "G. Natta", Politecnico di Milano, Piazza Leonardo da Vinci 32, 20133 Milano, Italy

Emilio Parisini − *Department of Biotechnology, Latvian Institute of Organic Synthesis, LV-1006 Riga, Latvia; Department of Chemistry "G. Ciamician", University of Bologna, 40129 Bologna, Italy*

Complete contact information is available at: https://pubs.acs.org/10.1021/acssuschemeng.5c00737

Author Contributions

The manuscript was written through the contributions of all authors. All authors have given approval to the final version of the manuscript.

Notes

The authors declare no competing financial interest.

ACKNOWLEDGMENTS

The authors wish to thank the personnel of the Diamond Light Source (proposal number mx32544) for help with the data collection. E.P. thanks the Latvian Recovery and Resilience Fund (grant No. 74/OSI/ZG) for financial support. S.B. acknowledges the Latvian Recovery and Resilience Fund and the Latvian Institute of Organic Synthesis for student grants (No. ANM_OSI_DG_31 and No. IG-2025-02). E.P. and R.C. wish to thank the European Union's HORIZON-WIDERA-2023-ACCESS-04 programme for financial support under grant agreement 101159534 (WIDEnzymes). This manuscript reflects only the authors' views and opinions. Neither the European Union nor the granting authority can be considered responsible for them. A.C. thanks MIUR, Ministero dell'Istruzione, dell'Università e della Ricerca (Prin 2020, E53C2001365001 to MS), and G.D.R. thanks FARDSV2021.

ABBREVIATIONS

PET, polyethylene terephthalate; TPA, terephthalic acid; MHET, 2-hydroxyethylterephthalic acid; BHET, bis(2-hydroxyethyl) terephthalate; RP-HPLC, reverse phase high-performance liquid chromatography; SEM, scanning electron microscopy; AFM, atomic force microscopy; PCP, post-consumer plastic; CD, circular dichroism; Tm, melting temperature; RMSD, root mean square deviation; IMAC, immobilized metal affinity chromatography; MES, 2-(*N*-morpholino) ethanesulfonic acid; ESI-ORBITRAP-MS, electron spray ionization orbitrap mass spectrometry; LCC, leaf-branch compost cutinase; EC, enzyme commission number; isPETase, PETase from Ideonella sakaiensis; PETase SM14, PETase from *Streptomyces* sp. SM14; PE-H, polyester hydrolase; DSF, differential scanning fluorimetry; TSA, thermal shift assay

REFERENCES

(1) University of Georgia *More than 8.3 Billion Tons of Plastics Made: Most Has Now Been Discarded*; ScienceDaily, University of Georgia,

2017. https://www.sciencedaily.com/releases/2017/07/170719140939.htm (accessed 26 September 2024).

(2) Scott, G. *Polymers and the Environment*; Royal Society of Chemistry1999.

(3) Schwarz, A. E.; Ligthart, T. N.; Boukris, E.; van Harmelen, T. Sources, Transport, and Accumulation of Different Types of Plastic Litter in Aquatic Environments: A Review Study. *Mar. Pollut. Bull.* **2019**, *143*, 92−100.

(4) Nisticò, R. Polyethylene Terephthalate (PET) in the Packaging Industry. *Polym. Test.* **2020**, *90*, 106707.

(5) Fortune Business Insights *Polyethylene Terephthalate (PET) Market to Worth USD 91.37 Billion by 2030*; Fortune Business Insights, 2023. https://www.globenewswire.com/news-release/2023/05/08/2663018/0/en/Polyethylene-Terephthalate-PET-Market-to-Worth-USD-91-37-Billion-by-2030-Fortune-Business-Insights.html (accessed 22 September 2024).

(6) Eze, W. U.; Umunakwe, R.; Obasi, H. C.; Ugbaja, M. I.; Uche, C. C.; Madufor, I. C. Plastics Waste Management: A Review of Pyrolysis Technology. *Clean Technol. Recycl.* **2021**, *1* (1), 50−69.

(7) Suhaimi, N. A. S.; Muhamad, F.; Abd Razak, N. A.; Zeimaran, E. Recycling of Polyethylene Terephthalate Wastes: A Review of Technologies, Routes, and Applications. *Polym. Eng. Sci.* **2022**, *62* (8), 2355−2375.

(8) Yoshida, S.; Hiraga, K.; Takehana, T.; Taniguchi, I.; Yamaji, H.; Maeda, Y.; Toyohara, K.; Miyamoto, K.; Kimura, Y.; Oda, K. A Bacterium That Degrades and Assimilates Poly(Ethylene Terephthalate). *Science* **2016**, *351* (6278), 1196−1199.

(9) Feng, S.; Yue, Y.; Zheng, M.; Li, Y.; Zhang, Q.; Wang, W. *Is* PETase- and *Is* MHETase-Catalyzed Cascade Degradation Mechanism toward Polyethylene Terephthalate. *ACS Sustain. Chem. Eng.* **2021**, *9* (29), 9823−9832.

(10) Bååth, J. A.; Borch, K.; Jensen, K.; Brask, J.; Westh, P. Comparative Biochemistry of Four Polyester (PET) Hydrolases. *ChemBioChem* **2021**, *22* (9), 1627−1637.

(11) Buchholz, P. C. F.; Feuerriegel, G.; Zhang, H.; Perez-Garcia, P.; Nover, L.-L.; Chow, J.; Streit, W. R.; Pleiss, J. Plastics degradation by hydrolytic enzymes: The plastics-active enzymes database—PAZy. *Proteins: Struct., Funct., Bioinf.* **2022**, *90* (7), 1443−1456.

(12) dos Santos, A. M.; da Costa, C. H. S.; Silva, P. H. A.; Skaf, M. S.; Lameira, J. Exploring the Reaction Mechanism of Polyethylene Terephthalate Biodegradation through QM/MM Approach. *J. Phys. Chem. B* **2024**, *128* (31), 7486−7499.

(13) Liu, C.; Shi, C.; Zhu, S.; Wei, R.; Yin, C.-C. Structural and Functional Characterization of Polyethylene Terephthalate Hydrolase from Ideonella Sakaiensis. *Biochem. Biophys. Res. Commun.* **2019**, *508* (1), 289−294.

(14) Han, X.; Liu, W.; Huang, J.-W.; Ma, J.; Zheng, Y.; Ko, T.-P.; Xu, L.; Cheng, Y.-S.; Chen, C.-C.; Guo, R.-T. Structural Insight into Catalytic Mechanism of PET Hydrolase. *Nat. Commun.* **2017**, *8* (1), 2106.

(15) Khairul Anuar, N. F. S.; Huyop, F.; Ur-Rehman, G.; Abdullah, F.; Normi, Y. M.; Sabullah, M. K.; Abdul Wahab, R. An Overview into Polyethylene Terephthalate (PET) Hydrolases and Efforts in Tailoring Enzymes for Improved Plastic Degradation. *Int. J. Mol. Sci.* **2022**, *23* (20), 12644.

(16) Liu, F.; Wang, T.; Yang, W.; Zhang, Y.; Gong, Y.; Fan, X.; Wang, G.; Lu, Z.; Wang, J. Current Advances in the Structural Biology and Molecular Engineering of PETase. *Front. Bioeng. Biotechnol.* **2023**, *11*, 1263996.

(17) Tournier, V.; Topham, C. M.; Gilles, A.; David, B.; Folgoas, C.; Moya-Leclair, E.; Kamionka, E.; Desrousseaux, M.-L.; Texier, H.; Gavalda, S.; Cot, M.; Guémard, E.; Dalibey, M.; Nomme, J.; Cioci, G.; Barbe, S.; Chateau, M.; André, I.; Duquesne, S.; Marty, A. An Engineered PET Depolymerase to Break down and Recycle Plastic Bottles. *Nature* **2020**, *580* (7802), 216−219.

(18) Ding, K.; Levitskaya, Z.; Sana, B.; Pasula, R. R.; Kannan, S.; Adam, A.; Sundaravadanam, V. V.; Verma, C.; Lim, S.; Ghadessy, J. F. Modulation of PETase Active Site Flexibility and Activity on Morphologically Distinct Polyethylene Terephthalate Substrates by Surface Charge Engineering. *Biochem. Eng. J.* **2024**, *209*, 109420.

(19) Arnal, G.; Anglade, J.; Gavalda, S.; Tournier, V.; Chabot, N.; Bornscheuer, U. T.; Weber, G.; Marty, A. Assessment of Four Engineered PET Degrading Enzymes Considering Large-Scale Industrial Applications. *ACS Catal.* **2023**, *13* (20), 13156−13166.

(20) Kawai, F.; Oda, M.; Tamashiro, T.; Waku, T.; Tanaka, N.; Yamamoto, M.; Mizushima, H.; Miyakawa, T.; Tanokura, M. A Novel Ca2+-Activated, Thermostabilized Polyesterase Capable of Hydrolyzing Polyethylene Terephthalate from Saccharomonospora Viridis AHK190. *Appl. Microbiol. Biotechnol.* **2014**, *98* (24), 10053−10064.

(21) Oda, M.; Yamagami, Y.; Inaba, S.; Oida, T.; Yamamoto, M.; Kitajima, S.; Kawai, F. Enzymatic Hydrolysis of PET: Functional Roles of Three Ca2+ Ions Bound to a Cutinase-like Enzyme, Cut190*, and Its Engineering for Improved Activity. *Appl. Microbiol. Biotechnol.* **2018**, *102* (23), 10067−10077.

(22) Han, W.; Zhang, J.; Chen, Q.; Xie, Y.; Zhang, M.; Qu, J.; Tan, Y.; Diao, Y.; Wang, Y.; Zhang, Y. Biodegradation of Poly(Ethylene Terephthalate) through PETase Surface-Display: From Function to Structure. *J. Hazard. Mater.* **2024**, *461*, 132632.

(23) Schmidt, J.; Wei, R.; Oeser, T.; Belisário-Ferrari, M. R.; Barth, M.; Then, J.; Zimmermann, W. Effect of Tris, MOPS, and Phosphate Buffers on the Hydrolysis of Polyethylene Terephthalate Films by Polyester Hydrolases. *FEBS Open Bio* **2016**, *6* (9), 919−927.

(24) Almeida, E. L.; Carrillo Rincón, A. F.; Jackson, S. A.; Dobson, A. D. W. In Silico Screening and Heterologous Expression of a Polyethylene Terephthalate Hydrolase (PETase)-Like Enzyme (SM14est) With Polycaprolactone (PCL)-Degrading Activity, From the Marine Sponge-Derived Strain Streptomyces Sp. SM14. *Front. Microbiol.* **2019**, *10*, 2187.

(25) Magalhães, R. P.; Cunha, J. M.; Sousa, S. F. Perspectives on the Role of Enzymatic Biocatalysis for the Degradation of Plastic PET. *Int. J. Mol. Sci.* **2021**, *22* (20), 11257.

(26) Joo, S.; Cho, I. J.; Seo, H.; Son, H. F.; Sagong, H.-Y.; Shin, T. J.; Choi, S. Y.; Lee, S. Y.; Kim, K.-J. Structural Insight into Molecular Mechanism of Poly(Ethylene Terephthalate) Degradation. *Nat. Commun.* **2018**, *9* (1), 382.

(27) Bollinger, A.; Thies, S.; Knieps-Grünhagen, E.; Gertzen, C.; Kobus, S.; Höppner, A.; Ferrer, M.; Gohlke, H.; Smits, S. H. J.; Jaeger, K.-E. A Novel Polyester Hydrolase From the Marine Bacterium Pseudomonas Aestusnigri – Structural and Functional Insights. *Front. Microbiol.* **2020**, *11*, 114.

(28) Di Rocco, G.; Taunt, H. N.; Berto, M.; Jackson, H. O.; Piccinini, D.; Carletti, A.; Scurani, G.; Braidi, N.; Purton, S. A PETase Enzyme Synthesised in the Chloroplast of the Microalga Chlamydomonas Reinhardtii Is Active against Post-Consumer Plastics. *Sci. Rep.* **2023**, *13* (1), 10028.

(29) Samak, N. A.; Jia, Y.; Sharshar, M. M.; Mu, T.; Yang, M.; Peh, S.; Xing, J. Recent Advances in Biocatalysts Engineering for Polyethylene Terephthalate Plastic Waste Green Recycling. *Environ. Int.* **2020**, *145*, 106144.

(30) Austin, H. P.; Allen, M. D.; Donohoe, B. S.; Rorrer, N. A.; Kearns, F. L.; Silveira, R. L.; Pollard, B. C.; Dominick, G.; Duman, R.; El Omari, K.; Mykhaylyk, V.; Wagner, A.; Michener, W. E.; Amore, A.; Skaf, M. S.; Crowley, M. F.; Thorne, A. W.; Johnson, C. W.; Woodcock, H. L.; McGeehan, J. E.; Beckham, G. T. Characterization and Engineering of a Plastic-Degrading Aromatic Polyesterase. *Proc. Natl. Acad. Sci. U.S.A.* **2018**, *115* (19), No. E4350.

(31) Kitadokoro, K.; Kakara, M.; Matsui, S.; Osokoshi, R.; Thumarat, U.; Kawai, F.; Kamitani, S. Structural Insights into the Unique Polylactate-degrading Mechanism of *Thermobifida Alba* Cutinase. *FEBS J.* **2019**, *286* (11), 2087−2098.

(32) Botos, I.; Wlodawer, A. The Expanding Diversity of Serine Hydrolases. *Curr. Opin. Struct. Biol.* **2007**, *17* (6), 683−690.

(33) Mukhtar, H. Industrial Applications and Production Sources of Serine Alkaline Proteases: A Review. *J. Bacteriol. Mycol.* **2016**, 3 (1), 191.

(34) Hofer, F.; Kraml, J.; Kahler, U.; Kamenik, A. S.; Liedl, K. R. Catalytic Site pK_a Values of Aspartic, Cysteine, and Serine Proteases:

Constant PH MD Simulations. *J. Chem. Inf. Model.* **2020**, *60* (6), 3030−3042.

(35) Charlier, C.; Gavalda, S.; Grga, J.; Perrot, L.; Gabrielli, V.; Löhr, F.; Schörghuber, J.; Lichtenecker, R.; Arnal, G.; Marty, A.; Tournier, V.; Lippens, G. Exploring the PH Dependence of an Improved PETase. *Biophys. J.* **2024**, *123* (12), 1542−1552.

(36) Craik, C. S.; Roczniak, S.; Largman, C.; Rutter, W. J. The Catalytic Role of the Active Site Aspartic Acid in Serine Proteases. *Science* **1987**, *237* (4817), 909−913.

(37) Škvarla, J.; Luxbacher, T.; Nagy, M.; Sisol, M. Relationship of Surface Hydrophilicity, Charge, and Roughness of PET Foils Stimulated by Incipient Alkaline Hydrolysis. *ACS Appl. Mater. Interfaces* **2010**, *2* (7), 2116−2127.

(38) Biscarini, F.; Ong, Q. K.; Albonetti, C.; Liscio, F.; Longobardi, M.; Mali, K. S.; Ciesielski, A.; Reguera, J.; Renner, C.; De Feyter, S.; Samorì, P.; Stellacci, F. Quantitative Analysis of Scanning Tunneling Microscopy Images of Mixed-Ligand-Functionalized Nanoparticles. *Langmuir* **2013**, *29* (45), 13723−13734.

(39) Di Lauro, M.; Berto, M.; Giordani, M.; Benaglia, S.; Schweicher, G.; Vuillaume, D.; Bortolotti, C. A.; Geerts, Y. H.; Biscarini, F. Liquid-Gated Organic Electronic Devices Based on High-Performance Solution-Processed Molecular Semiconductor. *Adv. Electron. Mater.* **2017**, *3* (9), 1700159.

(40) Mohanan, N.; Montazer, Z.; Sharma, P. K.; Levin, D. B. Microbial and Enzymatic Degradation of Synthetic Plastics. *Front. Microbiol.* **2020**, *11*, 580709.

(41) Polêto, M. D.; Lemkul, J. A. Structural and Electronic Properties of Poly(Ethylene Terephthalate) (PET) from Polarizable Molecular Dynamics Simulations. *Macromolecules* **2025**, *58* (1), 403−414.

(42) Park, C.; Raines, R. T. Quantitative Analysis of the Effect of Salt Concentration on Enzymatic Catalysis. *J. Am. Chem. Soc.* **2001**, *123* (46), 11472−11479.

(43) Carr, C. M.; Keller, M. B.; Paul, B.; Schubert, S. W.; Clausen, K. S. R.; Jensen, K.; Clarke, D. J.; Westh, P.; Dobson, A. D. W. Purification and Biochemical Characterization of SM14est, a PET-Hydrolyzing Enzyme from the Marine Sponge-Derived Streptomyces Sp. SM14. *Front. Microbiol.* **2023**, *14*, 1170880.

3. Pielikums

Appendix 3

Bhattacharya, S.; * Castagna, R.; * Estiri, H.; * Upmanis, T.; Gautieri, A.; Parisini, E.
Development of a Highly Active Engineered PETase Enzyme for Polyester Degradation

The FEBS Journal, 2025, 23 August, article ID febs.70228
doi:10.1111/febs.70228

Publikācija un tās pielikums pieejams bez maksas izdevēja mājaslapā
The Publication and Supporting Information is available free of charge on the publisher's website

These authors contributed equally to this work.

The FEBS Journal

FEBS PRESS
science publishing by scientists

Development of a highly active engineered PETase enzyme for polyester degradation

Shapla Bhattacharya[1,2], Rossella Castagna[1,3], Hajar Estiri[1], Toms Upmanis[1,4], Andrea Ricci[5], Alfonso Gautieri[5] and Emilio Parisini[1,6]

1 Department of Biotechnology, Latvian Institute of Organic Synthesis, Riga, Latvia
2 Institute of Chemistry and Chemical Technology, Faculty of Natural Sciences and Technology, Riga Technical University, Latvia
3 Dipartimento di Chimica, Materiali e Ingegneria Chimica "G. Natta", Politecnico di Milano, Milan, Italy
4 Faculty of Chemistry, University of Latvia, Riga, Latvia
5 Biomolecular Engineering Lab, Dipartimento di Elettronica, Informazione e Bioingegneria, Politecnico di Milano, Milan, Italy
6 Department of Chemistry "G. Ciamician", University of Bologna, Italy

Keywords
enzymatic depolymerization; PETase; plastic degradation; rational protein engineering; thermal stability

Correspondence
A. Gautieri, Biomolecular Engineering Lab, Dipartimento di Elettronica, Informazione e Bioingegneria, Politecnico di Milano, Piazza Leonardo da Vinci 32, 20133 Milano, Italy
Tel: +39 0223993515
E-mail: alfonso.gautieri@polimi.it
and
E. Parisini, Department of Biotechnology, Latvian Institute of Organic Synthesis, Aizkraukles 21, LV-1006, Riga, Latvia
Tel: +371 67014875
E-mail: emilio.parisini@osi.lv

Shapla Bhattacharya, Rossella Castagna and Hajar Estiri contributed equally to this work.
Dedicated to the memory of Prof. George M. Sheldrick.

(Received 20 January 2025, revised 14 June 2025, accepted 6 August 2025)

doi:10.1111/febs.70228

Polyethylene terephthalate (PET) accounts for ≈6% of global plastic production, contributing considerably to the global solid-waste stream and environmental plastic pollution. Since the discovery of PET-depolymerizing enzymes, enzymatic PET recycling has been regarded as a promising method for plastic disposal, particularly in the context of a circular economy strategy. However, because the PET-degrading enzymes developed so far suffer from relatively limited thermostability and low catalytic efficiency, as well as degradation product inhibition, their large-scale industrial applications are still largely hampered. To overcome these limitations, we engineered the current PET-hydrolyzing enzyme gold standard [the ICCG variant of leaf-branch compost cutinase (LCC-ICCG)] using *in silico* protein design methods to develop a PET-hydrolyzing enzyme that features enhanced thermal stability and PET depolymerization activity. Our mutant, LCC-ICCG-C09, features a 3.5 °C increase in melting temperature relative to the LCC-ICCG enzyme. Under optimal reaction conditions (68 °C), the engineered enzyme hydrolyzes amorphous PET material into terephthalic acid (TPA) with a two-fold higher efficiency compared to LCC-ICCG. Owing to its enhanced properties, LCC-ICCG-C09 may be a promising candidate for future applications in industrial PET recycling processes.

Abbreviations
BHET, bis(hydroxyethyl)terephthalate; CD, circular dichroism; DSF, differential scanning fluorimetry; EG, ethylene glycol; HPLC, high-performance liquid chromatography; IPTG, isopropyl 1thioβD galactopyranoside; LB, Luria–Bertani broth; LCC, leaf-branch compost cutinase; MD, molecular dynamics; MeCN, acetonitrile; MHET, mono(hydroxyethyl)terephthalate; PDB, Protein Data Bank; PET, polyethylene terephthalate; PMSF, phenylmethylsulfonyl fluoride; pNPA, p-nitrophenyl acetate; RMSD, root mean square deviations; T_m, melting temperature; TPA, terephthalic acid.

293, 443–455 © 2025 The Author(s). *The FEBS Journal* published by John Wiley & Sons Ltd on behalf of Federation of European Biochemical Societies.

Introduction

Worldwide plastic production reached 390 million metric tons in 2021, of which 90.2% comes from fossil-based production and only the remaining 9.8% comes from post-consumer plastic recycling or bio-based plastics [1]. This massive production and usage of plastics, along with their very long persistence in the environment, has led to an extreme global pollution threat, especially in marine environments [2–5].

Polyethylene terephthalate (PET), the most abundant synthetic polyester in the environment, has an average lifetime of 25–50 years and accounts for 6.2% of the total plastic production [1]. It is widely used in the production of textile fibers and resins for single-use beverage bottles and packaging. Polyethylene terephthalate is a thermoplastic polymer that is composed of terephthalic acid (TPA) and ethylene glycol (EG) subunits. Nowadays, PET is, to a large extent, mechanically recycled, a process that results in a significant loss of the material's properties and value [6]. Harsh chemical treatments involving the use of sulfuric acid at 150 °C or carried out under alkaline conditions in the presence of hazardous chemical catalysts (e.g., methyltrioctylammonium bromide) are also used, leading to the depolymerization of PET into its monomeric building blocks via ester bonds cleavage. However, the use of such harsh conditions makes it problematic to expand this treatment on a large scale.

In 1977, Tokiwa and Suzuki proposed using lipase enzymes to degrade polymeric materials [7]. Indeed, enzymes work in mild conditions and can replace hazardous chemicals, a concept known as green chemistry. The first report of an efficient PET hydrolase (from *Thermobifida fusca*) was published in 2005 [8]. Since then, numerous thermally stable PET hydrolases and their related enzymes from the cutinase group (EC. 3.1.1.74) have been identified in different organisms [9–13]. The search for thermostable PET hydrolases is driven by the fact that PET can be more effectively hydrolyzed at temperatures close to its glass transition temperature (≈70–80 °C in air, ≈60–70 °C in water). Near the glass transition temperature, the polymer chains become more flexible, enabling PET hydrolases to function optimally. In 2016, Yoshida *et al.* [14] reported on a mesophilic bacterium (*Ideonella sakaiensis*) that can thrive on an amorphous PET film as its primary carbon source already at 30 °C, making the enzyme responsible for PET hydrolysis (*Is*PETase) the best option for PET waste decomposition. This work spurred a great deal of interest and several efforts in providing enhanced *Is*PETase mutants. However, since *Is*PETase is heat-labile, the enzyme quickly loses its activity at temperatures above 40 °C. Therefore, more suitable scaffolds have also been explored, such as, for instance, the Leaf-branch Compost Cutinase (LCC), a naturally occurring PETase that has been reported to outperform all other known PET-degrading enzymes and to present a melting temperature (T_m) of 84.7 °C. This enzyme has been noticeably engineered in 2020 by Tournier *et al.* [15] leading to the so-called ICCG variant (also known as LCC-ICCG, or ICCG for brevity), which, in two different accounts, is reported to feature a T_m of 91.7 or 94.0 °C (Table 1).

To the best of our knowledge, this variant is currently considered to be the gold standard PETase enzyme [16]. Despite its remarkable stability, the sequence space for even a small enzyme like LCC is astounding (20^{293} or 10^{381} theoretical possible sequences), leaving room to search for even more stable and active enzymes. Here, we set out to design improved PETase enzymes starting from the LCC-ICCG variant and using design strategies similar to those that we used previously with other classes of enzymes [17–20]. Our working hypothesis is that improving the thermal stability would be beneficial for the PETase enzymatic activity, as observed in notable examples (IsPETase < LCC < LCC-ICCG). For this reason, we set out to improve LCC-ICCG thermal stability, expecting further beneficial effects such as, for instance, higher expression yield and enhanced enzymatic activity.

The field of computational design of thermostable proteins is relatively mature, with several established available methods that can help to generate a library of mutants and rank them. The easiest and more

Table 1. Relevant PETase enzymes reported in the literature.

Parent enzyme	Name	Year	Tm (°C)	Ref.
*Is*PETase	(wild type)	2016	46.0	Yoshida *et al.* [14]
*Is*PETase	IsPETaseTM	2019	57.6	Son *et al.* [44]
LCC	(wild type)	2020	84.7	Tournier *et al.* [15]
LCC	LCC-ICCG	2020	94.0	Tournier *et al.* [15]
LCC	LCC-ICCG	2023	91.7	Arnal *et al.* [28]
*Is*PETase	—	2021	61.2	Meng *et al.* [45]
*Is*PETase	IsPETaseTM$^{K95N/F201I}$	2021	61.6	Brott *et al.* [46]
*Is*PETase	DuraPETase	2021	77.0	Cui *et al.* [47]
*Is*PETase	HotPETase	2022	82.5	Bell *et al.* [25]
PES-H1	L92F/Q94F	2022	86.7	Pfaff *et al.* [48]
*Is*PETase	FastPETase	2023	67.1	Lu *et al.* [49]
*Is*PETase	DepoPETase	2023	69.4	Shi *et al.* [50]

common approach involves the introduction of one or more disulfide bonds, which can rigidify the backbone of the protein and make it more stable. Other stabilization methods generally aim at extending the intramolecular hydrogen bonding network, creating intermolecular salt-bridges, or providing better packing of the hydrophobic core (e.g., PROSS) [21]. The Rosetta Supercharge method is meant to improve the stability of the protein by making the surface more hydrophilic, a feature that is usually associated with more stable proteins [22].

While these methods are fast and have been successfully used, most of them use an implicit solvent model (i.e., the solvent is modeled with a continuum rather than with explicit atoms) and assume a rigid backbone (which may limit the long-range structural effects of a mutation). To overcome these limitations, we included a further computational filter based on Molecular Dynamics simulations in explicit water. By using an orthogonal method, we aimed at screening and ranking on a common platform the most promising mutants generated by the methods described above.

Our efforts led to the development of three variants that feature T_m values higher than current PETases and, for one of them (LCC-ICCG-C09), further enhanced catalytic activity on amorphous PET films.

Results

In silico design and selection of stabilizing mutants

Enzyme engineering was initiated using the LCC-ICCG variant reported by Tournier *et al.* [15], a mutant of the wild-type leaf-branch compost cutinase (LCC) bearing four point substitutions: F243I, Y127G, S283C, and D238C. The latter two substitutions introduce a second disulfide bond, complementing the native C275–C292 bond. In both wild-type and mutant enzymes, the catalytic site is centered on residue S165. The crystal structure of the inactive S165A LCC-ICCG variant is available in the Protein Data Bank (PDB ID: 6THS). Our design strategy followed established protocols [17–19] beginning with the reversion of residue 165 to the catalytically active serine. Residues within 5 Å of S165 were excluded from mutagenesis to preserve active site integrity. Three distinct computational methods were employed, yielding three separate series of variants.

The use of the Rosetta Supercharge method [22] which aimed at increasing the charge on the surface of the enzyme, led to the identification of 1 000 potential enzyme variants, from which those 10 that featured the best Rosetta score (which we named C01-C10) were selected for further analysis. PROSS design [21] produced 9 variants (P01-P09), and Disulfide-by-Design [23] identified 125 enzyme variants, from which we selected the best 10, named X01-X10.

The 29 candidate enzyme variants originating from the different computational screening methods were then subject to 1 μs molecular dynamics (MD) simulations in explicit water and ranked based on their stability as assessed by RMSF analysis [17]. Our MD-based ranking led to the selection of six candidate mutants (C08, C09, P06, P08, X05, X09) for experimental production and characterization (Fig. 1, Fig. S1 and Table 2).

Thermal stability

The six candidate enzymes were expressed in *E. coli* and purified. The final yields of all the enzymes were around 16 mg·L^{-1} of bacterial culture (see yield in Table S1). Wild-type LCC, a naturally occurring PETase, has a T_m of 84.7 °C. This enzyme has been previously engineered by Tournier *et al.* [15] leading to the LCC-ICCG variant with a reported T_m of 94.0 °C (93.6 °C in our own assessment, a difference that could be attributed to that fact that, for T_m measurements, Tournier *et al.* used differential scanning fluorimetry (DSF), whereas we used circular dichroism (CD)). Indeed, during the thermal stability assessment of the enzymes, it became apparent that the determination of its melting temperature (T_m) via differential scanning fluorimetry (DSF) was unreliable. Specifically, the denaturation curve could not be accurately derived due to the T_m approaching 100 °C, which is the upper operational limit of the Applied Biosystems 7500 Real-Time PCR System utilized for the DSF measurements. As a result, a complete unfolding transition (typically indicated by a plateau) could not be observed for the enzymes within the instrumental constraints. To overcome this limitation and enable a consistent comparison across all enzyme variants, we employed CD spectroscopy. This technique facilitated the accurate determination of T_m values for all proteins examined in the study. Consequently, we propose that the discrepancy in the T_m of ICCG reported by Tournier *et al.* compared to our findings likely arises from the methodological differences between DSF and CD-based measurements.

After our enzyme design campaign, we tested the thermal stability of the six engineered variants (Table 3); we found that the C09 ($T_m = 97.1$ °C) and X05 ($T_m = 96.9$ °C) variants have a higher T_m than the reference LCC-ICCG ($T_m = 93.6$ °C). The X09

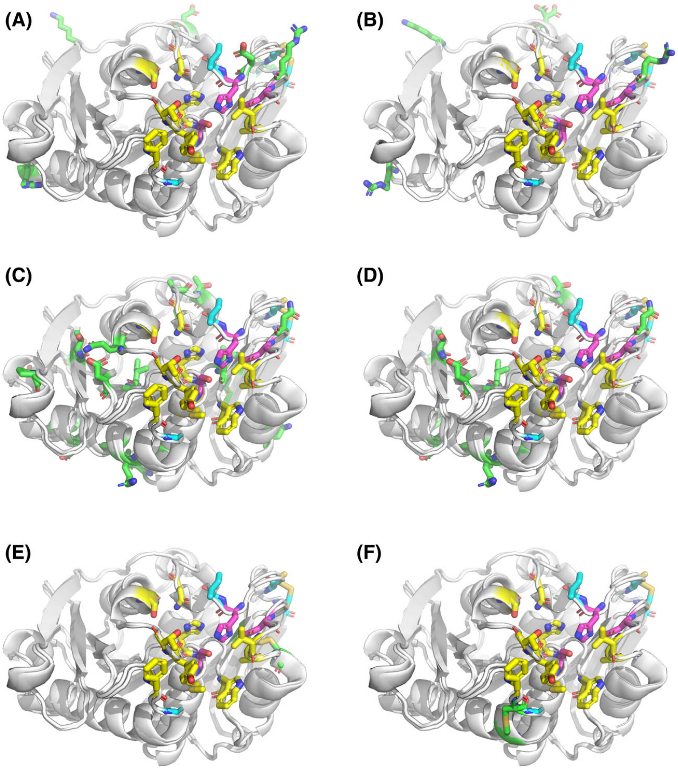

Fig. 1. Structural comparison of the enzyme variants selected for experimental characterization. Pink sticks represent the catalytic triad, cyan sticks represent the four substitutions introduced in LCC-ICCG, and green sticks represent additional substitutions introduced in each new variant (A: C08, B: C09, C: P06, D: P08, E: X05, F:X09). Figures are generated with the software PyMol [51].

($T_m = 93.8$ °C) variant exhibits similar thermal stability to LCC-ICCG (Fig. S2). We did not determine the melting temperature of P06 and P08 due to their negligible enzymatic activity in preliminary experiments, while for C08 it was not possible to obtain a reliable fit.

Enzymatic activity

Terephthalic acid (TPA) is one of the major degradation products of the activity of the enzymes on PET. This compound can be detected by liquid chromatography (HPLC), which allows a precise quantification of product formation. Given the potential absorption spectra overlaps of the degradation products that will affect the absorption spectra recording in spectrophotometric methods, we chose HPLC for its higher specificity and precision in quantifying the enzymatic reaction products as also described in the literature [24]. To assess enzymatic activity, aliquots of the enzymatic reactions were harvested at multiple time points and analyzed by HPLC for the quantification of TPA production (Fig. 2A). Minor degradation products (MHET and BHET) were also assessed (Fig. S3). We used an enzyme concentration of 40 nM (equivalent to 1.2 $\mu g \cdot mL^{-1}$ enzyme in the reaction mixture) and an amorphous PET film of 8.4 mg in a 2 mL microcentrifuge tube to evaluate the PET degradation activity of the different mutants. The enzyme concentration corresponds to $\approx 0.3\ mg_{ENZYME}/g_{PET}$, a ratio lower than the one reported in the original LCC-ICCG paper ($3\ mg_{ENZYME}/g_{PET}$), but in agreement with the range reported in the literature ($0.2\text{–}3\ mg_{ENZYME}/g_{PET}$) [25–28] The experiments were done at 68 °C, the temperature at which PET degradation is typically carried out in bioreactors at an industrial scale to work below

Table 2. List of substitutions relative to the sequence of the wild-type LCC enzyme. In bold are the substitutions already present in the LCC-ICCG scaffold.

Enzyme	Number of substitutions	Substitutions
LCC-ICCG [15]	4	Y127G, D238C, F243I, S283C
C08	11	S48D, S57K, **Y127G**, S145R, A209R, **D238C**, S241D, **F243I**, N276D, N278K, **S283C**
C09	13	S36D, Q40R, S48D, S57K, **Y127G**, S145R, A209R, **D238C**, **F243I**, N276D, N278K, **S283C**, Q293K
P06	16	V75T, L84E, M91I, N120D, **Y127G**, S133R, S136L, N140D, A156P, I174A, A209N, **D238C**, **F243I**, A250T, S253A, **S283C**
P08	26	S64P, V75T, L84E, M91I, A99Q, N120D, **Y127G**, S133R, S136L, N140D, R143V, A152S, A156P, I174A, N178D, T188C, A209N, Q224N, V233M, V235I, **D238C**, **F243I**, N248S, A250T, S253A, **S283C**
X05	6	**Y127G**, G206C, V215C, **D238C**, **F243I**, **S283C**
X09	6	D126C, **Y127G**, S130C, **D238C**, **F243I**, **S283C**

Table 3. Assessed melting temperature for different PETases and improvement with respect to the LCC wild-type enzyme. The estimation of T_m is sensitive to the experimental setup and conditions, which could explain the difference between the reported T_m and the T_m determined by us. For proper comparison, we assessed the T_m of LCC-ICCG using the same setup that we used for the measurement of the T_m of our engineered enzymes. The melting temperature was not measured for P06 and P08, while for C08 it was not possible to obtain a reliable fit. n.d., not determinable; n.m., not measured.

Enzyme	T_m (°C)	ΔT_m (°C)	References
WT-LCC	84.7	–	Tournier *et al.* [15]; Pirillo *et al.* [24]
LCC-ICCG	94.0	+9.3	Tournier *et al.* [15]
LCC-ICCG	91.7	+7.0	Arnal *et al.* [17]
LCC-ICCG[a]	93.6 ± 2.1	+8.9	
C09	97.1 ± 0.8	+12.4	
X05	96.9 ± 2.9	+12.2	
X09	93.8 ± 1.0	+9.1	
C08	n.d.		
P06	n.m.		
P08	n.m.		

[a] Reassessed in this work.

the glass transition temperature of PET ($T_g \approx 70$ °C). If we exclude the first few hours, where ICCG performs better, at 68 °C the mean TPA concentration at the different time points is significantly higher for the C09 mutant than for ICCG up until day 6 (144 h, Fig. 2A,B and Figs S3–S5). Moreover, the specific activity of C09 is also significantly higher (≈2-fold) than that of the gold standard LCC-ICCG over the same length of time (Fig. 2C). All other enzymes show similar or weaker performances compared to LCC-ICCG (X09, C08, X05). At 68 °C, complete sample degradation could be observed with C09 already at day 4 (data not shown), a feature not seen with any of the other enzymes, including LCC-ICCG. The percentage of weight loss after 6 days of reactions for all the enzymes is shown in Fig. 2D and in Fig. S3D. In order to assess the general functionality of the different PETase variants, we also tested the esterase activity for the PETase variants using p-nitrophenyl acetate (pNPA) as a substrate. The specific activity against pNPA is highest for C09 and C08, followed by ICCG and X09. The mutants X05, P06, and P08 have the lowest specific activity (Fig. S6).

Enzyme structure

We determined the crystal structure of C09 to assess whether the substitutions lead to changes in the structure of the enzyme. The structure was determined at 1.28 Å resolution. We compared the predicted secondary structure content based on CD with the experimental results, showing good alignment between the CD-based prediction and the crystallographic structure (Table S2). The structural comparison of the C09 variant with the parent enzymes shows no significant changes in the folding, as observed by the minimal change in RMSD with respect to the WT (0.257 Å) and to the LCC-ICCG variant (0.152 Å). The position and orientation of the catalytic triad (D210, H242, and S265) overlap perfectly with the catalytic triad in the parent enzymes (Fig. 3A). Although we observe that increased stability leads to higher enzymatic activity, a mechanistic explanation of the phenomenon is elusive. We hypothesize that the increase in stability provided by the additional surface charges in the C09 variant may help to keep the surface-exposed catalytic site in place even at high temperatures, such as those used to test the activity of the enzyme (68 °C). Indeed, all the substitutions introduced in the design process are found mostly on the surface of the enzyme and away from the catalytic triad (Fig. 3B; Fig. S7) and are thus unlikely to affect the activity directly. Rather, the substitutions may reduce the proportion of the enzyme that may denature over time, and/or prevent the unfolding of the exposed catalytic triad. The denaturation (and the consequent loss of activity) is

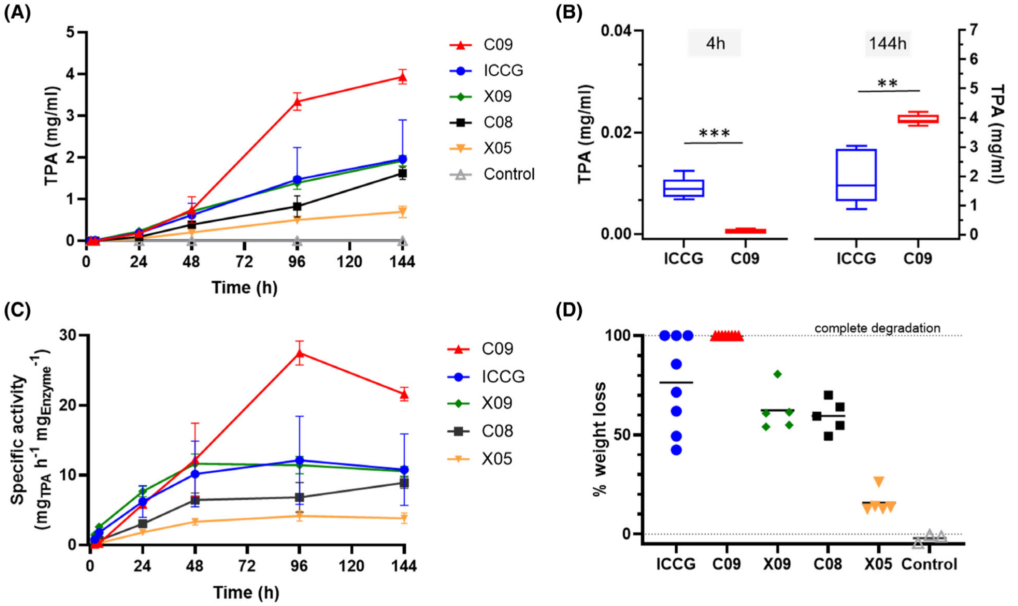

Fig. 2. Comparison of polyethylene terephthalate (PET) depolymerization over time for all enzymes. (A) Terephthalic acid (TPA) production over time at 68 °C (LCC-ICCG – C09 – X05 – X09 – C08 40 nM, pH 8.0). Means ± standard deviations ($n = 5$) are shown. Data points have been reused in Figs S3A and S5. (B) Comparison of TPA production at 68 °C at 4 h and at 144 h. $^{**}P < 0.01$; $^{***}P < 0.001$ (one-tailed unpaired Welch's *t*-test). Means ± standard deviations ($n = 5$) are shown. Data points have been reused in Fig. S5. (C) Enzyme-specific activity at the different time points (LCC-ICCG – C09 – X05 – X09 – C08 40 nM, 68 °C, pH 8.0). Means ± standard deviation ($n = 5$) are shown. Data points at 144 h have been reused in Fig. S6B. (D) Percentage of PET film weight loss after treatment (6 days at 68 °C, LCC-ICCG and C09 $n = 8$, X09 – C08 –X05 $n = 5$, control $n = 3$). The mean % of weight loss (black bar) for LCC-ICCG at day 6 is 76%, while it is 100% for C09.

expected to be negligible only for $T < T_m$ [29]. Therefore, by increasing the T_m to 97.1 °C, the denaturation effects may be significantly reduced at the working temperature (68 °C), thus possibly explaining the gain in activity of the C09 design. The stabilization of the catalytic triad is confirmed by MD simulations, which show that at increasing temperatures C09 features a lower RMSF, in particular near the key catalytic residue H242 (Fig. 3C).

Discussion

Despite *Is*PETase being initially considered a promising enzyme for PET degradation, multiple studies have shown that thermophilic PET hydrolases (e.g., LCC), when operating at temperatures above 65 °C, outperform mesophilic enzymes in PET biorecycling [30]. Since its publication in 2020, the LCC-ICCG variant has been considered the state-of-the-art PETase enzyme. Hence, starting from this variant, we set out to engineer a novel enzyme with enhanced thermal stability and enzymatic activity. The resulting LCC-ICCG-C09 design featured a significant improvement in terms of thermal stability ($T_m = 97.1$ °C) with respect to the gold standard LCC-ICCG (+3.5 °C). Under optimal reaction conditions (68 °C) and at laboratory scale, the LCC-ICCG-C09 enzyme hydrolyzed low-crystallinity PET materials into TPA with a 2-fold higher efficiency compared to LCC-ICCG. The LCC-ICCG-C09 variant may represent a further step towards PET biorecycling. However, further work will be needed to test this enzyme in industrially relevant conditions. The LCC-ICCG-C09 variant could also provide the basis for further rounds of enzyme engineering.

Recent studies reported in the literature adopted similar approaches to ours, introducing substitutions to the LCC-ICCG enzyme to boost its performance and reporting different degrees of success [26,28,31,32] However, as reported in relevant reviews [33,34] direct

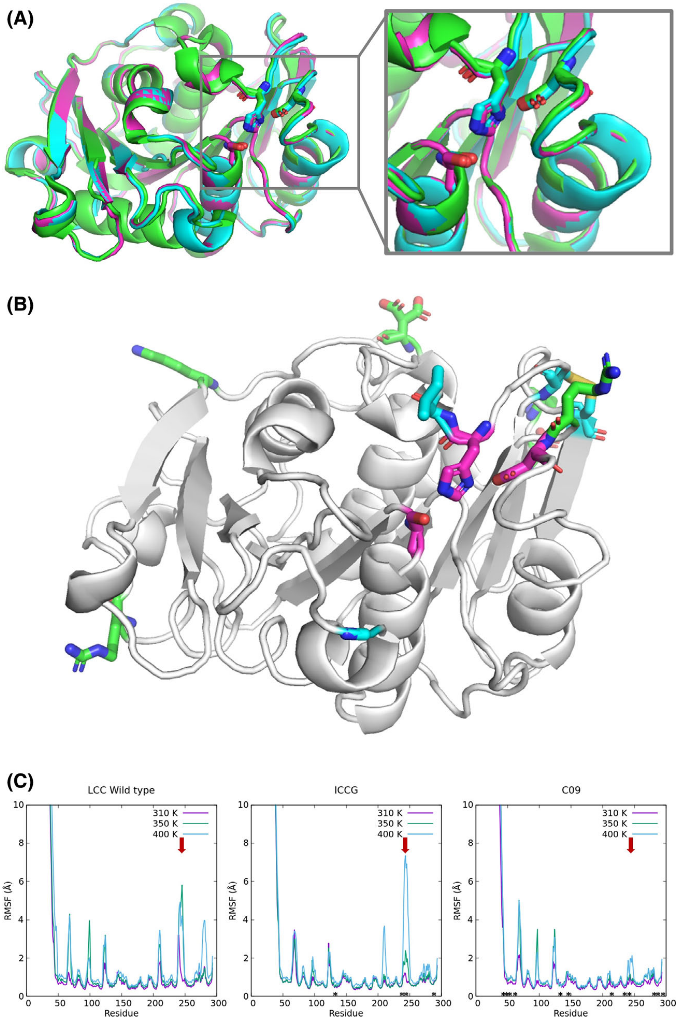

Fig. 3. Structural comparison of relevant PETase enzymes: wild-type LCC (green), ICCG variant (cyan), and C09 variant (pink). The overall structural alignment shows no significant differences between the enzymes, including the position and the orientation of the catalytic triad (A). Panel B shows the position of mutations (sticks) in ICCG (cyan) and C09 (pink) with respect to the catalytic site (pink sticks). Panel C shows a comparison between the Root Mean Square Fluctuation (RMSF) of LCC, LCC-ICCG, and C09 at different temperatures (310, 350, and 400 K). The RMSF profiles show that the mutations (indicated with an asterisk) introduced in the C09 variant reduce the structural fluctuations of the enzyme, in particular near the catalytic residue H242 (red arrows). Figures in panel A and B are generated with the software PyMol [51].

comparison of enzymatic performances is challenging due to the numerous variables involved in the experimental settings (PET crystallinity, PET form, PET concentration, enzyme concentration, temperature, salt type and concentration, pH, etc.). In this light, only a direct comparison with a recognized gold standard in the same experimental conditions can provide reliable information.

Although the field of PETase engineering is very dynamic and is providing highly optimized enzymes, several issues still need to be thoroughly investigated to improve enzymatic PET degradation [34]. One of the major challenges is related to the economic viability of enzymatic degradation. Another challenge, more directly related to protein engineering, concerns the acidification of the medium due to the release of TPA, which reduces the performance of the PETase enzymes known to date. Hence, possible directions for enzyme engineering research could be directed towards the design of acid-tolerant PETase enzymes. Finally, while our study primarily compares newly developed enzymes with the current gold standard in a laboratory setting, we recognize the need for industrial-scale validation, such as testing with post-consumer PET in bioreactors.

Materials and methods

In silico design and selection of stabilizing mutants

We started our enzyme engineering process from the LCC-ICCG enzyme reported by Tournier *et al.* [15]. This engineered enzyme is a mutant of the wild-type leaf-branch compost cutinase (LCC) carrying 4 point mutations: F243I, Y127G, S283C, and D238C. The last two substitutions are designed to induce the formation of a second disulfide bond, in addition to the native one (C275-C292). In both enzymes, the catalytic site is centered on residue S165. The structure of the LCC-ICCG engineered enzyme is available in the Protein Data Bank (PDB code: 6THS) as the inactivated S165A variant.

In our design strategy, we applied protocols used in previous works [17–19] starting from the LCC-ICCG mutant structure after reverting amino acid 165 from Alanine to the catalytically active Serine. All residues within a distance of 5 Å from S165 were excluded from the design and were therefore left unchanged. The design was done using three separate methods, resulting in three different series of variants.

The first design strategy (C-series) was performed using the Rosetta Supercharge tool [22]. This tool was employed to reengineer the protein surface with amino acids that present a high net charge, which is reported to prevent aggregation of partially unfolded states. The design produced 1024 enzyme variants, and the best 10 based on the internal score were kept for further ranking. The Rosetta Supercharge tool directly provides a 3D model in PDB format for the proposed mutants.

In the second design strategy (P-series) we used the PROSS web server [21] to generate 9 different enzyme designs with improved packing, hydrogen bond networks, and salt bridge networks. PROSS directly provided the PDB structure of the proposed variants.

The third design strategy (X-series) employed the Disulfide-by-Design web server [23] a tool for disulfide bond prediction that allows finding pairs of amino acids that can carry cysteine substitutions in the correct orientation to form disulfides. A total of 150 pair substitutions were generated and, based on the internal scoring system, the best 10 of them were retained for further testing. In this case, we used the “Mutate Residue” tool in VMD to modify the proposed positions to cysteines.

Overall, our design campaign produced 29 different enzyme variants that were then evaluated using MD simulations; then ranked according to the method described in previous works [17–20] Briefly, we solvated each molecular model with a 15 Å pad of TIP3P water, and we introduced counter ions to neutralize the system charge, resulting in a final simulation box of ≈30.000 atoms. Hydrogen mass repartitioning was applied to allow a time step of 4 fs [35]. The systems were subjected to 1000 energy minimization steps, and it equilibrated for 1 ns at a pressure of 1 atm and at a temperature of 300 K with NAMD software [36] using AMBER19SB force field [37] non-bonded cutoff of 12 Å, rigid bonds, and particle-mesh Ewald long-range electrostatics. During the equilibration simulation, the Cα atoms of the protein were restrained by a 10 $\text{kcal·mol}^{-1}\text{·Å}^{-2}$ spring constant. The 1 μs production runs were performed using a NVT ensemble whereby all the parameters (non-bonded cutoff, and PME) were the same as in the equilibration phase. All simulations were run in triplicates. Root mean square deviations (RMSD) were monitored after each MD run to assess structural convergence, while root mean square fluctuations (RMSF) were calculated to assess the improved stability of the design. As a result, the two best structures from each design series were selected, namely design LCC-ICCG-C08, LCC-ICCG-C09, LCC-ICCG-P06, LCC-ICCG-P08, LCC-ICCG-X05, LCC-ICCG-X09. In the remainder of this document, the “LCC-IGGC-” prefix of enzyme names is omitted for brevity.

Protein expression and purification

The different codon-optimized nucleotide sequences of the designed PETase mutants were cloned in a pET26b(+) bacterial expression vector (Novagen, Malvern, Worcestershire, UK), together with a C-terminal 6His-tag. All the different mutants were transformed and expressed in *Escherichia coli* BL21 Star (DE3) cells (Invitrogen, Carlsbad, CA, USA). A sample of 4 mL of an overnight culture of the selected strain grown in the presence of 50 $\mu\text{g·mL}^{-1}$ kanamycin was inoculated into 2 L of Luria–Bertani broth (LB) at 37 °C, supplemented with 50 mg·L^{-1} kanamycin and grown until $\text{OD}_{600} = 0.6$. The expression was induced with isopropyl 1-thio-β-D-galactopyranoside (IPTG) at a final concentration of 0.1 mM followed by overnight incubation at 18 °C and

220 rpm. Cells were collected by centrifugation and resuspended in lysis buffer (20 mM Tris/HCl pH 8.0, 300 mM NaCl) supplemented with 0.2 mM protease phenylmethylsulfonyl fluoride (PMSF) and DNAse and then lysed by sonication on ice. After centrifugation (45 000 ***g*** for 40 min at 4 °C), the soluble fraction of the cell lysate was passed through a 0.45 µm filter and then loaded onto a HisTrap HP 5 mL (GE Healthcare, Chicago, IL, USA) column equilibrated with buffer A (20 mM Tris/HCl pH 8.0, 300 mM Nacl and 10 mM imidazole). The Ni affinity column was washed using 10 column volumes of buffer A. Before elution, five column volumes (CV) of buffer A supplemented with 50 mM imidazole were used to remove unspecific proteins from the resin. Then, the bound His-tagged enzyme was eluted with the same buffer supplemented with 500 mM imidazole in a linear gradient. The protein eluted completely with 250 mM imidazole. The eluted fraction was loaded onto a PD-10 desalting column pre-equilibrated with buffer C (20 mM Tris/HCl pH 8.0, 300 mM NaCl) for buffer exchange. Buffer exchange was performed simultaneously after the protein was purified. The desired protein was concentrated to ≈2 $\mathrm{mg \cdot mL^{-1}}$ using an Amicon 20 centrifugal filter with a molecular cutoff of 10 kDa and stored at −80 °C. Protein concentration was assessed using a NanoDrop OneC (Thermo Fisher Scientific, Waltham, MA, USA). Sample purity was evaluated by 12% SDS/PAGE. The final yields of all the enzymes were around 16 $\mathrm{mg \cdot L^{-1}}$ of bacterial culture.

Circular dichroism

Circular dichroism (CD) measurements were performed on a Jasco J-1500 spectropolarimeter at 20 °C. CD was performed to detect the secondary structure of different variants and to measure the thermostability of the enzyme. The spectra were determined with the following parameters: continuous scanning mode with a scanning speed of 50 $\mathrm{nm \cdot min^{-1}}$, band width 0.1 nm, data pitch 0.1 nm at 20 °C. A 1.0 mm path length quartz cuvette was used for 5 µM samples of different enzymes in 20 mM Tris/HCl pH 8.0, 150 mM NaCl. Thermal denaturation curves were measured in 1.0 mm path length cuvettes closed with a parafilm on protein solutions. Protein denaturation was induced upon increasing the temperature at a rate of 1 $\mathrm{°C \cdot min^{-1}}$ from 20 °C to 120 °C. The ellipticity at 222 nm was recorded at intervals of 0.2 °C using a 1-nm bandwidth and a response of 10 s.

The determination of the midpoints of the thermal denaturation curves (T_m) was done by fitting the data to a sigmoidal transition curve using a modified sigmoidal model [38]:

$$\mathrm{CD} = \frac{(b \cdot T - c) - (d \cdot T - e)}{\left(1 + \left(\frac{T}{a}\right)^{f}\right) + (d \cdot T - e)} \tag{1}$$

where T is the temperature, a represents the melting temperature (T_m), and the terms ($b{\cdot}T - c$) and ($d{\cdot}T - e$) account for baseline drift at low and high temperatures, respectively. The parameter f controls the steepness of the transition. This model allows for accurate fitting of CD (circular dichroism) data across the full thermal range, capturing both transition and baseline behavior (Fig. S2).

The secondary structures of all the different variants were measured at 200–250 nm wavelengths and 20 °C. Ellipticity was plotted versus wavelength with GraphPad Prism 10 software. Each recorded spectrum was the average of three scans (Figs S8, S9). CD spectra for the C09 variant were further analyzed using the K2D algorithm of the DichroWeb tool [39] (Table S2).

Enzymatic reaction

Bis(hydroxyethyl)terephthalate (BHET), mono(hydroxyethyl) terephthalate (MHET), terephthalic acid (TPA), and ethylene glycol (EG) are the major depolymerization products of the activity of the enzymes on PET. These compounds can be separated efficiently on a C18 reversed-phase high-performance liquid chromatography HPLC column, thus allowing a precise quantification of product formation. All enzyme reactions were performed at a concentration of 40 nM at 68 °C in quintuplicates in 2.0 mL microcentrifuge tubes in the reaction buffer (500 mM Tris/HCl pH 8.0, 300 mM NaCl). Amorphous, 250 µm-thick PET films (product number ES301445/11) were purchased from Goodfellow USA and cut into 6 mm diameter circular pellets using a hole puncher. Individual pellets, whose weight was around 8.4 mg, were then placed in 2 mL microcentrifuge tubes. The esterase activity of enzyme variants was assessed by monitoring the hydrolysis of p-nitrophenyl acetate (pNPA) [24]. Reactions were performed at a concentration of 0.1–1.0 µM in a 96-well microplate at 25 °C using 1 mM pNPA in a buffer containing 20 mM Tris/HCl (pH 8.0) and 300 mM NaCl. Enzymatic activity was quantified by measuring the increase in absorbance at 405 nm (Clariostar Plus), corresponding to the formation of p-nitrophenolate ($\varepsilon = 11.6\ \mathrm{mM^{-1} \cdot cm^{-1}}$) (see Fig. S6).

Reversed-phase liquid chromatography

The different compounds produced by PET hydrolytic enzymes (TPA, as well as BHET and MHET) were quantified by reversed-phase HPLC (Tables S3–S5). HPLC analyses were performed on a Shimadzu LC-2030C 3D Plus system equipped with a PDA detector, a column oven, and an autosampler (Shimadzu, Kyoto, Japan). Separations were carried out using a Kinetex C18 column (2.7 µm; 4.6 × 150 mm, Phenomenex, Torrance, CA, USA). Column temperature was maintained at 40 °C with a flow rate of 1 $\mathrm{mL \cdot min^{-1}}$. For the mobile phase, 0.1% H_3PO_4 (solvent A) and MeCN (solvent B) were used. The linear gradient mode used for the elution was as follows: 0 min, 10% B; 0–15 min, 10–40% B; 15–18 min, 40–65% B; 18–20 min, 65% B; 20–23 min, 65–10% B; 23–25 min, 10% B. At every time interval, 100 µL of the sample was collected from the reaction vial placed at the set temperature. The 0–72 h samples were diluted 21 times (50 µL of the provided sample was transferred to autosampler vial and diluted in 1 mL of 10% MeCN +0.1% H_3PO_4), whereas the 96 h and 144 h samples were diluted 101 times (10 µL of the provided sample was transferred to autosampler vial and diluted in 1 mL of 10% MeCN +0.1% H_3PO_4). Detection was accomplished via measurement of UV adsorption at 240 nm; 20 µL of each sample was injected into the system, and the degradation products were quantified against standard calibration curves ranged 0.1, 1.0, 5.0, 10.0, 50.0 (for TPA and MHET) and 0.09, 0.9, 4.4, and 43.9 (for BHET) $\mu g{\cdot}mL^{-1}$.

Protein crystallization

Crystals of the C09 mutant were grown at room temperature using the vapor diffusion method by mixing a 2 µL drop of a 10 $mg{\cdot}mL^{-1}$ protein sample with a 2 µL drop of a solution containing 0.1 M Sodium citrate tribasic dihydrate pH 5.6, 20% v/v 2-Propanol, 20% w/v Polyethylene glycol 4000. Crystals, which appeared after one week, were frozen in liquid nitrogen using 25% (v/v) glycerol as a cryoprotectant prior to X-ray diffraction data collection.

Structure determination and refinement

For the structure of the C09 mutant, the initial phases were obtained by molecular replacement using Phaser [40] and the atomic coordinates of the crystal structure of a Leaf-branch compost bacterial cutinase homolog (PDB entry 4EB0) as a search model. Refinement was performed by alternating rounds of REFMAC5 [41] and manual adjustments in Coot [42] Water molecules were added both manually and automatically using the Coot_refine tool from the CCP4 package [43] The crystallographic table is shown in the SI file in Table S6.

Acknowledgements

The authors wish to thank the personnel of the Diamond Light Source (proposal number mx32544) for help with the data collection. EP thanks the European Regional Development Fund (ERDF) project BioDrug (No. 1.1.1.5/19/A/004), the Latvian Council of Science, and the Latvian Recovery and Resilience Fund (Grant No. lzp-2020/2-0013 and grant No. 74/OSI/ZG) for financial support. SB acknowledges the Latvian Recovery and Resilience Fund and the Latvian Institute of Organic Synthesis for student grants (No. ANM_OSI_DG_31 and No. IG-2025-02). RC acknowledges the MICS (Made in Italy – Circular and Sustainable) Extended Partnership and received funding from Next-Generation EU (Italian PNRR – M 4 C2, Invest 1.3 – DD 1551.11–10-2022, PE00000004) CUP MICS C93C220052800. EP and AG wish to thank the European Union's HORIZON-WIDERA-2023-ACCESS-04 program for financial support under grant agreement 101159534 (WIDEnzymes). This manuscript reflects only the authors' views and opinions. Neither the European Union nor the granting authority can be considered responsible for them. We acknowledge the CINECA award under the ISCRA initiative (Grant code IsB26_W2EB and IsCa2_REZYME) for the availability of high-performance computing resources and support. Graphs and statistical analysis were done with GraphPad Prism 10 software. Structure figures were generated using PyMol. The graphical abstract was created with BioRender (Castagna, R. (2025) https://BioRender.com/hm2wjzf). Open access publishing facilitated by Universita degli Studi di Bologna, as part of the Wiley - CRUI-CARE agreement.

Conflict of interest

The authors declare no conflict of interest.

Author contributions

SB, RC contributed to methodology, investigation, formal analysis, writing, and editing of the manuscript. HE, TU, AR contributed to investigation. AG, EP conceptualized and designed the research, contributed to formal analysis, writing, and editing of the manuscript. All authors reviewed and approved the final version of the manuscript.

Data availability statement

All data generated or analyzed during this study are included in this published article and its Supporting Information file. The final crystallographic coordinates of the crystal structure of the C09 mutant (accession code: 8CMV) are available in the RCSB PDB (https://www.rcsb.org).

References

1 PlasticsEurope (2022) Plastics—The Facts.
2 Dick Vethaak A & Legler J (2021) Microplastics and human health: knowledge gaps should be addressed to ascertain the health risks of microplastics. *Science (1979)* **371**, 672–674.
3 Kopatz V, Wen K, Kovács T, Keimowitz AS, Pichler V, Widder J, Vethaak AD, Hollóczki O & Kenner L (2023) Micro- and Nanoplastics breach the blood–brain

barrier (BBB): biomolecular Corona's role revealed. *Nanomaterials* **13**, 1–10.

4 Windheim J, Colombo L, Battajni NC, Russo L, Cagnotto A, Diomede L, Bigini P, Vismara E, Fiumara F, Gabbrielli S *et al.* (2022) Micro- and Nanoplastics effects on protein folding and amyloidosis. *Int J Mol Sci* **23**, 10329.

5 Gabbrielli S, Colnaghi L, Mazzuoli-Weber G, Redaelli A & Gautieri A (2023) In silico analysis of Nanoplastics' and -amyloid fibrils' interactions. *Molecules* **28**, 388.

6 Ragaert K, Delva L & Van Geem K (2017) Mechanical and chemical recycling of solid plastic waste. *Waste Manag* **69**, 24–58.

7 Tokiwa Y & Suzuki T (1977) Hydrolysis of polyesters by lipases. *Nature* **270**, 76–78.

8 Müller RJ, Schrader H, Profe J, Dresler K & Deckwer WD (2005) Enzymatic degradation of poly(ethylene terephthalate): rapid hydrolyse using a hydrolase from *T. fusca*. *Macromol Rapid Commun* **26**, 1400–1405.

9 Thumarat U, Nakamura R, Kawabata T, Suzuki H & Kawai F (2012) Biochemical and genetic analysis of a cutinase-type polyesterase from a thermophilic *Thermobifida alba* AHK119. *Appl Microbiol Biotechnol* **95**, 419–430.

10 Herrero Acero E, Ribitsch D, Steinkellner G, Gruber K, Greimel K, Eiteljoerg I, Trotscha E, Wei R, Zimmermann W, Zinn M *et al.* (2011) Enzymatic surface hydrolysis of PET: effect of structural diversity on kinetic properties of cutinases from Thermobifida. *Macromolecules* **44**, 4632–4640.

11 Wei R, Oeser T, Then J, Kühn N, Barth M, Schmidt J & Zimmermann W (2014) Functional characterization and structural modeling of synthetic polyester-degrading hydrolases from *Thermomonospora curvata*. *AMB Express* **4**, 1–10.

12 Kawai F, Oda M, Tamashiro T, Waku T, Tanaka N, Yamamoto M, Mizushima H, Miyakawa T & Tanokura M (2014) A novel Ca^{2+}–activated, thermostabilized polyesterase capable of hydrolyzing polyethylene terephthalate from Saccharomonospora viridis AHK190. *Appl Microbiol Biotechnol* **98**, 10053–10064.

13 Sulaiman S, Yamato S, Kanaya E, Kim JJ, Koga Y, Takano K & Kanaya S (2012) Isolation of a novel cutinase homolog with polyethylene terephthalate-degrading activity from leaf-branch compost by using a metagenomic approach. *Appl Environ Microbiol* **78**, 1556–1562.

14 Yoshida S, Hiraga K, Takehana T, Taniguchi I, Yamaji H, Maeda Y, Toyohara K, Miyamoto K, Kimura Y & Oda K (2016) A bacterium that degrades and assimilates poly(ethylene terephthalate). *Science* **351**, 1196–1199.

15 Tournier V, Topham CM, Gilles A, David B, Folgoas C, Moya-Leclair E, Kamionka E, Desrousseaux ML, Texier H, Gavalda S *et al.* (2020) An engineered PET depolymerase to break down and recycle plastic bottles. *Nature* **580**, 216–219.

16 Radley E, Davidson J, Foster J, Obexer R, Bell EL & Green AP (2023) Engineering enzymes for environmental sustainability. *Angew Chem Int Ed Engl* **62**, e202309305.

17 Rigoldi F, Donini S, Giacomina F, Sorana F, Redaelli A, Bandiera T, Parisini E & Gautieri A (2018) Thermal stabilization of the deglycating enzyme Amadoriase i by rational design. *Sci Rep* **8**, 3042.

18 Rigoldi F, Donini S, Torretta A, Carbone A, Redaelli A, Bandiera T, Parisini E & Gautieri A (2020) Rational backbone redesign of a fructosyl peptide oxidase to widen its active site access tunnel. *Biotechnol Bioeng* **117**, 3688–3698.

19 Gautieri A, Rigoldi F, Torretta A, Redaelli A & Parisini E (2022) In silico engineering of enzyme access tunnels. *Methods Mol Biol* **2397**, 203–225.

20 Estiri H, Bhattacharya S, Buitrago JAR, Castagna R, Legzdiņa L, Casucci G, Ricci A, Parisini E & Gautieri A (2023) Tailoring FPOX enzymes for enhanced stability and expanded substrate recognition. *Sci Rep* **13**, 18610.

21 Goldenzweig A, Goldsmith M, Hill SE, Gertman O, Laurino P, Ashani Y, Dym O, Unger T, Albeck S, Prilusky J *et al.* (2016) Automated structure- and sequence-based Design of Proteins for high bacterial expression and stability. *Mol Cell* **63**, 337–346.

22 Der BS, Kluwe C, Miklos AE, Jacak R, Lyskov S, Gray JJ, Georgiou G, Ellington AD & Kuhlman B (2013) Alternative computational protocols for supercharging protein surfaces for reversible unfolding and retention of stability. *PLoS One* **8**, e64363.

23 Craig DB & Dombkowski AA (2013) Disulfide by design 2.0: a web-based tool for disulfide engineering in proteins. *BMC Bioinformatics* **14**, 346.

24 Pirillo V, Pollegioni L & Molla G (2021) Analytical methods for the investigation of enzyme-catalyzed degradation of polyethylene terephthalate. *FEBS J* **288**, 4730–4745.

25 Bell EL, Smithson R, Kilbride S, Foster J, Hardy FJ, Ramachandran S, Tedstone AA, Haigh SJ, Garforth AA, Day PJR *et al.* (2022) Directed evolution of an efficient and thermostable PET depolymerase. *Nat Catal* **5**, 673–681.

26 Fritzsche S, Tischer F, Peukert W & Castiglione K (2023) You get what you screen for: a benchmark analysis of leaf branch compost cutinase variants for polyethylene terephthalate (PET) degradation. *React Chem Eng* **8**, 2156–2169.

27 Patel A, Chang AC, Mastromonaco A, Acosta Diaz M, Perry S, Ferki O, Ayafor C, Abid U, Wong HW, Xie D *et al.* (2023) Aqueous buffer solution-induced crystallization competes with enzymatic

depolymerization of pre-treated post-consumer poly (ethylene terephthalate) waste. *Polymer* **285**, 126370.

28 Arnal G, Anglade J, Gavalda S, Tournier V, Chabot N, Bornscheuer UT, Weber G & Marty A (2023) Assessment of four engineered PET degrading enzymes considering large-scale industrial applications. *ACS Catalysis* **13**, 13156–13166.

29 Bianco V, Pagès-Gelabert N, Coluzza I & Franzese G (2017) How the stability of a folded protein depends on interfacial water properties and residue-residue interactions. *J Mol Liq* **245**, 129–139.

30 Kawai F (2021) The current state of research on PET hydrolyzing enzymes available for biorecycling. *Catalysts* **11**, 1–10.

31 Ding Z, Xu G, Miao R, Wu N, Zhang W, Yao B, Guan F, Huang H & Tian J (2023) Rational redesign of thermophilic PET hydrolase LCCICCG to enhance hydrolysis of high crystallinity polyethylene terephthalates. *J Hazard Mater* **453**, 131386.

32 Zeng W, Li X, Yang Y, Min J, Huang JW, Liu W, Niu D, Yang X, Han X, Zhang L *et al.* (2022) Substrate-binding mode of a thermophilic PET hydrolase and engineering the enzyme to enhance the hydrolytic efficacy. *ACS Catalysis* **12**, 3033–3040.

33 Wei R, Von Haugwitz G, Pfaff L, Mican J, Badenhorst CPS, Liu W, Weber G, Austin HP, Bednar D, Damborsky J *et al.* (2022) Mechanism-based design of efficient PET hydrolases. *ACS Catalysis* **12**, 3382–3396.

34 Tournier V, Duquesne S, Guillamot F, Cramail H, Taton D, Marty A & André I (2023) Enzymes' power for plastics degradation. *Chem Rev* **123**, 5612–5701.

35 Hopkins CW, Le Grand S, Walker RC & Roitberg AE (2015) Long-time-step molecular dynamics through hydrogen mass repartitioning. *J Chem Theory Comput* **11**, 1864–1874.

36 Nelson MT, Humphrey W, Gursoy A, Dalke A, Kale LV, Skeel RD & Schulten K (1996) NAMD: a parallel, object oriented molecular dynamics program. *Int J Supercomp Appl High Perform Comput* **10**, 251–268.

37 Tian C, Kasavajhala K, Belfon KAA, Raguette L, Huang H, Migues AN, Bickel J, Wang Y, Pincay J, Wu Q *et al.* (2020) Ff19SB: amino-acid-specific protein backbone parameters trained against quantum mechanics energy surfaces in solution. *J Chem Theory Comput* **16**, 528–552.

38 Then J, Wei R, Oeser T, Gerdts A, Schmidt J, Barth M & Zimmermann W (2016) A disulfide bridge in the calcium binding site of a polyester hydrolase increases its thermal stability and activity against polyethylene terephthalate. *FEBS Open Bio* **6**, 425–432.

39 Miles AJ, Ramalli SG & Wallace BA (2022) DichroWeb, a website for calculating protein secondary structure from circular dichroism spectroscopic data. *Protein Sci* **31**, 37–46.

40 McCoy AJ, Grosse-Kunstleve RW, Adams PD, Winn MD, Storoni LC & Read RJ (2007) Phaser crystallographic software. *J Appl Cryst* **40**, 658–674.

41 Murshudov GN, Skubák P, Lebedev AA, Pannu NS, Steiner RA, Nicholls RA, Winn MD, Long F, Vagin AA, Skubak P *et al.* (2011) REFMAC5 for the refinement of macromolecular crystal structures. *Acta Crystallogr D Biol Crystallogr* **67**, 355–367.

42 Winn MD, Ballard CC, Cowtan KD, Dodson EJ, Emsley P, Evans PR, Keegan RM, Krissinel EB, Leslie AGW, McCoy A *et al.* (2011) Overview of the CCP4 suite and current developments. *Acta Crystallogr D Biol Crystallogr* **67**, 235–242.

43 Kovalevskiy O, Lebedev A & Krissinel E (2021) Helping researchers to solve their structures: automation and user guidance in CCP4 cloud. *Acta Crystallogr A Found Adv* **77**, C766.

44 Son HF, Cho IJ, Joo S, Seo H, Sagong HY, Choi SY, Lee SY & Kim KJ (2019) Rational protein engineering of thermo-stable PETase from Ideonella sakaiensis for highly efficient PET degradation. *ACS Catalysis* **9**, 3519–3526.

45 Meng X, Yang L, Liu H, Li Q, Xu G, Zhang Y, Guan F, Zhang Y, Zhang W, Wu N *et al.* (2021) Protein engineering of stable IsPETase for PET plastic degradation by Premuse. *Int J Biol Macromol* **180**, 667–676.

46 Brott S, Pfaff L, Schuricht J, Schwarz JN, Böttcher D, Badenhorst CPS, Wei R & Bornscheuer UT (2022) Engineering and evaluation of thermostable IsPETase variants for PET degradation. *Eng Life Sci* **22**, 192–203.

47 Cui Y, Chen Y, Liu X, Dong S, Tian Y, Qiao Y, Mitra R, Han J, Li C, Han X *et al.* (2021) Computational redesign of a PETase for plastic biodegradation under ambient condition by the GRAPE strategy. *ACS Catalysis* **11**, 1340–1350.

48 Pfaff L, Gao J, Li Z, Jäckering A, Weber G, Mican J, Chen Y, Dong W, Han X, Feiler CG *et al.* (2022) Multiple substrate binding mode-guided engineering of a thermophilic PET hydrolase. *ACS Catalysis* **12**, 9790–9800.

49 Lu H, Diaz DJ, Czarnecki NJ, Zhu C, Kim W, Shroff R, Acosta DJ, Alexander BR, Cole HO, Zhang Y *et al.* (2022) Machine learning-aided engineering of hydrolases for PET depolymerization. *Nature* **604**, 662–667.

50 Shi L, Liu P, Tan Z, Zhao W, Gao J, Gu Q, Ma H, Liu H & Zhu L (2023) Complete depolymerization of PET wastes by an evolved PET hydrolase from directed evolution. *Angew Chem Int Ed Engl* **62**, e202218390.

51 DeLano WL (2002) Pymol: an open-source molecular graphics tool. *CCP4 Newsletter Protein Crystallogr* **40**, 82–92.

Supporting information

Additional supporting information may be found online in the Supporting Information section at the end of the article.

Fig. S1. Sequence alignment.

Fig. S2. Representative melting curves.

Fig. S3. Product formation and PET film degradation.

Fig. S4. Time course of the terephthalic acid (TPA) production from different enzymes.

Fig. S5. Terephthalic acid (TPA) production from different enzymes.

Fig. S6. Comparison of the specific activity of each enzyme variant against p-Nitrophenyl Acetate (pNPA) and Polyethylene terephthalate (PET).

Fig. S7. Electrostatic potential surfaces, calculated by the Adaptive Poisson-Boltzmann Solver module as implemented in PyMol for ICCG (A) and C09 (B).

Fig. S8. Secondary structure measurements by circular dichroism.

Fig. S9. Secondary structure measurements by circular dichroism.

Table S1. Production yields of the recombinant enzyme variants.

Table S2. Experimental and predicted secondary structures for the C09 enzyme.

Table S3. Terephthalic Acid (TPA) production as measured by high-performance liquid chromatography.

Table S4. Mono(hydroxyethyl)terephthalate (MHET) production as measured by high-performance liquid Chromatography.

Table S5. Bis(hydroxyethyl)terephthalate (BHET) production as measured by high-performance liquid chromatography.

Table S6. Diffraction data collection and refinement statistics.

4. Pielikums
Appendix 4

Berselli, A.; Carletti, A.; Menziani, M. C.; **Bhattacharya, S**.; Castagna, R.; Parisini, E.; Di Rocco, G.; Muniz-Miranda, F.

The Effect of Ionic Strength on PETase Enzymes: An Experimental and Computational Study

Protein Science, 2026, 35, e70386
doi:10.1002/pro.70386

Publikācija un tās pielikums pieejams bez maksas izdevēja mājaslapā

The Publication and Supporting Information is available free of charge on the publisher's website

Received: 29 July 2025 | Revised: 29 October 2025 | Accepted: 31 October 2025

DOI: 10.1002/pro.70386

RESEARCH ARTICLE

The effect of ionic strength on PETase enzymes: An experimental and computational study

Alessandro Berselli[1] | **Alan Carletti**[2] | **Maria Cristina Menziani**[1] | **Shapla Bhattacharya**[3,4] | **Rossella Castagna**[3,5] | **Emilio Parisini**[3,6] | **Giulia di Rocco**[2] | **Francesco Muniz-Miranda**[1]

[1]Department of Chemical and Geological Sciences (DSCG), University of Modena and Reggio Emilia (UNIMORE), Modena, Italy

[2]Department of Life Sciences (DSV), University of Modena and Reggio Emilia (UNIMORE), Modena, Italy

[3]Department of Biotechnology, Latvian Institute of Organic Synthesis, Riga, Latvia

[4]Faculty of Natural Sciences and Technology, Riga Technical University, Riga, Latvia

[5]Department of Chemistry, Materials and Chemical Engineering "G. Natta", Politecnico di Milano, Milan, Italy

[6]Department of Chemistry "G. Ciamician", University of Bologna, Bologna, Italy

Correspondence
Alessandro Berselli and Francesco Muniz-Miranda, Department of Chemical and Geological Sciences (DSCG), University of Modena and Reggio Emilia (UNIMORE), Via Campi, 103, 41125 Modena, Italy.
Email: alessandro.berselli@unimore.it and francesco.munizmiranda@unimore.it

Funding information
Ministero dell'Università e della Ricerca, Grant/Award Number: 2022W9XTYB

Review Editor: Lynn Kamerlin

Abstract

Over recent decades, various enzymes capable of breaking down polyethylene terephthalate (PET) have emerged as sustainable tools for plastic waste management. Among them, IsPETase from *Ideonella sakaiensis* 201-f6 stands out for its high catalytic activity at low temperatures. However, the discovery of the PETase-like enzyme from the marine sponge *Streptomyces* sp. SM14 (PETaseSM14) has introduced a new class of biocatalysts active at high-salt concentrations, whose structural and catalytic properties remain poorly understood. This study explores the structural and catalytic behavior of both IsPETase and PETaseSM14 under varying ionic strength (from 150 to 900 mM of NaCl concentration) using all-atom molecular dynamics simulations and in vitro assays. Results reveal that the flexible, enlarged binding site of IsPETase improves substrate accommodation but also causes catalytic residue displacement and rapid deactivation, particularly under high-salt conditions. In contrast, PETaseSM14 has a smaller, more rigid binding pocket that undergoes moderate widening upon salt concentration increasing, thus promoting water and substrate recruitment. Additionally, active forms of both enzymes bind PET chains in conformations similar to those found in amorphous PET. These findings offer key structural insights that can inform future enzyme engineering efforts for effective PET degradation tailored to diverse environmental conditions.

KEYWORDS

Ideonella Sakaiensis 201-f6, molecular dynamics simulations, PETase, salt tolerance, Streptomyces sp. SM14

1 | INTRODUCTION

The abuse and improper waste management of plastic materials has become a pressing issue for human health. Due to their persistency in nature, plastics accumulated in the environment are fragmented into smaller pieces, originating microplastics that migrate via rivers and oceans, forming accumulating zones named "garbage patches" (Lee et al., 2022). As a consequence of the widespread

---

Abbreviations: AFM, atomic force microscopy; BHET, bis(hydroxyethyl) terephthalate; CG, coarse-grained; CGenFF, CHARMM general force field; DFT, density functional theory; HPLC, high performance liquid chromatography; MD, molecular dynamics; MHET, mono(hydroxyethyl) terephthalate; PAZy, plastic-active enzymes database; PBCs, periodic boundary conditions; PET, polyethylene terephthalate; QM/MM, quantum mechanics/molecular mechanics; RMSD, root-mean-square deviation; RMSF, root-mean-square fluctuation; SASA, solvent accessible surface area; TPA, terephthalic acid; WT, wild type.

diffusion of these exogenous materials in the habitats, many organisms adapted their metabolism to use plastic compounds as a new source of carbon, leading to the development of several plastic-degrading enzymes (Ruginescu & Purcarea, 2024).

The first reports of microbial strains capable of degrading aliphatic synthetic polyesters date back to the 1970s (Potts et al., 1973; Tokiwa & Suzuki, 1977), but the role of enzymes in plastic depolymerization was recognized about 30 years later, with the documentation of the biocatalytic hydrolysis of polyethylene terephthalate (PET) (Müller et al., 2005). Since that discovery, the number of PET-active enzymes isolated and characterized increased considerably, offering a great opportunity for humans to exploit the naturally evolved biotechnological systems to face the environmental challenge of plastic pollution (Samak et al., 2020; Wei & Zimmermann, 2017; Zimmermann & Billig, 2011).

Today, the plastic-active enzymes database (PAZy) (Buchholz et al., 2022) includes 311 distinct wild-type (WT) PET hydrolytic enzymes biochemically characterized. Most of them exhibit peak activity under thermophilic conditions, close to the glass transition temperature of PET (~61°C for amorphous dry PET and ~79°C for high-crystallinity dry PET, reduced by up to 16°C in water; Chen et al., 1998; Groeninckx et al., 1974; Launay et al., 1999), due to the formation of flexible and enzyme-accessible amorphous domains (Alves et al., 2002). The isolation of the enzyme PETase from the bacterial strain *Ideonella Sakaiensis* 201-f6 (referred to as IsPETase hereafter) (Yoshida et al., 2016), in 2016, represented a turning point in this field. By converting PET mainly into mono- and bis-hydroxyethyl terephthalate (MHET, BHET) and terephthalic acid (TPA), this enzyme outperformed other homologous cutinases (Müller et al., 2005; Silva et al., 2005; Sulaiman et al., 2012; Yoshida et al., 2016) in terms of catalytic activity at low temperatures thanks to the enhanced flexibility of its binding site, which facilitates the substrate recruitment even for relatively rigid PET chains (Berselli et al., 2021; Fecker et al., 2018). As a drawback of the higher binding site's plasticity, the catalytic efficiency of IsPETase drops at higher temperatures, hindering industrial application (de Castro et al., 2017; Kawai et al., 2024). For this reason, in recent years, huge efforts have been made to engineer mutants of IsPETase featuring higher catalytic activity and thermostability (Arnal et al., 2023; Bell et al., 2022; Cui et al., 2021; Cui et al., 2024; Joo et al., 2018; Lu et al., 2022; Son et al., 2019; Sun et al., 2021). While IsPETase adapted to work at relatively low temperatures (~37°C), the structure of other PETase-like enzymes optimized towards the conditions of their native habitat. A remarkable example is the marine-sponge derived *Streptomyces* sp. SM14 PETase (referred to as PETaseSM14 hereafter) (Almeida et al., 2019; Carr et al., 2023). Although belonging to the same family as IsPETase, this enzyme exhibits distinctive structural characteristics that evolved to adapt to the high-salt conditions of the marine environment. Indeed, in a previous study performed by some of us (Carletti et al., 2025), it was shown that PETaseSM14 exerts catalytic activity enhanced in the presence of high concentrations of NaCl, peaking at 900 mM. This characteristic is contrary to that observed for IsPETase, which degrades PET under low salt conditions but quickly deactivates with the increasing ionic strength.

From a structural point of view, IsPETase and PETaseSM14 are serine hydrolases, characterized by a conserved Gly-x1-Ser-x2-Gly motif and a catalytic triad composed of serine (S155/S160 in PETaseSM14 and IsPETase, respectively), histidine (H234/H237 in PETaseSM14 and IsPETase, respectively) and aspartate (D202/D206 in PETaseSM14 and IsPETase, respectively) that exert the PET hydrolysis (Almeida et al., 2019; Austin et al., 2018; Berselli et al., 2021; Fecker et al., 2018; Joo et al., 2018). Both enzymes consist of a single domain, resembling the typical folding of an α/β hydrolase (Ollis et al., 1992), characterized by a central nine-stranded twisted β-strand, surrounded by seven α-helices (Figure 1a). The binding site of the two proteins include the catalytic triad, a methionine (M157/M161) and a tyrosine (Y88/Y87), whose backbone form the *oxyanion hole* that stabilize the intermediate states during the reaction (Berselli et al., 2025; Burgin et al., 2024; Jerves et al., 2021). Moreover, a tryptophane (W181/W185) and an isoleucine (I204/I208), together with the tyrosine side chain, constitute a superficial hydrophobic scaffold that anchor the PET chains for binding (Figure 1b) (Berselli et al., 2024; Joo et al., 2018).

However, relevant differences exist between the two enzymes. For instance, the IsPETase W159 is replaced by a histidine (H155) in PETaseSM14 (residue x1 in the Gly-x1-Ser-x2-Gly motif). Moreover, IsPETase is characterized by (i) an extra turn extension of the α 2-helix due to a three-residue insertion (Figure S1), (ii) the inclusion of three 3_{10}-helices, and (iii) the presence of two disulfide bonds (C203-C239 and C273-C289) that confer enhanced flexibility to the binding site, helping substrate recognition and binding (Berselli et al., 2021; Fecker et al., 2018).

Although the halophilic nature of PETaseSM14 and the low salt tolerance of IsPETase have been experimentally assessed (Almeida et al., 2019; Carletti et al., 2025; Carr et al., 2023), a precise molecular understanding of how salt concentrations affects their structure and PET binding at the catalytic site is still lacking.

In this study, we expand our previous assessment of the salt-concentration-dependent enzymatic activities of PETaseSM14 and IsPETase (originally performed on post-consumer plastics) (Carletti

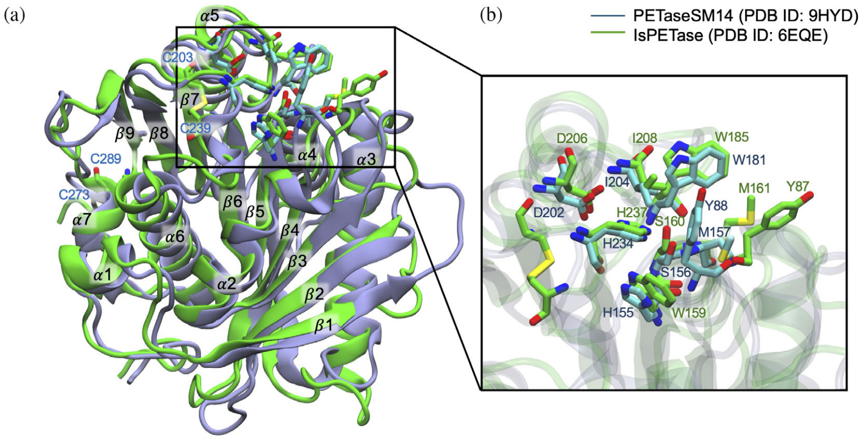

FIGURE 1 Three-dimensional structure of PETaseSM14 and IsPETase. (a) Structural superposition of the crystallographic structure of PETaseSM14 (blue structure, PDB ID: 9HYD) (Carletti et al., 2025) and IsPETase (green structure, PDB ID: 6EQE) (Austin et al., 2018). (b) Close-up view of the enzymes' binding sites.

et al., 2025) by using PET powder as a uniform substrate. We combine experimental assays with all-atom molecular dynamics (MD) simulations to investigate how different ionic strengths (150 and 900 mM NaCl) influence the structural plasticity of the enzymes' binding sites and their interaction with PET chains modeled as entangled 9-mer slabs (Sahihi et al., 2024).

Our findings elucidate the mechanistic differences in flexibility, hydration, and active-site stability that underlie the divergent salt responses of these homologous enzymes, and provide insights for specific targeted modifications to enhance the catalytic performance of PETase-like enzymes across different habitats.

2 | RESULTS

2.1 | PETaseSM14 and IsPETase exhibit different activity profiles in the presence of NaCl

The activity of IsPETase and PETaseSM14 was evaluated in previous work using PET film and post-consumer plastic as substrates (Carletti et al., 2025; Di Rocco et al., 2023). The optimal reaction conditions established in those studies were applied here to assess the enzymatic activity on pure PET powder. PETaseSM14 and IsPETase activities were assessed using 5 mg mL^{-1} of PET powder and allowing the reaction to run for 72 h in the presence of 0, 150, 300, 700, and 900 mM of NaCl. Calibration curves for TPA were generated using standard solutions and the relative standard deviation was evaluated for three consecutive runs, yielding a solid linear relationship ($r^2 = 0.9974$ for TPA signal at 1.7 min and $r^2 = 0.9998$ for TPA signal at 2.1 min) (Figure S2). The linear regression parameters were then used to quantify the TPA concentration of all samples. The amount of TPA released from the enzymatic activity is reported in Figure 2 as a function of salt concentration, including values at 150 and 900 mM of NaCl, consistent with those used in the simulations reported hereafter. In the presence of NaCl, the two enzymes displayed opposite behaviors:

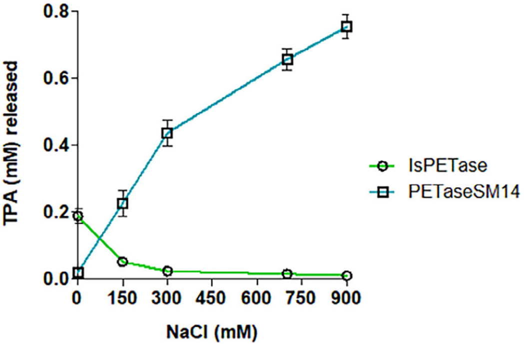

FIGURE 2 Analysis of the activity in the presence of 0, 150, 300, 700, and 900 mM NaCl on PET powder after 72 h of incubation at 37°C with 400 rpm for (green line) IsPETase, (blue line) PETaseSM14. The protein concentration was 1 μM and the buffer used are: 100 mM Tris–HCl buffer at pH 8.0 for IsPETase and 100 mM Tris–HCl pH 9.0 for PETaseSM14. The data and the associated errors are reported as the mean and standard deviation of the triplicate. When not visible, the error bars fall within the size of the symbols.

PETaseSM14 exhibited a pronounced increase in TPA production, achieving the highest activity at 900 mM of salts, as remarked in a previous study (Carletti et al., 2025). In contrast, IsPETase activity was drastically reduced in the presence of high salts concentration, showing a decrease of almost 90% in TPA release at 900 mM of NaCl.

Therefore, analytical investigation shows that a greater amount of NaCl exerts a positive impact on PETaseSM14 activity but inhibits IsPETase. However, the structural basis of these effects remains unclear. In the following, we integrate these experimental findings with a detailed in silico analysis to investigate how variations in ionic strength influence the structural properties of the two enzymes and to provide a molecular-level understanding of their contrasting responses to salt concentration.

2.2 | PETaseSM14 and IsPETase exhibit different flexibility of the binding domains

Given the different activity observed for the two enzymes at varying ion concentrations, we performed a molecular-level comparison of their structural properties and their PET-binding characteristics using MD simulations. To investigate the enzyme-substrate interactions, each protein was adsorbed onto a PET slab, used as a proxy for a realistic substrate (Sahihi et al., 2024), and solvated at 150 and 900 mM of NaCl concentrations.

The structural stability of these systems was assessed by computing the root-mean square deviation (RMSD) of the protein backbones over time. The results reported in Figure S3a show that each system reaches a plateau between 1.3 and 1.8 Å after approximately 100 ns of MD simulation, indicative of global stability of the tertiary structures. Despite the similarities in terms of global rearrangements highlighted for the four systems, relevant differences are found in the local displacements of the protein domains, as shown by the root-mean square fluctuations (RMSF) displayed in Figure S3b. In particular, the regions corresponding to residues from 200 to 210 (labeled as domain “1”) and from 230 to 250 (labeled as domain “2”) include the catalytic residues D202/D206 and H234/H237 in PETaseSM14 and IsPETase, respectively (Figure S3c).

The analysis reveals that amino acid stretches with RMSF values of 1.8 and 2.7 Å for IsPETase (green and red traces for 150 and 900 mM of ion concentration, respectively). In contrast, values below 1 Å are observed for PETaseSM14 at 150 mM (blue trace), with a marginal increase observed at 900 mM (orange trace). This difference is mainly due to the well-known three-residue insertion in the α 6–β 8 loop of IsPETase (Figure S1), which confers to the enzyme's binding site a higher flexibility compared to PETaseSM14, and the other homologous serine hydrolases (Austin et al., 2018; Berselli et al., 2021; Berselli et al., 2024; Fecker et al., 2018; Joo et al., 2018). This characteristic is peculiar to IsPETase and it is crucial for the recruitment of the PET substrate, enabling this enzyme to outperform other hydrolases in terms of catalytic efficiency under mild conditions (low temperature and physiological ion concentration) (Fecker et al., 2018; Han et al., 2017; Joo et al., 2018). Additionally, from the superposition of the crystallographic conformations of the binding sites of the two enzymes (Figure 1b, IsPETase in green, PDB ID: 6EQE [Austin et al., 2018], PETaseSM14 in cyan, PDB ID: 9HYD [Carletti et al., 2025]) it can be observed an optimal overlap of the side chains of each amino acid, except for Y87/Y88. Indeed, this residue faces the I204 and W181 side chains in PETaseSM14, whereas it is shifted away from the binding site and exposed to the bulk solvent in IsPETase.

2.3 | The widening of the IsPETase binding site compromises the stability of the catalytic triad

The structural differences between the binding sites of PETaseSM14 and IsPETase result in distinct degrees of opening and overall size of the cleft, modulating the accessibility of both the solvent and the substrate.

To quantitatively assess the extent of cleft opening under different ionic strengths, we measured the inter-residue distances between the key hydrophobic solvent-exposed amino acids responsible for the binding and stabilization of the PET chains. The atoms considered in each calculation are listed in Table 1. Specifically, the distances between Y87/Y88 and I208/I204 (d1, Figure 3a), and between Y87/Y88 and W185/W181 (d2, Figure 3b), were used as geometric proxies to estimate the width of the cleft and the surface available for substrate accommodation. In PETaseSM14, d1 remains stable between 6.5 and 7.0 Å at both 150 and 900 mM concentrations (Figure 3a, blue and orange traces, respectively). On the other hand, IsPETase exhibits a considerably larger d1 value of approximately 9 Å, on average, at 150 mM, which increases to around 10.7 Å at 900 mM (Figure 3a, green and red traces, respectively). Regarding d2, PETaseSM14 shows an increase from ~8.5 Å at 150 mM to ~10.5 Å at 900 mM, whereas IsPETase maintains a constant value around 10–10.5 Å across both conditions. These results suggest that the inherently narrower and more rigid cleft of PETaseSM14 undergoes moderate widening at elevated ionic strength, with d2 increasing by 2 Å on average. Conversely, the cleft of IsPETase is already wide at 150 mM and exhibits only a slight expansion at 900 mM.

This structural variability has direct implications for substrate accessibility and the stability of the catalytic

TABLE 1 Atoms used in the calculation of inter-residue distances.

Distance	System	Residue1 (Atom1)	Residue2 (Atom2)
d1	PETaseSM14	Y88 (OH)	I204 (CD1)
d1	IsPETase	Y87 (OH)	I208 (CD1)
d2	PETaseSM14	Y88 (OH)	W181 (CG)
d2	IsPETase	Y87 (OH)	W185 (CG)
d3	PETaseSM14	S156 (OG)	H234 (ND1)
d3	IsPETase	S160 (OG)	H237 (ND1)
d4	PETaseSM14	H155 (ND1)	N238 (CG)
d4	IsPETase	W159 (CG)	N241 (CG)

Note: The atoms considered in the calculation of each distance (d1–d4) for the two enzymes are defined according to the CHARMM nomenclature.

site. While a more open cleft in IsPETase may facilitate rapid substrate recruitment, excessive widening, particularly under high salt conditions, could destabilize the local interaction network that supports the catalytic triad. Disruption of this architecture may impair the enzymatic activity, as observed experimentally under high ionic strength (Carletti et al., 2025).

2.4 | Histidine 155 helps stabilizing the catalytic triad in PETaseSM14

To understand whether the different sizes of the enzymes' binding pockets at the two ion concentrations affect the integrity of the catalytic triad, we monitored the distance between the catalytic S160/S156 and H237/H234 side chains during the simulated trajectories (Figure 4a, d3). From this analysis, it can be observed that the d3 distance in PETaseSM14 is stable at both conditions. At 150 mM, values between 3.0 and 5.0 Å are reached (blue trace), with only a transient oscillation between 380 and 450 ns. Even greater stability is observed at 900 mM, at which d3 is confined between 2.5 and 3.0 Å for the first 400 ns, slightly increasing up to 5 Å only during the last part of the simulation (orange trace).

A different trend is observed for IsPETase. At 150 mM, the d3 distance is maintained stable below 5.0 Å for ~100 ns, then shifting to values up to 15.0 Å in the rest of the MD simulation (green trace). The disruption of the S160-H237 interaction is observed at an earlier point in the trajectory, approximately 40 ns, at 900 mM. At that time, d3 starts to increase, reaching values of around 20 Å by the end of the simulation (red trace). Based on this evidence, when the catalytic S160/S156 interacts with H237/H234 (d3 ~ 5 Å), the enzyme is defined as *active*, because this configuration can initiate the hydrolysis of the PET chain (Figure 4c) (Austin et al., 2018; Berselli et al., 2024; Fecker et al., 2018). On the other hand, when d3 is disrupted, the enzyme becomes *inactive*, since the catalytic histidine is too far from the serine and the enzyme is not able to depolymerize the substrate even if it is correctly bound to the active site.

This structural rearrangement is associated with the remodeling and opening of the IsPETase binding sites. Indeed, we found that the disruption of d3 correlates with the stability of the interaction between the residue adjacent to the catalytic serine, W159 in IsPETase and H155 in PETaseSM14, with the conserved N241/N238 side chain (Figure 4b, d4). In particular, it can be observed that d4 remains stable in PETaseSM14 during the MD simulations, with average values of ~5.0 Å at both 150 mM (blue trace) and 900 mM (orange trace) of NaCl concentration, respectively. On the other hand, the same distance (d4) between W159 and N241 slowly increases over time for IsPETase at 150 mM of ion concentration (green trace), remaining stably below 5 Å for ~120 ns, then increasing up to ~6 Å for the successive 180 ns and ultimately reaching values of ~8 Å in the last part of the MD simulation. Moreover, the d4 interaction is lost more rapidly in the MD simulation performed at 900 mM of ion concentration (red trace), increasing from ~5 to ~7.5 Å within the first 40 ns, and eventually reaching ~9 Å by the end of the trajectory.

Notably, the displacement of W159 away from N241 results in the insertion of its indole side chain between S160 and H237 (Figure 4c). This rearrangement, which coincides with the transition from the active to the inactive state in IsPETase, prevents reformation of the catalytic contact, rendering the process largely irreversible within the simulated timescale. In contrast, in PETaseSM14, H155 remains stably bound to N238 throughout the simulations, regardless of NaCl concentration (Figure 4b, d4). This configuration allows S156 and H234 to align properly within the binding cleft (Figure 4c), maintaining the enzyme in an active conformation for approximately 85% of the simulation time at 150 mM NaCl and throughout the entire trajectory at 900 mM. Furthermore, unlike IsPETase, PETaseSM14 exhibits a reversible transition between active and inactive states, as shown by the temporary fluctuations of d3 (Figure 4a), which return to a stable value of ~5 Å for the remainder of the simulation.

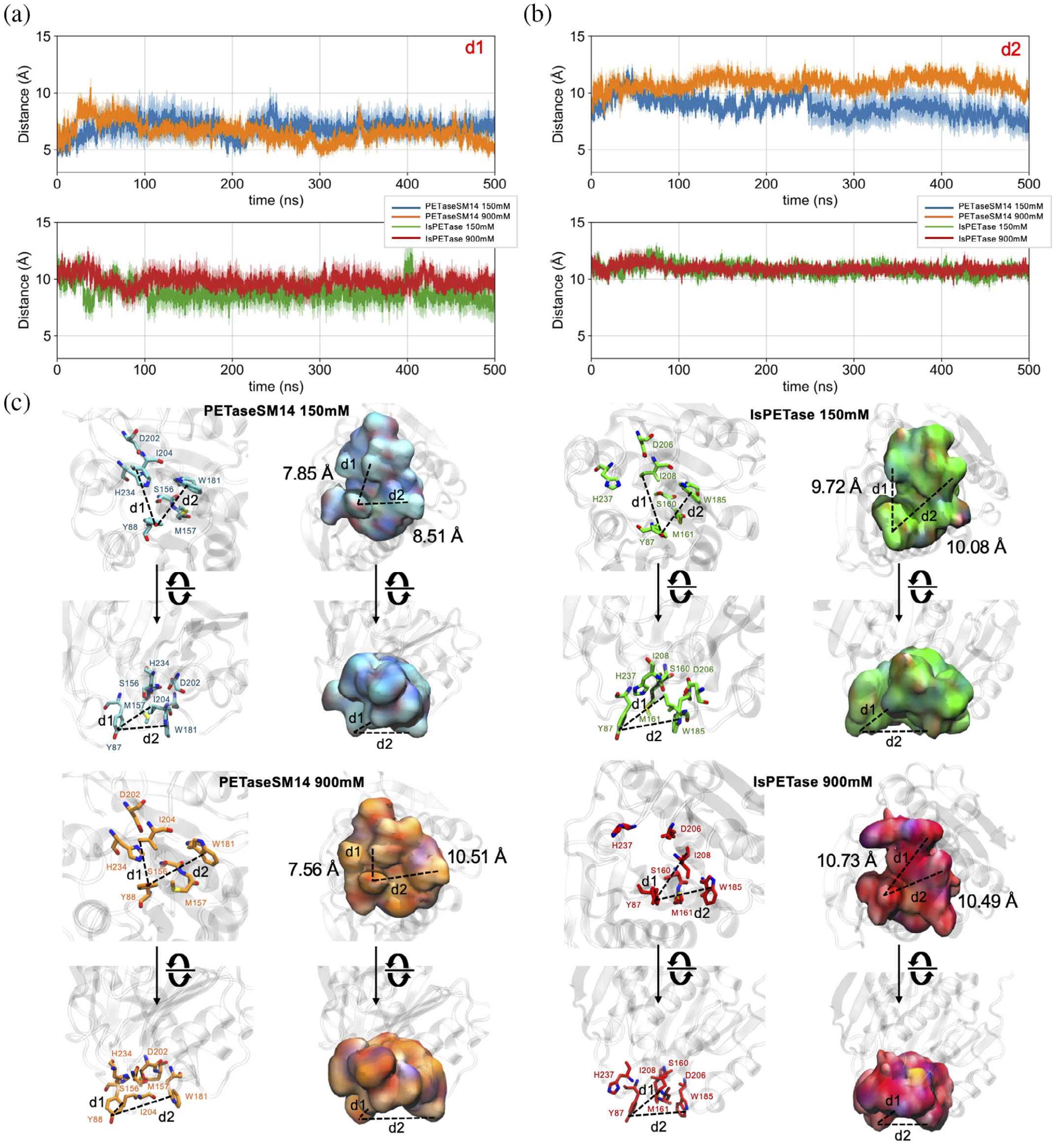

FIGURE 3 Size of the PETaseSM14 and IsPETase binding sites. The distances between (a) tyrosine and isoleucine side chains (d1) and between (b) the tyrosine and tryptophan side chains (d2) were calculated during the 500 ns-long MD simulations. The value and the associated error are reported as the average and standard deviation over the three independent replicas performed for each system. (c) Representative snapshots of the PETaseSM14 and IsPETase binding sites at varying NaCl concentrations. The d1 and d2 average values, calculated from MD simulations, are indicated.

2.5 | PETaseSM14 binding site recruits more water at a high ion concentration

The changes in size and conformation of the binding pocket observed for the two enzymes are expected to influence their accessibility to both the solvent and the substrate. As an initial assessment of the binding site hydration, we calculated the solvent-accessible surface area (SASA) of the enzymes' binding crevices (Figure 5a). This analysis showed that the solvent-

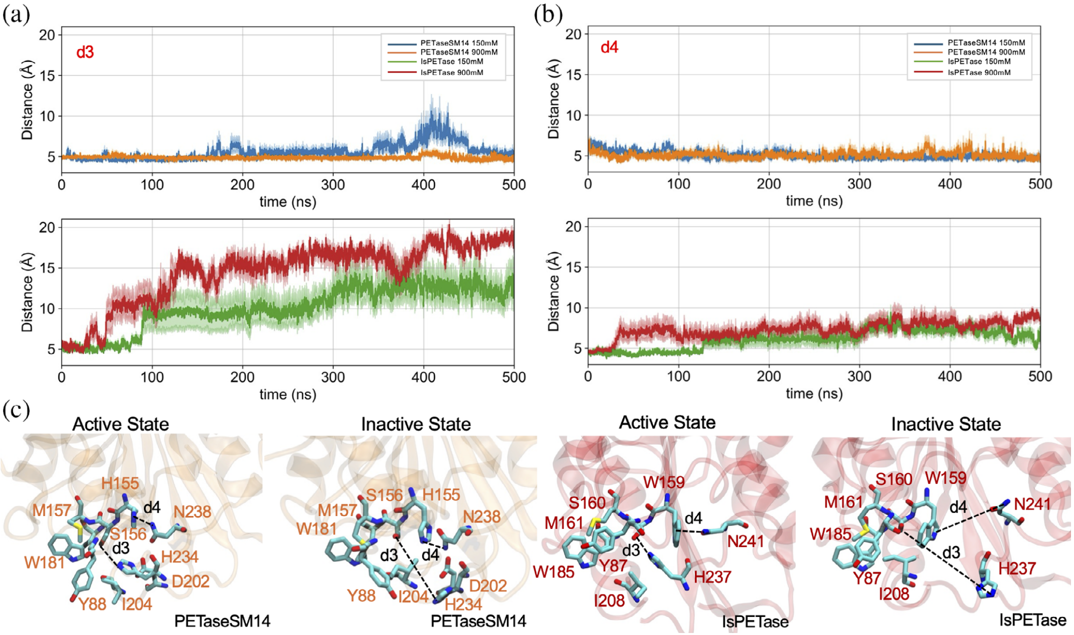

FIGURE 4 Catalytic triad stability in PETaseSM14 and IsPETase. The distances between (a) the catalytic serine and histidine side chains (d3) and between (b) H155 or W159, in PETaseSM14 and IsPETase, respectively, and the adjacent asparagine (d4) were calculated over the course of 500 ns-long MD simulations. The value and the associated error are reported as the average and standard deviation over the three independent replicas performed for each system. (c) Representative snapshots of the active and inactive states of the PETaseSM14 and IsPETase active sites are shown.

exposed surface area of PETaseSM14 is significantly lower than that found for IsPETase (Table S1). Interestingly, however, a modest yet significant ∼10% increase in solvent-exposed surface is observed for PETaseSM14 when the NaCl concentration increases from 150 to 900 mM. On the other hand, the SASA is almost identical in IsPETase at the two different conditions. This structural characteristic correlates with the number of water molecules that populate the cavity during the MD simulations (Figure 5b). This feature was calculated by adopting a 6 Å-cutoff from the catalytic serine, which is buried at the bottom of the catalytic cleft and serves as the key site for the enzymatic activity. The average number of water molecules recruited by the binding site increases by ∼35% in PETaseSM14 with raising ion concentration (Table S1). On the other hand, the binding site of IsPETase remains well hydrated under both conditions, with the number of water molecules changing by <10% as the ion concentration increases from 150 to 900 mM (Table S1). The variation in water-accessible volume within the active sites of the two enzymes at different NaCl concentrations is highlighted by the tunnels sampled with Caver (Chovancova et al., 2012). In these analyses, tunnels originating near the active site were identified from conformations obtained during MD simulations. Figure 5c highlights the most representative pathways, selected after clustering and distinguished by different colors. Notably, in PETaseSM14 at 150 mM NaCl, the tunnel openings remain largely confined to the protein surface, with only minimal penetration into the enzyme interior. At 900 mM, however, although the superficial opening of the active site remains comparable to that at lower salt concentration, the accessible tunnels extend deeper into the active site, protruding further into the protein core. By contrast, in IsPETase at both 150 and 900 mM NaCl, the tunnels consistently span a broader surface volume and penetrate more extensively into the active site.

2.6 | The increased ionic strength weakens the network of interactions within the binding site

The electrostatic potential surfaces of the two enzymes calculated at the two ion concentrations are reported in Figure 6a, b. At both conditions, PETaseSM14 exhibits a predominant acidic character (red regions) consistent with its lower isoelectric point (pI = 6.34) compared to

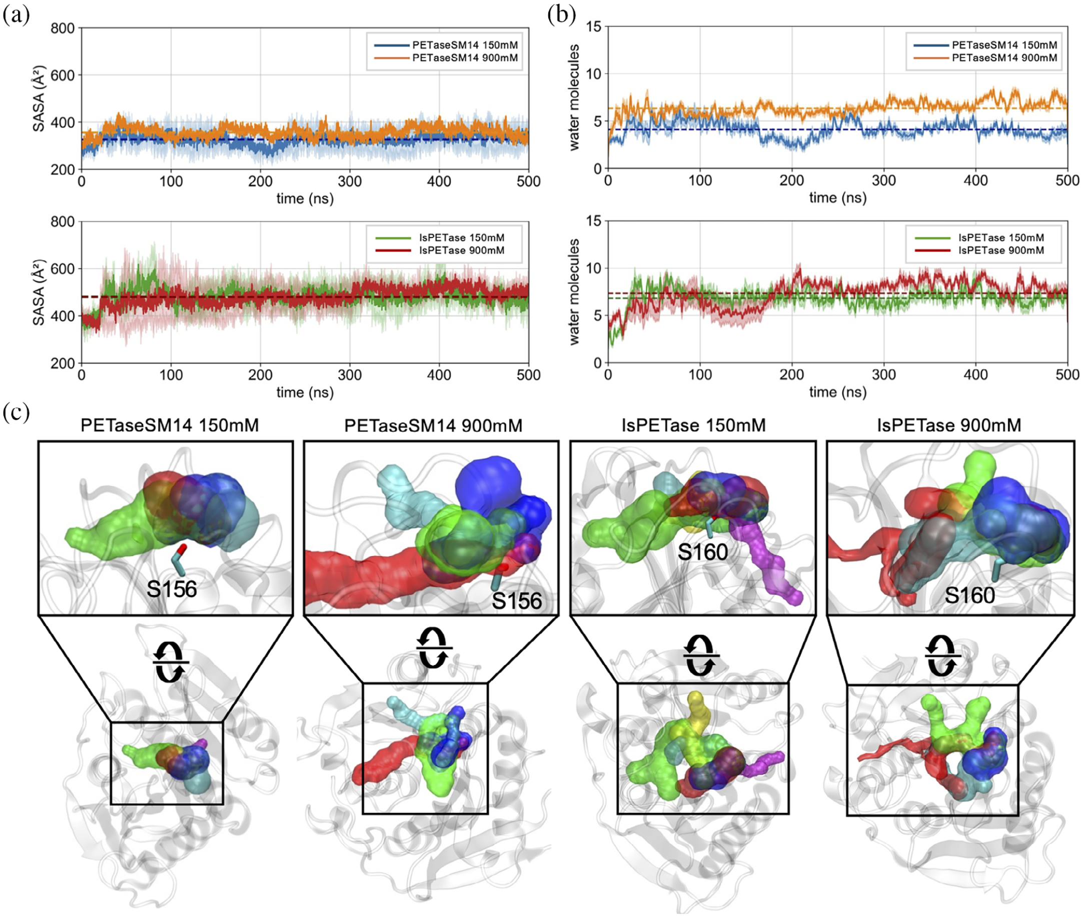

FIGURE 5 Hydration of the PETaseSM14 and IsPETase binding sites. (a) Solvent accessible surface area (SASA) and (b) number of water molecules inside the binding sites of PETaseSM14 (upper panels) and IsPETase (lower panels) during 500-ns long MD simulations at 150 and 900 mM NaCl concentrations. The profiles and the associated errors are reported as the mean and standard deviation over the three replicas performed for each system. (c) Protein tunnels sampled near the active site with Caver (Chovancova et al., 2012). The most representative pathways obtained from clustering are shown in different colors. Calculations were initiated from the Oγ atom of the catalytic serine, whose side chain is depicted as sticks.

IsPETase and establishing preferential contacts with cations (Figure S4a). On the other hand, IsPETase displays a basic character, with a pI = 9.54, and mainly interacts with anions (Figure S4b). However, the increase in the number of ions in solution to 900 mM (Figure 6b) reduces the extension of the charged surfaces of both PETaseSM14 and IsPETase in comparison to that observed at 150 mM (Figure 6a). This variation arises from the increasing number of interactions between the ions and the charged residues of the two enzymes, along with the decrease in the permittivity of the solvent under high-salt conditions, which drops from ~73.6 at 150 mM to ~65.8 at 900 mM NaCl concentration (Buchner et al., 1999).

Interestingly, cation interactions occur predominantly on surface-exposed protein regions that are distant from the active site of both enzymes (Figure S4c). Conversely, both PETaseSM14 and IsPETase form contacts with Cl^- near the active site, particularly at high-salt concentrations (Figure S4d). This increase in protein-anion interactions in the region surrounding the binding sites is expected to loosen the local stabilizing interaction network, particularly in IsPETase. To explore this hypothesis, we calculated the distances map between each residue of the binding site of the two enzymes (Figure 5c) as the average over values calculated from the simulated trajectories. By comparing the interactions pattern between residues in PETaseSM14 at the two ion concentrations, minimal

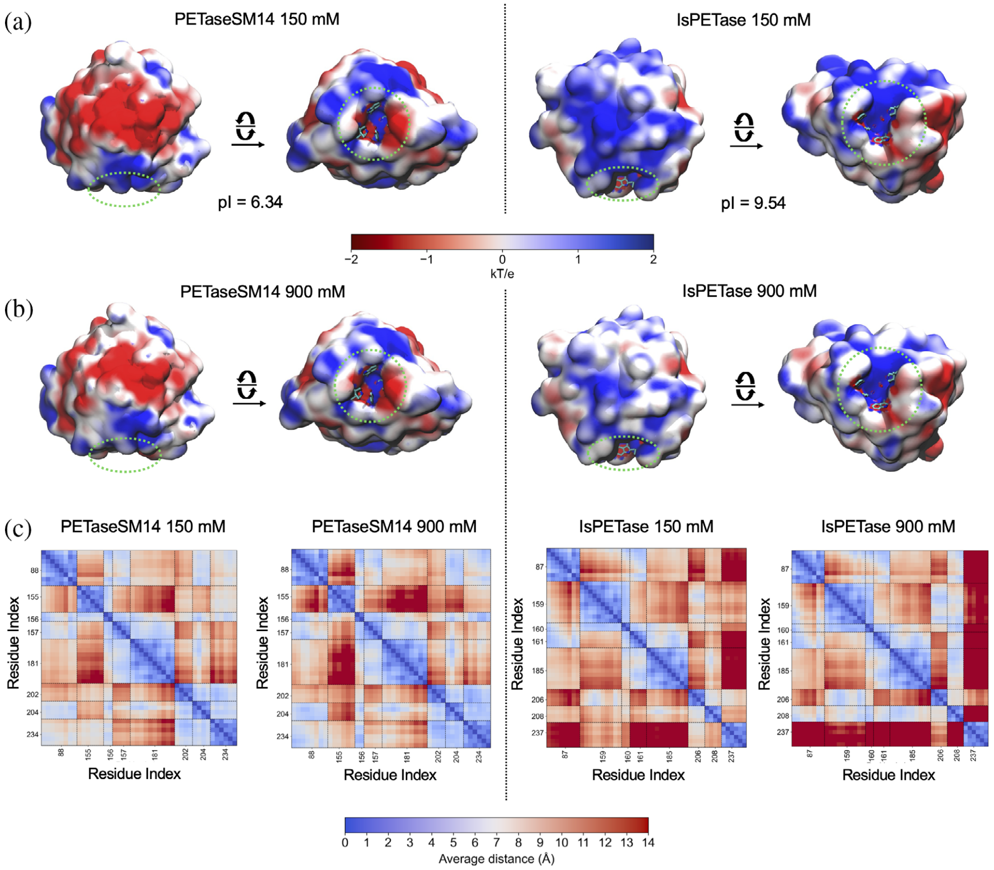

FIGURE 6 Effect of ion concentrations on the PETaseSM14 and IsPETase. Electrostatic potential surface of PETaseSM14 and IsPETase at (a) 150 mM and (b) 900 mM of NaCl concentration. The binding site locations and key residues are indicated with the green dotted circles. (c) Distance maps of residues forming the PETaseSM14 and IsPETase binding sites at the two ion concentrations. The maps report the average values of each cross-distance calculated over the three 500-ns MD simulation replicas. The color scale ranges from 0 Å (blue spots) to ≥14 Å (red spots).

variations are observed, with the distances between the pairs W155 and Y88, W155 and W181, W155 and I204, and M157 and H234 subjected to minimal increase at 900 mM. Importantly, the catalytic triad, composed of S156, H234, and D202, maintains inter-residue distances consistently below 5 Å at both ionic strengths. This observation aligns with the *active/inactive* state transition described in Figure 4a, further supporting the structural integrity and conformational stability of the active site across varying ionic environments.

On the other hand, significant changes are observed in IsPETase. Even at 150 mM, the distances between residues belonging to the active site appear markedly larger than those observed in PETaseSM14, as pinpointed by the abundance of orange and red-colored spots in Figure 5c, indicative of distances exceeding 9 Å. This pattern is consistent with the inherently broader and flexible binding site of IsPETase, which facilitates the efficient accommodation of the substrate under physiological conditions. Notably, at 150 mM, H237 is located more than 14 Å away from Y87, W185, and M161 (dark red regions), while some contacts are still observed with S160, W159 and D206 and I208. However, these interactions are entirely lost at 900 mM, owing to the rapid displacement of H237 that leads to the *inactivation* of IsPETase. This shift is accompanied by the movement of W159 towards D206 and I208 at 900 mM, which reflects the accelerated transition from the *active* to the *inactive* conformation of IsPETase under the high-salt conditions previously described (Figure 4c).

2.7 | PET-bound *trans:gauche* ratio increases at the increase of ion concentration

Finally, we examined the interactions between the enzymes' active site and the PET chains localized at the surface of the slab. In order to characterize whether the model of amorphous PET employed in this work represented a realistic proxy of a physical sample, we calculated the distributions of the *trans* (Figure S5a) and *gauche* (Figure S5b) conformers in the bulk of the PET slab. Indeed, several experimental data showed that the percentage of the O–C–C–O dihedral angle corresponding to the *gauche* conformation (angle absolute value ∼70°) ranges between 75% and 88% (Cunningham et al., 1974; Guévremont et al., 1995; Rodríguez-Cabello et al., 1996; Wei et al., 2019), whereas the *trans* conformation (angle absolute value ∼180°) corresponds to ∼14% of the total distribution (Schmidt-Rohr et al., 1998; Wei et al., 2019). Notably, the *trans:gauche* ratio calculated in the PET bulks of our MD simulations is around 14:82 in each system (Figure S6; distributions shown in Figure S5c,d), revealing a remarkable agreement with the data available in the literature (Cunningham et al., 1974; Guévremont et al., 1995; Rodríguez-Cabello et al., 1996; Wei et al., 2019). However, when we considered only the fraction of PET bound to the active site of the enzymes, these distributions changed significantly. The monomers bound to PETaseSM14 at 150 mM are almost exclusively in the *gauche* conformation (Figure S6a), with only 0.26% of the *trans* state observed. On the other hand, in the PETaseSM14 at 900 mM (Figure S6b) and IsPETase at 150 mM (Figure S6c), the *trans:gauche* distribution closely resembles that observed in the bulk. Finally, in the IsPETase at 900 mM (Figure S6d), the ratio considerably drifts from that observed in the PET bulk, with ∼32% of *trans* and only ∼56% of *gauche* conformation.

These variations are attributed to the different sizes and accessibility of the enzymes' binding site at varying ion concentrations. At 150 mM, the binding cleft of PETaseSM14 remains relatively rigid and narrow. This prevents PET chains from being accommodated in the *trans* conformation, which requires more spatial freedom due to its extended geometry. Instead, at higher ion concentrations, the binding site of PETaseSM14 becomes capable of recruiting PET chains in a conformational distribution that mirrors that of the bulk phase.

A similar scenario is observed for IsPETase at 150 mM, whose naturally wider and more flexible binding cleft enables the recruitment of both *trans* and *gauche* PET conformers with bulk-like statistics.

2.8 | The hydrophobic and aromatic residues stabilize the PET binding onto the catalytic site

A precise assessment of the contacts established by each residue of the enzyme's catalytic site with PET (Figure 7a) reveals that the most frequent interactions are provided by the aliphatic I208/I204 and the aromatic W185/W181 and Y87/Y88 side chains, collectively contributing to ∼75% of the total enzyme-PET contacts. In particular, these aromatic residues are known to play crucial roles in the substrate recognition and correct positioning within the active site by establishing stacking interactions with the benzene groups of the PET chains (Austin et al., 2018; Berselli et al., 2024). The time traces of the contacts formed by the side chains of W185/W181 and Y87/Y88 with the aromatic moieties of the PET chains (Figure S7) show distinct trends. For tryptophan, W185 in IsPETase forms approximately 20% more interactions with PET than W181 in PETaseSM14. Furthermore, the average values obtained at 900 mM are approximately 10% higher than those obtained at 150 mM for both enzymes. (Figure S7a). The average contact numbers for tyrosine in PETaseSM14 at 150 mM and 900 mM are slightly higher than in IsPETase at the same salt concentrations. Both systems establish ∼15–20% more contacts at 900 mM than at 150 mM (Figure S7b). These results indicate that aromatic residues remain essential for coordinating substrate chains in both systems, with tryptophan contributing more contacts in IsPETase and tyrosine contributing more in PETaseSM14. Regarding the other residues of the binding site, a notable substrate exposure is observed for M161/M157 and H234/H237. In particular, the latter shows a significant 43% increase in the average contact number for IsPETase at 900 mM compared to 150 mM. This is consistent with the displacement of this residue towards the enzyme's surface during MD simulations, resulting in increased exposure to the substrate bulk (Figure 3a).

Finally, contacts between PET and the catalytic serine, which is buried at the bottom of the binding site, are the least frequent. Nevertheless, notable differences emerge between the two enzymes. Indeed, due to the broad and shallow architecture of the IsPETase binding site, PET chains establish approximately four times more interactions with S160 than with S156 in PETaseSM14 at both ion concentrations, indicating an improved capacity to accommodate the substrate near the catalytic center.

However, the trend changes significantly when considering the subset of configurations where the catalytic

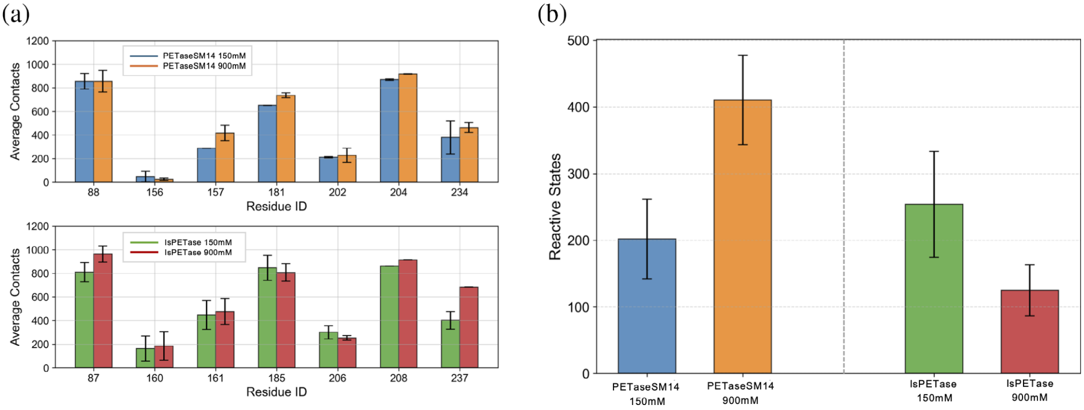

FIGURE 7 Interactions between PET and the PETaseSM14 and IsPETase binding sites. (a) Contacts between the PET chains and the residues forming the binding sites of PETaseSM14 (upper panel) and IsPETase (lower panel). The bars and the associated errors report the average and standard deviation of the total contacts established in each of the three 500-ns-long MD simulation replicas. (b) Number of *reactive* configurations sampled during the 500-ns-long MD simulations, averaged over the three replicas performed for each system.

serine is simultaneously in contact with (i) one ester C-atom of a PET chain and (ii) the enzyme binding site and the catalytic histidine (i.e., in the active state; Figure 7b). Under these conditions, with the enzyme in an active state (Figure 4) and effectively bound to the substrate, the system is primed for catalysis, and we refer to these configurations as *reactive* states. Based on statistics from our MD simulations, the average number of *reactive* states for PETaseSM14 is ∼20% lower than those obtained for IsPETase at 150 mM (blue and green bar, respectively). However, at the higher NaCl concentration, the number of reactive states observed for IsPETase decreases by approximately 50% (Figure 7b, red bar), while that for PETaseSM14 doubles (Figure 7b, orange bar) relative to their respective values at 150 mM.

3 | DISCUSSION

IsPETase, secreted by *Ideonella Sakaiensis* 201-f6, and PETaseSM14, expressed by the marine sponge *Streptomyces* sp. SM14, are characterized by the same catalytic scaffold; however, significant differences have evolved to adapt each enzyme to its native environment. Activity assays on PET powder degradation performed in this study and supporting evidence from the literature (Carletti et al., 2025; Carr et al., 2023; Weigert et al., 2022) indicate that NaCl concentration exerts a positive effect on the activity of PETaseSM14, consistent with its hypersaline marine origin, while having a negative effect on IsPETase. To date, this phenomenon has been observed using analytical techniques such as HPLC, SEM, and AFM, which do not elucidate the structural basis of these effects.

To address this gap, we employed molecular modeling and MD simulations to deliver a detailed structural comparison and molecular-level explanation of the experimentally observed differences between the two homologous plastic-degrading enzymes. The results obtained from 500-ns-long MD simulations reveal that the IsPETase binding site is significantly wider and more flexible than that found for PETaseSM14. While this characteristic is beneficial for substrate binding at low ion concentration (150 mM), the excessive plasticity of the active site leads to the fast *inactivation* of IsPETase at a higher ion concentration (900 mM). The quick displacement of the catalytic residue H237 from S160 is triggered by the flipping of the W159 side chain, impairing the enzyme's ability to initiate hydrolysis, even when the substrate is correctly positioned within the binding site. The role of W159 in IsPETase has been assessed via site-directed mutagenesis in a number of previous studies (Austin et al., 2018; Joo et al., 2018), in which this residue was replaced with a histidine. This mutation narrows the binding cleft, thus making the enzyme more structurally similar to other homologous cutinases. However, its impact on enzymatic activity remains a matter of debate. The bulky tryptophan side chain contributes to a shallower binding cleft compared to that of other hydrolases (Karunatillaka et al., 2022). While this characteristic is suggested by Joo et al. (2018) to facilitate substrate uptake and turnover, the W159H/S238F double variant characterized by Austin et al. (Austin et al., 2018) outperformed the WT enzyme in terms of crystalline PET degradation, suggesting a potentially different functional outcome.

By contrast, PETaseSM14 remains more rigid and undergoes minor, yet beneficial, conformational rearrangements during MD simulations at high ionic strength.

Indeed, the slight opening of the binding crevice observed at 900 mM improves the recruitment of water and the substrate, while always maintaining the catalytic triad in an *active* state. In particular, under high-salt conditions, the binding site of PETaseSM14 accommodates an average of ~2 additional water molecules compared to the low-salt conformation, with the water-accessible volume extending deeper into the active site relative to that observed at 150 mM. Given the mechanistic role of water in the catalytic mechanism of hydrolases (Berselli et al., 2025; Burgin et al., 2024; García-Meseguer et al., 2023; Jerves et al., 2021), we suggest that the enhanced hydration of the PETaseSM14 binding site observed at high salinity contributes to sustained catalytic turnover.

To model PET binding, and consistent with a previous study on a similar system (Sahihi et al., 2024), we adopted 9-monomers-long PET chains to reproduce the amorphous polymer sample. Indeed, this size represents the minimal length to form an entangled network between polymeric chains, and it is considered an optimal trade-off between accuracy in the reproduction of the mechanical features of amorphous PET and the computational cost (Aharoni, 1978; Roberge et al., 2004). The ability of PETaseSM14 at 900 mM and IsPETase at 150 mM to accommodate PET chains in the same conformational distribution observed in the bulk suggests greater substrate compatibility and potentially enhanced catalytic efficiency compared to PETaseSM14 at 150 mM or IsPETase at 900 mM. This is particularly relevant given that conformational transitions between *trans* and *gauche* states are extremely slow at room temperature (Wei et al., 2019), and the presence of a pre-organized binding site capable of accommodating the substrate without requiring extensive conformational rearrangements could significantly enhance enzymatic turnover by making the process less entropically demanding.

Nevertheless, while the modest remodeling of the PETaseSM14 binding site does not substantially improve substrate penetration towards the catalytic serine, PET chains penetrate more efficiently in the broader and shallower cleft of IsPETase. Moreover, in both enzymes the substrate remains primarily stabilized by the surface-exposed tryptophan (W181/W185) and tyrosine (Y88/Y87) side chains. This observation aligns with a number of previous studies highlighting the role of hydrophobic and π-stacking interactions in PET stabilization (Austin et al., 2018; Berselli et al., 2024; da Costa et al., 2021; Fecker et al., 2018; Guo et al., 2023; Joo et al., 2018), as mutations in these residues were shown to be deleterious to the enzymatic activity of IsPETase (Austin et al., 2018; Han et al., 2017). However, the increased recruitment of water, the accommodation of PET chains with a bulk-like conformational distribution and the persistent stability of the catalytic scaffold in an *active* state observed for PETaseSM14 at 900 mM, significantly enhances the number of *reactive* configurations sampled during the MD simulations. Indeed, the states in which the enzyme is simultaneously in an *active* form and the PET chain is correctly positioned within the binding site of PETaseSM14 at 900 mM occur at approximately twice the frequency compared to 150 mM NaCl. In contrast, IsPETase exhibits approximately a 50% reduction in reactive states when transitioning from 150 to 900 mM NaCl. This trend mirrors the experimentally measured activity pattern, bridging molecular simulations insights with in vitro physiological responses and providing a molecular-level explanation of the structural adaptations that enable enzymatic activity across diverse environments.

The findings of this study help pave the way for precise engineering strategies aimed at enhancing the effectiveness of these biotechnologies in marine ecosystems, where the accumulation of micro- and nanoplastics is an urgent environmental concern.

4 | MATERIALS AND METHODS

4.1 | Production of PETases

The enzymes employed in this work were produced in accordance with previous studies (Carletti et al., 2025; Di Rocco et al., 2023). IsPETase from *Ideonella sakaiensis* 201-f6 was expressed and purified from the green microalga *Chlamydomonas reinhardtii*. We used a photosynthetic restoration strategy in which the enzyme is constitutively expressed in the chloroplast, as reported by Di Rocco et al. (2023). PETaseSM14 from the marine sponge *Streptomyces* sp. SM14 was produced in *Escherichia coli* BL21 (DE3) and purified as reported by Carletti et al. (2025).

4.2 | Enzyme activity assay

All chemicals used were of the highest purity available. All aqueous solutions were prepared in deionized water. For the TPA calibration curve reported in Figure S2 a pure TPA powder from Fluka chemicals (n.86420, purity >99%) was used. The enzymatic activity was evaluated using PET powder (Goodfellow, product code ES30-PD-000132, particle size 300 μm, crystallinity >50%) at the final concentration of 5 mg mL^{-1}, into 100 μL buffer containing 1 μM protein solution. Thermal and pH conditions assessed in previous works have been used (Carletti et al., 2025; Di Rocco et al., 2023), in particular: 100 mM Tris–HCl buffer at pH 8.0 for IsPETase and 100 mM Tris–HCl-pH 9.0 for PETaseSM14, incubated at 37°C. The NaCl concentrations tested were 0, 150, 300, 700 and 900 mM. After an incubation time of 72 h, the reaction tubes were vigorously mixed and centrifuged, then the supernatant was filtered and further analyzed by RP-

HPLC. For every set of reactions, two control samples were prepared following the same procedure: one without adding the protein, while the other without adding the substrate. The RP-HPLC analysis consists of a linear gradient procedure using an Agilent Poroshell 120 EC-C18 column, equilibrated with a mobile phase of 80:20 solution A (0.1% formic acid): solution B (100% acetonitrile). 20 μL of each sample were loaded into the column and eluted over a 20-min run at a flow rate of 1 mL/min, at room temperature with the following elution steps: 80:20 (solution A: solution B), followed by a 15-min linear gradient 20:50 (solution A: solution B), 2 min isocratic 50:50 (solution A: solution B), followed by 3 min linear gradient from 50:20 (solution A: solution B) and 2 min isocratic 80:20 (solution A: solution B). The absorbance was measured at 240 nm and 254 nm, to detect the carbonyl groups and aromatic rings of the reaction products. To determine peak areas, the baseline was drawn manually and calculated using instrument software. According to the chromatograms obtained (Figure S8), the reaction product with the highest retention time was BHET (2.9 min), followed by MHET (2.5 min, assumed) and TPA (1.7 and 2.1 min), which was the main product obtained.

4.3 | Preparation and equilibration of PET9 slab

The initial configuration and topology of the PET9 melt system was produced with the *polymer builder* tool of CHARMM-GUI (Figure S9a) (Choi et al., 2021; Jo et al., 2008). We generated a cubic system with size $\sim 60 \times 60 \times 60$ Å^3 and including 100 9-monomers-long PET chains, resulting a total of 20,000 atoms, and a density of ~ 1.23 g $\cdot$ cm^{-3}, in line with the experimental value (Thompson & Woods, 1955). This system was parametrized using the CHARMM general force field (CGenFF) (Vanommeslaeghe et al., 2010), which demonstrated successful performances in previous works on ion track formation in PET samples (Shen et al., 2023), ion conduction through PET nanopores (Cruz-Chu et al., 2009), and PET binding onto plastic degrading enzymes (Berselli et al., 2024; Polêto & Lemkul, 2025; Sahihi et al., 2024). Following the protocol prescribed by CHARMM-GUI, the coarse-grained (CG) model of the melted PET systems was equilibrated at 300 K, followed by the conversion to the all-atom structure, that is provided as an output to the user. This represents the starting structure for classical MD simulations, which was further minimized for 10,000 steps followed by 250 ps of equilibration in the NVT ensemble at a temperature of 300 K and the heavy atoms of the system restrained. Then, the system underwent a simulated annealing procedure to achieve an amorphous-like conformational distribution in the absence of positional restraints. This step was conducted by progressively heating the system from 300 to 750 K with a 50 K $\cdot$ ps^{-1} rate. Then, 4 ps of equilibration were carried out at 750 K, followed by cooling from 750 to 300 K with the same rate as that used for heating. We stress that this procedure did not require extensive simulations to achieve an accurate representation of amorphous PET sample thanks to the reliable initial configuration provided by CHARMM-GUI. After the simulated annealing step, further 250 ps of equilibration were carried out in the NVT ensemble at $T = 300$ K, followed by 1 ns of standard MD simulation in NPT at $T = 300$ K and $p = 1$ bar. Constant temperature and pressure were maintained by a Langevin thermostat and Nosé-Hoover Langevin barostat, respectively (Feller et al., 1995; Martyna et al., 1994). The oscillation piston period was set to 50.0 fs and the damping time scale to 25.0 fs. The damping coefficient of the Langevin thermostat was set to 1 ps^{-1}. Long-range electrostatic interactions were computed using the Particle Mesh Ewald (PME) algorithm (Darden et al., 1993), with spline interpolation order 6. Electrostatic and van der Waals (VdW) interactions were calculated with a cutoff of 12 Å as prescribed by the CHARMM force field. A switching function was applied, starting to take effect at 10 Å to obtain a smooth decay as indicated in Ref. (Steinbach & Brooks, 1994). Chemical bonds involving hydrogen atoms and heavy atoms were constrained with SHAKE (Ryckaert et al., 1977), enabling the adoption of a time step (δ t) of 2 fs. Each MD simulation was performed with NAMD (Phillips et al., 2005; Phillips et al., 2020).

4.4 | Assembly of enzyme-PET systems

To reproduce the system with the enzyme adsorbed onto the PET surface, we selected as a starting configurations the crystallographic structures of the IsPETase (PDB ID: 6EQE, resolution: 0.92 Å) (Austin et al., 2018) and PETaseSM14 (PDB ID: 9HYD, resolution: 1.43 Å) (Carletti et al., 2025). The CHARMM coordinate file for these structures were generated with the PDB reader of CHARMM-GUI (Jo et al., 2008), by specifying the protonation state of the histidine residues based on the pKa predicted with PropKa (Olsson et al., 2011). Then, using VMD (Humphrey et al., 1996), we manually positioned the enzyme structures and the equilibrated model of the melted PET within the same simulation box, with the catalytic serine (S160 in IsPETase, S156 in PETaseSM14) pointing towards the PET surface. At the initial stage, the enzyme and PET surface were kept separated by a minimal distance of 7 Å to prevent steric clashes and significant interactions (Figure S9b). The initial configurations of the enzyme-PET systems were solvated and added with the NaCl ion bath (150 or 900 mM) using the *solvate* and *autoionize* packages of VMD, respectively, while the topologies were built with *psfgen*. The ester bond between the nine PET monomers belonging to the same chain were preserved by adding the patch P00080. Moreover, the disulfide bonds between C203 and C239 and between C273 and C289 of IsPETase were included. The resulting solvated systems were included in rectangular boxes with size 90 × 90 × 150 Å^3, counting approximately 110,000 atoms each (Figure S9c).

4.5 | Molecular dynamics simulations

The solvated enzyme-PET systems at the two different ion concentrations were equilibrated following a multistep procedure. After 5 ps of energy minimization, the system was progressively heated to the selected temperature of 310 K. Then, 10 ns of equilibration were conducted in the NVT ensemble adopting a δ t = 1 fs, followed by 20 ns in NVT with δ t = 2 fs and 20 ns in NPT with δ t = 2 fs. This cumulative 50-ns-long equilibration was performed with progressive release of positional constraints to allow slow relaxation of the system and the diffusion of PET chains, allowing the adsorption of the enzyme onto the PET surface (Figure S9b). The timestep, timescale, ensemble and restraints adopted in each of the five 10-ns-long steps of equilibration are summarized in Table S2.

After the equilibration, 500 ns of standard MD simulations were performed maintaining only the minimal restraints as those used in the last step of equilibration to avoid roto-translation of the protein during the MD simulation (Figure S10). To ensure adequate statistics and reproducibility, each system was separately equilibrated and simulated in three independent replicas. The topology, coordinate and output files associated with each replica of each system (IsPETase-PET9 and PETaseSM14-PET9 at 150 and 900 mM of NaCl concentration) are freely available on Zenodo (https://zenodo.org/records/17412459). Rectangular PBCs were adopted to replicate the system and remove box surface effects. Chemical bonds involving hydrogen atoms and heavy atoms of the protein were constrained with SHAKE (Ryckaert et al., 1977), while those of water molecules were kept fixed with SETTLE (Miyamoto & Kollman, 1992). Each MD simulation was performed with NAMD (Phillips et al., 2005; Phillips et al., 2020) and the CHARMM36/CHARMM36m (Huang et al., 2017; Huang & MacKerell, 2013) force field under Langevin dynamics adopting the same parameters as those used for melted PET equilibration.

4.6 | Analysis of molecular dynamics simulations

4.6.1 | RMSD and RMSF

The backbone root-mean-square deviations (RMSD), the root-mean-square fluctuations (RMSF) of the enzyme, the inter-residue distances, and the inter-residue distance maps were calculated with MDAnalysis (Gowers et al., 2016; Michaud-Agrawal et al., 2011) and plotted with the *matplotlib* library of Python (https://matplotlib.org) (Hunter, 2007). The results and associated error are reported as the average and standard deviation over the three replicas performed for each system.

4.6.2 | Inter-residue distances

The distances calculated to assess the size of the active site cleft (d1, d2, Figure 3) or the active/inactive states (d3, d4, Figure 4) were calculated with MDAnalysis (Gowers et al., 2016; Michaud-Agrawal et al., 2011), and reported as the mean and standard deviation over the three replicas performed for each system. The atoms considered in each calculation are indicated in Table 1.

4.6.3 | SASA

The solvent-accessible surface area (SASA) of the binding sites of the protein (S156/S160, H234/H237, D204/D206, M157/M161, Y88/Y87 and W181/W185 in PETaseSM14/IsPETase) was calculated with VMD (Humphrey et al., 1996) using a probe radius of 1.4 Å.

4.6.4 | Water molecules inside the binding pocket

The number of water molecules inside the binding pocket was calculated with MDAnalysis (Gowers et al., 2016; Michaud-Agrawal et al., 2011) by considering a radius of 6 Å from the catalytic serine Oγ atom. This cutoff was selected as this is the distance between the catalytic serine Oγ atom and the Oγ atom of the Y87/Y88 side chain, which is the outermost, solvent-exposed residue of the binding site (Figure S11).

4.6.5 | Protein tunnels

The tunnels and the free volume near the active site of the system were sampled with Caver 3.0 (Chovancova et al., 2012). The Oγ atom of the catalytic serine was used as the starting point for the calculations. Configurations were sampled every 50 ns along each MD trajectory using the default parameters and the resulting tunnels were clustered using the average-link hierarchical algorithm with a threshold of 4.0.

4.6.6 | APBS

The electrostatic potential maps were computed with the adaptive Poisson-Boltzmann solver (APBS) code (Jurrus et al., 2018). The crystal structures of the two enzymes were used as input for the APBS calculations. Prior to the calculations, the NaCl concentrations and the solvent dielectric constants were set to match the conditions of the MD simulations. The dielectric constants were chosen based on the values reported in Ref. (Buchner et al., 1999) for the temperature $T = 308$ K, with 73.57 and 65.80 being the closest available values for the target concentrations of 150 and 900 mM, respectively.

4.6.7 | Isoelectric point

The isoelectric point (pI) of each protein was calculated with the ExPASy Analysis tool (Gasteiger et al., 2005).

4.6.8 | Contacts number

The contacts between ions and the enzyme's surface were calculated with MDAnalysis (Gowers et al., 2016; Michaud-Agrawal et al., 2011) adopting a cutoff of 5 Å.

4.6.9 | PET chains conformational distribution

The conformational distribution of the PET chains was calculated by considering the dihedral angles formed by the ethylene glycol unit of each monomer, composed of the atoms O3–C9–C10–O1, according to the PDB nomenclature used in the coordinate and topology files. Following the classifications proposed in Refs (Alves et al., 2002; Wei et al., 2019). the conformation was defined as *gauche* when the absolute value of the dihedral angle was 70° ± 20°, while it was defined as *trans* when the absolute value of the dihedral angle was 180° ± 20°. Dihedral angles of the substrate bound to the enzyme's binding site were calculated from the PET fraction within 8 Å of the catalytic serine, while those for the substrate bulk were obtained from the 100 PET chains excluding the bound fraction.

4.6.10 | Number of enzyme-PET reactive states

The number of *reactive* states was calculated with MDAnalysis (Gowers et al., 2016; Michaud-Agrawal et al., 2011) by counting the number of states in which the distance between the O γ atom of the catalytic serine side chain was simultaneously <5 Å away from the N ε atom of the catalytic histidine and from the ester carbon atom of a PET chain (C1 or C8 according to the PDB nomenclature used in the coordinate and topology files). The results and associated errors are reported as the average and standard deviation over the three replicas.

AUTHOR CONTRIBUTIONS

Alessandro Berselli: Conceptualization; investigation; writing – original draft; methodology; validation; visualization; writing – review and editing; formal analysis; project administration; data curation; resources. **Alan Carletti:** Conceptualization; investigation; writing – review and editing; visualization; methodology; data curation. **Maria Cristina Menziani:** Conceptualization; investigation; writing – review and editing; project administration; supervision; funding acquisition; resources. **Shapla Bhattacharya:** Writing – review and editing; validation. **Rossella Castagna:** Validation; writing – review and editing. **Emilio Parisini:** Writing – review and editing; validation; conceptualization. **Giulia di Rocco:** Conceptualization; supervision; writing – review and editing; visualization; validation; methodology; investigation; project administration. **Francesco Muniz-Miranda:** Project administration; funding acquisition; investigation; conceptualization; writing – review and editing; visualization; methodology; supervision; resources.

ACKNOWLEDGMENTS

We acknowledge CINECA awards under the ISCRA initiative (the Iscra C project HP10C1FZRH granted to Alessandro Berselli and the Iscra C project HP10C4M2EF granted to Francesco Muniz-Miranda), for the availability of high-performance computing resources and support. We are also grateful to Prof. Dr. Alfonso Pedone for enabling us access to the local computational cluster. The research was supported financially by the Italian "Ministero dell'Università e della Ricerca" (MUR) initiative PRIN 2022 on the project 2022W9XTYB entitled "Enzylearning" (020140_23_PRIN-2022 granted to FMM as "deputy PI") and the local "FAR2023-linea post-dottorato" initiative of UNIMORE. Alan Carletti thanks MIUR, Ministero dell'Istruzione, dell'Università e della Ricerca (PRIN 2020, E53C2001365001 to MS). Shapla Bhattacharya acknowledges the Latvian Recovery and Resilience Fund and the Latvian Institute of Organic Synthesis for student grants (No. ANM_OSI_DG_31 and No. IG-2025-02). Emilio Parisini thanks the Latvian Recovery and Resilience Fund (grant No. 74/OSI/ZG) for financial support. Emilio Parisini and Rossella Castagna wish to thank the European Union's HORIZON-WIDERA-2023-ACCESS-04 programme for financial support under grant agreement 101159534 (WIDEnzymes). This manuscript reflects only the authors' views and opinions. Neither the European Union nor the granting authority can be considered responsible for them. Open access publishing facilitated by Universita degli Studi di Modena e Reggio Emilia, as part of the Wiley - CRUI-CARE agreement.

CONFLICT OF INTEREST STATEMENT

The authors declare no conflict of interest.

DATA AVAILABILITY STATEMENT

All MD simulations were produced with NAMD3 (https://www.ks.uiuc.edu/Research/namd/). Trajectories were analyzed with VMD (https://www.ks.uiuc.edu/Research/vmd/) and the Python library MDAnalysis (https://www.mdanalysis.org). NAMD (https://www.ks.uiuc.edu/Research/namd/license.html) and VMD (https://www.ks.uiuc.edu/Research/vmd/current/LICENSE.html) are distributed free of charge for non-exclusive, non-commercial use. MDAnalysis is available under the "GNU general public license" (https://www.gnu.org/licenses/old-licenses/gpl-2.0.html). Data for PET slab equilibration, initial structure and topology of each PETase-PET system at two ion concentrations and intermediate coordinate, input and output files (every 10 ns) for the three 500-ns-long replicas of each system and the HPLC data analysis are publicly available on Zenodo. https://zenodo.org/records/17412459. Each additional file can be provided by the authors upon reasonable request.

ORCID

Alessandro Berselli https://orcid.org/0000-0002-2241-3530
Alan Carletti https://orcid.org/0009-0009-5353-865X
Maria Cristina Menziani https://orcid.org/0000-0003-3428-5297
Shapla Bhattacharya https://orcid.org/0000-0002-1286-5138
Rossella Castagna https://orcid.org/0000-0002-9284-3165
Emilio Parisini https://orcid.org/0000-0002-5529-0039
Giulia di Rocco https://orcid.org/0000-0002-3187-2210
Francesco Muniz-Miranda https://orcid.org/0000-0002-7614-2326

REFERENCES

Aharoni SM. Unperturbed dimensions and critical molecular weight for entanglement of poly(ethylene terephthalate) and poly(ethylene isophthalate). Die Makromolekulare Chemie. 1978;179:1867–71.

Almeida EL, Carrillo Rincón AF, Jackson SA, Dobson ADW. In silico screening and heterologous expression of a polyethylene terephthalate hydrolase (PETase)-like enzyme (SM14est) with Polycaprolactone (PCL)-degrading activity, from the marine sponge-derived strain Streptomyces sp. SM14. Frontiers in Microbiology. 2019;10:2187.

Alves NM, Mano JF, Balaguer E, Meseguer Dueñas JM, Gómez Ribelles JL. Glass transition and structural relaxation in semi-crystalline poly(ethylene terephthalate): a DSC study. Polymer. 2002;43:4111–22.

Arnal G, Anglade J, Gavalda S, Tournier V, Chabot N, Bornscheuer UT, et al. Assessment of four engineered PET degrading enzymes considering large-scale industrial applications. ACS Catalysis. 2023;13:13156–66.

Austin HP, Allen MD, Donohoe BS, Rorrer NA, Kearns FL, Silveira RL, et al. Characterization and engineering of a plastic-degrading aromatic polyesterase. Proceedings of the National Academy of Sciences of the United States of America. 2018;115:E4350–7.

Bell EL, Smithson R, Kilbride S, Foster J, Hardy FJ, Ramachandran S, et al. Directed evolution of an efficient and thermostable PET depolymerase. Nature Catalysis. 2022;5:673–81.

Berselli A, Menziani MC, Muniz-Miranda F. Structure and energetics of PET-hydrolyzing enzyme complexes: a systematic comparison from molecular dynamics simulations. Journal of Chemical Information and Modeling. 2024;64:8236–57.

Berselli A, Menziani MC, Piccini G, Muniz-Miranda F. Molecular-level mechanistic insights into PETase-catalyzed plastics hydrolysis from accurate QM/MM free energy calculations. ACS Catalysis. 2025;15:10702–21.

Berselli A, Ramos MJ, Menziani MC. Novel pet-degrading enzymes: structure-function from a computational perspective. ChemBioChem. 2021;22:2032–50.

Buchholz PCF, Feuerriegel G, Zhang H, Perez-Garcia P, Nover L-L, Chow J, et al. Plastics degradation by hydrolytic enzymes: the plastics-active enzymes database—PAZy. Proteins: Structure, Function, and Bioinformatics. 2022;90:1443–56.

Buchner R, Hefter GT, May PM. Dielectric relaxation of aqueous NaCl solutions. Journal of Physical Chemistry A. 1999;103:1–9.

Burgin T, Pollard BC, Knott BC, Mayes HB, Crowley MF, McGeehan JE, et al. The reaction mechanism of the Ideonella sakaiensis PETase enzyme. Communications Chemistry. 2024;7:1–14.

Carletti A, Bhattacharya S, Pedroni S, Berto M, Bonettini R, Castagna R, et al. Functional and structural characterization of PETase SM14 from marine-sponge Streptomyces sp. active on polyethylene terephthalate. ACS Sustainable Chemistry & Engineering. 2025;13:7460–8.

Carr CM, Keller MB, Paul B, Schubert SW, Clausen KSR, Jensen K, et al. Purification and biochemical characterization of SM14est, a PET-hydrolyzing enzyme from the marine sponge-derived Streptomyces sp. SM14. Frontiers in Microbiology. 2023;14:1170880.

Chen Y, Lin Z, Yang S. Plasticization and crystallization of poly(ethylene terephthalate) induced by water. Journal of Thermal Analysis and Calorimetry. 1998;52:565–8.

Choi YK, Park S-J, Park S, Kim S, Kern NR, Lee J, et al. CHARMM-GUI polymer builder for modeling and simulation of synthetic polymers. Journal of Chemical Theory and Computation. 2021;17:2431–43.

Chovancova E, Pavelka A, Benes P, Strnad O, Brezovsky J, Kozlikova B, et al. CAVER 3.0: a tool for the analysis of transport pathways in dynamic protein structures. PLoS Computational Biology. 2012;8:e1002708.

Cruz-Chu ER, Ritz T, Siwy ZS, Schulten K. Molecular control of ionic conduction in polymer nanopores. Faraday Discussions. 2009;143:47–62.

Cui Y, Chen Y, Liu X, Dong S, Tian Y, Qiao Y, et al. Computational redesign of a PETase for plastic biodegradation under ambient condition by the GRAPE strategy. ACS Catalysis. 2021;11:1340–50.

Cui Y, Chen Y, Sun J, Zhu T, Pang H, Li C, et al. Computational redesign of a hydrolase for nearly complete PET depolymerization at industrially relevant high-solids loading. Nature Communications. 2024;15:1417.

Cunningham A, Ward IM, Willis HA, Zichy V. An infra-red spectroscopic study of molecular orientation and conformational changes in poly(ethylene terephthalate). Polymer. 1974;15:749–56.

da Costa CHS, dos Santos AM, Alves CN, Martí S, Moliner V, Santana K, et al. Assessment of the PETase conformational changes induced by poly(ethylene terephthalate) binding. Proteins. 2021;89:1340–52.

Darden T, York D, Pedersen L. Particle mesh Ewald: an N·log (N) method for Ewald sums in large systems. The Journal of Chemical Physics. 1993;98:10089–92.

de Castro AM, Carniel A, Nicomedes Junior J, da Conceição Gomes A, Valoni É. Screening of commercial enzymes for poly(ethylene terephthalate) (PET) hydrolysis and synergy studies on different substrate sources. Journal of Industrial Microbiology & Biotechnology. 2017;44:835–44.

Di Rocco G, Taunt HN, Berto M, Jackson HO, Piccinini D, Carletti A, et al. A PETase enzyme synthesised in the chloroplast of the microalga Chlamydomonas reinhardtii is active against post-consumer plastics. Scientific Reports. 2023;13:10028.

Fecker T, Galaz-Davison P, Engelberger F, Narui Y, Sotomayor M, Parra LP, et al. Active site flexibility as a Hallmark for efficient PET degradation by I. sakaiensis PETase. Biophysical Journal. 2018;114:1302–12.

Feller SE, Zhang Y, Pastor RW, Brooks BR. Constant pressure molecular dynamics simulation: the Langevin piston method. The Journal of Chemical Physics. 1995;103:4613–21.

García-Meseguer R, Ortí E, Tuñón I, Ruiz-Pernía JJ, Aragó J. Insights into the enhancement of the poly(ethylene terephthalate) degradation by FAST-PETase from computational modeling. Journal of the American Chemical Society. 2023;145:19243–55.

Gasteiger E, Hoogland C, Gattiker A, Duvaud S, Wilkins MR, Appel RD, et al. Protein identification and analysis tools on the ExPASy server. In: Walker JM, editor. The proteomics protocols handbook. Springer Protocols Handbooks. Totowa, NJ: Humana Press; 2005. p. 571–607. https://doi.org/10.1385/1-59259-890-0:571

Gowers RJ, Linke M, Barnoud J, Reddy TJE, Melo MN, Seyler SL, et al. MDAnalysis: a python package for the rapid analysis of molecular dynamics simulations. Proc SciPy. 2016;2016:98–105.

Groeninckx G, Berghmans H, Overbergh N, Smets G. Crystallization of poly(ethylene terephthalate) induced by inorganic compounds. I. Crystallization behavior from the glassy state in a low-temperature region. Journal of Polymer Science Polymer Physics Edition. 1974;12:303–16.

Guévremont J, Ajji A, Cole KC, Dumoulin MM. Orientation and conformation in poly(ethylene terephthalate) with low draw ratios as characterized by specular reflection infra-red spectroscopy. Polymer. 1995;36:3385–92.

Guo X, Jiang Y, Xie D, Zhou Y. Computational investigation on the binding modes of PET polymer to PETase. Journal of Biomolecular Structure & Dynamics. 2023;42(13):6842–8.

Han X, Liu W, Huang J-W, Ma J, Zheng Y, Ko T-P, et al. Structural insight into catalytic mechanism of PET hydrolase. Nature Communications. 2017;8:1–6.

Huang J, MacKerell AD. CHARMM36 all-atom additive protein force field: validation based on comparison to NMR data. Journal of Computational Chemistry. 2013;34:2135–45.

Huang J, Rauscher S, Nawrocki G, Ran T, Feig M, de Groot BL, et al. CHARMM36m: an improved force field for folded and intrinsically disordered proteins. Nature Methods. 2017;14:71–3.

Humphrey W, Dalke A, Schulten K. VMD: visual molecular dynamics. Journal of Molecular Graphics. 1996;14(33–38):27–8.

Hunter JD. Matplotlib: a 2D graphics environment. Computing in Science & Engineering. 2007;9:90–5.

Jerves C, Neves RPP, Ramos MJ, da Silva S, Fernandes PA. Reaction mechanism of the PET degrading enzyme PETase studied with DFT/MM molecular dynamics simulations. ACS Catalysis. 2021;11:11626–38.

Jo S, Kim T, Iyer VG, Im W. CHARMM-GUI: a web-based graphical user interface for CHARMM. Journal of Computational Chemistry. 2008;29:1859–65.

Joo S, Cho IJ, Seo H, Son HF, Sagong H-Y, Shin TJ, et al. Structural insight into molecular mechanism of poly(ethylene terephthalate) degradation. Nature Communications. 2018;9:382.

Jurrus E, Engel D, Star K, Monson K, Brandi J, Felberg LE, et al. Improvements to the APBS biomolecular solvation software suite. Protein Science. 2018;27:112–28.

Karunatillaka I, Jaroszewski L, Godzik A. Novel putative polyethylene terephthalate (PET) plastic degrading enzymes from the environmental metagenome. Proteins. 2022;90:504–11.

Kawai F, Iizuka R, Kawabata T. Engineered polyethylene terephthalate hydrolases: perspectives and limits. Applied Microbiology and Biotechnology. 2024;108:404.

Launay A, Thominette F, Verdu J. Water sorption in amorphous poly(ethylene terephthalate). Journal of Applied Polymer Science. 1999;73:1131–7.

Lee M, Kim H, Ryu H-S, Moon J, Khant NA, Yu C, et al. Review on invasion of microplastic in our ecosystem and implications. Science Progress. 2022;105:368504221140766.

Lu H, Diaz DJ, Czarnecki NJ, Zhu C, Kim W, Shroff R, et al. Machine learning-aided engineering of hydrolases for PET depolymerization. Nature. 2022;604:662–7.

Martyna GJ, Tobias DJ, Klein ML. Constant pressure molecular dynamics algorithms. The Journal of Chemical Physics. 1994; 101:4177–89.

Michaud-Agrawal N, Denning EJ, Woolf TB, Beckstein O. MDAnalysis: a toolkit for the analysis of molecular dynamics simulations. Journal of Computational Chemistry. 2011;32:2319–27.

Miyamoto S, Kollman PA. SETTLE: an analytical version of the SHAKE and RATTLE algorithm for rigid water models. Journal of Computational Chemistry. 1992;13:952–62.

Müller R-J, Schrader H, Profe J, Dresler K, Deckwer W-D. Enzymatic degradation of poly(ethylene terephthalate): rapid hydrolyse using a hydrolase from *T. fusca*. Macromolecular Rapid Communications. 2005;26:1400–5.

Ollis DL, Cheah E, Cygler M, Dijkstra B, Frolow F, Franken SM, et al. The α/β hydrolase fold. Protein Engineering. 1992;5:197–211.

Olsson MHM, Søndergaard CR, Rostkowski M, Jensen JH. PROPKA3: consistent treatment of internal and surface residues in empirical pKa predictions. Journal of Chemical Theory and Computation. 2011;7:525–37.

Phillips JC, Braun R, Wang W, Gumbart J, Tajkhorshid E, Villa E, et al. Scalable molecular dynamics with NAMD. Journal of Computational Chemistry. 2005;26:1781–802.

Phillips JC, Hardy DJ, Maia JDC, Stone JE, Ribeiro JV, Bernardi RC, et al. Scalable molecular dynamics on CPU and GPU architectures with NAMD. The Journal of Chemical Physics. 2020;153: 044130.

Polêto MD, Lemkul JA. Structural and electronic properties of poly(ethylene terephthalate) (PET) from polarizable molecular dynamics simulations. Macromolecules. 2025;58:403–14.

Potts JE, Clendinning RA, Ackart WB, Niegisch WD. The biodegradability of synthetic polymers. In: Guillet J, editor. Polymers and ecological problems. Boston, MA: Springer US; 1973. p. 61–79. https://doi.org/10.1007/978-1-4684-0871-3_4

Roberge M, Prud'homme RE, Brisson J. Molecular modelling of the uniaxial deformation of amorphous polyethylene terephthalate. Polymer. 2004;45:1401–11.

Rodríguez-Cabello JC, Merino JC, Quintanilla L, Pastor JM. Deformation-induced conformational changes in stretched samples of amorphous poly(ethylene terephthalate). Journal of Applied Polymer Science. 1996;62:1953–64.

Ruginescu R, Purcarea C. Plastic-degrading enzymes from marine microorganisms and their potential value in recycling technologies. Marine Drugs. 2024;22:441.

Ryckaert J-P, Ciccotti G, Berendsen HJC. Numerical integration of the cartesian equations of motion of a system with constraints: molecular dynamics of n-alkanes. Journal of Computational Physics. 1977;23:327–41.

Sahihi M, Fayon P, Nauton L, Goujon F, Devémy J, Dequidt A, et al. Probing enzymatic PET degradation: molecular dynamics analysis of Cutinase adsorption and stability. Journal of Chemical Information and Modeling. 2024;64:4112–20.

Samak NA, Jia Y, Sharshar MM, Mu T, Yang M, Peh S, et al. Recent advances in biocatalysts engineering for polyethylene terephthalate plastic waste green recycling. Environment International. 2020;145:106144.

Schmidt-Rohr K, Hu W, Zumbulyadis N. Elucidation of the chain conformation in a glassy polyester, PET, by two-dimensional NMR. Science. 1998;280:714–7.

Shen W, Wang X, Zhang G, Kluth P, Wang Y, Liu F. Illustrating the atomic structure and formation mechanism of ion tracks in polyethylene terephthalate with molecular dynamics simulations. Nuclear Instruments and Methods in Physics Research, Section B: Beam Interactions with Materials and Atoms. 2023;535:102–11.

Silva CM, Carneiro F, O'Neill A, Fonseca LP, Cabral JSM, Guebitz G, et al. Cutinase: a new tool for biomodification of synthetic fibers. Journal of Polymer Science Part A: Polymer Chemistry. 2005;43:2448–50.

Son HF, Cho IJ, Joo S, Seo H, Sagong H-Y, Choi SY, et al. Rational protein engineering of Thermo-stable PETase from Ideonella sakaiensis for highly efficient PET degradation. ACS Catalysis. 2019;9:3519–26.

Steinbach PJ, Brooks BR. New spherical-cutoff methods for long-range forces in macromolecular simulation. Journal of Computational Chemistry. 1994;15:667–83.

Sulaiman S, Yamato S, Kanaya E, Kim J-J, Koga Y, Takano K, et al. Isolation of a novel Cutinase homolog with polyethylene terephthalate-degrading activity from leaf-branch compost by using a metagenomic approach. Applied and Environmental Microbiology. 2012;78:1556–62.

Sun J, Cui Y, Wu B. Chapter ten: GRAPE, a greedy accumulated strategy for computational protein engineering. In: Weber G, Bornscheuer UT, Wei R, editors. Methods in enzymology. Enzymatic Plastic Degradation. Volume 648. Amsterdam: Academic Press; 2021. p. 207–30.

Thompson AB, Woods DW. Density of amorphous polyethylene terephthalate. Nature. 1955;176:78–9.

Tokiwa Y, Suzuki T. Hydrolysis of polyesters by lipases. Nature. 1977;270:76–8.

Vanommeslaeghe K, Hatcher E, Acharya C, Kundu S, Zhong S, Shim J, et al. CHARMM general force field: a force field for drug-like molecules compatible with the CHARMM all-atom additive biological force fields. Journal of Computational Chemistry. 2010;31:671–90.

Wei R, Song C, Gräsing D, Schneider T, Bielytskyi P, Böttcher D, et al. Conformational fitting of a flexible oligomeric substrate does not explain the enzymatic PET degradation. Nature Communications. 2019;10:5581.

Wei R, Zimmermann W. Biocatalysis as a green route for recycling the recalcitrant plastic polyethylene terephthalate. Journal of Microbiology and Biotechnology. 2017;10:1302–7.

Weigert S, Perez-Garcia P, Gisdon FJ, Gagsteiger A, Schweinshaut K, Ullmann GM, et al. Investigation of the halophilic PET hydrolase PET6 from vibrio gazogenes. Protein Science. 2022;31:e4500.

Yoshida S, Hiraga K, Takehana T, Taniguchi I, Yamaji H, Maeda Y, et al. A bacterium that degrades and assimilates poly(ethylene terephthalate). Science. 2016;351:1196–9.

Zimmermann W, Billig S. Enzymes for the biofunctionalization of poly(ethylene terephthalate). Advances in Biochemical Engineering/Biotechnology. 2011;125:97–120.

SUPPORTING INFORMATION

Additional supporting information can be found online in the Supporting Information section at the end of this article.

How to cite this article: Berselli A, Carletti A, Menziani MC, Bhattacharya S, Castagna R, Parisini E, et al. The effect of ionic strength on PETase enzymes: An experimental and computational study. Protein Science. 2026; 35(1):e70386. https://doi.org/10.1002/pro.70386

5. Pielikums

Appendix 5

Perazzoli, A.; *** Bhattacharya, S.;** * Rozanov, L.; Marinello, S.; Van Aken, E.; Delanghe, J.; Castagna, R.; Parisini, E.; Gautieri, A.

Structure-guided Engineering of Fructosyl Peptide Oxidase Expands Access to Glycated Protein Substrates

Manuscript under review.

**These authors contributed equally to this work.*

Structure-guided Engineering of Fructosyl Peptide Oxidase Expands Access to Glycated Protein Substrates

Alessio Perazzoli[1,2,±], Shapla Bhattacharya[1,3,±], Leonid Rozanov[1], Sara Marinello[7], Elisabeth Van Aken[4], Joris Delanghe[5], Rossella Castagna[1,6], Emilio Parisini[1,2,*], Alfonso Gautieri[7,*]

[1] Department of Biotechnology, Latvian Institute of Organic Synthesis, Aizkraukles 21, LV-1006, Riga (Latvia)
[2] Department of Chemistry "G. Ciamician", University of Bologna, Via Gobetti 85, 40129 Bologna (Italy)
[3] Faculty of Materials Science and Applied Chemistry, Riga Technical University, Paula Valdena 3, LV-1048 Riga (Latvia)
[4] Department of Head and Skin, Ghent University, Corneel Heymanslaan 10, 9000 Ghent, Belgium.
[5] Department of Diagnostic Sciences, Ghent University, Corneel Heymanslaan 10, 9000 Ghent, Belgium.
[6] Dipartimento di Chimica, Materiali e Ingegneria Chimica "Giulio Natta", Politecnico di Milano, piazza L. da Vinci 32, 20133 Milano (Italy)
[7] Biomolecular Engineering Lab, Dipartimento di Elettronica, Informazione e Bioingegneria, Politecnico di Milano, Piazza Leonardo da Vinci 32, 20133 Milano (Italy)

[±] These two authors contributed equally to this work
[*] To whom correspondence should be addressed: Emilio Parisini (emilio.parisini@osi.lv), Alfonso Gautieri (alfonso.gautieri@polimi.it)

Keywords

Protein engineering, protein deglycation, access tunnel, fructosyl peptide oxidase, molecular modeling, advanced glycation end-products

Abstract

Fructosyl Peptide Oxidases (FPOX) are FAD-dependent enzymes that catalyze the oxidative cleavage of glycated amino acids and short peptides, yielding hydrogen peroxide, glucosone, and free amines. These enzymes are currently utilized in diabetes diagnostics, particularly for the quantification of glycated hemoglobin (HbA1c) and glycated albumin, by acting on glycation-derived peptides released via proteolysis. Despite their clinical utility, the therapeutic application of FPOX enzymes in reducing protein glycation *in vivo* is limited by their poor activity on full-length proteins due to steric hindrance at the active site. In this study, we applied a rational design approach to enhance the catalytic accessibility of *Phaeosphaeria nodorum* FPOX (*Pn*FPOX), building on a previously engineered variant with an expanded access tunnel. We targeted additional gating residues using Rosetta-based protein design and molecular dynamics simulations, followed by experimental screening of high-scoring mutants. One of our newly engineered variants, *Pn*FPOX-A14, demonstrated enhanced activity against a range of substrates, including glycated peptides and *ex vivo* glycated human tissues. Notably, *Pn*FPOX-A14 activity against glycated proteins highlights its potential as a therapeutic tool to mitigate the accumulation of Advanced Glycation End-products (AGEs), which contribute to aging and diabetic complications. Our findings establish a foundation for expanding the diagnostic and therapeutic applications of FPOX enzymes in glycation-related disorders.

Introduction

Fructosyl Peptide Oxidases (FPOX) (also referred to as Fructosyl Amino Acid Oxidases, FAOX)[1–3], are a class of FAD-dependent enzymes that are found in fungi and bacteria and that are able to cleave low molecular weight Amadori product (i.e., glycated amino acids and short peptides) to yield a free amine, glucosone and hydrogen peroxide[4].

Today, members of this class of enzymes are used in detection kits designed for the measurement of glycated haemoglobin (HbA1c), a long-term biomarker for diabetes management (lifespan ~ 3 months)[5,6]. Current diabetes monitoring kits are based on a first proteolytic digestion of HbA1c, which releases single amino acids from the protein, including its N-terminal glycation-prone valine. Then, the FPOX enzyme binds glycated valine and hydrolyzes it producing hydrogen peroxide which, in turn, is measured in a colorimetric assay using horseradish peroxidase and a suitable chromophore[7]. Using a similar mechanism, the FPOX enzymes find potential use in the detection of glycated albumin, a short to mid-term glycemic marker for diabetes (glycated albumin has a 3 weeks half-life)[8].

FPOX enzymes are also regarded as promising therapeutic tools for the prevention or the reduction of protein glycation in biological tissues[9,10]. Glycation is the spontaneous, non-enzymatic and irreversible reaction between a sugar moiety and a protein, leading to a covalent adducts, collectively referred to as Advanced Glycation End-Products (AGEs)[11]. This process leads to both direct and indirect damage, causing structural and functional alterations in biological macromolecules like proteins and nucleic acids[12,13], and triggering signaling pathways through the receptor for AGEs (RAGE). These changes impact inflammation-related pathways, particularly nicotinamide adenine dinucleotide phosphate (NADPH) oxidase and the nuclear factor κB (NFκB) pathway[14]. Ultimately, AGEs lead to a cascade of adverse clinical outcomes including arterial stiffening[15], atherosclerosis[16], nephropathy[17], retinopathy[18] and neuropathy[19]. So far, the use of FPOX to prevent protein glycation is precluded because these enzymes generally show limited activity on large peptides[20] and thus are believed to be inactive on whole proteins due to their buried active site and to the narrow tunnel that restricts access to the catalytic pocket.

The use of FPOX as diagnostic enzymes for diabetes monitoring and their use as therapeutic tools to reduce molecular ageing (i.e., the build-up of glycation products) would benefit from the development of improved FPOX enzymes that are capable of reacting with full-length glycated proteins. In previous works, our group has reported successful engineering campaigns aimed at widening the access tunnel to the catalytic site of *Phaeosphaeria nodorum* FPOX (*Pn*FPOX)[21–26]. These efforts led to a FPOX mutant (X02C) that presents high activity and stability together with a wider access tunnel with respect to the parental enzyme *Pn*FPOX [26].

In this study, we apply a rational design approach to further engineer the *Pn*FPOX enzyme variant X02C by addressing gating structural elements that were left unchanged in previous engineering attempts, with the goal to provide a wider access to the catalytic site. Our design process involved the use of targeted optimization using Rosetta-based design[27] and extensive molecular dynamics

(MD) simulations, followed by experimental validation of a small number of selected high-scoring mutants. In our validation procedure, we assessed the activity of the selected mutants against small glycated amino acids (fructosyl-Valine, fV). We tested the engineered enzymes on *ex vivo* glycated human eye lens tissues and found that that *Pn*FPOX-A14 was also able to reduce protein glycation, suggesting its potential as a therapeutic agent against molecular ageing.

Results and Discussion

Loop design and selection

To identify the most suitable regions for structural modification of the previously developed X02C design[26], we aligned the sequence (see Figure S1) and superimposed the structure (based on PDB ID: 8BJY) (Figure 1A) of this mutant with other FPOXs that showed high activity towards larger glycated substrates: *Pn*FPOX[28], FPOX-C[28], *An*FPOX-47[29]. The structure superimposition shows a common tridimensional arrangement with a distribution of the conserved residues over the entire sequences, especially in the key secondary structure motifs that define the FAD-binding region. The tunnel leading to the active site of the enzyme is defined by two loops and two helical structures (Figure 1B). The two loops, corresponding to residue K407-P413 and A344-H347 in the X02C enzyme (denoted as L1 and L2 in Figure 1B), are highly conserved within the FPOX family and contain critical catalytic residues. One helix, spanning residues I61-S67 (H1 in Figure 1B) was previously targeted in our efforts to expand the active site[21,26]. The largest structural component of the tunnel is a long alpha helix, encompassing residues K97-L114 (H2 in Figure 1B). Although this helix is structurally conserved across homologous enzymes, it exhibits sequence variability and was a primary focus for structural redesign.

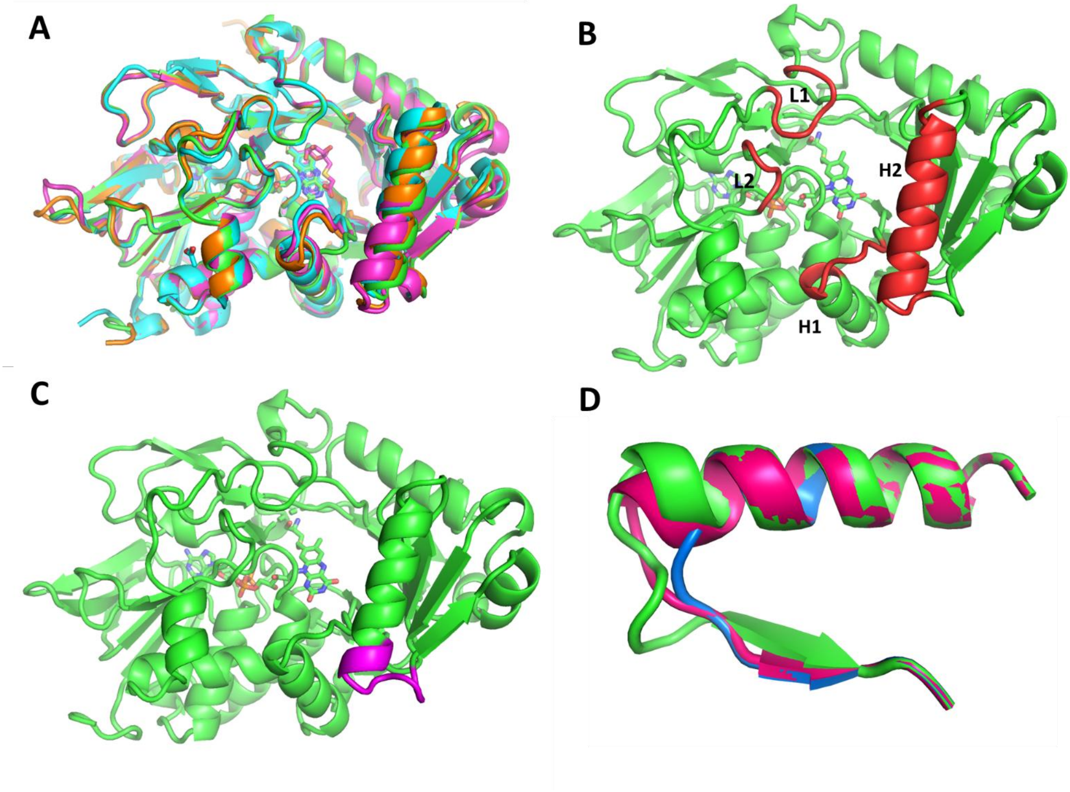

Figure 1 – Structures of FPOX enzymes. *(A) Structural alignment of X02C (green), PnFPOX (cyan), FPOX-C (orange) and AnFPOX-47 (pink), showing a high structural similarity. (B) Gating structures in the X02C enzyme (red color). L1 and L2 carry highly conserved catalytic residues, H1 was the focus of previous engineering efforts[26], while H2 is the focus of this work. (C) The pink region highlights the section of X02C enzyme that is removed and replaced with a shortened loop. (D) Side view of the X02C H2 helix (green) redesigned with a 2 amino acid loop (blue) or a 5 amino acid loop (red).*

To improve access to the catalytic pocket, we selected an 8-residue region (Figure 1C), corresponding to residues 110 to 117, for modification. This region was replaced with shorter loops ranging from 2 to 5 amino acids in length (Figure 1D). Additionally, we redesigned amino acids within a 5 Å radius of the removed amino acids to compensate for the loss of interactions due to the loop redesign. For each loop length, we generated 516 models, resulting in a total of 2’064 possible variants. The enzyme variants were labelled with a letter (A for loops with 2 amino acids, B for 3 amino acids, C for 4 amino acids, and D for 5 amino acids) followed by a ranking number based on their position in the Rosetta ranking (e.g., A1 through A516). For each loop length, the 20 highest-ranking structures were selected, amounting to 80 models in total. These selected variants were then subjected to molecular dynamics (MD) simulations for further analysis.

Design selection though MD simulations

The analysis of 100 ns MD simulations conducted at 300 K did not reveal any single variant or group of variants with significantly higher structural stability compared to the reference enzyme X02C. Specifically, we evaluated the Root Mean Square Deviation (RMSD) of the entire protein and the Root Mean Square Fluctuation of the redesigned loop (local RMSF), including three residues upstream and downstream of the modification site. To select a subset of mutants for further analysis, we assessed three parameters: the overall RMSD, the average local RMSF and the standard deviation of the local RMSF. A total of 11 variants exhibiting lower values than X02C for at least two of the three parameters were shortlisted for subsequent simulations at higher temperatures (350 K and 400 K).

Simulations at higher temperatures provided better differentiation of structural stability among the variants, revealing that for some engineered enzymes the structural elements near the remodelled section exhibited enhanced stability with respect to X02C. To quantify the stabilization effect, we performed linear regression analysis on the local RMSF values across the three temperatures. The angular coefficient from the regression was used as a metric for thermal stability (see Figure S2). All the selected variants exhibited a lower angular coefficient than X02C, indicating a smaller increase in RMSF values with rising temperatures. This trend suggests that the redesigned loops confer greater structural stability relative to the reference enzyme. Based on these findings, five variants with the lowest angular coefficient were selected for experimental validation, namely *Pn*FPOX-A2, *Pn*FPOX-A14, *Pn*FPOX-D7, *Pn*FPOX-D11, and *Pn*FPOX-D18.

Thermal stability

All enzyme variants showed good expression yield (14-25 mg/L) compared to the X02C parental enzyme (29 mg/L), with the exception of *Pn*FPOX-A2 (6 mg/L) (Table S2). The thermal stability of the parental enzyme X02C, wild-type *Pn*FPOX, and the engineered *Pn*FPOX variants was evaluated by circular dichroism (CD) spectroscopy (see Table 1 and Figures S3-S8). *Pn*FPOX showed a melting temperature (T_m) of 53.5 ± 0.1 °C, indicating lower conformational stability under thermal stress in comparison to the engineered variant X02C, which exhibited a T_m of 63.3 ± 0.1 °C, as previously reported[26]. Analysis by CD spectroscopy showed that the engineered *Pn*FPOX variants feature moderately enhanced Tm values. *Pn*FPOX-A2 exhibited a Tm of 53.9 ± 0.1 °C, which is essentially unchanged relative to the wild-type, suggesting that the mutations conferred minimal structural stabilization. Conversely, *Pn*FPOX-A14 (57.2 ± 0.1 °C), *Pn*FPOX-D7 (56.7 ± 0.1 °C), *Pn*FPOX-D11 (58.0 ± 0.1 °C), and *Pn*FPOX-D18 (56.3 ± 0.1 °C) displayed a consistent increase in Tm of approximately 2.8–4.5 °C relative to *Pn*FPOX. These observations indicate that the introduced mutations in *Pn*FPOX-A14, *Pn*FPOX-D7, *Pn*FPOX-D11, and *Pn*FPOX-D18 likely contribute to improved structural integrity. While none of the variants surpassed the thermostability of the X02C scaffold, the gains observed in several mutants represent meaningful improvements over the parental *Pn*FPOX enzyme. Notably, *Pn*FPOX-D11 exhibited the highest thermal stability among the engineered constructs (Table 1).

Table 1. *Melting temperature of the enzymes determined by CD spectroscopy*

Enzyme	T_m [°C]
*Pn*FPOX	53.5 ± 0.1
X02C	63.3 ± 0.1
*Pn*FPOX-A2	53.9 ± 0.1
*Pn*FPOX-A14	57.2 ± 0.1
*Pn*FPOX-D7	56.7 ± 0.1
*Pn*FPOX-D11	58.0 ± 0.1
*Pn*FPOX-D18	56.3 ± 0.1

Crystal structure analysis

While we attempted the crystallization of all the different *Pn*FPOX mutants described herein, we managed to obtain only crystals of *Pn*FPOX-D7, whose structure was solved at 2.1 Å resolution. *Pn*FPOX-D7 crystalized in P1 space group with two protein molecules in the asymmetric unit. Variant D7 was generated by deletion of eight residues from the C-terminal turn of helix IV of X02C and replacement with a shorter loop using Rosetta Remodel, and the corresponding electron density is shown in Figure S9. At a structural level, the overall architecture of the enzyme is maintained, showing that the introduced mutations did not interfere with conformational stability. Truncation of an α-helix by eight amino acids, followed by the reconstruction of a five amino acid loop, led to enlargement of the access tunnel relative to the parent enzyme. Overall, the PnFPOX-D7 structure is highly superimposable with the theoretical model of the obtained by Rosetta, with an RMSD of 0.728 Å. When comparing the *Pn*FPOX-D7 crystal structure with the crystal structure of X02B (PDB ID 8BJY), a previous generation mutant, the RMSD is 0.731 Å, suggesting small differences. Structural alignment shows changes in the orientation of one of the active site residues, E278 with side chain pointing away from FAD. Additional changes include the orientation of W235, its side chain in *Pn*FPOX-D7 being positioned closer to the cofactor than in X02B (3.9 Å vs. 7.7 Å, respectively). Moreover, *Pn*FPOX-D7 features a wider bottleneck (2.64 Å) compared to X02B (2.55 Å) and the wild-type PnFPOX (2.2 Å) (Figure S10). The tunnel dimension was analyzed with CAVER 3.0.3[30] software using a probe radius of 1.4 Å, a shell depth of 5 Å, and a shell radius of 2 Å.

Enzyme activity

We measured the specific activity of the variants using the substrate fructosyl-valine under optimized assay conditions (Table 2). Wild-type *Pn*FPOX exhibited a specific activity of 25.10 ± 0.71 U mg^{-1}, which served as the baseline for comparison. The closely related *An*FPOX-47 variant displayed comparable activity (23.14 ± 0.31 U mg^{-1}). The parent enzyme X02C displayed reduced activity (19.52 ± 0.31 U mg^{-1}) compared to *Pn*FPOX, which highlights a trade-off between thermostability and catalytic efficiency, as observed previously. Among the *Pn*FPOX variants, *Pn*FPOX-A14, *Pn*FPOX-D7, *Pn*FPOX-D11, and *Pn*FPOX-D18 demonstrated activities similar to the wild-type levels. Specifically, D7 and D18 showed the highest specific activities (26.22 ± 1.08 U mg^{-1} and 26.21 ± 0.87 U mg^{-1}, respectively), indicating that catalytic efficiency was retained. Similarly, *Pn*FPOX-D11 retained high specific activity (26.21 ± 1.27 U mg^{-1}). By contrast, the *Pn*FPOX-A2 variant exhibited significantly impaired catalytic activity (7.71 ± 10.69 U mg^{-1}), accompanied by a large standard deviation, suggesting instability and pointing to deleterious effects of the mutations on enzyme function or folding.

Table 2. *Comparison of the enzymatic specific activity (U/mg) on Fructosyl-valine. Tests were performed in triplicates.*

Enzyme	Specific activity (U/mg)
*An*FPOX-47	23.14 ± 0.31
*Pn*FPOX	25.10 ± 0.71
X02C	19.52 ± 0.31
*Pn*FPOX-A2	7.71 ± 10.69
*Pn*FPOX-A14	23.73 ± 0.14
*Pn*FPOX-D7	26.22 ± 1.08
*Pn*FPOX-D11	26.21 ± 1.27
*Pn*FPOX-D18	26.21 ± 0.87

Enzymatic activity on glycated tissues

The FPOX enzymes have also been proposed as therapeutic agents[24,31,32] for mitigating molecular ageing by targeting advanced glycation end-products (AGEs), which accumulate in human tissues over time and contribute to various age-related diseases. To explore the ability of engineered FPOX variants to deglycate complex biological matrices, we conducted *ex vivo* experiments using human cataractous lens fragments—a tissue known to accumulate high levels of AGE-modified crystallins.

Lens samples were incubated with different FPOX enzymes for up to 3 hours, and AGE content was assessed via fluorescence measurements at two characteristic emission peaks (449 nm and 490 nm) (Figure S11). All tested FPOX enzymes demonstrated deglycating activity, as evidenced by a measurable decrease in AGE-associated fluorescence intensity over time (Figure 2A and Table S2-S3). Among the tested variants, the engineered *Pn*FPOX-A14 mutant exhibited the highest deglycation efficiency, reducing fluorescence by approximately 85% relative to baseline levels (Figure 2B).

These findings indicate that FPOX enzymes, particularly the PnFPOX-A14 mutant, are capable of breaking AGE-protein crosslinks within dense, insoluble tissue matrices. This highlights their potential as a novel enzymatic approach for reversing protein glycation in age-related diseases and may serve as a foundation for the development of therapeutic strategies aimed at restoring protein function.

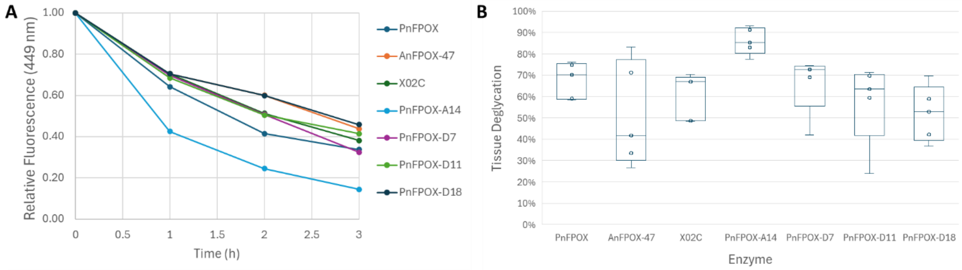

Figure 2 – FPOX Deglycation Activity on human tissue samples. *(A) Fluorescence Reduction at 490 nm. The deglycation activity of FPOX enzymes was evaluated by monitoring the decrease in AGE-related intrinsic fluorescence in human lens tissue samples. Normalized fluorescence intensity at 490 nm—a characteristic emission peak associated with AGEs—was measured over time. All tested FPOX variants demonstrated the ability to reduce fluorescence, indicating effective cleavage or modification of AGE moieties. Comparable trends were observed at the 449 nm emission peak; however, results are presented here for the 490 nm peak due to its higher signal intensity and better signal-to-noise ratio. (B) Deglycation Efficiency at 3-Hour Endpoint. The extent of tissue deglycation was quantified by comparing the fluorescence signal at the 3-hour time point to baseline values. All enzymes showed measurable activity, resulting in a reduction of AGE-related fluorescence. Among them, the engineered PnFPOX-A14 enzyme exhibited the*

highest deglycation efficiency, with a pronounced decrease in fluorescence intensity, highlighting its superior activity in modifying or removing AGE modifications from protein-rich tissue matrices. These results support the potential of FPOX enzymes, particularly the PnFPOX-A14 variant, as effective biocatalysts for reversing protein glycation in human tissues—a promising step toward therapeutic applications targeting AGE accumulation in degenerative and age-related conditions.

Molecular mechanism of protein deglycation

Normal mode analysis (NMA) was used to qualitatively assess the intrinsic dynamics of wild-type *Pn*FPOX and the engineered variants X02C and *Pn*FPOX-A14, offering a plausible explanation for the improved activity of *Pn*FPOX-A14 on larger substrates. Among the calculated modes, Modes 2 and 3 were selected for visualization and comparison because they capture functionally relevant motions near the active site. While the overall motion patterns were broadly similar across all three structures, notable differences in local flexibility were observed. In particular, *Pn*FPOX-A14 exhibited increased mobility in the α-helix at the entrance of the catalytic tunnel (residues 100–120), the region targeted during variant design to enhance substrate accessibility (Figures 3-4 and Supplementary Animation S12). Together, these results suggest that the engineered variant *Pn*FPOX-A14 has a more flexible tunnel entrance, which may facilitate binding and processing of bulkier glycated proteins, consistent with the design objective of improving activity toward larger substrates.

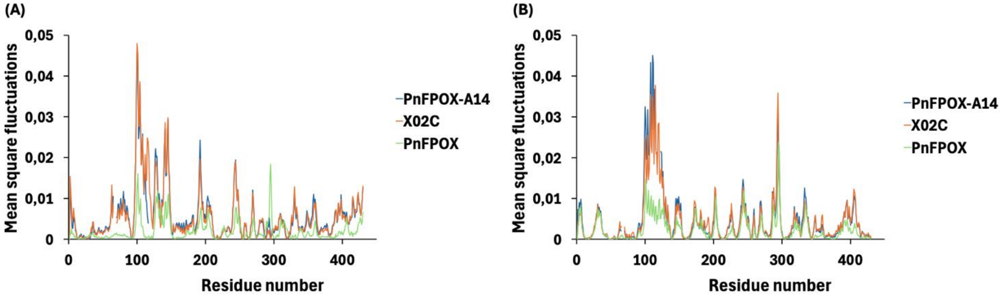

Figure 3 – Results of Normal Mode Analysis. *Mean-square fluctuation profiles for Mode 2 (A) and Mode 3 (B) of PnFPOX, X02C and PnFPOX-A14, with terminal residues removed.*

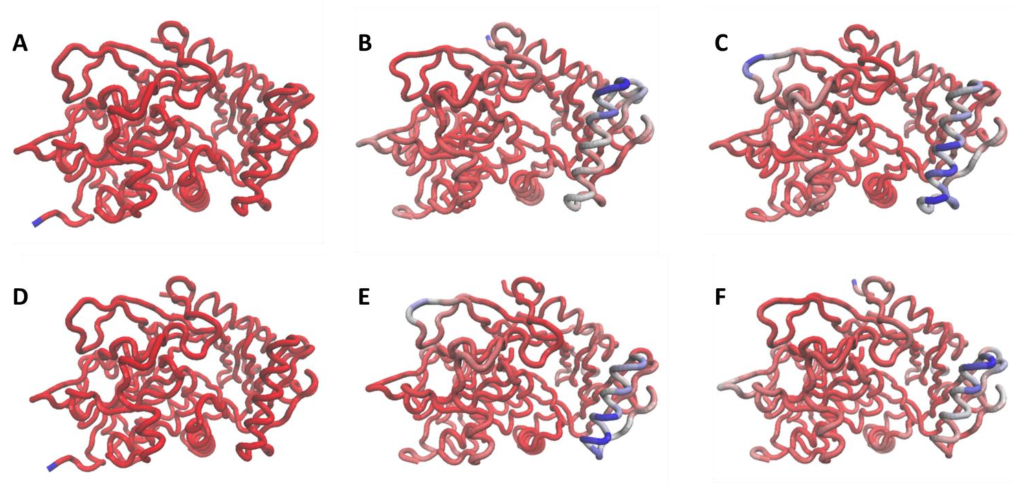

Figure 4 - Cartoon representations of the FPOX enzymes color-coded based on structural mobility. *Mobility is calculated by NMA, where blue color indicates mobile regions and red color indicates rigid regions. Figures A-C represents Mode 2 (for PnFPOX, X02C and PnFPOX-A14, respectively), while figures D-F represents Mode 3 (for PnFPOX, X02C and PnFPOX-A14, respectively).*

Conclusions

Using a rational *in silico* computational design and screening approach, we developed engineered FPOX enzymes with an expanded catalytic access tunnel, while preserving the enzyme's structural integrity and catalytic function. This design required remodeling the enzyme's backbone, a task unachievable with conventional techniques such as single-point mutagenesis and highly improbable through directed evolution. Moreover, we demonstrated that FPOX retains catalytic activity on intact proteins, providing a novel strategy for repairing proteins modified by advanced glycation end-products (AGEs). Recent studies by Delanghe *et al.*[33] have shown that *ex vivo* injections of FAOX enzymes reduce AGE levels in the retina and drusen, as evidenced by lighter coloration and decreased autofluorescence. These findings underscore the therapeutic potential of FPOX in addressing glycation-induced damage. By demonstrating FPOX's ability to deglycate proteins *in vitro*, our work contributes to advancing therapeutic approaches against molecular aging.

Our findings also mark a step toward developing *in vitro* diagnostic tools for glycated albumin and hemoglobin, leveraging a direct enzymatic oxidation system. These assays could address the increasing demand for efficient and cost-effective diabetes monitoring tests. By eliminating the requirement for preliminary protein digestion, the procedure is simplified, test times are reduced, and costs are lowered. More broadly, our strategy of modifying the access tunnel offers an efficient approach to designing novel enzymes, significantly reducing the time and cost associated with the experimental production and characterization of enzyme variants. Our work aligns with the growing interest in *in silico* methods for engineering improved enzymes tailored to industrial needs, supporting the broader goal of expanding biocatalyst use to enhance chemical processes sustainably, in line with Green Chemistry principles.

Materials and Methods

Enzyme structure redesign

The sequence alignment of *Pn*FPOX (PDB ID 5T1E)[28], FAOX-C[28], *An*FPOX-47 (PDB entry: 6A6S)[29] and X02C was performed using Clustal Omega software[34], and ESPript3[35] for the graphical representation. The structure of FAOX-C was obtained using AlphaFold[36], while the structure of X02C was obtained by homology modelling though Swiss Model[37] using the highly homologous enzyme X02B (PDB entry 8BJY) as template. The structural alignment was obtained with Pymol software[38].

The redesign of the X02C enzyme was carried out using Missing Loop[39] coupled with Remodel[40] functions of RosettaCommons. The Loop Modeling function was applied to close the gap of the removed backbone segment and to rebuild it using 2 to 5 residues. Since during loop reconstruction the start and the end point are fixed, we employed the kinematic closure protocol. In addition to Loop Modeling, we remodeled the 5 Å surrounding region to account for interactions that were lost upon truncation. This was done while freezing all those residues that are within 4 Å from the FAD cofactor and those highly conserved residues identified from the sequence alignment with homologous proteins. Repacking of an outer shell within 8 Å of the designable region was also allowed. Design runs were performed using the Rosetta Remodel function. A Blueprint file specified the positions designated for design, repacking, or freezing.

MD simulations

In order to identify the most stable mutations, we evaluated the structural stability of the designed enzymes via molecular dynamics simulations. To this end, 100 ns molecular dynamics simulations were conducted following previously published protocols[21,23,26,41,42].

We used AMBER19SB forcefield[43] for standard residues, water (TIP3P) and ions, while we used the general amber force field (GAFF)[44] for modelling the FAD cofactor. The molecular model was solvated with an 8 Å pad of TIP3P water and counter ions were added to neutralize the system charge, resulting in a final simulation box of ≈ 50’000 atoms for each mutant. Hydrogen mass repartitioning was applied, enabling a 4-fs time step. The system underwent 2’000 steps of energy minimization, followed by a 100-ps equilibration at 1 atm and 300 K using the NAMD software[45], a non-bonded cut-off of 9 Å, rigid bonds and particle-mesh Ewald long-range electrostatics, and a NPT ensemble. The system was minimized and equilibrated under constant pressure and temperature (NPT) conditions in order to relax the volume of the periodic box. During the equilibration simulation, the atoms of the backbone of the protein were restrained by a 1 kcal $mol^{-1}Å^{-2}$ spring constant. The 100 ns production runs were performed using a NVT ensemble whereby all the parameters (non-bonded cut-off, and PME) were the same as in the equilibration phase. To evaluate the thermal stability of the designed enzymes, additional MD simulations were conducted at 350 K and 400 K, while other parameters remained unchanged.

Model Evaluation

The designed models were assessed for structural stability via MD simulations. To evaluate the stability of the reconstructed loop and its impact on the overall structure of the enzyme, we analyzed the Root Mean Square Deviation (RMSD) of the entire protein and the Root Mean Square Fluctuation (RMSF) of the redesigned loop, including the three adjacent amino acids preceding and following the reconstructed loop. Specifically, we evaluated the average RMSD, average RMSF, median RMSF and RMSF Standard Deviation. These parameters were derived from the MD simulations conducted at 300 K, excluding the first 50 ns of the trajectory. Enzyme designs exhibiting at least three parameters out of four parameters with lower values than the X02C reference were selected for further evaluation. The 11 models that satisfied the specified requirements were subjected to 100-ns simulations at higher temperatures (350 K and 400 K). The five variants exhibiting the lowest rate of RMSF increase across temperature increments were selected for experimental validation[23].

Normal Mode Analysis

Normal mode analysis (NMA) was performed with ProDy [46], an open-source Python package that implements the Anisotropic Network Model (ANM) [47] to characterize collective motions in protein structures. An elastic network was built using Cα atoms, with harmonic springs connecting residue pairs within a 15 Å cutoff. The lowest non-trivial normal modes were calculated to probe the proteins' intrinsic dynamics. The resulting modes were visualized and qualitatively examined using Normal Mode Wizard (NMWiz), a VMD plug-in that provides color-coded maps of residue mobility and vectors indicating the direction of motion [46]. Mean-square fluctuations for each mode were also computed to generate residue-level mobility profiles along the protein sequence. This workflow was applied to wild-type PnFPOX (PDB ID: 5T1E), X02C, and PnFPOX-A14 to compare intrinsic flexibility and to assess the mobility of structural elements near the catalytic tunnel entrance.

Protein expression and purification

The DNA sequences of the designed FPOX mutants were cloned into a pET17(b) expression vector (Novagen, Malvern, Worcestershire, UK) to express C-terminal 6His-tagged proteins. All of the generated mutants (*Pn*FPOX-A2, *Pn*FPOX-A14, *Pn*FPOX-D7, *Pn*FPOX-D11, *Pn*FPOX-D18) and reference enzymes (*Pn*FPOX, X02C, *An*FPOX47) were transformed into chemically competent SHuffle T7 E.Coli cells (New England Biolabs, Ipswich, MA, USA). For each enzyme, 50 mL of overnight culture were inoculated into 4L of Luria-Bertani (LB) broth supplemented with ampicillin at a concentration of 100 mg/L and grown at 37°C until reaching an OD_{600} = 0.6. Protein expression was induced by supplementing the culture with 1-thio-β-d-galactopyranoside (IPTG) at final concentration of 0.1 mM, followed by an overnight incubation at 18 °C with shaking at 200 rpm. Cells were harvested using centrifugation and resuspended in lysis buffer (50 mM Tris-HCl pH 7.4, 150 mM NaCl and 5% glycerol) supplemented with 0.2mM protease phenylmethylsulfonyl fluoride (PMSF), 5 µL DNAse (Thermo Fisher Scientific, Waltham, MA, USA) and 0.5 mM flavin adenine dinucleotide (FAD). Upon lysing the cells via sonication on ice, the soluble fraction was collected and filtered through a 0.45-micron filter. The filtered solution was loaded onto a 5mL a HisTrap HP 5 mL (Cytiva, Marlborough, MA, USA) column pre-equilibrated with binding buffer (50 mM Tris-HCl pH 7.4, 150 mM NaCl, 5% glycerol, 20 mM imidazole). The column was washed with 10 column volumes of binding buffer and the samples were eluted with 10 column volumes of elution buffer (50 mM Tris-HCl pH 7.4, 150 mM NaCl, 5% glycerol 400 mM imidazole) using a gradient. The best fractions were collected and subjected to size exclusion chromatography using a Hiprep 26/60 Sephacryl S-100 column (Cytiva) pre-equilibrated with lysis buffer (50 mM Tris-HCl pH 7.4, 150 mM NaCl, 5% glycerol). Fractions containing the desired protein were collected, and their concentrations were measured using a NanoDrop spectrophotometer (Thermo Fisher Scientific, Waltham, MA, USA). The samples were flash frozen in liquid nitrogen and their purity was assessed by 12% SDS-PAGE.

Circular dichroism

Circular dichroism (CD) measurements were conducted on a Jasco J-1500 spectrophotometer at 20°C to evaluate the secondary structure and the thermostability of the enzymes. Spectra were averaged over five scans, performed with 5 µM samples of the various FPOX mutants diluted in a buffer solution containing 50 mM Tris pH 8.0, 150 mM NaCl, 5% glycerol. Measurements were carried out using a 1.0 mm pathlength quartz cuvette, with secondary structure analysis performed at 20°C across wavelength of 200–250 nm. Mean residue ellipticity [θ]MR was calculated and plotted versus wavelength. Thermal denaturation curves were generated with 5 µM samples in sealed 1.0 mm path length cuvettes. Denaturation was induced by raising the temperature at a rate of 1 °C/min from 5 to 95 °C. Ellipticity at 222 nm was recorded at 0.2 °C intervals using a 1-nm bandwidth and a 10-second response time. Midpoints of the thermal-denaturation curves (T_m) were determined by fitting the data to a sigmoidal transition curve using the Boltzmann function.

Protein crystallization

Crystals of the D7 mutant were grown at 4°C using the vapor diffusion method. A 2 µL aliquot of a 10 mg/ml protein sample was mixed with 2 µL of a solution containing 0.1 M Tris base pH 8.0, 5% ethanol, and 18-8% of different Polyethylene glycol (PEG) types, with best results obtained using PEG 8K. Crystals appeared within 1 day and were frozen in 25% (v/v) glycerol prior to X-ray diffraction data collection.

Data collection and processing

Diffraction data from the D7 mutant data were obtained using a Eiger2 XE 16M detector and a radiation of λ = 0.9763Å on the I03 beamline at the Diamond Light Source (Oxfordshire, United Kingdom). Data processing was performed using the with AutoPROC package[48]. Data collection and refinement statistics are summarized in Table S1.

Structure determination and refinement

For *Pn*FPOX-D7 structure determination, initial data was obtained through molecular replacement using Phaser, with the atomic coordinates of the X02B FPOX mutant (PDB code 8BJY) serving as the starting model. Refinement was performed through iterative rounds of manual adjustments in Coot and automated refinement using REFMAC5[49]. Water molecules were added manually and automatically using the refine tool in Coot from the CCP4 cloud package[50]. The final coordinates of the *Pn*FPOX-D7 mutant were deposited in the Protein Data Bank (PDB code: 9HJ5).

Enzymatic activity

The enzymatic activity of all mutants was assessed by measuring the amount of glucosone produced from the substrate over time at room temperature. Glucosone production was quantified by measuring absorbance at 322 nm (glucosone $\varepsilon_{322} = 149.25\ M^{-1}\ cm^{-1}$) using a CLARIOstar Plus platereader (BMG LABTECH) at 25 °C. Reaction mixtures (200 µL) contained 20 mM Tris HCl pH 7.4, 20 mM o-phenylenediamine, and 2 mM of fructosyl-valine as a substrate. After a 1 min pre-incubation, the enzyme was added at a final concentration of 1 mg/mL. One unit is defined as the amount of enzyme necessary for a reaction to produce 1 µmol of glucosone per minute. The specific activity of the enzyme is expressed as U/mg of the enzyme.

Enzymatic activity on glycated tissues

To check whether the FPOX mutants show activity on AGEs, we tested the various FPOX mutants on human cataractic lens fragments. Human lens fragments were obtained by phacoemulsification during cataract surgery. Lens fragments from around 20 patients were pooled and stored at -20°C. After freezing the fragments, small amounts were put in a black 96-well plate. Forty microliter of enzyme (1 mg/ml) was added to each well containing lens fragments. Immediately after adding the enzyme, a baseline UV-fluorescent spectrum was measured. After the baseline measurement the 96-well plate was incubated for 1 hour at 37°C. After each hour a new measurement was taken till 3 hours were passed. Each enzyme was tested on five different lens fragments[51]. The comparative results are depicted in a relative percentage in decrease (or increase) of the UV-fluorescent signal at two maxima (449 and 490 nm). Also a mean of the 5 wells is calculated. Since some AGEs are fluorescent in the UV spectrum, a decrease in fluorescence indicates their degradation.

Acknowledgements

The authors wish to thank the personnel of the I03 beamline at the Diamond Light Source (proposal number mx32544) for help with the data collection. E.P. thanks the Latvian Recovery and Resilience Fund (grant No. 74/OSI/ZG) and the Innovation Fund – Long-Term Research Programme (OSI_PIP_BioPhoT-2025/1-0091) funded by the Latvian Ministry of Economics for financial support. S.B. acknowledges the Latvian Recovery and Resilience Fund and the Latvian Institute of Organic Synthesis for student grants (No. ANM_OSI_DG_31 and No. IG-2026-04). R.C., E.P., and A.G. wish to thank the European Union's HORIZON-WIDERA-2023-ACCESS-04 programme for financial support under grant agreement 101159534 (WIDEnzymes). This manuscript reflects only the authors' views and opinions. Neither the European Union nor the granting authority can be considered responsible for them. We acknowledge the CINECA award under the ISCRA initiative (Grant code IsB26_W2EB and IsCa2_REZYME) for the availability of high-performance computing resources and support.

Author Contributions

Conceptualization: EP, AG; methodology: EVA, JD, RC, EP, AG; formal analysis: AP, SB, LR, EVA, JD, RC, EP, AG; investigation: EVA, JD, AP, SB, SM, LR; resources: EVA, JD, RC, EP, AG; data curation: AP, SB, LR, EVA, JD, SM, RC, EP, AG; writing, review and editing: AP, SB, LR, EVA, JD, RC, EP, AG; supervision: EVA, JD, RC, EP, AG; funding acquisition: RC, EP, AG. All authors have read and agreed to the published version of the manuscript.

Additional information

The authors declare that they have no conflicts of interest with the contents of this article.

References

1. Miura S, Ferri S, Tsugawa W, Kim S, Sode K (2008) Development of fructosyl amine oxidase specific to fructosyl valine by site-directed mutagenesis. Protein Engineering Design & Selection 21:233–239.

2. Kim S, Miura S, Ferri S, Tsugawa W, Sode K (2009) Cumulative effect of amino acid substitution for the development of fructosyl valine-specific fructosyl amine oxidase. Enzyme Microb. Technol. 44:52–56.

3. Miura S, Ferri S, Tsugawa W, Kim S, Sode K (2006) Active site analysis of fructosyl amine oxidase using homology modeling and site-directed mutagenesis. Biotechnol. Lett. 28:1895–1900.

4. Mennella C, Borrelli RC, Vinale F, Ruocco M, Fogliano V (2005) Substrate specificity of amadoriase I from Aspergillus fumigatus. Ann. N. Y. Acad. Sci. 1043:837–44.

5. Rahmatabadi SS, Bashiri H, Soleymani B (2024) A comprehensive review on fructosyl peptide oxidase as an important enzyme for present hemoglobin A1c assays. Biotechnol. Appl. Biochem.:1–14.

6. Lin H, Yi J (2017) Current status of HbA1c biosensors. Sensors 17:1798.

7. Collard F, Zhang J, Nemet I, Qanungo KR, Monnier VM, Yee VC (2008) Crystal structure of the deglycating enzyme fructosamine oxidase (Amadoriase II). Journal of Biological Chemistry 283:27007–27016.

8. Hatada M, Tsugawa W, Kamio E, Loew N, Klonoff DC, Sode K (2016) Development of a screen-printed carbon electrode based disposable enzyme sensor strip for the measurement of glycated albumin. Biosens. Bioelectron.:1–7.

9. Monnier VM, Wu X (2003) Enzymatic deglycation with amadoriase enzymes from Aspergillus sp. as a potential strategy against the complications of diabetes and aging. Biochem Soc Trans 31:1349–1353.

10. Song H, Ma H, Shi J, Liu Y, Kan C, Hou N, Han J, Sun X, Qiu H (2023) Optimizing glycation control in diabetes: An integrated approach for inhibiting nonenzymatic glycation reactions of biological macromolecules. Int. J. Biol. Macromol. 243.

11. Paul RG, Bailey AJ (1996) Glycation of collagen: The basis of its central role in the late complications of ageing and diabetes. International Journal of Biochemistry & Cell Biology 28:1297–1310.

12. Gautieri A, Redaelli A, Buehler MJ, Vesentini S (2013) Age- and diabetes-related nonenzymatic crosslinks in collagen fibrils: Candidate amino acids involved in Advanced Glycation End-products. Matrix Biology 34:89–95.

13. Snedeker JG, Gautieri A (2014) The role of collagen crosslinks in ageing and diabetes - the good, the bad, and the ugly. Muscles Ligaments Tendons J. 4:303–308.

14. Qiu H-Y, Hou N-N, Shi J-F, Liu Y-P, Kan C-X, Han F, Sun X-D (2021) Comprehensive overview of human serum albumin glycation in diabetes mellitus. World J. Diabetes 12:1057–1069.

15. Sell DR, Monnier VM (2012) Molecular Basis of Arterial Stiffening: Role of Glycation - A Mini-Review. Gerontology 58:227–237.

16. Del Turco S, Basta G (2012) An update on advanced glycation endproducts and atherosclerosis. Biofactors 38:266–274.

17. Goh SY, Cooper ME (2008) The role of advanced glycation end products in progression and complications of diabetes. Journal of Clinical Endocrinology & Metabolism 93:1143–1152.

18. Nagaraj RH, Linetsky M, Stitt AW (2012) The pathogenic role of Maillard reaction in the aging eye. Amino Acids 42:1205–1220.

19. Vincent AM, Russell JW, Low P, Feldman EL (2004) Oxidative stress in the pathogenesis of diabetic neuropathy. Endocr. Rev. 25:612–628.

20. Qian Y, Zheng J, Lin ZL (2013) Loop engineering of amadoriase II and mutational cooperativity. Appl. Microbiol. Biotechnol. 97:8599–8607.

21. Rigoldi F, Donini S, Torretta A, Carbone A, Redaelli A, Bandiera T, Parisini E, Gautieri A (2020) Rational backbone redesign of a fructosyl peptide oxidase to widen its active site access tunnel. Biotechnol. Bioeng.:3688–3698.

22. Rigoldi F, Gautieri A, Dalle Vedove A, Lucarelli AP, Vesentini S, Parisini E (2016) Crystal structure of the deglycating enzyme amadoriase i in its free form and substrate-bound complex. Proteins 84:744–758.

23. Rigoldi F, Donini S, Giacomina F, Sorana F, Redaelli A, Bandiera T, Parisini E, Gautieri A (2018) Thermal stabilization of the deglycating enzyme Amadoriase I by rational design. Sci. Rep. 8:3042.

24. Rigoldi F, Spero L, Dalle Vedove A, Redaelli A, Parisini E, Gautieri A (2016) Molecular dynamics simulations provide insights into the substrate specificity of FAOX family members. Mol. BioSyst. 12:2622–2633.

25. Rigoldi F, Donini S, Redaelli A, Parisini E, Gautieri A (2018) Review: Engineering of thermostable enzymes for industrial applications. APL Bioeng. 2:011501.

26. Estiri H, Bhattacharya S, Buitrago JAR, Castagna R, Legzdiņa L, Casucci G, Ricci A, Parisini E, Gautieri A (2023) Tailoring FPOX enzymes for enhanced stability and expanded substrate recognition. Sci. Rep. 13.

27. Kaufmann KW, Lemmon GH, Deluca SL, Sheehan JH, Meiler J (2010) Practically useful: what the Rosetta protein modeling suite can do for you. Biochemistry 49:2987–98.

28. Ferri S, Miyamoto Y, Sakaguchi-Mikami A, Tsugawa W, Sode K (2013) Engineering fructosyl peptide oxidase to improve activity toward the fructosyl hexapeptide standard for HbA1c measurement. Mol. Biotechnol. 54:939–943.

29. Ogawa N, Kimura T, Umehara F, Katayama Y, Nagai G, Suzuki K, Aisaka K, Maruyama Y, Itoh T, Hashimoto W, et al. (2019) Creation of haemoglobin A1c direct oxidase from fructosyl peptide oxidase by combined structure-based site specific mutagenesis and random mutagenesis. Sci. Rep. 9:942.

30. Chovancova E, Pavelka A, Benes P, Strnad O, Brezovsky J, Kozlikova B, Gora A, Sustr V, Klvana M, Medek P, et al. (2012) CAVER 3.0: A Tool for the Analysis of Transport Pathways in Dynamic Protein Structures. PLoS Comput. Biol. 8.

31. Wu X, Monnier VM (2003) Enzymatic deglycation of proteins. Arch Biochem Biophys 419:16–24.

32. Monnier VM, Wu X (2003) Enzymatic deglycation with amadoriase enzymes from Aspergillus sp. as a potential strategy against the complications of diabetes and aging. Biochem. Soc. Trans. 31:1349–53.

33. Delanghe JR, Diana J, Mavungu D, Beerens K, Himpe J, Bostan N, Speeckaert MM, Vrielinck H, Vral A, Broeke C Van Den, et al. (2024) Fructosyl Amino Oxidase as a Therapeutic Enzyme in Age-Related Macular Degeneration. :1–13.

34. Sievers F, Wilm A, Dineen D, Gibson TJ, Karplus K, Li WZ, Lopez R, McWilliam H, Remmert M, Soding J, et al. (2011) Fast, scalable generation of high-quality protein multiple sequence alignments using Clustal Omega. Mol. Syst. Biol. 7:539.

35. Robert X, Gouet P (2014) Deciphering key features in protein structures with the new ENDscript server. Nucleic Acids Res. 42.

36. Jumper J, Evans R, Pritzel A, Green T, Figurnov M, Ronneberger O, Tunyasuvunakool K, Bates R, Žídek A, Potapenko A, et al. (2021) Highly accurate protein structure prediction with AlphaFold. Nature 596:583–589.

37. Waterhouse A, Bertoni M, Bienert S, Studer G, Tauriello G, Gumienny R, Heer FT, De Beer TAP, Rempfer C, Bordoli L, et al. (2018) SWISS-MODEL: homology modelling of protein structures and complexes. Nucleic Acids Res. 46:W296–W303.

38. DeLano WL (2002) Pymol: An open-source molecular graphics tool. CCP4 Newsletter On Protein Crystallography 40:82–92.

39. Mandell DJ, Coutsias EA, Kortemme T (2009) Sub-angstrom accuracy in protein loop reconstruction by robotics-inspired conformational sampling. Nat. Methods 6:551–552.

40. Huang PS, Ban YEA, Richter F, Andre I, Vernon R, Schief WR, Baker D (2011) Rosettaremodel: A generalized framework for flexible backbone protein design. PLoS One 6:e24109.

41. Gautieri A, Rigoldi F, Torretta A, Redaelli A, Parisini E (2022) In Silico Engineering of Enzyme Access Tunnels. Methods in Molecular Biology 2397:203–225.

42. Rigoldi F, Gautieri A, Dalle Vedove A, Lucarelli AP, Vesentini S, Parisini E (2016) Crystal structure of the deglycating enzyme Amadoriase I in its free form and substrate-bound complex. Proteins: Structure, Function and Bioinformatics 84:744–758.

43. Tian C, Kasavajhala K, Belfon KAA, Raguette L, Huang H, Migues AN, Bickel J, Wang Y, Pincay J, Wu Q, et al. (2020) Ff19SB: Amino-Acid-Specific Protein Backbone Parameters Trained against Quantum Mechanics Energy Surfaces in Solution. J. Chem. Theory Comput. 16:528–552.

44. Wang JM, Wolf RM, Caldwell JW, Kollman PA, Case DA (2004) Development and testing of a general amber force field. J. Comput. Chem. 25:1157–1174.

45. Phillips JC, Braun R, Wang W, Gumbart J, Tajkhorshid E, Villa E, Chipot C, Skeel RD, Kalé L, Schulten K (2005) Scalable molecular dynamics with NAMD. J. Comput. Chem. 26:1781–1802.

46. Bakan A, Meireles LM, Bahar I (2011) ProDy: Protein Dynamics Inferred from Theory and Experiments. Bioinformatics 27:1575–1577.

47. Atilgan AR, Durell SR, Jernigan RL, Demirel MC, Keskin O, Bahar I (2001) Anisotropy of Fluctuation Dynamics of Proteins with an Elastic Network Model. Biophys. J. 80:505–515.

48. Vonrhein C, Flensburg C, Keller P, Sharff A, Smart O, Paciorek W, Womack T, Bricogne G (2011) Data processing and analysis with the autoPROC toolbox. urn:issn:0907-4449 67:293–302.

49. Murshudov GN, Skubák P, Lebedev AA, Pannu NS, Steiner RA, Nicholls RA, Winn MD, Long F, Vagin AA (2011) REFMAC5 for the refinement of macromolecular crystal structures. urn:issn:0907-4449 67:355–367.

50. Potterton L, Agirre J, Ballard C, Cowtan K, Dodson E, Evans PR, Jenkins HT, Keegan R, Krissinel E, Stevenson K, et al. (2018) CCP4i2: the new graphical user interface to the CCP4 program suite. urn:issn:2059-7983 74:68–84.

51. De Bruyne S, van Schie L, Himpe J, De Somer F, Everaert I, Derave W, Van den Broecke C, Huizing M, Bostan N, Speeckaert M, et al. (2021) A potential role for fructosamine-3-kinase in cataract treatment. Int. J. Mol. Sci. 22:3841.

Shapla Bhattacharya dzimusi 1997. gadā Indijā. *Banasthali Vidyapith* (Indija) ieguvusi bakalaura (2019) un maģistra (2021) grādu biotehnoloģijā, absolvējot studijas ar zelta medaļu. Kopš 2021. gada novembra strādājusi Latvijas Organiskās sintēzes institūtā, kas pēc tā reorganizācijas 2026. gada 31. maijā iekļāvās Nacionālajā pētniecības un inovāciju institūtā (*NIRI*; Latvija). Viņas pētījumi ir snieguši ieguldījumu plastmasu noārdošu enzīmu inženierijā un uzlabotu *FPOX* variantu izstrādē diabēta diagnostikai. Ir sešu recenzētu publikāciju autore, devusi ieguldījumu divu patentu izstrādē un saņēmusi apbalvojumus par izciliem stenda ziņojumiem "*BioDrug*" konferencē, *EMBO* semināros un *FEBS* konferencē. Zinātniskās intereses ietver proteīnu inženieriju, strukturālo bioloģiju, proteīnu biofiziku, enzīmu tehnoloģijas, kā arī ilgtspējīgu un biomedicīnisku biotehnoloģisko risinājumu izstrādi.

Shapla Bhattacharya was born in 1997 in India. She obtained her Bachelor's degree in Biotechnology (2019) and her Master's degree in Biotechnology (2021), graduating as a Gold Medalist, from Banasthali Vidyapith, India. Since November 2021, she worked at the Latvian Institute of Organic Synthesis, which became part of the National Institute of Research and Innovation (NIRI), Latvia, following its establishment on May 31, 2026. Her research has contributed to the engineering of plastic-degrading enzymes and the development of improved FPOX variants for diabetes diagnostics. She has authored six peer-reviewed publications, contributed to two patents, and received Outstanding Poster Awards at the BioDrug Conference, EMBO workshops, and the FEBS conference. Her research interests include protein engineering, structural biology, protein biophysics, enzyme technology, and the development of sustainable and biomedical biotechnological solutions.